Quantum Optics of Small Structures

Proceedings of the Colloquium,
Amsterdam, 23 and 24 September 1999

Quantum Optics of Small Structures

Edited by D. Lenstra, T.D. Visser and K.A.H. van Leeuwen

Preface

Parallel developments in quantum optics, atomic and molecular physics and condensed matter physics have realized the control of small optical systems, either in free space, in fibers, at interfaces or in semiconductors. Quantum optics of small material systems offers many exciting possibilities, both for fundamental research and for applications. In this context, the most obvious definition of small is: on the order of the wavelength. A more precise definition of is: sufficiently small that only one or a few optical modes come into play. This "mesoscopic" state of affairs implies that quantum noise is dominant. The material involved can be, on the one hand, semiconductor, glass, polymer, rare-earth or dye doped medium. On the other hand, trapped atomic or molecular species also present valuable model systems.

This text is taken from the document proposing the Royal Netherlands Academy of Arts and Sciences to adopt an international workshop on Quantum Optics of Small Structures as an official Academy Colloquium. The Colloquium was held 23 and 24 September 1999 in the 17th century "Trippenhuis" in the center of Amsterdam, home of the Academy. The meeting was organized by Daan Lenstra and Taco Visser of the Vrije Universiteit in Amsterdam. The present book contains most of the invited and contributed papers that were presented either as lectures or as posters.

One reason for organizing this workshop was the initiation of a research program - carrying the same name - funded by the (Dutch) Foundation for Fundamental Research on Matter (FOM) in 1998. Although internationally the above-described field is booming, often under the heading of Cavity Quantum Electrodynamics, a visible activity cluster in The Netherlands concentrating on fundamental optoelectronic research was clearly lacking. Through the new FOM-program a clear link should develop between modern optics and fields like microlasers, nanophysics and quantum optics. Thus, the Academy Colloquium provided the forum for international experts and Dutch scientists to meet and exchange ideas, and helped establishing a strong, coherent and visible research program in The Netherlands with considerable international impact.

The papers presented in these proceedings are organized in four parts, according to the four main sessions of the Academy Colloquium, but it must be emphasized that these parts have only vague boundaries. The collection of papers presented here will give the reader a good impression of the work that that has been presented and discussed during the workshop. We hope that with these papers all interested scientists who were not able to attend the Academy Colloquium on Quantum Optics of Small Structures can share in the synergy of that succesful meeting.

Daan Lenstra, Taco Visser and Ton van Leeuwen, Editors
Amsterdam, March 2000

Contents

Part I

Photonic Materials

G. Kurizki, A. Kofman, T. Opatrný and A. Kozhekin

Quantum Optics in Photonic Band Structures

Abstract

We address several generic quantum optical processes that undergo basic modifications in photonic crystals: (a) spontaneous formation of atomic coherence; (b) two-photon binding and entanglement; (c) self-induced transparency and gap solitons.

1   Introduction

Dielectric structures whose refractive index is periodically modulated on a submicron scale, known as photonic crystals (PCs) [1] are attracting considerable interest at present. Optical processes involving many atoms or excitons in such (PCs) undergo *basic modifications* as compared to the corresponding processes in open space or in bulk media. Here we survey our recent results on these modifications, which we attribute to three fundamental properties of PCs: (a) *Modified density of modes (DOM)*, which is characterized in PCs, by strong suppression of the background DOM within photonic band gaps (PBGs), by *sharp band-edge cutoffs* and *intra-gap* narrow lines associated with *defects* [1]. Many of the results detailed below (Sec. 2,3) stem from the failure of perturbation theory and the onset of strong field-atom (-exciton) coupling near sharp band edges or narrow lines in various PCs [2]. (b) *Band-edge and Bragg reflections*, which cause *spatial interference* effects in pulse propagation through the structure (Sec. 4). (c)*Photon effective masses*, which are associated with band-dispersion effects in PCs, and allow (*i*) photon "binding" to one or many atoms (Sec. 3), or (*ii*) Kerr-nonlinear inter-photon binding corresponding to quantum-soliton states [3].

2   Spontaneously formed coherence in PCs

A fundamental process relying on mode-density spectra in such structures is spontaneously induced coherence, due to strong coupling effects. We have developed an *exact* (non-perturbative) theory of near-resonant interaction with quantized fields having arbitrary DOM spectra [2]. This theory implies that an excited two-level system, whose resonance lies near a band-edge or narrow line in the DOM of the vacuum field would *spontaneously* evolve into a superposition of single-photon dressed states. This is a generalization of vacuum Rabi splitting, which occurs when the atom is near-resonant with a narrow mode. For a finite-width band, the states are pushed away from the edge, the ones ending up in the allowed band decay, whereas the ones pushed into the gap do not. Remarkably, there *can be multiple stable dressed states* in a *coherent superposition*, as many as there are gaps in the DOM.

In Fig.1 we show the splitting of an excited state $|e\rangle$ into superposed stable states, oscillating at band-gap frequencies ω_j, each consisting of superposed zero-photon $|e, 0\rangle$ and
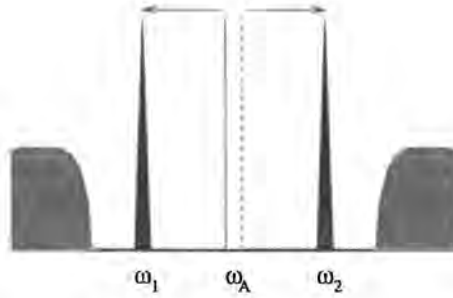
Figure 1: Splitting of an atomic excited state (dashed) into superposed stable dressed states in gaps (narrow lines) and decaying states (broad line shapes).

one-photon $|g, 1_\omega\rangle$ states, weighted by the field-dipole coupling $\kappa(\omega)$ and DOM $\rho(\omega)$

$$|e\rangle \rightarrow |\Psi_{1+2}\rangle = \sum_{j=1,2} c_j \left[|e, \{0\}\rangle \right.$$

$$\left. - \int \frac{\kappa\rho(\omega)}{\omega - \omega_j} |g, 1_\omega\rangle \, d\omega \right] \exp\left(\imath\omega_j t\right) \tag{1}$$

The amplitudes of these states, c_j, and their eigenfrequencies ω_j are *controllable* by the atomic transition detuning from cutoff and by the band DOM $\rho(\omega)$. This *spontaneous coherence control* opens interesting perspectives for lasing without inversion (LWI) in PCs containing 3-level atoms which have one resonant transition near a band edge.

3 Two-photon bound states by resonant interactions with atoms in PCs

The one-dimensional interaction of light with a system of atoms has been shown, by Bethe's ansatz, to produce multi-photon correlated states (referred to as string states) [4]. However, the energy of the two-photon correlated state in the string model is *exactly the same* as that of the unbound state. This makes any direct observation of the string two-photon state highly difficult.

We study here a principally new mechanism, whereby *group-velocity dispersion* in a 1D PC where light interacts with a collection of two-level atoms may lead to the production of a bound two-photon state with *lowered energy*, which makes its creation more favorable. The construction of two-photon solutions is then possible. Group-velocity dispersion may be obtained in a PC *outside* the band gap. This dispersion allows us to control the characteristics of the diphoton bound state.

We shall consider a one-dimensional structure, in which all the relevant mode frequencies ω are not too far from the atomic resonance Ω, i.e.

$$|\Omega - \omega| \ll \Omega \tag{2}$$

Introducing the notation $\lambda = k - k_0$, we can write the dispersion relation as

$$\omega(k) = \Omega + v_{gr}\lambda + \zeta\lambda^2 \tag{3}$$

Quantum Optics in Photonic Band Structures

where $v_{gr} = \partial\omega(k)/\partial k|_{k=k_0}$ is the group velocity (we use units $\hbar = c = 1$) and the last term corresponds to the inverse effective "mass" of the photon, $\zeta = 1/2\ \partial^2\omega(k)/\partial k^2|_{k=k_0}$ being the group velocity dispersion.

In what follows we shall use the field operator $\epsilon^+(x)$, which is the Fourier transform from k to x of the photon creation operator $a^+(\lambda)$

$$\epsilon(x) = \int_{-\infty}^{\infty} \frac{d\lambda}{2\pi} a(\lambda) e^{i\lambda x} \tag{4}$$

One-photon eigenstates of this system can be obtained in the Wigner-Weisskopf form [5]

$$\begin{aligned}
|\lambda\rangle &= \int_{-\infty}^{\infty} dx\ \hat{\Psi}^\dagger(\lambda, x)|0\rangle \\
&= \int_{-\infty}^{\infty} dx\ e^{i\lambda x} f(\lambda, x) \epsilon^+(x)|0\rangle \\
&+ \sum_j g_j(\lambda) S_j^+|0\rangle
\end{aligned} \tag{5}$$

where $S_j^\pm$ are the pseudospin operators of the j-th two-level atom, which is located at the point x_j and the field amplitude envelope $f(\lambda, x)$ and atomic excitation $g_j(\lambda)$ are obtained from the Schrödinger equation $\mathcal{H}|\lambda\rangle = \omega(\lambda)|\lambda\rangle$.

We search for a two-photon solution in the Bethe-ansatz form

$$\begin{aligned}
|\lambda_1, \lambda_2\rangle = \int\int_{-\infty}^{\infty} dx_1\, dx_2\ &\mathcal{A}_{\lambda_1,\lambda_2}(x_1 - x_2) \\
&\times \hat{\Psi}^\dagger(\lambda_1, x_1) \hat{\Psi}^\dagger(\lambda_2, x_2) \otimes |0\rangle
\end{aligned} \tag{6}$$

Here the Bethe factor $\mathcal{A}_{\lambda_1,\lambda_2}(x_1 - x_2)$ reflects the appearance of photon-photon correlations. The two-photon bound state "diphoton" corresponds to complex λ's

$$\begin{aligned}
\lambda_1 &= \Lambda + i\gamma \\
\lambda_2 &= \Lambda - i\gamma
\end{aligned} \tag{7}$$

with positive γ (the inverse width of the correlation length of the diphoton state).

We have the following equation for the inverse correlation length of the diphoton

$$\begin{aligned}
-4\zeta^2\gamma^3 + [2(v_{gr} + 2\zeta\Lambda)^2 \\
+ 4\zeta(v_{gr}\Lambda + \zeta\Lambda^2)]\gamma = \eta
\end{aligned} \tag{8}$$

To first order in the velocity dispersion ζ the inverse width of the diphoton may be estimated as

$$\gamma \approx \frac{\eta}{2v_{gr}^2 + 12v_{gr}\zeta\Lambda} \tag{9}$$

and is of the order of the inverse life time of the excited atomic level.

The binding energy of the diphoton state is

$$\mathcal{E} = -2\zeta\gamma^2 \tag{10}$$

Thus for positive group-velocity dispersion ζ, the energy of the diphoton state is lower than the energy of the unbound state. We have considered the case when corrections due to group-velocity dispersion are small $\zeta\Lambda \ll v_{gr}$. In this case the width of the diphoton state may be estimated to be close to the natural line-width of the resonant atoms, $\gamma \sim \eta \sim 10^9$ s^{-1}, and the group-velocity dispersion coefficient for the photonic band gap structure may be estimated to be inversely–proportional to the band-width of the forbidden zone $\Delta\omega \sim 10^{12}$ s^{-1}. In this case the binding energy of the diphoton would be of the order of 10^6 s^{-1}.

4 Self-induced transparency in photonic band structures: gap solitons near absorption resonances

Pulse propagation in a non-uniform resonant medium, e.g., a periodic array of resonant films, can destroy self-induced transparency (SIT) [6], because the pulse area is then split between the forward and backward (reflected) coupled waves, and is no longer conserved [7]. Should we then anticipate severely hampered transmission through a medium whose resonance lies in a reflective spectral domain (photonic band gap) of a PC (a Bragg reflector)? We have shown analytically and numerically [8, 9, 10] that it is possible for the pulse to overcome the band-gap reflection and produce SIT in a near-resonant medium embedded in a Bragg reflector. The predicted SIT propagation is a *principally new type of a soliton*, which does not obey any of the familiar soliton equations, such as the non-linear Schrödinger equation (NLSE) or the sine-Gordon equation.

Qualitatively, the SIT soliton in a PC may be understood as the addition of a near-resonant non-linear refractive index to the modulated index of refraction of the Bragg structure. When this addition compensates the linear modulation, then there is no band gap and soliton propagation is possible (Fig.2).

The proposed mechanism of gap solitons is revealed in a periodic array of thin layers of *resonant two-level systems* (TLS) separated by half-wavelength nonabsorbing dielectric layers, i.e., a *resonantly absorbing Bragg reflector* (RABR). Such a RABR has been shown by us to have, for *any* Bragg reflectivity, a vast family of stable solitons, both standing and moving [9, 10]. As opposed to the 2π-solitons arising in self induced transparency, i.e., resonant field – TLS interaction in a uniform medium, gap solitons in a RABR can have an *arbitrary* pulse area. The main innovation of our findings is that they demonstrate an unexpected property of a RABR with active layers. The RABR with thin active layers provides, to the best of our knowledge, the first example of a nonlinear optical medium in which *stable* bright and dark solitons exist for the *same values* of the model's parameters (at different frequencies).

The periodic grating gives rise to band gaps in the system's linear spectrum, i.e., the medium is totally reflective for waves whose frequency is inside the gaps. The central frequency of the fundamental gap is $\omega_c = k_c c/n_0$, c being the vacuum speed of light, and the gap edges are located at the frequencies $\omega_{1,2} = \omega_c(1 \pm a_1/4)$, where a_1 is the grating modulation
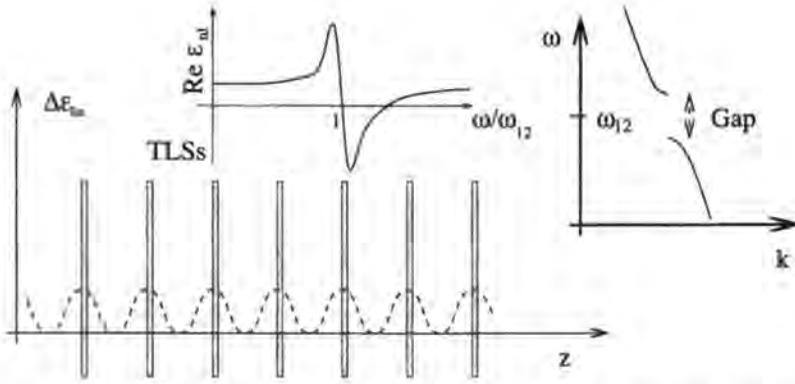
Figure 2: The first-harmonic modulation $\Delta\epsilon_1 \cos 2kz$ of the linear refractive index (dashed curve) in a structure of periodically alternating layers. This modulation can be canceled by the near-resonant nonlinear response Re ϵ_{nl} (inset), if it has the opposite sign to $\Delta\epsilon_1$ at the TLS positions.

depth. We further assume that *very thin* TLS layers (much thinner than $1/k_c$) whose resonance frequency ω_0 is close to the gap center ω_c, are placed at the maxima of the modulated refraction index. In other words, the thin active layers are placed at the points z_{layer} such that $\cos(k_c z_{layer}) = \pm 1$. Quantum wells embedded in Bragg mirrors are adequately described as TLS layers.

The electric field $E(z,t)$ can be decomposed into cosine and sine spatial components, having the dimensionless slowly varying amplitudes Σ_+ and Σ_-, respectively,

$$
\begin{aligned}
E(z,t) \;=\; &\hbar(\mu\tau_0)^{-1} \left(\text{Re} \; \left[\Sigma_+(z,t)e^{-i\omega_c t}\right] \cos k_c z \right. \\
&\left. - \; \text{Im} \; \left[\Sigma_-(z,t)e^{-i\omega_c t}\right] \sin k_c z \right),
\end{aligned} \tag{11}
$$

where μ is the transition dipole moment of the TLS, and the characteristic absorption time of the field by the TLS is $\tau_0 = n_0 \mu^{-1}\sqrt{\hbar/2\pi\omega_c\varrho_0}$, with ϱ_0 being the TLS density (averaged over z).

The equations for the field envelope in the symmetric mode Σ_+ and the polarization envelope P form a *closed system*,

$$
\begin{aligned}
\frac{\partial^2 \Sigma_+}{\partial \tau^2} - \frac{\partial^2 \Sigma_+}{\partial \zeta^2} \;=\; &-\eta^2 \Sigma_+ + 2i(\eta - \delta)P \\
&- 2\sqrt{1 - |P|^2}\, \Sigma_+,
\end{aligned} \tag{12}
$$

$$
\frac{\partial P}{\partial \tau} = -\; i\delta P \; -\sqrt{1 - |P|^2}\, \Sigma_+, \tag{13}
$$

where dimensionless time τ, coordinate ζ, and detuning δ are defined as follows:

$$
\tau \equiv t/\tau_0, \; \zeta \equiv (n_0/c\tau_0)\, x, \; \delta \equiv (\omega_0 - \omega_c)\tau_0. \tag{14}
$$

The dimensionless modulation strength η is the ratio of the TLS absorption distance to the Bragg reflection distance, which can be expressed as $\eta = a_1\omega_c\tau_0/4$. The envelope of the antisymmetric field component Σ_- is driven by $\partial P/\partial \zeta$.
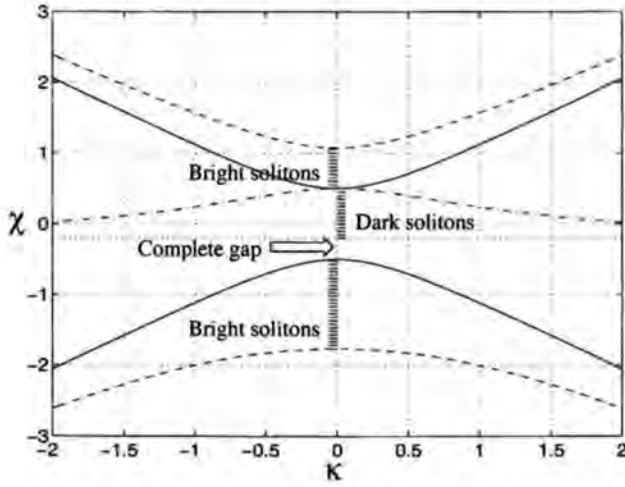
Figure 3: The dispersion curves (dimensionless frequency χ versus dimensionless wavevector k) at $\eta = 0.5$ and $\delta = -0.2$. The solid lines show the dispersion branches corresponding to the "bare" (noninteracting) grating, while the dashed and dash-dotted lines stand for the dispersion branches of the grating "dressed" by the active medium. The frequency bands that support the standing dark and bright solitons are shaded. The arrow indicates a complete gap, where no field propagation takes place.

The spectrum produced by the linearized version of Eqs. (12) and (13) is obtained on assuming the TLS population to be uninverted; we then arrive at the dispersion relation for the wavenumber κ and frequency χ. Different branches of the dispersion relation are shown in Fig. 3. The roots $\chi = \pm\sqrt{\kappa^2 + \eta^2}$ (corresponding to the solid lines in Fig. 3) originate from the driven equation for Σ_- and represent the dispersion relation of the Bragg reflector with the gap $|\chi| < \eta$, that does not feel the interaction with the active layers. The important roots are described by the dashed and dash-dotted lines; they will be shown to correspond to bright or dark solitons in the indicated (shaded) bands.

Stationary solutions for the symmetric-mode field envelope Σ_+ and polarization envelope P are sought in the form $\Sigma_+ = e^{-i\chi\tau}S(\zeta)$ and $P = i\,e^{-i\chi\tau}\mathcal{P}(\zeta)$ with real $\mathcal{P}$ and S. Bright solitons can be shown to appear in two frequency bands χ; the lower band being $\chi_1 < \chi < \min\{\chi_2, -\eta, \delta\}$, and the upper band $\max\{\chi_1, \eta, \delta\} < \chi < \chi_2$, where the boundary frequencies $\chi_{1,2}$ are given by $\chi_{1,2} \equiv (1/2)\left[\delta - \eta \mp \sqrt{(\eta + \delta)^2 + 8}\right]$. The lower band exists for all values $\eta > 0$ and δ, while the upper one only exists for $\delta > \eta - 1/\eta$, which follows from the requirement $\chi_2 > \eta$. An example of bright solitons is depicted in Fig. 4. Note that, depending on the parameters η, δ and χ, the main part of the soliton's energy can be carried either by the Σ_+ or the Σ_- mode.

Dark solitons (DS's) are obtained similarly to the bright ones. The condition for their existence determines the following frequency interval χ (η is defined to be positive): $\max\{\delta, -\eta\} < \chi < \min\{\chi_2, \eta\}$, and $\delta < \eta$. The DS frequency range is marked by shading (to the right
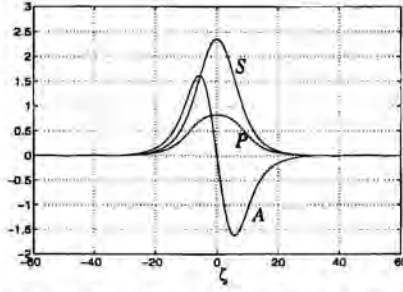
Figure 4: A typical example of a bright soliton. The variables S, $\mathcal{P}$, and $\mathcal{A}$ are plotted as a function of ζ for the parameters $\eta = 0.2$, $\delta = -2$, and $\chi = 0.4$.
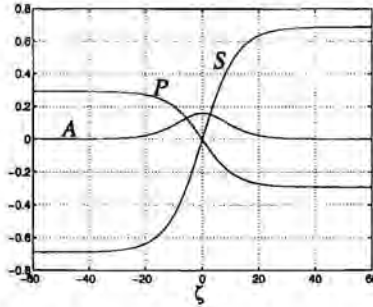
Figure 5: A typical example of a dark soliton, presented in terms of the variables S, $\mathcal{P}$ and $\mathcal{A}$. The parameters are $\eta = 0.6$, $\delta = -2$, and $\chi = 0.25$.

from zero) in Fig. 3. An example of a DS amplitude in the Σ_+ mode, together with the corresponding quantities $\mathcal{P}$ and $\mathcal{A}$, are plotted in Fig. 5. The DS frequency band *always coexists* with one or two bands supporting the bright solitons. Quite naturally, the bright and dark solitons cannot have the same frequency.

Let us now discuss the experimental conditions for the realization of the solitons. Excitons in periodic quantum wells can, under certain conditions (such as low densities [11]) be described as effective two-level systems (TLS's). We consider their surface density to be $\approx 10^{10} - 10^{11}$ cm^{-2}. Structures occupying a region of approximately 100 absorption lengths would require a device of the total width of approximately 1 mm to 1 cm, which corresponds to $\approx 10^3$ to 10^4 unit cells. The modulation of the refraction index can be as high as $a_1 \approx 0.3$, so that the parameter η can vary from 0 to 10^2. The intensities of the applied laser field corresponding to $\Sigma_\pm \approx 1$ are then of the order $10^6 - 10^7$ W/cm^2. The dephasing time is currently $1/\Gamma_2 \approx 10^{-13}$ s. Decreasing the dephasing rate appears to be the main experimental challenge.

5 Conclusions

Strong field-atom coupling near band-edge cutoff or a narrow defect line in a PC has been shown to allow unprecedented control of the following properties: (a) *Single-atom* spontaneously-induced *coherence*, which can give rise to lasing without inversion (LWI). (b) Photon binding, resulting in stable propagation in resonant media has been connected with photon effective masses. (c) Gap solitons have revealed their capacity for "filtering" undesired pulse shapes and creating self-induced "cavities".

The above novel features offer the first glimpses into the remarkable possibilities offered by field confinement in PCs for the design and control of coherent/cooperative processes.

References

[1] E. Yablonovitch. J. Opt. Soc. Am. B 10(1993) 283–302
[2] A. Kofman, G. Kurizki, B. Sherman. J. Mod. Opt. 41(1994) 353–384
[3] Z. Cheng, G. Kurizki. Phys. Rev. Lett. 75(1995) 3430–3433
[4] V.I. Rupasov, V.I. Yudson. Sov. Phys. JETP 60(1984) 927–934
[5] V. Weisskopf, E. Wigner. Z. Phys. 63(1930) 54–73
[6] S.L. McCall, E.L. Hahn. Phys. Rev. 183(1969) 457–485
[7] A. Maimistov, A.M. Basharov, S.O. Elyutin, Yu.M. Sklyarov. Phys. Rep. 191(1990) 1–108
[8] A. Kozhekin, G. Kurizki. Phys. Rev. Lett. 74(1995) 5020–5023
[9] A. Kozhekin, G. Kurizki, B. Malomed. Phys. Rev. Lett. 81(1998) 3647–3650
[10] T. Opatrný, B.A. Malomed, G.Kurizki. Phys. Rev. E (1999) in press
[11] G. Khitrova, H.M. Gibbs, F. Jahnke, M. Kira, S.W. Koch. Rev. Mod. Phys. (1999) in press
[12] A.G. Kofman, G. Kurizki. Opt. Commun. 153(1998) 251–256

Author's address

G. Kurizki, A. Kofman and T. Opatrný:
Department of Chemical Physics,
Weizmann Institute of Science,
761 00 Rehovot,
Israel;

T. Opatrný:
Department of Theoretical Physics,
Palacký University,
Svobody 26, 779 00 Olomouc,
Czech Republic;

A. Kozhekin:
Institute of Physics and Astronomy,
University Aarhus,
DK-8000,
Denmark.

M. Doosje, B.J. Hoenders and J. Knoester

Photonic Band-Gap Optimisation in Inverted FCC Photonic Crystals

Abstract

We present results of band-structure calculations for inverted photonic crystal structures. We consider a structure of air spheres in a dielectric background, arranged in an FCC lattice, with cylindrical tunnels connecting each pair of neighbouring spheres. The width of the band gap is optimised by applying a gradient search method and varying two geometrical parameters: the ratios R/a and R_c/R, where a is the lattice constant, R the sphere radius and R_c the cylinder radius. We find that the maximal gap width in this type of photonic-crystal structure, with air spheres and cylinders in silicon, is $\Delta\omega/\omega_0 = 9.59\%$.

1 Introduction

Photonic crystals, and their effect on the propagation of electromagnetic waves, have been studied intensively over the past few decades. A photonic crystal is a material with a spatially periodic dielectric function $\varepsilon(\mathbf{r})$. Its dispersion relation $\omega(\mathbf{k})$, i.e. the photonic band structure, shows *photonic band gaps* between the bands, characterised by their central frequency ω_0 and spectral width $\Delta\omega$. The investigation of this type of dielectric structures, possessing large band gaps, is motivated e.g. by the desired ability to control spontaneous emission of radiation from atoms [1].

A new type of photonic crystal is the inverted FCC photonic crystal, consisting of a regular structure of spherical air holes in a dielectric medium [2, 3]. These air-sphere crystals are created using dried (polystyrene or silica) colloidal crystals, also known as artificial opals. Their structure is usually a close-packed ($\phi = 74\%$) stacking of colloidal spheres. At the stage of thermal annealing (sintering) of the artificial opal, the volume-filling fraction increases above 74%. This effect is modelled by means of cylindrical connections between each pair of neighbouring spheres. After sintering, the empty voids in the opal structure are infiltrated with titania (TiO_2). Then the original colloidal spheres are removed by chemical etching [2]. This air-sphere crystal, with a lattice constant matching the range of wavelengths of visible and near-infrared light, provides a good opportunity to establish a photonic band gap. However, a full photonic band gap has not been measured in these crystals yet, probably due to the use of materials like titania [2] or carbon [3], whose index of refraction n is not sufficiently high.

In this work we present results of the optimisation of the calculated photonic band gap in the FCC structure of air spheres with connecting air tunnels, surrounded by silicon. The photonic band structure of these crystal structures were calculated by means of the
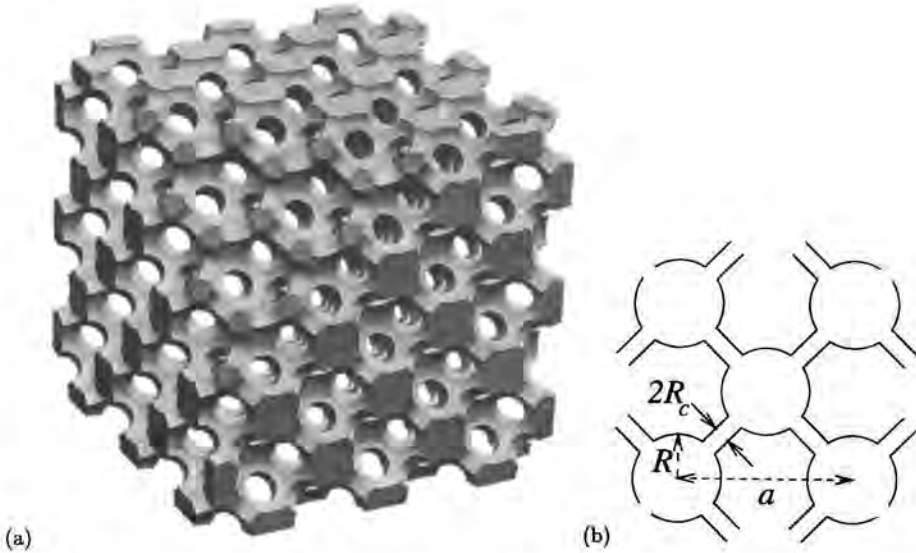
Figure 1: (a) Three-dimensional visualisation of an FCC air-sphere crystal with non-overlapping air spheres, each of them connected to all of its 12 nearest neighbours by cylindrical air tunnels. The particular structure shown here has geometrical parameters, which for a silicon background (grey) optimise the band gap (see section 3). (b) Schematic cross-section of the structure in Fig. 1(a) with the definition of the lengths a, R and R_c indicated.

plane-wave expansion method [4, 5]. Two parameters were varied in our band-structure calculations, namely the ratios R/a and R_c/R. Here R is the sphere radius, R_c is the cylinder radius and a is the lattice constant of the FCC lattice. The gap width increases substantially when the ratio R_c/R increases from zero to 0.4. By applying a gradient search method in combination with the variation of the two parameters mentioned above, we obtain the geometrical parameters for which the relative gap width $\Delta\omega/\omega_0$ reaches its maximum.

2   The method of calculation

We will consider the inverted opals described in the Introduction. We will use silicon (Si; $n = 3.415$) as our choice for the dielectric. To be specific, we consider an FCC structure, with lattice constant a, of non-overlapping air spheres of radius R, each of them connected to its twelve nearest neighbours by a cylindrical air tunnel of radius R_c. A three-dimensional visualisation of this structure is given in Fig. 1(a).

The crystal structure is represented by a Fourier series for the inverse dielectric function
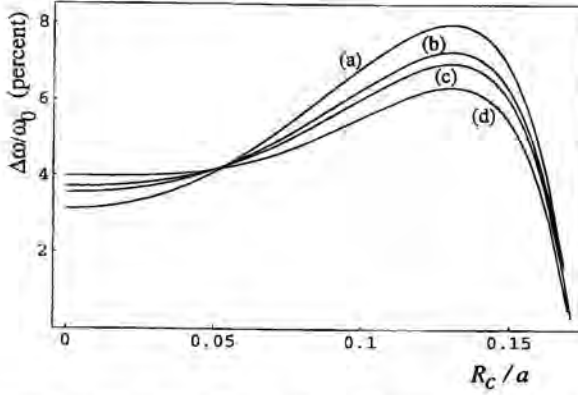
Figure 2: Relative width of the full photonic band gap between bands 8 and 9 in the FCC inverted opals, as a function of R_c/a. The background material is silicon (Si, $n = 3.415$). The number of plane waves used is $N = 339$. The four curves have been calculated for (a) $R/a = 0.3437$, (b) $R/a = 0.3486$, (c) $R/a = 0.3504$ and (d) $R/a = 0.3536$. For $R_c = 0$, this corresponds to $\phi = 68\%$, $\phi = 71\%$, $\phi = 72\%$ and $\phi = 74\%$, respectively.

$\eta(\mathbf{r})$:

$$\eta(\mathbf{r}) = \frac{1}{\varepsilon(\mathbf{r})} = \sum_m \eta_m \exp(-i\mathbf{g}_m \cdot \mathbf{r}), \tag{1}$$

where m labels the three-dimensional set of reciprocal-lattice vectors $\mathbf{g}_m$. We have derived analytical expressions for the coefficients η_m for the structure under consideration.

Also the magnetic field $\mathbf{H}$ is written as a Fourier series,

$$\mathbf{H}(\mathbf{r}, t) = \exp(i\omega t) \sum_m \sum_{\mathbf{k}} \sum_{\lambda=1}^{3} h_m^\lambda(\mathbf{k}) \hat{\mathbf{u}}_m^\lambda \exp(-i\mathbf{k}_m \cdot \mathbf{r}), \tag{2}$$

known as the Bloch-wave expansion. Here, for any label m, $\{\hat{\mathbf{u}}_m^1, \hat{\mathbf{u}}_m^2, \hat{\mathbf{u}}_m^3\}$ is a right-handed orthonormal basis for Euclidian space, chosen such that $\hat{\mathbf{u}}_m^3 \parallel \mathbf{k}_m$. Furthermore, $\mathbf{k}_m = \mathbf{k} + \mathbf{g}_m$ and the summation over $\mathbf{k}$ denotes the summation over all wave vectors within the first Brillouin Zone.

Substitution of the Fourier expansions for $\eta(\mathbf{r})$ and $\mathbf{H}(\mathbf{r}, t)$ into Maxwell's equations yields the matrix equation

$$\sum_l k_l k_m \eta_{m-l} \begin{bmatrix} \hat{\mathbf{u}}_m^2 \cdot \hat{\mathbf{u}}_l^2 & -\hat{\mathbf{u}}_m^2 \cdot \hat{\mathbf{u}}_l^1 \\ -\hat{\mathbf{u}}_m^1 \cdot \hat{\mathbf{u}}_l^2 & \hat{\mathbf{u}}_m^1 \cdot \hat{\mathbf{u}}_l^1 \end{bmatrix} \begin{bmatrix} h_l^1(\mathbf{k}) \\ h_l^2(\mathbf{k}) \end{bmatrix} = \left(\frac{\omega}{c}\right)^2 \begin{bmatrix} h_m^1(\mathbf{k}) \\ h_m^2(\mathbf{k}) \end{bmatrix}, \quad k_m = |\mathbf{k}_m|. \tag{3}$$

The $\lambda = 3$ components of the magnetic field vanish because $\nabla \cdot \mathbf{H} = 0$. The eigenvalues of the matrix involved in this equation, are real-valued, non-negative quantities, to be identified with $(\omega/c)^2$.
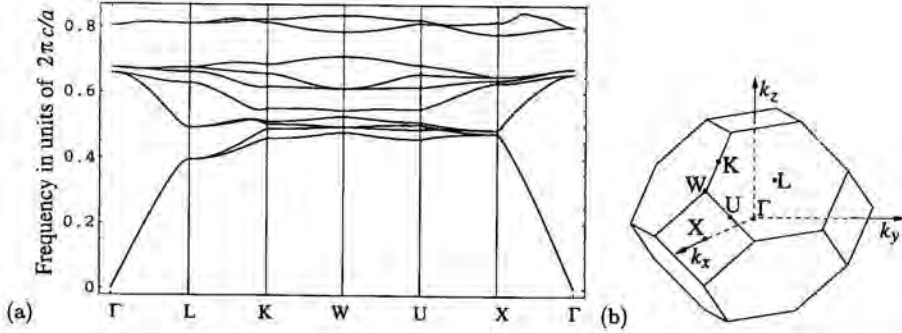
Figure 3: (a) Photonic band structure of an FCC inverted opal with silicon ($n = 3.415$) as dielectric medium and with the optimal parameters $R/a = 0.3201$ and $R_c/R = 0.398$. The optimal relative width of the full gap between the 8th and 9th bands is $\Delta\omega/\omega_0 = 9.59\%$ at $\omega_0/2\pi = 0.746c/a$. The volume-filling fraction of air spheres and cylinders in this structure is $\phi = 66.3\%$. The number of plane waves used is $N = 1037$. (b) The first Brillouin Zone for the FCC lattice (BCC in reciprocal space).

3 Results and discussion

Our main interest is the dependence of the relative width $\Delta\omega/\omega_0$ of the full photonic band gap between the 8th and 9th bands, on the parameters R/a and R_c/a. In Fig. 2, we plot the relative gap width as a function of R_c/a for four different values of R/a. These results were obtained using 339 plane waves. It is known that, for this type of crystal structure, one needs $N \sim 10^3$ plane waves in order to reach convergence of the band structure well below 1% [6]. We used such high values for N only when optimising the band gap and calculating the density of states (see below). The relative errors in the band gap at $N = 339$ appear to be in the order of 6%. Although this is by no means full convergence, it suffices to provide considerable insight in the behaviour of the band structure upon varying parameters, as we will see below.

From Fig. 2, we observe that at first, when the cylindrical air holes are very narrow, their effect on the gap width is rather small. While the main purpose of the tunnels between neighbouring air spheres in these inverted opal structures, is to serve as passageways through which the original colloidal material is removed, in addition these holes have a positive influence on the width of the band gap for larger values of R_c, as is observed in Fig. 2. For the crystal structure presently under consideration, the largest gap width is achieved around $R_c/R = 0.4$, and it tends to increase when the value of R/a decreases. Curve (d) in Fig. 2, which gives the dependence of the gap width on the cylinder radius for *close-packed* spheres, agrees well with the results of Busch and John [6]. A remarkable feature in Fig. 2 is the observation that the four curves nearly cross at one point for $R_c/a \approx 0.052$, where the gap width $\Delta\omega/\omega_0 \approx 4.2\%$. We were unable to establish whether this feature has any physical
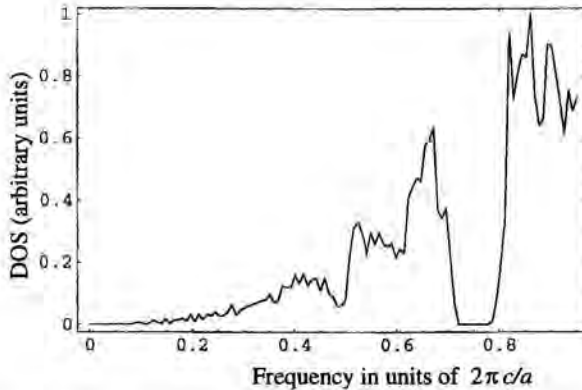
Figure 4: Density of states corresponding to the photonic band structure depicted in Fig. 3(a).

significance.

Now we turn to the optimisation of the relative width of the band gap, performing a two-parameter variation calculation, based on a gradient search method. This method consists of successively determining the gap width $f \equiv \Delta\omega/\omega_0$ and the gradient

$$\nabla f \equiv (\mathrm{d}f/\mathrm{d}(R/a), \mathrm{d}f/\mathrm{d}(R_c/R)),$$

for certain values of R/a and R_c/R, and adjusting R/a and R_c/R such that a step is taken in the direction of ∇f. Thus we reach the maximal value of f by following the path of steepest ascent.

In a first "crude" approach towards the maximal gap, we used band-structure calculations with $N = 339$, as before. We started at $(R/a = 0.3437, R_c/R = 0.37)$, which yielded the maximal gap width as shown in Fig. 2, curve (a). Following the path of steepest ascent, we reached $(R/a = 0.3200, R_c/R = 0.398)$, for which $f = 9.3\%$ and $\nabla f \approx 0$. The central frequency of the gap obtained in this way, is $\omega_0/2\pi = 0.744c/a$. The error in this result is in the order of 6%.

The calculated band structures depend significantly on the number of plane waves considered. It is accepted quite generally that for $N \sim 10^3$, the error in the results for the lowest-lying photonic bands is well below 1% (for the type of crystals that we consider). Thus, a more reliable value for the gap width of our structure is obtained by doing the calculation using 1037 plane waves. This yields a value of $\Delta\omega/\omega_0 = 9.59\%$. Further fine-tuning of the optimum, using 1037 plane waves and starting from the optimum obtained above, yields negligible changes: $\Delta\omega/\omega_0 = 9.59\%$ at $(R/a = 0.3201, R_c/R = 0.398)$. We remark that with only 339 plane waves (which allows for much faster computing), the optimal parameters were determined very accurately, i.e. within a 0.1% margin.

The central frequency of the gap is $\omega_0/2\pi = 0.746c/a$. The photonic band structure for this geometry is shown in Fig. 3(a). The corresponding density of states is shown in Fig. 4.

This figure clearly demonstrates the existence of a full gap.

In general, the width of the photonic band gap depends strongly on the dielectric contrast and on the volume-filling fraction. We point out that for the optimised structure described above, the volume-filling fraction of silicon is only 33.7%, i.e., the optimal band gap occurs in a rather empty structure (see Fig. 1(a)). The controlled preparation and manipulation of such empty crystal structures will be a real challenge for material scientists and experimentalists. It will be worthwhile to investigate whether also for other classes of geometries such empty structures optimise the band gap.

References

[1] E. Yablonovitch. Phys. Rev. Lett. 58(1987) 2059–2062
[2] J.E.G.J. Wijnhoven, W.L. Vos. Science 281(1998) 802–804
[3] A.A. Zakhidov, R.H. Baughman, Z. Iqbal, C. Cui, I. Khayrullin, S.O. Dantas, J. Marti, V.G. Ralchenko. Science 282(1998) 897–901
[4] J.D. Joannopoulos, R.D. Meade, J.N. Winn. *Photonic crystals: Molding the flow of light.* Princeton University Press (1995)
[5] K.M. Ho, C.T. Chan, C.M. Soukoulis. Phys. Rev. Lett. 65(1990) 3152–3155
[6] K. Busch, S. John. Phys. Rev. E 58(1998) 3896–3908

Author's address

Institute for Theoretical Physics and Materials Science Centre,
University of Groningen,
Nijenborgh 4, 9747 AG Groningen,
The Netherlands.

Email address: B.J.Hoenders@phys.rug.nl

L. Kuipers, C. Peeters, E. Flück, M.L.M. Balistreri, A.M. Otter and
N.F. van Hulst

Looking into Photonic Structures with a Photon Scanning Tunnelling Microscope

Abstract

We present our first photon scanning tunnelling measurements of optical fields around tailor-made subwavelength structures. A new way to produce low-dimensional photonic crystals based on ion beam milling is also introduced.

1 Introduction

Already more than 50 years ago Purcell [1] realized that spontaneous emission from an atom could be strongly influenced by placing the atom in a cavity with dimensions of the order of the optical wavelength. Photonic crystals, by their nature, consist of building blocks of that dimension (see e.g. [2] (1D) and [3] (3D)) and also act as perfect mirrors in the direction of each stop gap. Thus, they are ideal candidates for gaining a high degree of control over spontaneous emission [4]. With the continued increase of possibilities for the production of submicron structures, it is therefore not surprising that photonic crystals for visible light have seen a tremendous research activity over the last few years. Here, we present focused ion beam (FIB) sputtering as a possible new tool for the production of the photonic structures.

Despite some notable exceptions [5, 6] most of the investigations of photonic materials are carried out with input-output measurements. In other words, light emerging from the material is monitored as a function of parameters of the incoming light (polarisation, wavelength, ...). The results are subsequently compared to theory. Here, we present our first steps to investigate light inside low-dimensional photonic crystals with a photon scanning tunnelling microscope (PSTM). Local studies have the distinct advantage over input-output investigations because they can directly determine the influence of heterogeneities on the optical field propagation.

2 Focused ion beam production of subwavelength photonic structures

Channel waveguides form the basis for our photonic structures. They consist of a Si_3N_4 ridge (height 22 nm & width 1.4 (m) on top of a 33 nm layer of Si_3N_4 on SiO_2. For a wavelength of 632.8 nm in air the only supported mode is the so-called TE_{00} mode with an in-plane
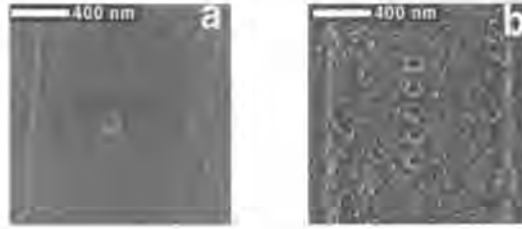
Figure 1: FIB image of subwavelength structures produced by FIB sputtering. A single air rod (a) and a periodic array of 5 air rods (b) have been fabricated in a channel waveguide.

polarisation. The effective index of refraction of this mode is 1.46, as calculated with the effective index method [7].

We have modified the waveguides by means of FIB sputtering. Figure 1a shows a FIB image of an air rod sputtered in a Si_3N_4 channel waveguide. The diameter of the rod is 110 nm. We have produced rods with diameters down to 30 nm. The minimally attainable diameter is not determined by the size of the focal spot ($\sim$ 10 nm) but by charging of the nonconducting Si_3N_4 during the sputter process. As a consequence, the diameter increases with increasing exposure. Separate measurements have confirmed that air rods produced with the FIB are perpendicular to the waveguide surface. As yet, we have not been able to establish the depth of the holes.

Figure 1b shows a FIB image of a periodic array of 5 air rods, each with a diameter of 90 nm. The diameter of the holes is the same for all holes to within the accuracy of the measurements from the FIB images ($\pm 5\%$). The distance between the centres of the air rods is 215 nm. The distance between the holes varies by less than 10 nm.

3   Photon scanning tunnelling microscopy of photonic structures

Figure 2 schematically depicts measurement with a PSTM on a waveguide structure. In the optical ray description light propagates through the waveguide by repeated total internal reflections. As a result an evanescent field is present above the waveguide surface. In the PSTM measurement a subwavelength aperture probe is held at a constant height above the sample surface. The height of the probe is such that it frustrates the evanescent field which, as a result, is transformed into a propagating wave. The output of the probe is monitored with a photomultiplier tube (PMT). As the probe is raster scanned over the surface an image can be constructed of the optical fields in the sample (see e.g. [8] and [9]). A topographic image is simultaneously obtained with the optical image from the height adjustments necessary to keep the height constant. The probe is fabricated from a single mode fibre by standard fibre pulling in order to obtain a sharp apex. In order to minimize stray light entering the probe it is covered with Al. The definition and throughput of the resulting probe is then further improved by sputtering its end face with a focused ion beam (FIB) [10].

Figures 3a and b show a height image (a) and an optical image (b) simultaneously ob-
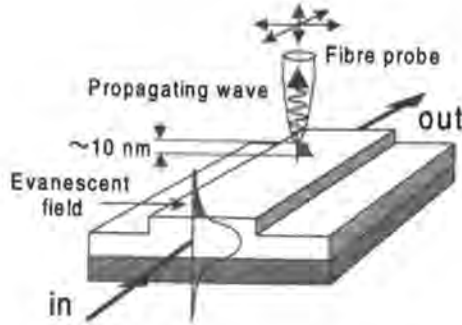
Figure 2: Schematic representation of a PSTM measurement. An aperture probe is raster scanned over the sample while the height above the surface is kept constant at ∼ 10 nm. As a result the evanescent field above the sample is frustrated and picked up by the probe.

tained with a PSTM around the hole depicted in fig. 1a. In the topographical image the hole is clearly visible in the centre of the waveguide. Light is coupled into the waveguide structure by means of a microscope objective (the direction of the incoming light is from top to bottom). In the optical image around the hole we observe a pattern attributed to interference of scattered and unscattered light. The fringes have a separation of 217 nm just in front of the hole. Within the experimental accuracy this value is equal to the expected half of the wavelength as determined by the effective index of the channel waveguide ($n_{eff} = 1.46$). Note that other techniques would not be able to resolve this interference pattern. It is clear that the light intensity just in front of the hole is higher than further away. We attribute the increase in intensity close to the hole to light scattered directly out of the waveguide into the aperture probe. The interference pattern is not mirror symmetric with respect to the axis of the waveguide. This asymmetry is probably the direct result of the hole being off-axis by ∼ 100 nm.

Figures 3c and 3d show the height image (c) and an optical image (d) obtained with the PSTM of the structure depicted in fig. 1b. Qualitatively the same optical pattern is observed as in the case of a single hole. Here however we observe two pronounced maxima 'followed' by a long (> 1μm) shadow. The two maxima and the three local maxima inside the shadow region are located at the 'down stream' air- Si_3N_4 interface of the air rods. Again the mirror symmetry is broken even though the array is less than 30 nm off-axis.

Figure 4 (left panel) shows a line trace of the detected optical intensity as a function of the position along the waveguide. It shows the interference fringes mentioned previously with an increased intensity and modulation depth close to the holes. A beating pattern is also just visible. The beating becomes clearer when the boxed area is Fourier transformed. The result of this transform is depicted in the right panel. It shows two distinct peaks: the expected peak at 217 nm and an unexpected peak at 262 nm. We attribute the peak at 262 nm to interference of light propagating inside the waveguide with light propagating above the waveguide.
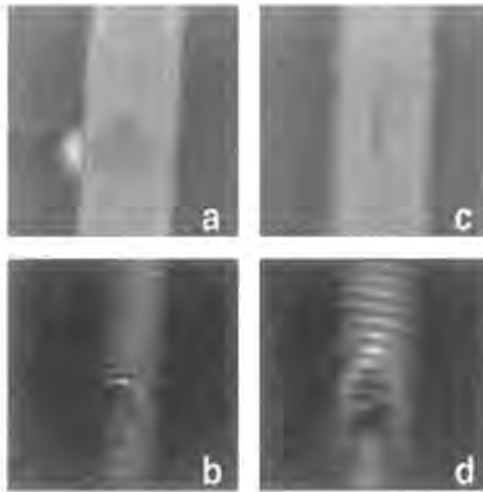
Figure 3: Height (a & c) and optical (b & d) images (4 μm × 4 μm) obtained with a PSTM.
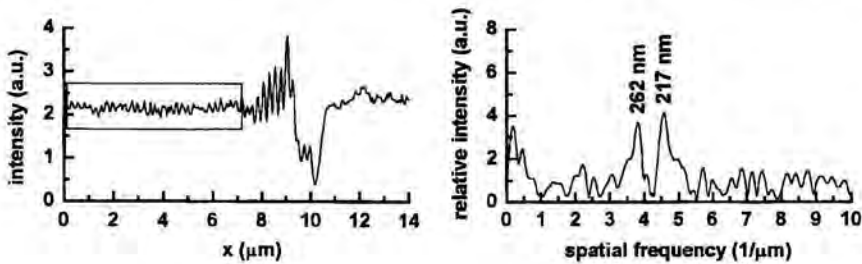
Figure 4: (left panel) Line trace of the optical signal of fig. 3d along the direction of the waveguide. The increased optical intensity due to scattering close to the first air rods (at 9.2 μm) is clearly visible. (right panel) Fourier transform of the boxed array showing two distinct spatial frequencies being present in the interference pattern.

4   Discussion

We have presented our first subwavelength photonic structures produced by focused ion beam sputtering. The technique is shown to have a high flexibility similar to that of electron beam lithography. The fabrication of nonperiodic structures like microcavities with dimensions of $\sim \lambda^3$ seems feasible. The advantage of the technique over e-beam lithography is that no resist is required for structure production.

We have mapped the optical fields around 2 different subwavelength objects (a single air rod and a periodic array of 5 air rods) with a resolution unattainable for other techniques.

Thus, we can observe interference of scattered and unscattered light. The optical images indicate that the production of 1D photonic structures requires a great positioning accuracy of the scatterers with respect to the waveguide structure. In the near future we will perform the same optical mapping as a function of wavelength. In addition, we will map the phase of the light by inserting the PSTM in one of the legs of a Mach-Zehnder interferometer.

5 Acknowledgements

References

[1] E.M. Purcell. Phys. Rev. 69(1946) 681
[2] J.S. Foresi, P.R. Villeneuve, J. Ferrera, E.R. Thoen, G. Steinmeyer, S. Fan, J.D. Joannopoulos, L.C. Kimerling, H.I. Smith, E.P. Ippen. Nature 390(1997) 143–145
[3] J.E.G.J. Wijnhoven, W.L. Vos. Science 281(1998) 802–804
[4] E. Yablonovitch. Phys. Rev. Lett. 58(1987) 2059–2062
[5] S.L. McCall, P.M. Platzman, R. Dalichaouch, D. Smith, S. Schultz. Phys. Rev. Lett. 67(1991) 2017–2020
[6] P.L. Phillips, J.C. Knight, B.J. Mangan, P.St.J. Russel, M.D.B. Charlton, G.J. Parker. J. Appl. Phys. 85(1999) 6337–6342
[7] K. Kogelnik. In T. Tamir, editors, *Integrated Optics*. Springer Verlag, Berlin (1975).
[8] N.F. van Hulst, N.P. de Boer, B. Bölger. J. Microsc.-Oxford 163(1991) 117–130
[9] A.G. Choo, M.H. Chudgar, H.E. Jackson, G.N. Debrabander, R.M. Kumar, J.T. Boyd. Ultramicroscopy 57(1995) 124–129
[10] J.A. Veerman, A.M. Otter, L. Kuipers, N.F. van Hulst. Appl. Phys. Lett. 72(1998) 3115–3117

Author's address

Applied Optics group, Dept. of Applied Physics, MESA$^+$ Research Insitute,
University of Twente,
P.O. Box 217, 7500 AE Enschede,
The Netherlands.

A. Moroz

Single Impurity in a Photonic Crystal

Abstract

Formulae for the density of states (DOS) and integrated DOS (IDOS) are discussed for the case when the dielectric constant ε is a general function of frequency.

1 Introduction

Photonic crystals are characterized by a periodically modulated dielectric constant ε. Some of such structures occur in nature, for instance, opals and nanostructured colour wings of butterflies [1]. There is a common belief that in the near future photonic crystals will give us the same control over photons as ordinary crystals do over electrons [2]. At the same time, photonic structures are of great promise to become a laboratory for testing fundamental processes involving interactions of radiation with matter in novel conditions.

Similar to the case of electrons moving in a periodic potential, photons can propagate in a given direction inside a photonic crystal only if their frequency falls within an allowed band. In the presence of impurities, localized photon modes can appear with frequencies within the forbidden bands (gaps), which separate the allowed bands (see Fig. 1). These localized modes can serve as resonance cavities with a very high quality factor [3]. In a finite crystal these modes are responsible for sharp transmission peaks at frequencies within a frequency gap of a parent system. Numerous applications involving impurities, for instance, efficient bandpass filters, channel drop filters, and waveguide crossing without cross-talk have been suggested thus far.

In the Schrödinger case, for an electron moving in a potential V, the density of states (DOS) $n(E)$ and the integrated DOS (IDOS) $N(E)$ are defined as

$$n(E) = \int n(E, \mathbf{x}) \, d\mathbf{x}, \qquad N(E) = \int_{-\infty}^{\omega} n(t) \, dt, \tag{1}$$

where $n(E, \mathbf{x})$ is the local DOS (LDOS),

$$n(E, \mathbf{x}) = -\frac{1}{\pi} \operatorname{Im} G(E; \mathbf{x}, \mathbf{x}). \tag{2}$$

$G(E; \mathbf{x}, \mathbf{x})$ here is the Green function, defined as the limit

$$G(E; \mathbf{x}, \mathbf{x}) = \lim_{s \to +0} \left\langle \mathbf{x} \left| [E + is - H]^{-1} \right| \mathbf{x} \right\rangle, \tag{3}$$

where H is the Hamiltonian. According to its definition, $N(E)$ describes the number of modes with $E' \leq E$ and $dN(E) = n(E) \, dE$. Formally,

$$n(E) = -\frac{1}{\pi} \operatorname{Im} \operatorname{Tr} G(E), \qquad (4)$$

$$N(E) = \frac{1}{\pi} \operatorname{Im} \operatorname{Tr} \ln G(E). \qquad (5)$$

One can show that $\operatorname{Im} G(E; \mathbf{x}, \mathbf{x}) \leq 0$ for any self-adjoint operator H. Hence, as expected, both $n(E)$ and $N(E)$ are positively defined.

The above formulae are derived under the assumption that the potential V is energy independent. However, for the Maxwell equations, the analogue of a potential V is

$$V = -\omega^2(\varepsilon - 1)/c^2, \qquad (6)$$

where ω is frequency, c is the speed of light in vacuum (set to one in the following), and the analogue of energy is $E = \omega^2/c^2$. Moreover, in all realistic cases the dielectric constant ε is a complicated function of frequency. Thus the potential in the Maxwell case is both explicitly and implicitly frequency dependent. Therefore a question arises what is the analogue of the formulae (4) and (5) in the Maxwell case. Note that previous discussions of a single impurity in a photonic crystal [4, 5, 6] dealt with the idealistic case of a nondispersive ε.

2 Dispersive impurity

It has been surprising to find out that in the dispersive Maxwell's case the formula (5) for the IDOS is still valid. Consequently, the change in the IDOS of a parent system induced by an impurity is given by

$$\Delta N(E) = -\frac{1}{\pi} \operatorname{Im} \operatorname{Tr} \ln[1 - G(E)W] \qquad (7)$$

where $G(E)$ is the Green function of unperturbed system and W is the difference of potentials with and without the impurity. However, the DOS of a parent system and the change in the DOS induced by an impurity are given by

$$
\begin{aligned}
n(E) &= -\tfrac{1}{\pi} \operatorname{Im} \operatorname{Tr} \left[G(E)(1 - dV/dE) \right], \\
\Delta n(E) &= -\tfrac{1}{\pi} \operatorname{Im} \operatorname{Tr} \left[G(E)(1 - dW/dE) \right].
\end{aligned}
\qquad (8)
$$

Note that in the nondispersive case, the first formula in (8) reduces to

$$
\begin{aligned}
n(E) &= -\frac{1}{\pi} \operatorname{Im} \operatorname{Tr} \left\{ G(E) \frac{d}{d\omega^2} \left[\omega^2 \varepsilon(\omega) \right] \right\} \\
&= -\frac{1}{\pi} \operatorname{Im} \operatorname{Tr} \left[G(E) \varepsilon \right],
\end{aligned}
\qquad (9)
$$

which has been used, for example, in [7].
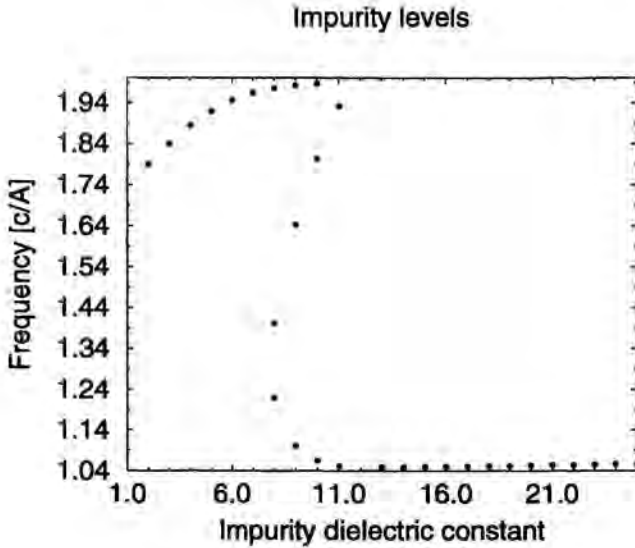
Figure 1: Substitutional impurity levels within the first forbidden band of a parent structure composed of alternating dielectric layers with $\varepsilon_1 = 1$ and $\varepsilon_2 = 12$. A is the length of a unit cell. The width of impurity layer is d_2 ($d_2/A = 0.4$), the same as of the layers with the dielectric constant ε_2.

As shown in [8], combining formulae (8) with the photonic analogue of the KKR method [9] allows one to treat efficiently the problem of dispersive impurities in a photonic crystal. Indeed, the impurity spectrum calculations using the plane-wave method are quite time consuming. The number of plane waves used to achieve convergence within 1% is typically 5×10^2, 2.5×10^4, and 7.5×10^5 in one, two, and three dimensions, respectively, [4]. On the other hand, using the photonic analogue of the KKR method [9], the impurity spectrum calculation in one dimension involves only matrices of the size 2×2. Even in three dimensions, the size of matrices involved do not exceed 300×300 [8].

3   Acknowledgements

References

[1] O. Graydon. OLE June 1998, p. 31
[2] E. Yablonovitch. Phys. Rev. Lett. 58(1987) 2059
[3] E. Yablonovitch, T. Gmitter, R. Meade, A. Rappe, K. Brommer, J.D. Joannopoulos. Phys. Rev. Lett. 67(1991) 3380
[4] P.R. Villeneuve, S. Fan, J.D. Joannopoulos. Phys. Rev. B 54(1996) 7837
[5] A. Figotin, V. Gorentsveig. Phys. Rev. B 58(1998) 180
[6] A.J. Ward, J.B. Pendry. Phys. Rev. B 58(1998) 7252
[7] A. Moroz. Europhys. Lett. 46(1999) 419
[8] A. Moroz. in preparation
[9] A. Moroz. Phys. Rev. B 51(1995) 2068

Author's address

FOM Institute AMOLF,
Kruislaan 407, 1098 SJ Amsterdam,
The Netherlands;

after Sept. 1, 1999:
I. Institut für Theoretische Physik,
Universität Hamburg,
Jungiustrasse 9, D-20355 Hamburg,
Germany.

T. Søndergaard

Spontaneous Emission Rate Alteration in Photonic Crystal Waveguides and Photonic Crystal Microcavities

Abstract

A model for spontaneous emission rate alteration based on the Fermi Golden rule and the position-dependent photon density of states is outlined. Numerical results are given for the rate of spontaneous emission in a waveguide and a microcavity, where the design is based on introducing a defect in a two-dimensional photonic crystal.

Photonic crystals represent a new promising class of periodic dielectric structures for control of light-matter interaction [1]. A new class of waveguides and microresonators, which we shall refer to as photonic crystal waveguides and photonic crystal microcavities, may be designed by introducing a defect in a photonic crystal. In this paper the alteration of spontaneous emission in the region of a line defect and a point defect in a two-dimensional photonic crystal is considered. Recently, a laser design based on introducing a defect in a two-dimensional photonic crystal was experimentally demonstrated [2]. The model for spontaneous emission used in this paper is based on the Fermi Golden rule and the position-dependent photon density of states (PDOS). The position-dependent PDOS for two-dimensional photonic crystals with no defects introduced has previously been considered by Søndergaard and Busch [3, 4]. The structures considered in this paper are approximated by a periodic structure using a supercell approximation, and for periodic structures the complex modes of the electric field may, in accordance with Bloch's theorem, be written on the form

$$\mathbf{E}_{\mathbf{k},n}(\mathbf{r}) = e^{i\mathbf{k}\cdot\mathbf{r}}\mathbf{U}_{\mathbf{k},n}(\mathbf{r}), \tag{1}$$

where $\mathbf{k}$ is a wave vector, n is the band number, and $\mathbf{U}_{\mathbf{k},n}(\mathbf{r})$ is a function with the same periodicity as the periodic structure. The corresponding angular frequency is denoted $\omega_{\mathbf{k},n}$. In terms of these modes the position-dependent PDOS is defined as

$$\mathcal{E}(\mathbf{r},\omega) = \sum_{\mathbf{k},n} \delta(\omega - \omega_{\mathbf{k},n}) \mid \mathbf{E}_{\mathbf{k},n}(\mathbf{r}) \mid^2, \tag{2}$$

where the energy of each mode within a period of the periodic structure is normalized to unity.

Enhancement and suppression of spontaneous emission is evaluated by comparing the PDOS (2) with the corresponding PDOS for a homogeneous dielectric with the same dielectric

Figure 1: The position-dependent photon density of states is shown for two positions A and B (see inset) within a two-dimensional photonic crystal waveguide. For comparison the density of states is also shown for a homogeneous dielectric with the same dielectric constant as the background material.

constant as the background material. The electric field distributions (1) are calculated using fully vectorial plane wave expansion theory and a variational principle [5].

Spontaneous emission rate alteration for a photonic crystal waveguide is considered in Figure 1. The photonic crystal waveguide and the supercell used as an approximation are shown as an inset. The photonic crystal is characterized by circular air-holes arranged on a triangular lattice, and the waveguide may be thought of as a line defect in the crystal. The frequency is normalized using the center-to- center air-hole spacing Λ. The diameter of the air-holes is 0.83Λ, and the width of the waveguide is given by $W = 1.2\Lambda$. The PDOS (2) is shown for the positions A and B within the waveguide. Also shown is the PDOS for a homogeneous dielectric with dielectric constant 13 (representative of GaAs at optical frequencies) corresponding to the photonic crystal background material. At both positions A and B the PDOS is below the parabolic curve for the homogeneous dielectric, and consequently the rate of spontaneous emission is reduced relative to the homogeneous dielectric.

Figure 2 shows the position-dependent PDOS for two positions A and B (see inset) in the region near a point-like defect in a two-dimensional photonic crystal. In this case the air-hole diameter is 0.86Λ, and a defect has been introduced by reducing the diameter of a single air-hole to 0.57Λ. As an inset the amplitude of the electric field squared is shown for a localized non-degenerate mode with frequency $\omega\Lambda/2\pi c = 0.374$. The amplitude of the electric field squared for this mode is strong at position A and close to zero at position B. The sum of the amplitudes of the electric field squared for two degenerate modes with frequency $\omega\Lambda/2\pi c = 0.382$ is also shown as an inset. In this case the amplitude is strong at position B and not so strong at position A. Accordingly, for the frequency $\omega\Lambda/2\pi c = 0.374$ a strong peak is seen in the PDOS at position A, whereas a strong peak is not seen at position B.
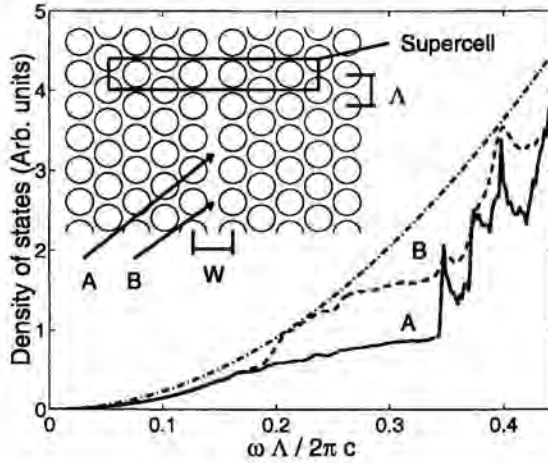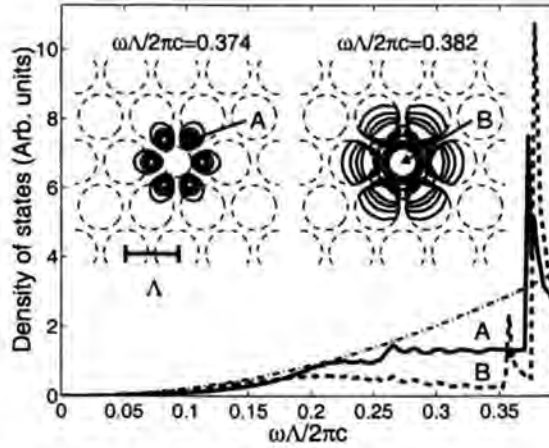
Figure 2: The position-dependent photon density of states is shown for two positions A and B (see inset) within a two-dimensional photonic crystal microcavity. For comparison the density of states is shown for a homogeneous dielectric with the same dielectric constant as the background material.

Similarly, the photon density of states is strong at position B and not so strong at position A for the frequency $\omega\Lambda/2\pi c = 0.382$. The PDOS for a homogeneous dielectric with dielectric constant 13 is also shown in Figure 2, and it is clear that the PDOS at position A for the frequency $\omega\Lambda/2\pi c = 0.374$ is enhanced relative to the PDOS for the homogeneous dielectric, and consequently the rate of spontaneous emission is enhanced.

A similar conclusion may be drawn for the frequency $\omega\Lambda/2\pi c = 0.382$ at position B. However, position B is at the center of an air-hole, whereas position A corresponds to a high-index material, where it is more natural to expect an emitter. Both for the case of the photonic crystal waveguide and the photonic crystal microcavity the PDOS is shown for two positions to illustrate that the PDOS depends strongly on position.

In conclusion, the numerical results show that the position-dependent photon density of states may depend strongly on the position within a photonic crystal waveguide and a photonic crystal microcavity. For the two positions considered within the waveguide spontaneous emission was not enhanced relative to the rate of spontaneous emission in a homogeneous dielectric with the same dielectric constant as the background material. However, for the case of a photonic crystal microcavity the photon density of states is strongly enhanced just above the cutoff frequency for a few localized modes, and in this case spontaneous emission may be enhanced.

Acknowledgements

References

[1] E. Yablonovitch. Phys. Rev. Lett. 58(1987) 2059–2062

[2] O. Painter, R.K. Lee, A. Scherer, A. Yariv, J.D. O'Brien, P.D. Dapkus, I. Kim. Science 284(1999)

[3] T. Søndergaard *et al.* In *CLEO'99*, 1999. JFA2, 23-28 May

[4] K. Busch, S. John. Phys. Rev. E 58(1998) 3896–3908

[5] R.D. Meade, A.M. Rappe, K.D. Brommer, J.D. Joannopoulos, O. L. Alerhand. Phys. Rev. B 48(1993) 8434–8437

Author's address

Research Center COM,
Technical University of Denmark,
Building 349, DK-2800 Lyngby,
Denmark.

Tel.: +45 45 88 14 44,
Fax: +45 45 93 65 81,
Email address: ts@com.dtu.dk.

J.A. Veerman, M.F. Garcia-Parajo, L. Kuipers and N.F. van Hulst

Quantum Jumps of Individual Emitters at Room Temperature

Abstract

Intersystem crossing jumps of individual molecules embedded in a polymer are observed in real-time. Both triplet state lifetime and crossing yield appear to vary in time. The range of the variation for a single molecule during long observation corresponds to the distribution for many individual molecules dispersed in space obtained during short observation: a direct manifestation of the ergodic principle of statistical physics.

1 Single molecules

Observations on an ensemble of emitters are blind for several intriguing phenomena that can directly be observed by studying individual emitters [1]: spectral and rotational jumps [2, 3, 4], photon-(anti)bunching [5, 6, 7] and discrete photobleaching. Moreover the monitoring of single emitters forms a powerful way to probe the dynamics of the local nano-environment: single molecule detection allows the inhomogeneity of the ensemble to be directly related to the real-time dynamics of the heterogeneity of the environment.

Here we focus on the three level system (Figure 1) as is common for organic fluorophores. Besides the repetitive transitions between the singlet S_0 and S_1 states, giving rise to fluorescence, the molecule has a small chance to undergo intersystem crossing (ISC) from S_1 to the triplet T_1 state. As long as T_1 remains occupied, the $S_0 (S_1$ transition does not occur and the fluorescence is interrupted temporarily. After decaying to S_0 fluorescence restarts. Thus, as the lifetime of T_1 is much longer than that of S_1, the fluorescence photons are emitted in bunches separated by dark periods that occur when the molecule is in T_1: so-called photon bunching. Fast integration of the fluorescence photons over time intervals shorter than the duration of the dark periods can identify the time length of each excursion to T_1 [8, 7]. We have exploited the unique advantage of this real-time method to obtain time-resolved T_1 state dynamics. We find that single molecular T_1 lifetimes vary in time. A suitable length of time (~ 10 s) is found over which the distribution of T_1 lifetimes of one molecule becomes similar to the distribution of constant T_1 lifetimes obtained from many individual molecules during short observation times [9].

2 Real-time intersystem crossing dynamics

Experiments were performed on $DiIC_{18}$ molecules immobilized in a PMMA host. DiI has a high fluorescence quantum-yield and relatively low bleaching rate (10^{-6}-10^{-8}). Previous
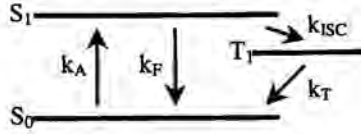
Figure 1: Three level energy scheme describing single molecule fluorescence. S_0, S_1 are the singlet ground and excited states; k_A, k_F the absorption and fluorescence rates; T_1 the first excited triplet state, k_{ISC} the $S_1 - T_1$ intersystem crossing rate; k_T the $T_1 - S_0$ transition rate. The intersystem crossing rate is much smaller than the fluorescence decay rate, and the T_1 lifetime (k_T^{-1}) is much longer than the S_1 lifetime ($\sim k_F^{-1}$).

studies at the single molecule level [10, 11] already yielded information about the fluorescence spectrum, fluorescence lifetime, orientation, quantum jumps to T_1 and intensity fluctuations.

Our experimental approach involves the excitation of individual molecules by a local sub-wavelength light source in a near-field optical configuration [12, 4, 13]. An excitation intensity of ~ 10 kW/cm^2 is delivered at a 70 nm spot, yielding single molecule fluorescence signal up to 106 photon counts/s (close to saturation of the S_0-S_1 transition), which allows a time resolution of 30 μs.

In order to monitor the fluorescence of a single molecule continuously as a function of time, we positioned the near-field source directly above a molecule. All molecules in this study (several hundreds) were illuminated and monitored until irreversible photobleaching. Figure 2a shows a 15 ms timetrace of the fluorescence of a single DiI molecule. Clearly the emission switches abruptly from a high to a low intensity level and back due to singlet-triplet quantum jumps. Figure 2b shows a total 3.5 second observation interval in image format, with 5 orders of magnitude dynamic range in time and a few thousand triplet excursions. From such a fluorescence time trace both a T_1 state decay time (τ_T) and intersystem crossing yield (Y_{ISC}) can be extracted. The duration of the dark periods was determined directly by selecting a signal level to discriminate between emission ('light' periods) and dark periods. A histogram of the duration of all dark periods within a certain observation time interval yields an exponential decay with a typical decay time (τ_T) for that interval. Figure 3a shows such a histogram that was obtained by evaluating the fluorescence during an observation time interval of 2.8 seconds. Similarly, a typical Y_{ISC} is obtained from the exponential decay of the number of photon counts in the light periods.

We have determined τ_T and Y_{ISC} of 80 different molecules embedded in PMMA. For a fraction of these molecules, the histograms of the dark period duration and the number of counts of the light periods could be described by a single exponential relation. This indicates that both τ_T and Y_{ISC} were constant during the entire observation time for each of these molecules at their specific location. We obtain not only a mean value for τ_T and Y_{ISC}, but also the full distribution for these subsets of molecules. In Figure 3b the distribution of τ_T is given for this subset in PMMA (51 molecules). The distribution peaks at 170 (s. The distribution of Y_{ISC} for the same set of molecules yields a peak value of 2.2×10^{-4}. The width of the distribution is caused by the spatial heterogeneity of the sample, which results in a different local environment for each investigated molecule.

Surprisingly, we found that for a considerable fraction of the molecules (35%) the his-
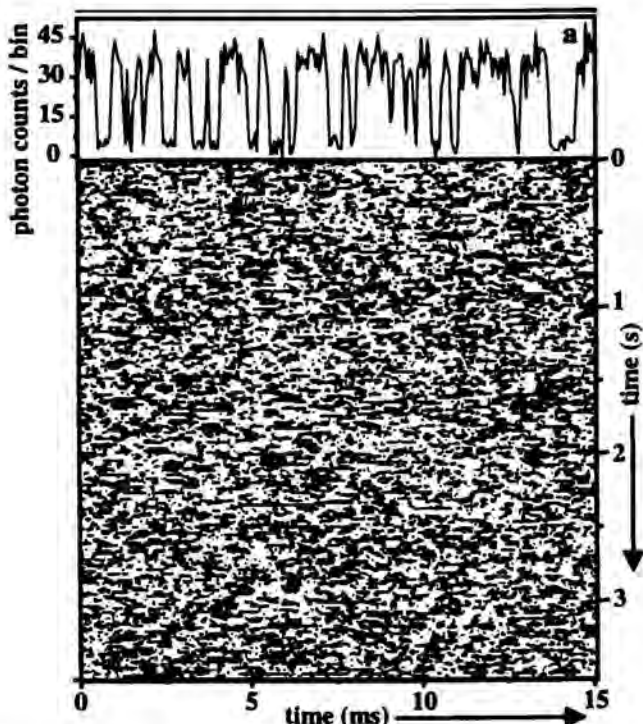
Figure 2: (a) Single molecule fluorescence timetrace with 57 μs integration time per point. The fluorescence drops repeatedly to a low level due to transitions to T_1. (b) Image with 3.5 s of fluorescence blinking. The gray level represents the photon count rate during a 57 μs bin: bright streaks are due to S_0-S_1 cycling; dark streaks represent residence in the triplet state.

tograms of τ_T and Y_{ISC} could not be described by a simple single exponential decay. Closer inspection of the dynamics of these molecules reveals that τ_T is not constant in time. Fig. 4a displays a clear occurrence of a jump in intersystem crossing dynamics. To take the variation into account we determined τ_T over 400 ms intervals (typically 600 triplet excursions). Fig. 4b shows τ_T of a single molecule as a function of the observation time. The molecule displays τ_T variations on a characteristic time scale of about 1 second, ranging from 0.12 to 0.28 milliseconds until irreversible photo-bleaching occurs after 13 seconds. Histograms of the relative occurrence of the different values of τ_T for the long-lived molecule of Fig. 4b are shown in Fig. 4c over the entire observation period. Superimposed to the histogram is also the distribution of τ_T as plotted in Fig. 3b for spatially dispersed short-lived molecules. It is found that the relative occurrence in time of τ_T for the individual molecule matches a large part of the distributions of the constant τ_T for the set of spatially dispersed molecules. We find that this similarity is exhibited for all molecules with a time-varying τ_T (and Y_{ISC}). Furthermore, the longer the observation time, the stronger the overlap becomes. We find that variations in τ_T and Y_{ISC} for a single molecule occur on a time scale of 0.2 to 20 seconds.
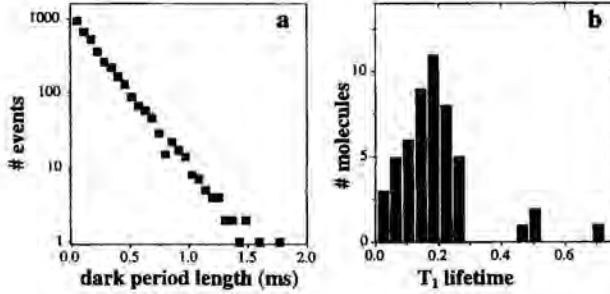
Figure 3: (a) Histogram of the length of the 'dark' periods for a single DiIC18 molecule over an observation time of 2.8 seconds. The single exponential decay corresponds to a mean T_1 lifetime of $216 \pm 5 \, \mu s$. (b) Distribution of T_1 lifetimes of 51 spatially dispersed $DiIC_{18}$ molecules. Heterogeneity of the PMMA environment of the molecules accounts for the range of different T_1 lifetimes.

3 Discussion and conclusion

The time-dependent behavior of τ_T and Y_{ISC} can be understood if one considers that the polymer host constitutes a semi-rigid environment, which is dynamic in nature at room temperature [10, 4]. As a result, photodynamical parameters such as τ_T and Y_{ISC} can indeed vary with time. For instance, variations of the local oxygen concentration, related to local conformational dynamics of the polymer host [14], could be involved in the observed variation in τ_T, both in space and in time.

Finally, a major conclusion can be drawn from the similarity of the two distributions of Fig. 4c for τ_T, one of them representing the behavior of one molecule in time, and the other representing the snapshot behavior of different molecules separated in space. The similarity indicates that all environmental sites become indistinguishable from each other in time. A molecule that would be observable for a sufficiently long period would indeed exhibit the same distribution of τ_T and Y_{ISC} occurrences as a set of molecules dispersed in space at a single moment in time. Therefore, we observe that our measurements satisfy the ergodic principle of statistical physics, stating that for a physical stationary system a time-average is equivalent to an ensemble average.

4 Acknowledgements

Quantum Jumps of Individual Emitters at Room Temperature
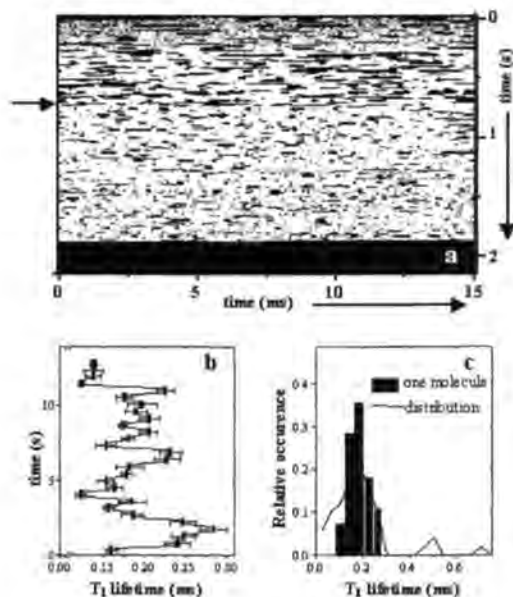
Figure 4: (a) Image of fluorescence blinking with discrete bleach after 1.8 s. The intersystem crossing dynamics changes abruptly after 0.7 s (arrow). (b) Trajectory of the T_1 lifetime of a single DiIC18 molecule as a function of time. (c) Histograms of the relative occurrence of the T_1 lifetimes for the single molecule in (b) (bars), and distribution of T_1 lifetimes for spatially dispersed molecules in PMMA (line).

References

[1] T. Basché, W.E. Moerner, M. Orrit, U.P. Wild, editors. *Single-Molecule Optical Detection, Imaging and Spectroscopy.* VCH, Weinheim (1997)

[2] T. Ha, Th. Enderle, D.S. Chemla, P.R. Selvin, S. Weiss. Phys. Rev. Lett. 77(1996) 3979

[3] H.P. Lu, X.S. Xie. Nature 385(1997) 143

[4] A.G.T. Ruiter, J.A Veerman, M.F. Garcia-Parajo, N.F. van Hulst. J. Phys. Chem. A 101(1997) 7318

[5] M. Orrit, J. Bernard. Phys. Rev. Lett. 65(1990) 2716

[6] T. Basché, W.E. Moerner, M. Orrit, H. Talon. Phys. Rev. Lett. 69(1992) 1516

[7] T. Ha, Th. Enderle, D.S. Chemla, P.R. Selvin, S. Weiss. Chem. Phys. Lett. 271(1997) 1

[8] T. Basché, S. Kummer, C. Bräuchle. Nature 373(1995) 132

[9] J.A. Veerman, M.F. Garcia-Parajo, L. Kuipers, N.F. van Hulst. Phys. Rev. Lett. 83(1999)

[10] J.J. Macklin, J.K. Trautman, T.D. Harris, L.E. Brus. Science 272(1996) 255

[11] K.D. Weston, S.K. Buratto. J. Phys. Chem. A 102(1998) 3635

[12] E. Betzig, R.J. Chichester. Science 262(1993) 1422

[13] J.A. Veerman, A.M. Otter, L Kuipers, N.F. van Hulst. Appl. Phys. Lett. 72(1998) 3115

[14] K. Schmidt-Rohr, A.S. Kulik, H.W. Beckham, A. Ohlemacher, U. Pawelzik, C. Boeffel, H.W. Spiess. Macromolecules 27(1994) 4733

Author's address

Applied Optics group, Fac. of Applied Physics, MESA$^+$ Research Institute,
University of Twente,
P.O. Box 217, 7500 AE Enschede,
The Netherlands.

Part II
Spontaneous Emission Control

D. Lenstra, C.L.A. Hooijer, K. Allaart and G. Harel

Quantum Description of Light Emitted from Semiconductor Microstructures

Abstract

We present a quantum mechanical formalism to study the interaction between the active region in a semiconductor device and the electromagnetic field. The method explicitly avoids decomposition into modes. Instead, use is made of the classical Green tensor for the passive structure. We derive an expression for the spontaneous emission rate generally valid for localized and delocalized interactions. As an application, we calculate the spontaneous emission factor β_{sp} for an edge-emitting three-layer (waveguide) structure with a quantum well as a function of the width of the middle layer and the position of the quantum well in it.

In view of apparent developments towards miniaturization of semiconductor devices as well as realization of schemes where semiconductor lasers emit light with non-classical properties [1, 2, 3, 4], there is an obvious need for a general quantum mechanical framework in which one is able to treat the electromagnetic field, the electron dynamics and the interaction between electrons and the electromagnetic field in a quantized way for general geometries. Such a framework could already today be necessary to understand the basic operation of quantum optical devices (noise properties, photon statistics and correlations). It should also allow for a straightforward integration with existing quantum mechanical models for the full electron dynamics in the active region [5] and in semiconductors in general [6].

The present paper reports on our approach towards such a general framework and the results obtained thus far. A key role in our quantum mechanical theory is played by the *classical* Green tensor of the passive dielectric structure, i.e., the full device with its active constituents like quantum wells removed. Most of the existing semiconductor light emitting devices can be described in this manner. In our approach we deal directly with the electromagnetic field operators, rather than creation and annihilation operators for the natural modes of the structure. Thus we avoid certain complications connected to the lossy character of a mode as a consequence of the open nature of any dielectric structure. The problem is formulated by defining the Hamiltonian in a generalized Coulomb gauge and the basic commutation relations. Then in the Heisenberg picture the equations of motion for the relevant operators are straightforwardly derived. An important position is taken by the inhomogeneous operator wave equation for the electromagnetic vector potential in which the source term reflects the field-matter interaction. This equation can be implicitly solved

for the vector potential in terms of the classical Green tensor pertaining to the dielectric structure that remains after removing the active constituents. From here on it is possible to build further towards a more comprehensive theory that includes the analysis of higher order correlation functions, stimulated emission, squeezing and lasing. In the present paper we focus on the application of the theory developed so far to the fundamental problem of spontaneous emission.

A general formula for the spontaneous emission rate is derived that, unlike the usual result based on localized electric dipole interaction, takes the delocalized character of the electron states fully into account (electric current rather than electric dipole interaction). Moreover, the orientation of the current matrix element, i.e., the polarization associated with the transition, is taken into account. Next, we apply this formula to a multilayer dielectric configuration with a quantum well and we obtain explicit results for three-layer waveguide structures, a problem that received significant attention recently, both theoretical and experimental [7, 8, 9]. Not only can we demonstrate the strength and elegance of our method [10], and completely confirm the theoretical results obtained in [9], but we also calculate the spontaneous emission factor β_{sp} for a selected mode in a three-layer edge emitter.

An important advantage of our method is that it allows a consistent Hamiltonian formulation of the problem, without running into difficulties associated with the open character of the system. The field is quantized directly, without invoking a modal decomposition, while the electromagnetic features are separated, in a way, from the quantum-mechanical ones. It is assumed that the (classical) Green tensor for the full device geometry without the active carriers is known. In practice it may not be an easy task to calculate the Green tensor for a realistic multilayer device. On the other hand, for a given structure, it needs only be done once. This Green tensor is then used as input for the quantum mechanical equations of motion.

1 Derivation of equations of motion

In this section the Heisenberg equations of motion for the relevant operators in a light emitting dielectric device will be derived. The Hamiltonian for such a device and the commutation relations for the operators need to be identified. For the charge carriers the well known fermion anti-commutation relations hold. For the field operators the situation is not so straightforward [11, 12, 13, 14] and indeed is different from the vacuum case. We distinguish two interacting parts in the light-emitting device. One part consists of the free charge carriers (the electrons in the conduction band and the holes in the valence band) the quantum transitions of which produce or absorb (incoming) light. Usually these occur only in a small subregion of the system, e.g. a quantum well. The other part is passive and constitutes all the rest of the device, including the various interfaces that give rise to reflection like in a cavity or to guided, radiation and substrate modes like in a waveguide. Here only bound charges interact with the field. We neglect absorption in this part, which is a reasonable approximation in the optically relevant regime. The dielectric properties (that arise due to the interaction with the bound charges) are then accounted for by a real dielectric function $\varepsilon(\mathbf{r})$ that is only space-dependent. This dielectric space may be considered as an effective vacuum, in which the electromagnetic field may be quantized in a similar way as in the true

vacuum. This is shortly summarized in the next subsection.

1.1 Quantization of the electromagnetic field in a lossless dielectric structure

For the quantization of the field in the passive part we follow the lines of the extensive discussions by Knöll, Vogel and Welsch [11, 12], Glauber and Lewenstein [13], and Tip [14]. Note that this part of the system contains no free charges or currents. We introduce the vector potential field in the usual way as (in SI units)

$$\mathbf{B}(\mathbf{r}, t) = \nabla \times \mathbf{A}(\mathbf{r}, t) \tag{1}$$

$$\mathbf{E}(\mathbf{r}, t) = -\frac{\partial \mathbf{A}(\mathbf{r}, t)}{\partial t}. \tag{2}$$

In (2) one normally expects a scalar potential as well. However, this term is chosen to be zero due to the absence of free charges. For the vector potential we choose the generalized Coulomb gauge [11, 12, 13, 14]:

$$\nabla \cdot (\varepsilon(\mathbf{r}) \mathbf{A}(\mathbf{r}, t)) = 0. \tag{3}$$

Note that this is compatible with $\nabla \cdot \mathbf{D} = 0$, where $\mathbf{D} = -\varepsilon_0 \varepsilon(\mathbf{r}) \dot{\mathbf{A}}$. Identification of the proper canonical momentum density as the conjugate variable to $\mathbf{A}$ for quantization of the field requires special care, since the independent variables are non-trivial components of the vector field because of the generalized transversality condition (3). It can be shown that the canonically conjugate momentum density is given by [12]:

$$\Pi(\mathbf{r}, t) = \varepsilon_0 \varepsilon(\mathbf{r}) \dot{\mathbf{A}}(\mathbf{r}, t) = -\varepsilon_0 \varepsilon(\mathbf{r}) \mathbf{E}. \tag{4}$$

The Hamiltonian for the electromagnetic field then reads:

$$H_{diel} = \int d^3 r \frac{1}{2} \left[\frac{(\Pi(\mathbf{r}, t))^2}{\varepsilon_0 \varepsilon(\mathbf{r})} + \frac{(\nabla \times \mathbf{A}(\mathbf{r}, t))^2}{\mu_0} \right], \tag{5}$$

the integration extending over all space, with $\varepsilon(\mathbf{r}) \equiv 1$ everywhere outside the dielectric light emitting device. The canonical quantization condition is more complicated than in the usual Coulomb gauge, where it involves the transverse delta function [15]. Here, because of the generalized transversality condition (3), one obtains the equal-time commutators [12]:

$$[\hat{A}_\alpha(\mathbf{r}), \hat{E}_\beta(\mathbf{r}')] = -\frac{i\hbar}{\varepsilon_0} \delta^\varepsilon_{\alpha\beta}(\mathbf{r}, \mathbf{r}'). \tag{6}$$

where $\delta^\varepsilon_{\alpha\beta}(\mathbf{r}, \mathbf{r}')$ is the generalized transverse delta function [12, 13]. For a transverse vector field $\mathbf{X}^T(\mathbf{r})$ one has the relation:

$$\sum_\beta \int d^3 r' \varepsilon(\mathbf{r}) \delta^\varepsilon_{\alpha\beta}(\mathbf{r}, \mathbf{r}') X^T_\beta(\mathbf{r}') = X^T_\alpha(\mathbf{r}), \tag{7}$$

while for a longitudinal vector field $\mathbf{X}^L(\mathbf{r})$:

$$\sum_\beta \int d^3r' \delta^\varepsilon_{\alpha\beta}(\mathbf{r},\mathbf{r}')\varepsilon(\mathbf{r}')X^L_\beta(\mathbf{r}') = 0. \tag{8}$$

Note that with this definition the generalized transverse delta function differs by a constant factor $\varepsilon(\mathbf{r}) = \varepsilon$ from the usual transverse delta function when $\varepsilon(\mathbf{r})$ is independent of $\mathbf{r}$. In a number of recent papers [16, 17, 18, 19] it has been stressed that a real $\varepsilon(\mathbf{r})$ unequal to 1 violates the Kramers-Kronig relations and therefore causality. However, as a model valid for the limited frequency range of optical waves in a dielectric material it should be acceptable [8, 13, 19].

1.2 Hamiltonian

The *total* Hamiltonian for the system has to be derived by determining the energy associated with all the processes in the system. The active particles and the interaction are confined to the active region. The part of the Hamiltonian concerned with the electromagnetic field is given in (5). Now consider the free charge carriers in the active region. The particle Hamiltonian is split into a part which contains only the canonical variables of the particles, now written in terms of the electron field operators $\hat{\Psi}(\mathbf{r},t)$ as

$$\begin{aligned}
\hat{H}_{el} &= \int_{act.reg.} d^3r\, \hat{\Psi}^\dagger(\mathbf{r},t)\left(\frac{-\hbar^2}{2m_e}\nabla^2 + eU(\mathbf{r})\right)\hat{\Psi}(\mathbf{r},t) \\
&\quad + \frac{1}{2}\int\int_{act.\,reg.} d^3r\, d^3r'\, \hat{\Psi}^\dagger(\mathbf{r},t)\hat{\Psi}^\dagger(\mathbf{r}',t)V(\mathbf{r},\mathbf{r}')\hat{\Psi}(\mathbf{r}',t)\hat{\Psi}(\mathbf{r},t)
\end{aligned} \tag{9}$$

(in which $U(\mathbf{r})$ is the lattice potential and $V(\mathbf{r},\mathbf{r}')$ is the instantaneous Coulomb interaction), and the electron-field interaction Hamiltonian

$$\hat{H}_{int} = -\int_{act.reg.} d\mathbf{r}\, \hat{\mathbf{A}}(\mathbf{r},t)\cdot\hat{\mathbf{J}}(\mathbf{r},t) \tag{10}$$

with, in the case of a generalized Coulomb gauge (3), an operator $\hat{\mathbf{J}}(\mathbf{r},t)$ defined as:

$$\begin{aligned}
\hat{\mathbf{J}}(\mathbf{r},t) &= \frac{-i\hbar e}{2m_e}\left\{\hat{\Psi}^\dagger(\mathbf{r},t)\nabla\hat{\Psi}(\mathbf{r},t) - \left(\nabla\hat{\Psi}^\dagger(\mathbf{r},t)\right)\hat{\Psi}(\mathbf{r},t)\right\} \\
&\quad + \hat{\Psi}^\dagger(\mathbf{r},t)\hat{\Psi}(\mathbf{r},t)\left\{\frac{i\hbar e}{2m_e}\frac{\nabla\varepsilon(\mathbf{r})}{\varepsilon(\mathbf{r})} - \frac{e^2}{2m_e}\hat{\mathbf{A}}(\mathbf{r},t)\right\}.
\end{aligned} \tag{11}$$

The third term in this expression originates from $\nabla\hat{\mathbf{A}}$ and the condition (3). Note that $\hat{\Psi}(\mathbf{r},t)$ and therefore the region of integration extends in practice only over the active region to which the free charge carriers are confined.

When substituted in (10), the term in (11) proportional to $\hat{\mathbf{A}}(\mathbf{r},t)$ is often neglected on the basis of arguments that the electromagnetic radiation fields are weak compared to the

atomic field strengths [20, 21]. The term with the gradient of $\varepsilon(\mathbf{r})$ in (11) is also expected to be of minor importance, because the dielectric constant is by definition a macroscopic quantity, representing the effect of the average polarization of bound charges over a region that is large compared to atomic dimensions [22]. For the active layer it is a somewhat hypothetical quantity, referring to the system without the free carriers and will not differ very much from the dielectric constants of the surrounding layers. From now on, we will neglect these terms and identify $\hat{\mathbf{J}}(\mathbf{r}, t)$ with the electromagnetic current:

$$\hat{\mathbf{J}}(\mathbf{r}, t) \approx \hat{\mathbf{J}}_{EM}(\mathbf{r}, t) \approx \frac{-i\hbar e}{2m_e} \left\{ \hat{\Psi}^\dagger(\mathbf{r}, t)\nabla\hat{\Psi}(\mathbf{r}, t) - \left(\nabla\hat{\Psi}^\dagger(\mathbf{r}, t)\right)\hat{\Psi}(\mathbf{r}, t) \right\} \tag{12}$$

It is only the transverse current which acts as a source of the electromagnetic field. This follows from the the operator Maxwell equation, which can be expressed as:

$$\begin{aligned} \hat{\mathbf{J}}_{EM}(\mathbf{r}, t) &= -\frac{\partial}{\partial t}\hat{\mathbf{D}}(\mathbf{r}, t) + \nabla \times \hat{\mathbf{H}}(\mathbf{r}, t) \\ &= -\frac{1}{i\hbar}[\varepsilon_0\varepsilon(\mathbf{r})\hat{\mathbf{E}}(\mathbf{r}, t), \hat{H}_{int}], \end{aligned} \tag{13}$$

where the second equality in (13) follows from the Heisenberg equations of motion (see (15)) for the displacement operator. Using (6) and (7) one obtains:

$$\hat{J}_{EM,\alpha}(\mathbf{r}, t) = \int\limits_{act.reg.} d^3r'\varepsilon(\mathbf{r})\sum_\beta \delta^\varepsilon_{\alpha\beta}(\mathbf{r}, \mathbf{r}')\hat{J}_\beta(\mathbf{r}', t) = \hat{J}^T_{EM,\alpha}(\mathbf{r}, t), \tag{14}$$

where $\hat{J}_\beta(\mathbf{r}', t)$ is the β-component of $\hat{\mathbf{J}}(\mathbf{r}, t)$ and $\alpha, \beta = x, y, z$. Since the current $\hat{\mathbf{J}}_{EM}(\mathbf{r}, t)$ is transverse, we will denote it from here on as $\hat{\mathbf{J}}^T_{EM}(\mathbf{r}, t)$.

1.3 Equations of motion

In the Heisenberg picture the operators are time-dependent, while the states are time-independent. An advantage of this picture is that the electromagnetic field operators satisfy equations that resemble as close as possible the classical electromagnetic field equations. By assuming the interaction switched on at $t = 0$, all expectation values can be evaluated in the free-field state of the system at $t = 0$. For an operator $\hat{F}$ that has no explicit time-dependence, the Heisenberg equation of motion is given by:

$$\frac{d}{dt}\hat{F} = \frac{1}{i\hbar}[\hat{F}, \hat{H}]. \tag{15}$$

For the vector potential operator $\hat{\mathbf{A}}(\mathbf{r}, t)$ one deduces the following vector wave equation, by application of (15) with the Hamiltonians (5) and (10), using relation (14) and the gauge condition (3):

$$\nabla \times \nabla \times \hat{\mathbf{A}}(\mathbf{r}, t) + \frac{\varepsilon(\mathbf{r})}{c^2}\frac{\partial^2}{\partial t^2}\hat{\mathbf{A}}(\mathbf{r}, t) = \mu_0\hat{\mathbf{J}}^T_{EM}(\mathbf{r}, t). \tag{16}$$

After time-Fourier transformation of (16) the formal solution in terms of $\hat{\mathbf{J}}^T_{EM}(\mathbf{r}',\omega)$ is obtained as:

$$\hat{\mathbf{A}}(\mathbf{r},\omega) = \hat{\mathbf{A}}_{free}(\mathbf{r},\omega) + \int d^3r'\, \overset{\leftrightarrow}{G}(\mathbf{r},\mathbf{r}',\omega) \cdot \hat{\mathbf{J}}^T_{EM}(\mathbf{r}',\omega), \tag{17}$$

in which the Green tensor satisfies the equation:

$$\sum_k \left[\partial_i^r \partial_k^r - \delta_{ik} \left(\Delta^r + \frac{\omega^2}{c^2}\varepsilon(\mathbf{r}) \right) \right] G_{kj}(\mathbf{r},\mathbf{r}',\omega) = \mu_0 \delta_{ij}\delta(\mathbf{r}-\mathbf{r}') \tag{18}$$

and $\hat{\mathbf{A}}_{free}(\mathbf{r},\omega)$ is a solution of the homogeneous equation, representing the electromagnetic field operator for the passive dielectric structure.

The operator for the electron field is expanded in a basis set:

$$\hat{\Psi}(\mathbf{r},t) = \sum_\gamma \hat{c}_\gamma(t)\varphi_\gamma(\mathbf{r}), \tag{19}$$

where the label γ indicates quantum numbers of Bloch states, i.e., band index n and wave vector k [6]. For the operator $\hat{c}_\gamma(t)$ the Fermion anti-commutation rules hold:

$$\hat{c}_\gamma(t)\hat{c}_{\gamma'}(t) = -\hat{c}_{\gamma'}(t)\hat{c}_\gamma(t), \tag{20}$$
$$\hat{c}_\gamma(t)\hat{c}^\dagger_{\gamma'}(t) = \delta_{\gamma\gamma'} - \hat{c}^\dagger_{\gamma'}(t)\hat{c}_\gamma(t). \tag{21}$$

In the same representation the current operator (14) can be expressed as:

$$\hat{J}^T_{EM,\alpha}(\mathbf{r},t) = \sum_{\gamma,\gamma'} \hat{c}^\dagger_\gamma(t)\hat{c}_{\gamma'}(t)j^T_{\alpha,\gamma\gamma'}(\mathbf{r}), \tag{22}$$

with

$$j^T_{\alpha,\gamma\gamma'}(\mathbf{r}) = \int\limits_{act.reg.} d^3r'\varepsilon(\mathbf{r}) \sum_\beta \delta^\varepsilon_{\alpha\beta}(\mathbf{r},\mathbf{r}')j_{\beta,\gamma\gamma'}(\mathbf{r}'), \tag{23}$$

and

$$j_{\beta,\gamma\gamma'}(\mathbf{r}) = \left\{ -\frac{i\hbar e}{2m_e} \left(\varphi^*_\gamma(\mathbf{r})\nabla_\beta\varphi_{\gamma'}(\mathbf{r}) - \left(\nabla_\beta\varphi^*_\gamma(\mathbf{r})\right)\varphi_{\gamma'}(\mathbf{r}) \right) \right\}. \tag{24}$$

If the adopted basis representation $\varphi_\gamma(\mathbf{r})$ is that of the mean-field (Hartree-Fock) solutions, the many-body Hamiltonian for the electrons (9) is represented as [23, 24, 25]:

$$\hat{H}_{el} = \sum_\gamma E_\gamma \hat{c}^\dagger_\gamma(t)\hat{c}_\gamma(t) + \frac{1}{4}\sum_{\beta\beta'\gamma\gamma'}' V_{\beta\beta'\gamma\gamma'}\hat{c}^\dagger_\beta(t)\hat{c}^\dagger_{\beta'}(t)\hat{c}_{\gamma'}(t)\hat{c}_\gamma(t).$$

The prime on the summation in (1.3) indicates that Coulomb interaction terms already included in the mean-field energies E_γ must be discarded in order to avoid double counting.

The equation of motion for the current density (22) is determined by Heisenberg equations of motion for a pair of electron creation and annihilation operators:

$$\frac{d}{dt}(\hat{c}_\gamma^\dagger(t)\hat{c}_{\gamma'}(t)) = -\frac{1}{i\hbar}\sum_\alpha \int_{el.ext} d^3r \left\{ \hat{c}_\gamma^\dagger(t)\hat{c}_\alpha(t)\hat{\mathbf{A}}(\mathbf{r},t)\cdot \mathbf{j}_{\gamma'\alpha}^T(\mathbf{r}) - \hat{c}_\alpha^\dagger(t)\hat{c}_{\gamma'}(t)\hat{\mathbf{A}}(\mathbf{r},t)\cdot \mathbf{j}_{\alpha\gamma}^T(\mathbf{r}) \right\}$$

$$+\frac{1}{i\hbar}(E_{\gamma'}-E_\gamma)\hat{c}_\gamma^\dagger(t)\hat{c}_{\gamma'}(t)$$

$$+\frac{1}{i\hbar}\left[\hat{c}_\gamma^\dagger(t)\hat{c}_{\gamma'}(t), \frac{1}{4}\sum_{\beta\beta'\alpha\alpha'}' V_{\beta\beta'\alpha\alpha'}\hat{c}_\beta^\dagger(t)\hat{c}_{\beta'}^\dagger(t)\hat{c}_{\alpha'}(t)\hat{c}_\alpha(t)\right]. \tag{25}$$

The last term in this expression entails the many-electron problem and can be approximated in various ways to obtain a closed set of equations that can be solved [6]. In the next section, which is intended to illustrate the use of the Green tensor, we shall treat (25) only in its simplest (free-carrier) approximation, i.e., we disregard the last term.

2 Application to spontaneous emission

2.1 Derivation of the spontaneous emission rate

The method we use to derive the spontaneous emission rate is adapted from the methods commonly used in quantum optics [26] and in particular inspired by [27]. On the basis of the equation of motion (25), we will derive an expression for the occupation number of the conduction band ($\gamma = \gamma' = 2, \mathbf{k}$) of the form:

$$\frac{d}{dt} < \hat{c}_{2\mathbf{k}}^\dagger(t)\hat{c}_{2\mathbf{k}}(t) > = -\Gamma_{SE} < \hat{c}_{2\mathbf{k}}^\dagger(t)\hat{c}_{2\mathbf{k}}(t) > + \cdots \tag{26}$$

in which the brackets indicate expectation values, the factor Γ_{SE} is interpreted as the coefficient of spontaneous emission and the dots represent terms of more complicated form. From inspection of (25) it is clear that, neglecting the electron-electron interaction, a result of the form (26) must be obtained from the first line on the right hand side of (25) which contains the field operator $\hat{\mathbf{A}}(\mathbf{r},t)$. This field operator, which describes the creation of a photon in the process that we consider, consists according to (17) of a free part and a part generated by the (transverse) electromagnetic current. Since we are interested in optical transitions, only terms with optical frequencies of the current $\hat{\mathbf{J}}_{EM}^T(\mathbf{r},t)$ are relevant here. These are the terms of (22) for which γ and γ' refer to different bands. For them, we use the zero-order expression for the elements of the density operator:

$$\hat{c}_{n\mathbf{k}}^\dagger(t)\hat{c}_{n'\mathbf{k}'}(t) = \hat{c}_{n\mathbf{k}}^\dagger(0)\hat{c}_{n'\mathbf{k}'}(0)e^{-i\omega_{n'n}t}; \quad (n \neq n') \tag{27}$$

with $\omega_{n'n} = \frac{1}{\hbar}(E_{n'\mathbf{k}'}-E_{n\mathbf{k}})$. Then substitution of the current (22) into (17) yields:

$$\hat{\mathbf{A}}(\mathbf{r},t) = \hat{\mathbf{A}}_{free}(\mathbf{r},t) + \sum_{n'\neq n,\mathbf{k}'}\int_{act.reg.} d^3r' \overset{\leftrightarrow}{G}(\mathbf{r},\mathbf{r}',\omega_{n'n})\hat{c}_{n\mathbf{k}}^\dagger(t)\hat{c}_{n'\mathbf{k}'}(t)\cdot \mathbf{j}_{nn'}^T(\mathbf{r}',\mathbf{k},\mathbf{k}'), \tag{28}$$

with $j_{nn'}^T(\mathbf{r}, \mathbf{k}, \mathbf{k}') \equiv j_{nkn'k'}^T(\mathbf{r})$. The use of (27) in the intermediate step implies a limitation to lowest order in the field operator $\hat{\mathbf{A}}(\mathbf{r}, t)$ (note that the fermion operators are coupled via (25) to the field operator) and thereby higher order processes such as the re-absorption of emitted photons are neglected.

The summation in (28) splits in two parts, one in which all terms have a negative frequency content ($E_q < E_p$):

$$\hat{\mathbf{A}}_{opt}^{\,-}(\mathbf{r}, t) = \hat{\mathbf{A}}_{free}^{\,-}(\mathbf{r}, t) + \sum_{q<p,\mathbf{k}_q,\mathbf{k}_{p_{act.reg.}}} \int d^3r\, \overset{\leftrightarrow}{G}(\mathbf{r}, \mathbf{r}', \omega_{qp}) \cdot j_{pq}^T(\mathbf{r}', \mathbf{k}_p, \mathbf{k}_q) \hat{c}_{p\mathbf{k}_p}^\dagger(t) \tilde{c}_{q\mathbf{k}_q}(t) \quad (29)$$

and the other part which is its Hermitian conjugate $\hat{\mathbf{A}}_{opt}^{\,+}(\mathbf{r}, t) = [\hat{\mathbf{A}}_{opt}^{\,-}(\mathbf{r}, t)]^\dagger$, in which all the terms have a positive frequency content. The former can be associated with a photon creation operator while the latter is associated with a photon annihilation operator. Calculation of the spontaneous emission is most easily performed by normal ordering of the operators [27, 28, 29, 30], which implies that these photon creation operators are put on the left and the photon annihilation operators are put on the right in operator-product expressions. In this way one loses all vacuum expectation values containing factor $\hat{\mathbf{A}}_{free}^{\pm}$; i.e, contributions of the free field, and the spontaneous emission is regarded as the radiation reaction of the current source back on itself. Moreover we adopt the familiar rotating wave approximation [29], in which creation of a photon is accompanied by transition of an electron to an energetically lower state and the annihilation of a photon by the opposite transition. Substitution of (28) into (25) for $\gamma = \gamma' = (n, \mathbf{k})$ and omitting the last commutator in (25) then yields the Heisenberg equation of motion:

$$\frac{d}{dt}\left(\hat{c}_{n\mathbf{k}}^\dagger(t)\hat{c}_{n\mathbf{k}}(t)\right) = \frac{1}{i\hbar}\int d^3r \quad \left[\hat{\mathbf{A}}^{-}(\mathbf{r}, t) \cdot \hat{\mathbf{J}}_{n\mathbf{k}}^{<\dagger}(\mathbf{r}, t) - \hat{\mathbf{J}}_{n\mathbf{k}}^{<}(\mathbf{r}, t) \cdot \hat{\mathbf{A}}^{+}(\mathbf{r}, t)\right.$$
$$\left. -\hat{\mathbf{A}}^{-}(\mathbf{r}, t) \cdot \hat{\mathbf{J}}_{n\mathbf{k}}^{>\dagger}(\mathbf{r}, t) + \hat{\mathbf{J}}_{n\mathbf{k}}^{>}(\mathbf{r}, t) \cdot \hat{\mathbf{A}}^{+}(\mathbf{r}, t)\right], \quad (30)$$

in which

$$\hat{\mathbf{J}}_{n\mathbf{k}}^{<}(\mathbf{r}, t) \equiv \sum_{m<n,\mathbf{k}'} j_{nm}^T(\mathbf{r}, \mathbf{k}, \mathbf{k}')\hat{c}_{n\mathbf{k}}^\dagger(t)\hat{c}_{m\mathbf{k}'}(t),$$

$$\hat{\mathbf{J}}_{n\mathbf{k}}^{>}(\mathbf{r}, t) \equiv \sum_{m>n,\mathbf{k}'} j_{mn}^T(\mathbf{r}, \mathbf{k}', \mathbf{k})\hat{c}_{m\mathbf{k}'}^\dagger(t)\hat{c}_{n\mathbf{k}}(t). \quad (31)$$

Since the integrand in (30) is anti-Hermitian, one obtains for the expectation value of this equation, in any state of the form $|\varphi_{el}> |0_{field}>$ with arbitrary electronic state and vacuum photonic state,

$$\frac{d}{dt} < \hat{c}_{n\mathbf{k}}^\dagger(t)\hat{c}_{n\mathbf{k}}(t) >=$$

$$-\frac{2}{\hbar}\left\{\sum_{m>n,\mathbf{k}'}\sum_{q<p,\mathbf{k}_p\mathbf{k}_q} \mathrm{Im}\left[I(n, \mathbf{k}, m, \mathbf{k}', p, \mathbf{k}_p, q, \mathbf{k}_q) < (\hat{c}_{p\mathbf{k}_p}^\dagger(t)\hat{c}_{q\mathbf{k}_q}(t)\hat{c}_{n\mathbf{k}}^\dagger(t)\hat{c}_{m\mathbf{k}'}(t)) >\right]\right.$$

$$\left. + \sum_{m<n,\mathbf{k}'}\sum_{q>p,\mathbf{k}_p\mathbf{k}_q} \mathrm{Im}\left[I(n, \mathbf{k}, m, \mathbf{k}', p, \mathbf{k}_p, q, \mathbf{k}_q) < (\hat{c}_{n\mathbf{k}}^\dagger(t)\hat{c}_{m\mathbf{k}'}(t)\hat{c}_{p\mathbf{k}_p}^\dagger(t)\hat{c}_{q\mathbf{k}_q}(t)) >\right]\right\} \quad (32)$$

where

$$I(n, \mathbf{k}, m, \mathbf{k}', p, \mathbf{k}_p, q, \mathbf{k}_q) \equiv \int\limits_{act.\,reg.} \int d^3r d^3r' \mathbf{j}_{nm}^T(\mathbf{r}, \mathbf{k}, \mathbf{k}') \cdot \overset{\leftrightarrow}{G}(\mathbf{r}, \mathbf{r}', \omega_{qp}) \cdot \mathbf{j}_{pq}^T(\mathbf{r}', \mathbf{k}_p, \mathbf{k}_q). \quad (33)$$

Equation (32) expresses the time evolution of the carrier number operator corresponding to band n and wave vector $\mathbf{k}$ in the first Brillouin zone as a net result of two contributions: transitions of electrons to band n and transitions from band n to other bands. We will now consider the simple case of just two bands, an upper band labeled 2 (conduction band) and a lower band 1 (valence band). Then (32) for the occupation operator of the conduction band can be written as:

$$\frac{d}{dt} < \hat{c}_{2\mathbf{k}}^\dagger(t)\hat{c}_{2\mathbf{k}}(t) > =$$

$$-\frac{2}{\hbar} \sum_{\mathbf{k}', \mathbf{k}_1} \mathrm{Im} \left\{ I(2, \mathbf{k}, 1, \mathbf{k}', 1, \mathbf{k}_1, 2, \mathbf{k}) < \hat{c}_{2\mathbf{k}}^\dagger(t)\hat{c}_{2\mathbf{k}}(t)(\delta_{\mathbf{k}'\mathbf{k}_1} - \hat{c}_{1\mathbf{k}_1}^\dagger(t)\hat{c}_{1\mathbf{k}'}(t)) > \right\}$$

$$-\frac{2}{\hbar} \sum_{\mathbf{k}', \mathbf{k}_1, \mathbf{k}_2 \neq \mathbf{k}} \mathrm{Im} \left\{ I(2, \mathbf{k}, 1, \mathbf{k}', 1, \mathbf{k}_1, 2, \mathbf{k}_2) < \hat{c}_{2\mathbf{k}}^\dagger(t)\hat{c}_{1\mathbf{k}'}(t)\hat{c}_{1\mathbf{k}_1}^\dagger(t)\hat{c}_{2\mathbf{k}_2}(t) > \right\}. \quad (34)$$

The first term on the right hand side of (34) describes, apart from a correction due to a possible Pauli blocking of the final state $\mathbf{k}'$ in the valence band, the effect of decay by spontaneous emission of intial conduction band state $\mathbf{k}$. The second term on the right hand side of (34) contains combinations of $\hat{c}$-operators that give rise to quantum interference among multiple radiation pathways, some of which are similar to those occuring in $\vee$-type atomic systems [31, 32]. Such effects may lead, in principle, to much faster decay than resulting from the first term. However, in realistic situations the necessary coherences for such enhancement are most probably not observable. Therefore, we will neglect such effects here. We may now find the coefficient of spontaneous emission from the term on the right hand side of (34) that is proportional to $< \hat{c}_{2\mathbf{k}}^\dagger(t)\hat{c}_{2\mathbf{k}}(t) >$. This coefficient is:

$$\Gamma_{SE} = \frac{2}{\hbar} \sum_{\mathbf{k}'} \mathrm{Im}[I(2, \mathbf{k}, 1, \mathbf{k}', 1, \mathbf{k}', 2, \mathbf{k})] =$$

$$= \frac{2}{\hbar} \mathrm{Im} \sum_{\mathbf{k}'} \int\limits_{act.} dr \int\limits_{reg} dr' \mathbf{j}_{21}^T(\mathbf{r}, \mathbf{k}, \mathbf{k}') \cdot \overset{\leftrightarrow}{G}(\mathbf{r}, \mathbf{r}', \omega_{2\mathbf{k},1\mathbf{k}'}) \cdot \mathbf{j}_{12}^T(\mathbf{r}', \mathbf{k}', \mathbf{k}). \quad (35)$$

The form of (35) is reminiscent of the traditional Fermi Golden Rule result for the spontaneous emission rate, which reads:

$$\Gamma_{SE,GR} = \frac{2\pi}{\hbar} | < f|H_{int}|i > |^2 \rho(E). \quad (36)$$

The current densities $\mathbf{j}^T$ play parts similar to the transition matrix elements in (36), while the Green tensor takes account of the electromagnetic contribution to the density of final states $\rho(E)$. Our basic result has a simple interpretation in terms of the (self) radiation reaction energy of the emitting current in its own emitted field [33].
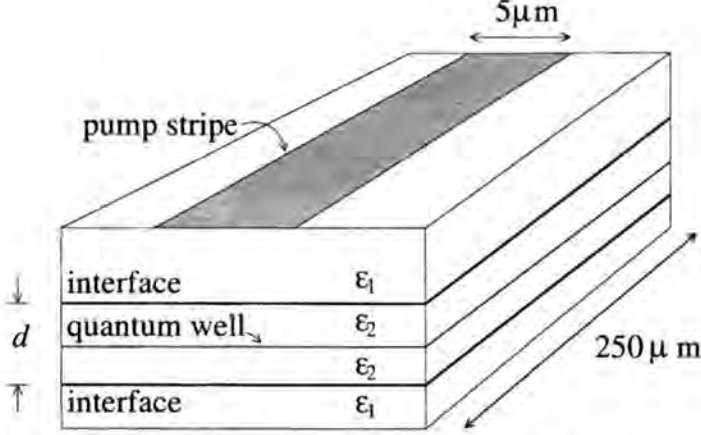
Figure 1: A typical edge-emitting laser. The pump stripe on the top determines the pumped region of the quantum well, and this in turn determines the opening angle of the laser mode.

3 The β_{sp}-factor

Applications of (35) to a quantum well in a dielectric multilayer configuration can be found elsewhere in these proceedings [34] as well as in [10]. These concern calculations of spontaneous emission rates and their variations as functions of width of the guiding layer and the position of the quantum well therein. As another application, we will present here a calculation of the spontaneous emission beta-factor, β_{sp}, for an edge-emitting structure. By its definition [35], this factor is the spontaneous emission rate into a given (laser) mode as a fraction of the total spontaneous emission rate. These emission rates may be calculated using (35), in which for the emission into a lasing mode the corresponding contribution to the total Green tensor should be retained as follows. For a dielectric configuration that occupies a finite region in space, the mode of interest for lasing will, in most cases, manifest itself by a simple pole of $\overset{\leftrightarrow}{G}(\mathbf{r}, \mathbf{r}', \omega)$ in the complex ω-plane at $\omega = \omega_{mode}$. Then the propagator of this mode may be constructed by the prescription:

$$\overset{\leftrightarrow}{G^{red}}(\mathbf{r}, \mathbf{r}', \omega) = \left[\lim_{\zeta \to \omega_{mode}} (\zeta - \omega_{mode}) \overset{\leftrightarrow}{G}(\mathbf{r}, \mathbf{r}', \zeta) \right] \frac{1}{\omega - \omega_{mode}}, \tag{37}$$

and the β_{sp}-factor is obtained as:

$$\beta_{sp} = \frac{\mathrm{Im} \sum_{\mathbf{k}'} \int\limits_{act.} dr \int\limits_{reg} dr' \mathbf{j}_{21}^T(\mathbf{r}, \mathbf{k}, \mathbf{k}') \cdot \overset{\leftrightarrow}{G^{red}}(\mathbf{r}, \mathbf{r}', \omega_{2\mathbf{k}, 1\mathbf{k}'}) \cdot \mathbf{j}_{12}^T(\mathbf{r}', \mathbf{k}', \mathbf{k})}{\mathrm{Im} \sum_{\mathbf{k}'} \int\limits_{act.} dr \int\limits_{reg} dr' \mathbf{j}_{21}^T(\mathbf{r}, \mathbf{k}, \mathbf{k}') \cdot \overset{\leftrightarrow}{G}(\mathbf{r}, \mathbf{r}', \omega_{2\mathbf{k}, 1\mathbf{k}'}) \cdot \mathbf{j}_{12}^T(\mathbf{r}', \mathbf{k}', \mathbf{k})}. \tag{38}$$

Since the Green tensor for a finite dielectric object such as, e.g., a VCSEL, is quite complicated and, in fact, at present not available to us, we have adopted the model of a multilayer
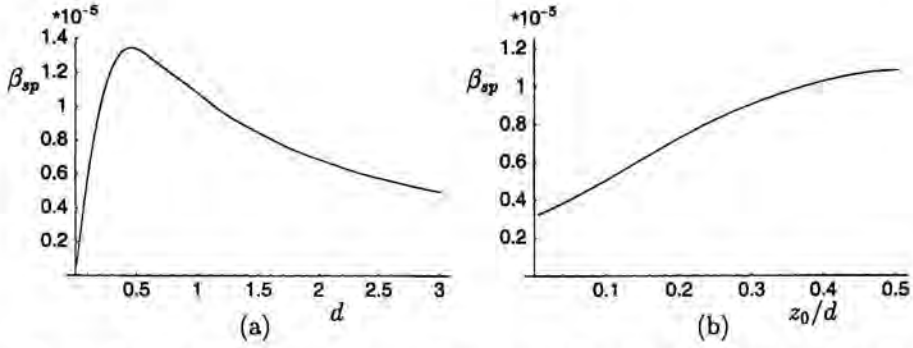
Figure 2: (a) β_{sp} of the fundamental guided mode versus width of the middle layer d, with the active quantum well at the center of the layer. (b) β_{sp} versus position of the quantum well z_0/d, for fixed width $d = \lambda/2$ ($z_0/d = 0$ means quantum well at the interface and $z_0/d = 1/2$ means quantum well at the center).

configuration with infinite extension in the lateral direction, for which the Green tensor is known in analytic form [8].

A complication that arises in the case of a dielectric structure with finite extent is that the mode spectrum has also guided modes which form continuous branches, so that the prescription (37) cannot be applied. However, we have shown in [10] that in this case the contribution of individual guided modes, for a given frequency ω_{gap} of the electronic transition between the conduction band and the valence band, can be identified as residues of $\overset{\leftrightarrow}{G}$ at poles in the complex k-plane, where k is the lateral wavenumber. The contribution of a single guided mode is then given by integration over all lateral directions of $\mathbf{k}$. For a typical edge-emitting laser, with structure as shown in Fig. 1, lasing can only occur in lateral directions within the activated layer, roughly determined by the orientation of the pump stripe. For typical stripe dimensions of 5 μm by 250 μm, this implies restriction of the lasing modes to an angle $\psi \simeq 2 \times 10^{-2}$ rad out of the 2π continuum of guided modes with a given k.

Another complication is that in a real device the emission spectrum is not monochromatic but has a width $\Delta\omega_{sp} \simeq 3\text{THz}$ [36], while the selected longitudinal mode has a natural width $\Delta\omega_{mode} \simeq 30\text{GHz}$ due to outcoupling losses. Therefore, we take as an estimate of β_{sp} for a realistic structure the fraction $(\psi/2\pi)(\Delta\omega_{mode}/\Delta\omega_{sp}) \simeq 10^{-4}/\pi$ of the contribution of the fundamental guided mode of the same layered configuration with infinite lateral extension.

We previously calculated the total spontaneous emission rate as a function of layer width for a three-layer waveguide fabricated from $Al_xGa_{1-x}As$ with a quantum well embedded at the center of the middle layer [10, 34]. The quantum well is very thin and has dielectric constant equal to that of the middle layer. For the case of a three-layer waveguide fabricated from $Ga_xAl_{1-x}As$ with $x = 0.50$, $x = 0$ and $x = 0.50$ respectively, we now calculate the β_{sp}-factor, as described above, for the fundamental guided mode, i.e., the first guided mode to be born with increasing width d of the middle layer, starting from $d = 0$. The β_{sp}-factor as a function of d is plotted in Fig. 2(a). The width d is given in units of $\lambda/2$, where λ is the vacuum wavelength associated with the electronic transition frequency ω_{gap}. It is seen

that as d increases from 0, the β_{sp}-factor rises steeply, obtains a maximum near $d = \lambda/4$ and then decreases monotonously. This can be explained as follows. First it should be realized that the spontaneous emission rate into the mode of interest is proportional to the value of the mode intensity at the location of the emitter, i.e., the quantum well, whereas the total spontaneous emission rate does not change much with increasing width [10]. One can show that for small d the intensity at the center of the middle layer scales as $I \propto \sqrt{k_{gm}^2(d) - \varepsilon_1 \frac{\omega^2}{c^2}}$, where $k_{gm}(d)$ is the pole in the complex k-plane associated with the mode of interest, given by [10]:

$$d\sqrt{\varepsilon_2 \frac{\omega^2}{c^2} - k_{gm}^2} - 2\arctan\left(\frac{\sqrt{k_{gm}^2 - \varepsilon_1 \frac{\omega^2}{c^2}}}{\sqrt{\varepsilon_2 \frac{\omega^2}{c^2} - k_{gm}^2}}\right) = 0, \quad \sqrt{\varepsilon_1}\frac{\omega}{c} < k_{gm} \leq \sqrt{\varepsilon_2}\frac{\omega}{c}. \quad (39)$$

From this one finds that for small d, where k_{gm} is only slightly larger than $\sqrt{\varepsilon_1}\omega/c$, the mode intensity is proportional to d:

$$I \propto \frac{\omega^2}{2c^2}(\varepsilon_2 - \varepsilon_1)d, \quad (40)$$

which explains the initial linear increase of β_{sp} with d. In turn, for large d the mode intensity scales as $1/d$, which leads to the final $1/d$ decrease of the β_{sp}-factor.

The value of the β_{sp}-factor found here is on the order of 10^{-5}, depending on the width of the middle layer. This agrees well with estimates by others [35, 36, 37], based on various different approaches. Clearly, our technique provides a good approximation for the β_{sp}-factor and allows us to predict the general trends of its dependence on design parameters such as dielectric constants, quantum-well position, and width of the middle layer. As an example, we show in Fig. 2(b) the variation of β_{sp} with the position of the quantum well in the middle layer. Here the β_{sp}-factor clearly probes the mode intensity.

4   Acknowledgments

References

[1] Y. Yamamoto, W.H. Richardson. Optics and Photonics News 6(1995) 24–29
[2] S. Kakimoto, K. Shigihara, Y. Nagai. IEEE J. of Quantum Electron. 33(1997) 824–830
[3] C. Becher, E. Gehrig, J.-J. Boller. Phys. Rev. A 57(1998) 3952–3960
[4] J.-L. Vey, W. Elsasser. Opt. Lett. 23(1998) 721–723
[5] C. Lin, D. Deppe. IEEE J. Lightwav. Technol. 13(1995) 575–580
[6] W.W. Chow, S.W. Koch, M. Sangent III. *Semiconductor-laser physics*. Springer (1994)
[7] H. Rigneault, S. Monneret. Quantum Semiclassical Optics 9(1997)
[8] M.S. Tomaš. Phys. Rev. A 51(1995) 2545–2559

[9] H.P. Urbach, G.L.J.A. Rikken. Phys. Rev. A 57(1998) 3913–3930

[10] C.L.A. Hooijer, G.-X. Li, K. Allaart, D. Lenstra. In *SPIE proceedings 3625*, 1999. paper 3625-71, presented at Photonics West, 23-29 Jan. '99, San Jose, California

[11] L. Knöll, W. Vogel, D.-G. Welsch. Phys. Rev. A 36(1987) 3803

[12] W. Vogel, D.-G. Welsch. *Lectures on Quantum Optics.* Akademie Verlag, Berlin (1994)

[13] R.J. Glauber, M. Lewenstein. Phys. Rev. A 43(1991) 467–491

[14] A. Tip. Phys. Rev. A 56(1997) 5022–5041

[15] C. Cohen-Tannoudji, J. Dupont-Roc, G. Gynberg. *Photons and atoms; an introduction to quantum electrodynamics.* John Wiley & Sons, New York (1989)

[16] B. Huttner, S.M. Barnett. Phys. Rev. A 46(1992) 4306–4322

[17] H. Trung Dung, L. Knöll, D.-G. Welsch. Phys. Rev. A 57(1998) 3931–3942

[18] S. Scheel, L. Knöll, D.-G. Welsch. Phys. Rev. A 58(1998) 700

[19] T. Gruner, D.-G. Welsch. Phys. Rev. A 53(1996) 1818–1829

[20] M. Schubert, B. Wilhelmi. *Nonlinear Optics and Quantum Electronics.* John Wiley and Sons, New York (1986)

[21] L. Knöll, D.-G. Welsch. Prog. Quant. Electron. 16(1992) 135

[22] J.D. Jackson. *Classical Electrodynamics.* John Wiley and Sons, New York, 2nd edition, (1975)

[23] A. L. Fetter, J.D. Walecka. *Quantum theory of many particle systems.* McGraw-Hill, New York (1971)

[24] C. Kittel. *Quantum theory of solids.* John Wiley and Sons, New York (1963)

[25] H. Haug, S.W. Koch. *Quantum theory of the optical and electronic properties of semiconductors.* World Scientific, Singapore (1990)

[26] L. Allen, J.H. Eberly. *Optical resonace and two-level atoms.* John Wiley (1975). Section 2.4 and Chapter 7

[27] H.J. Kimble, L. Mandel. Phys. Rev. A 13(1976) 2123–2144

[28] J.R. Ackerhalt, P.L. Knight, J.H. Eberly. Phys. Rev. Letters 30(1973) 456–460

[29] J.R. Ackerhalt, J.H. Eberly. Phys. Rev. D 10(1974) 3350–3375

[30] P.W. Milonni, J.R. Ackerhalt, W.A. Smith. Phys. Rev. Letters 31(1973) 958–960

[31] Shi-Yao Zhu, Ricky C.F. Chan, C.P. Lee. Phys. Rev. A 52(1995) 710–716

[32] Peng Zhou, S. Swain. Phys. Rev. A 56(1997) 3011–3021

[33] G. Harel, I. Abrams. *Spontaneous emission in a cavity: quantum and classical radiation-reaction viewpoint.* elsewhere in these proceedings

[34] C.L.A. Hooijer, D. Lenstra, K. Allaart. *Probing field mode densities in a multilayer structure with a quantum well.* elsewhere in these proceedings

[35] K. Petermann. IEEE J. Quantum Elect. 15(1979) 566–570

[36] G.P. Agrawal, N.K. Dutta. *Semiconductor lasers.* Van Nostrand Reinhold, New york (1993)

[37] Y. Yamamoto, S. Machida, G. Björk. Phys. Rev. A 44(1991) 657–668

Author's address

Quantum Electronics Theory Group, Division of Physics and Astronomy,
Vrije Universiteit,
De Boelelaan 1081, 1081 HV Amsterdam,
The Netherlands.

Email address: lenstra@nat.vu.nl.

G. Bourdon, R. Adams, I. Robert, K. Nelep, I. Sagnes and I. Abram

Enhancement and Inhibition of Spontaneous Emission in Room-Temperature Semiconductor Microcavities

Abstract

We have fabricated planar semiconductor microcavities with metallic mirrors in which we have observed both enhancement and inhibition of spontaneous emission, at room temperature. Inhibition is an unambiguous signature of Cavity Quantum Electrodynamics effects, and its observation in these room-temperature semiconductor structures opens the way to novel devices with controlled spontaneous emission.

1 Introduction

Spontaneous emission of light is indispensable in the operation of optoelectronic devices: in Light Emitting Diodes (LED) it constitutes the useful output of the devices, while in semiconductor lasers it provides the first photon that triggers stimulated emission. However, as this phenomenon takes place generally in an uncontrolled way, a very large fraction of the emitted the light is lost. As a consequence, the energy efficiency of LED's is only of the order of a few percent, whereas in semiconductor lasers only 1 photon in 10^5 goes into the lasing mode while all other photons are lost and contribute to raising the threshold of operation of the laser, limiting its bandwidth and introducing noise. Clearly, if the directivity and the dynamics of spontaneous emission can be controlled, this may contribute to greatly increase the efficiency of light emitting diodes, reduce the threshold of lasers, possibly to the point of canceling it, or may lead to the realization of novel light sources with non-classical properties such as sources of controlled trains of single photons.

2 Cavity Quantum Electrodynamics in atoms

Over the last two decades, use of atomic systems, placed in optical cavities of dimensions of the order of the wavelength (called microcavities), has led to the demonstration of the possibility of controlling spontaneous emission, and gave rise to the field of Cavity Quantum Electrodynamics (CQED) [1]. In order to understand how spontaneous emission can be modified inside a cavity, one has to consider simply that this phenomenon is due to the coupling of the excited atomic states to the electromagnetic modes available. Thus, the different modal structure of the electromagnetic field in the microcavity as compared with that in free space produces a modification in the characteristics of spontaneous emission when an emitter is introduced inside such a microcavity.

Two situations are of particular interest. The first one concerns cavities that display very sharp resonances, so that their modal structure consists of a few discrete states. If an atom inside such a cavity couples to a single one of these states (a situation called the "strong coupling" regime) its spontaneous emission will involve a periodic exchange of the energy between the atom and the cavity mode (Rabi oscillations) and, in the spectrum of the light emerging from the cavity, this will give rise to a doublet (vacuum Rabi splitting), rather than to a single emission line at the atomic frequency.

The second situation concerns cavities in which the modal structure constitutes a continuum, such as planar microcavities with ideal metallic mirrors. In this situation, the atom will couple (in what is called the "weak coupling" regime), to the part of the continuum that is at the same frequency as the atomic transition and will undergo a radiative decay of its energy in favor of the electromagnetic modes of the cavity. Near the resonance frequencies of the cavity, the density of states in this continuum is higher than in free space, and this produces an enhancement of the spontaneous emission rate with respect to its value in free space. Below the cut-off frequency of the cavity, on the other hand, the density of electromagnetic states seen by a dipole parallel to the two mirrors falls to zero, implying that in this case there is no coupling between the dipole and the electromagnetic field in the cavity, and thus spontaneous emission is inhibited.

As the development of CQED has been based on considerations and experiments on single atoms that are subject only to the radiative interaction and are otherwise isolated from their environment, it is quite difficult to extend the principles of this theory to semiconductors. Semiconductors are complex material systems that possess very few of the simplifying features of isolated single atoms: In contrast to single atoms, semiconductors involve a very large number of atoms, their electronic excitations present a collective and delocalized character and are subject to numerous interactions with their environment that produce rapid processes of dephasing or energy relaxation.

3 Strong coupling in semiconductors

A major breakthrough in the direction of adapting CQED to semiconductors was accomplished in 1992, when the vacuum Rabi splitting was observed in planar microcavities with high reflectivity Bragg mirrors, containing semiconductor quantum wells, at low temperature [2]. Soon afterwards, it was demonstrated that the spontaneous emission lifetime of the excitons inside the cavity was strongly modified, in accordance with the "strong coupling" theory of CQED [3]. Two features of solid-state physics permit this complex system to meet some of the requirements of atomic CQED. The first one is the translational invariance of the planar cavity that introduces a wavevector selection rule according to which each quantum well exciton can couple to a single mode of the planar cavity, reproducing thus the state-to-state interaction conditions of the atomic "strong coupling" regime. The second one is the low temperature experimental conditions under which the exciton scattering by the thermal lattice vibrations is relatively slow, so that excitons retain essentially the same wavevector and thus satisfy the state-to-state interaction conditions throughout the experimental observation time. On the other hand, when the temperature is raised and the excitons to are rapidly scattered over all wavevectors, the "strong coupling" conditions are not met anymore.

In that case, the spontaneous emission lifetime of the excitons recovers its free space value [3], while the Rabi doublet in the spectrum need not be attributed to CQED, but rather to the classical refractive index variations of the spacer in the vicinity of the exciton frequency [4].

4   Weak coupling in semiconductors

Even though the thermal scattering of carriers in semiconductors compromises the modification of spontaneous emission in the "strong coupling" regime, surprisingly, it can be exploited to meet some of the conditions that permit such a modification under "weak coupling". To understand this, one has to consider that the scattering of carriers and the statistical occupation of a given region in wavevector space can be thought, in direct space, as corresponding to a localization of the extended wavefunctions of the carriers into a statistical distribution of small "coherence volumes" whose extent is given by the Fourier transform of the occupied region in wavevector space. The excited electronic states all of the lattice sites contained in each "coherence volume" are in phase and therefore emit cooperatively as a single dipole, with a spontaneous emission lifetime that is inversely proportional to the number of sites contained in the "coherence volume". At room temperature, the spontaneous emission lifetime in GaAs or InGaAs quantum wells at moderate carrier injection densities (10^{17} cm^{-3}) is of the order of 10 ns, a lifetime that corresponds to a collective oscillator strength of approximately 6×10^5 unit cells. This implies that, at room temperature, the elementary collective emitters have a diameter of the order of 200 Angstroms and thus can be considered to be point-like when compared with the wavelength of light emitted by the semiconductor. As a consequence, at room temperature, the CQED behavior of the spontaneous emission of a semiconductor quantum well inside a cavity will be analogous to that of a collection of randomly placed point emitters.

In considering the modification of spontaneous emission of a room temperature quantum well let us first examine the case of a planar cavity bounded by GaAs/AlAs Bragg mirrors. These mirrors present a high reflectivity for angles less than 20 degrees with respect to the normal, while for larger angles (which represent 95 percent of space) the reflectivity drops practically to zero. As a consequence, the spontaneous emission of a point emitter or a room temperature quantum well placed in such a cavity will not be modified appreciably and will retain essentially the same dynamics as in free space [5]. A different behavior is expected, however, for a point emitter placed in a cavity with metallic mirrors where a modification of the dynamics of spontaneous emission is possible. Indeed, metallic mirrors generally present a relatively constant reflectivity over all angles, even if its value is lower than that of Bragg mirrors, at normal incidence, because of dissipative losses in the metal of the order of a few percent. In particular, for GaAs cavities bounded by silver mirrors, preliminary calculations indicate that the spontaneous emission of a dipole oriented parallel to the mirrors should be enhanced by a factor of 4 if the spacer thickness is such that the cavity is resonant with the emitter, whereas for shorter cavities the spontaneous emission of a parallel dipole should be partially inhibited. Because the dissipative losses in the metal introduce additional channels of de-excitation for the dipole, inhibition can never the complete. For the case of silver, which is the metal with the smallest losses, inhibition is manifested by a reduction of the

spontaneous emission rate by a factor of 5 [5].

In general, when absorption losses increase, inhibition becomes weaker. Thus, the observation of this phenomenon requires a very careful control of all loss mechanisms. On the other hand, the observation of enhancement is more tolerant to radiative losses and persists even in the presence of absorption in the mirrors or lateral leaks in the cavity. Indeed, for modes that display a very high quality factor and a small volume, the emission rate may be larger than for all other directions of free space, including the leaks, thus permitting a direct observation of enhancement [6]. Under the same conditions, however, where the cavity presents substantial leaks, no inhibition can be observed. Enhancement due to the Purcell effect was recently observed at low temperatures in laterally confined semiconductor microcavities with Bragg mirrors [7]. It should be noted that, in addition to the radiative losses discussed above, there exist a large number of parasitic processes in semiconductors (in particular, non-radiative electron-hole recombination on defects or surface states) that can open fast decay channels for the electron-hole pairs thus masking any enhancement of the spontaneous emission decay rate due to CQED effects. The importance of observing inhibition of spontaneous emission as an unambiguous signature of CQED effects as well as the experimental difficulties associated with this observation were recognized [8] as early as 1981. Inhibition was first observed in Rydberg atoms [9] and was later observed at optical frequencies [10, 11], also in atoms. Until recently, it had never been observed in room temperature solid-state microcavities.

5 Experimental

With the aim of observing inhibition and enhancement of spontaneous emission in room temperature semiconductors, we carried out recently a series of experiments on the photoluminescence dynamics of InGaAs quantum wells placed in GaAs microcavities, bounded by silver mirrors. We fabricated 4 microcavities having spacers of different thickness: (a) 78 nm, (b) 90 nm, (c) 96 nm and (d) 102 nm, each expected to exhibit enhancement or inhibition. A schematic of the microcavity structure is given in Fig. 1.

The spacer of each cavity is an MOCVD-grown multi-layer structure containing in its center a 10 nm $In_{0.13}Ga_{0.87}As$ strained-layer quantum well, emitting at 950 nm at room temperature. The choice of a strained-layer quantum well is important because of the large splitting (40 meV) between the heavy and light hole bands. Because of this splitting, the emission at room temperature involves predominantly the heavy-hole to conduction band transition which is polarized parallel to the quantum well and the mirrors. A 20 nm $Al_{0.40}Ga_{0.60}As$ barrier is grown on either side of the quantum well to improve the confinement of the carriers, and 15 to 25 nm GaAs capping layers are introduced on both sides of the structure to obtain the right spacer thickness. Silver mirrors were evaporated on both sides of the sample. In order to improve the interface quantity between the silver and the GaAs, a 1.5 nm a layer of Cr metal was evaporated on the GaAs before depositing the silver. The introduction of this layer produces very strong dissipative losses and this reduces considerably the expected inhibition of spontaneous emission. Taking into account these losses, the expected inhibition corresponds to an emission rate reduced only by a factor of 1.6 with respect to the rate in the absence of the cavity. For each of the four samples the photoluminescence decay was
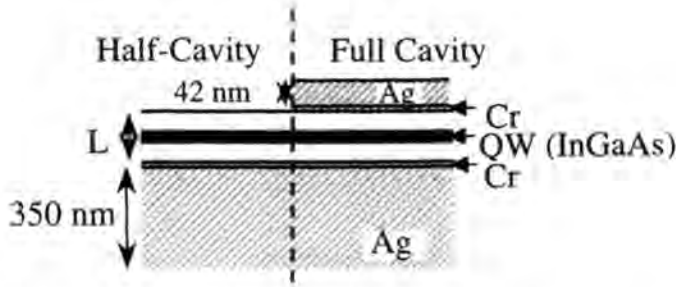
Figure 1: Schematic of microcavity structure. Left-hand side: "half cavity" consisting of semiconductor spacer and a silver mirror on one side only. Right hand side: "full cavity" consisting of semiconductor spacer with a silver mirror on either side. A thin chromium layer is introduced to improve the Ag-GaAs interface.

measured in three different stages of its fabrication process, namely (1) for the as-grown MOCVD spacer on its GaAs wafer, (2) for the spacer transferred on a silver mirror ("half cavity"), and finally (3) for the spacer on a silver mirror plus a 42 nm-thick silver layer evaporated on the free side of the spacer ("full cavity").

The samples were excited optically by a mode-locked Titanium-Sapphire laser tuned to 915 nm, delivering 1.5 ps-long pulses at 4 MHz, with the beam arriving at the sample at an incidence of 70 degrees. The spontaneous emission was collected at normal incidence through a microscope objective and was detected through a time-resolved photon-counting setup. For all samples, photoluminescence decay curves spanning 4 decades of emitted intensity were obtained for a series of 15 different incident intensities corresponding to carrier injection densities between 10^{14} and 10^{18} cm^{-3}. Examples of such decay curves, obtained for the half cavity and the full cavity of sample (b), are given in Fig. 2.

A visual comparison of the luminescence decay curves of the half cavity and the full cavity reveals immediately that the introduction of the top mirror produces a considerable modification in the dynamics of spontaneous emission: the luminescence decay becomes much faster, underscoring the enhancement of spontaneous emission. The decay curves were analyzed in terms of a non-exponential decay that could be fitted to the bimolecular radiative recombination law characteristic of semiconductors

$$\frac{dn}{dt} = -A_{nr}n - Bn_0 n - Bn^2$$

where n is the number of carriers injected, A_{nr} is the decay constant for non-radiative recombination, n_0 is the residual doping and B is the bimolecular radiative recombination constant. The value of B extracted from this fit is proportional to the spontaneous emission decay rate obtained from Fermi's Golden Rule. The injected carrier density n was calibrated by determining the incident intensity for which the bimolecular recombination constant B exhibits saturation, when the electron or hole quasi-Fermi levels reach their respective bands.
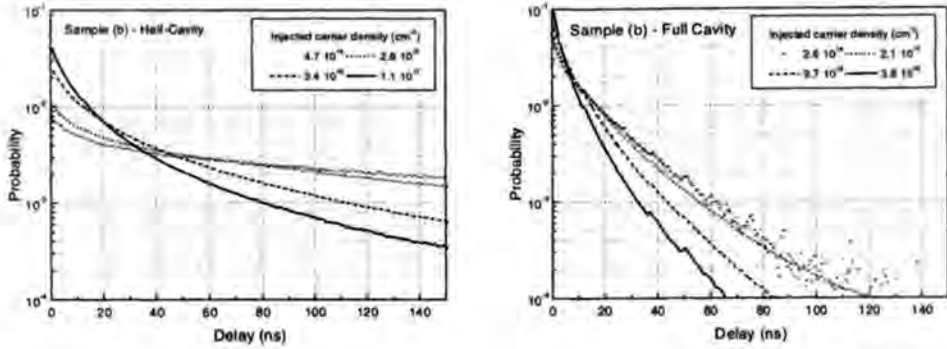
Figure 2: Dynamics of the luminescence decay in sample (b). Left-hand side: spontaneous emission in "half cavity". Right hand side: spontaneous emission in "full cavity".

For all the as-grown samples the B values were of the order of 1.6×10^{-10} s^{-1}cm^{-3} as in a quantum well embedded in a bulk semiconductor. For the half cavities the B values ranged between 1.7×10^{-10} s^{-1}cm^{-3} and 3.1×10^{-10} s^{-1}cm^{-3}, corresponding to enhancement by a factor that ranges respectively between 1.1 and 1.9, while for the full cavities the radiative recombination constant ranged from 1.0×10^{-10} s^{-1}cm^{-3} to 4.6×10^{-10} s^{-1}cm^{-3}, corresponding to inhibition by a factor of 1.6 and to enhancement by a factor of 3 respectively. The results are displayed in Fig. 3.

As can be seen in Fig. 3, the measured values for enhancement and inhibition as a function of cavity thickness follow the expected theoretical dependence, calculated by using the "weak coupling" model in which the dissipative losses due to the absorption in the mirrors have been explicitly taken into account by using the experimentally measured reflectivity of the Cr/Ag bi-layers. It should be noted that our results display a systematic deviation whereby the experimental measurements are 25 percent below the theoretical curve. This is probably due to the re-absorption of the emitted light by the quantum well which produces recycling of the excitation and thus changes the apparent emission lifetime, an effect that is not taken into account in our calculations.

The modification of the bimolecular combination constant B by the local electromagnetic environment of the quantum well inside the metallic microcavity in a way similar to that of isolated at terms in the "weak coupling" model is an experimental confirmation that the band-to-band transitions in room temperature semiconductors involve essentially randomly localized dipoles with coherence areas much smaller than the wavelength. At the same time, this result clearly indicates that the bimolecular radiative recombination process is not determined by a kinetic collisional bottleneck, in spite of all the rapid scattering and dephasing processes the carriers undergo at room temperature, but is a true radiative process subject to Cavity Quantum Electrodynamics effects.
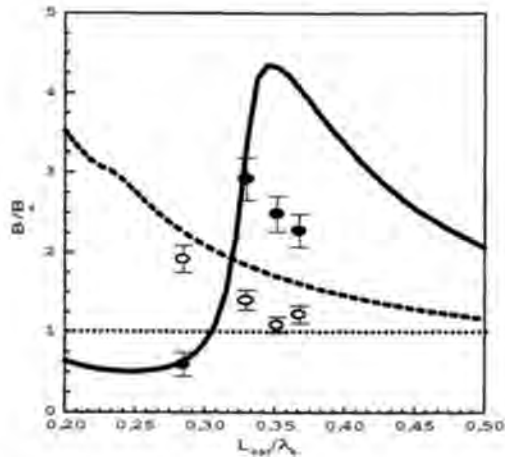
Figure 3: Modification of the bimolecular recombination constant (spontaneous emission rate) of a semiconductor quantum well in a metallic microcavity at room temperature, as a function of the cavity thickness. Full circles: experimental results for full cavities. Open circles: experimental results for half cavities. Full line: theoretical curve for full cavities. Dashed line: theoretical curve for half cavities. Dotted line: spontaneous emission in the absence of mirrors.

6 Conclusion

In conclusion, in our experiments we have demonstrated both enhancement and inhibition of spontaneous emission in room-temperature semiconductor quantum wells placed in microcavities with metallic mirrors. The observation of unambiguous CQED effects, such as enhancement and inhibition of spontaneous emission in room temperature semiconductor microcavities contributes towards the extension of the principles of CQED to complex systems such as semiconductors. This extension is a challenge analogous to that faced by scientists in the early 1960s, when the principles of laser theory, developed initially for isolated atoms or ions, were translated into the language of semiconductors [12] thus opening the way to the development of the semiconductor laser. The observation of CQED effects under conditions similar to those of operating optoelectronic devices (namely, at room temperature and under incoherent injection of the carriers) and the possibility of electrical injection afforded by the metallic mirrors permit us to envisage the design of optoelectronic devices that take advantage of CQED effects, such as high efficiency LED's, ultra-low threshold semiconductor lasers, or emitters producing non-classical light beams with strongly sub-Poissonian photon statistics or controlled trains of photons.

7 Acknowledgements

References

[1] S. Haroche. In J. Dalibard, J.M. Raimond, J. Zinn-Justin, editors, *Fundamental Systems in Optics*, Les Houches Session LIII, Elsevier, Amsterdam (1992) 767–940

[2] C. Weisbuch, M. Nishioka, A. Ishikawa, Y. Arakawa. Phys. Rev. Lett. 69(1992) 3314–3317

[3] B. Sermage, S. Long, I. Abram, J.Y. Marzin, J. Bloch, R. Planel, V. Thierry-Mieg. Phys. Rev. B 53(1996) 16516–16523

[4] Y. Zhu, D.J. Gauthier, S.E. Morin, Q. Wu, H.J. Carmichael, T.W. Mossberg. Phys. Rev. Lett. 64(1990) 2499–2502

[5] I. Abram, I. Robert, R. Kuszelewicz. IEEE J. Quantum Electron. 34(1998) 71–76

[6] E.M. Purcell. Phys. Rev. 69(1946) 681

[7] J.M. Gerard, B. Sermage, B. Gayral, B. Legrand, E. Costard, V. Thierry-Mieg. Phys. Rev. Lett. 81(1998) 1110–1113

[8] D. Kleppner. Phys. Rev. Lett. 47(1981) 233–236

[9] R.G. Hulet, E.S. Hilfer, D. Kleppner. Phys. Rev. Lett. 55(1985) 2137–2140

[10] W. Jhe, A. Anderson, E.A. Hinds, D. Meschede, L. Moi, S. Haroche. Phys. Rev. Lett. 58(1987) 666–669

[11] D.J. Heinzen, J.J. Childs, J.E. Thomas, M. S. Feld. Phys. Rev. Lett. 58(1987) 1320–1323

[12] M.G.A. Bernard, G. Duraffourg. Phys. Status Solidi 1(1961) 699–701

Author's address

France Telecom/CNET,
196 Avenue Henri Ravera, F-92220 Bagneux,
France.

G. Nienhuis, K. Joosten and S.M. Dutra

Photon Lifetimes in Laser Cavities and Excess Quantum Noise

Abstract

The concept of photon loss rates from laser cavities is discussed, and the fundamental difference between hot-cavity and cold-cavity loss rates is indicated. This difference gets particularly important in the presence of various loss channels. For a simple cavity model, a quantum mechanical expression is derived for the Hamiltonian that couples the quantized field inside the cavity to the outside world.

1 Introduction

Lossy resonators play an essential role in cavity QED as well as in laser physics. In many cases, the cavity modes are described simply by ignoring the losses. The output of the cavity is then calculated by assuming a field distribution corresponding to a perfect cavity. The coupling to the outside world is described by a cavity loss rate.

An important example of present interest is the excess noise factor of a laser. The linewidth of a quantum-limited single-mode laser can be expressed as [1]

$$\Delta\omega = K\Delta\omega_{\text{ST}} , \tag{1}$$

with $\Delta\omega_{\text{ST}}$ the Schawlow-Townes linewidth [2]

$$\Delta\omega_{\text{ST}} = \frac{\Gamma_{\text{h}}^2}{2P_{tot}} . \tag{2}$$

Here

$$\Gamma_{\text{h}} \equiv P_{tot}/W \tag{3}$$

is the loss rate of the lasing cavity (the 'hot-cavity loss rate'), defined as the ratio of the total power loss P_{tot} and the internal energy W of the laser. For simplicity, energies are expressed in units of the photon energy. The enhancement factor K can be expressed in terms of the non-orthogonality of the modes of the lossy cavity [3]. It is often assumed that the hot-cavity loss rate is identical to the inverse lifetime of a photon in the cavity without gain (the 'cold-cavity loss rate' Γ_{c}).

In this contribution we discuss the concept of cavity loss rates, both from a semiclassical and a quantum mechanical point of view. First we indicate that the hot-cavity loss rate cannot simply be identified with the inverse of the lifetime of a photon in the non-lasing cavity.

Moreover, unstable laser cavities generally lose power not only through their outcoupling mirror, but also into one or more other loss channels. Even when the total cold- and hot-cavity loss rates are identical, the relative distribution of the losses over the various loss channels may differ in the situation of a lasing system compared to a decaying cavity. This has implications for the experimental determination of the excess noise factor K.

In a simple model system of a half-sided open cavity, we discuss the form of the quantum mechanical Hamiltonian that describes the coupling of the internal modes of the cavity, and the external world. In earlier discussions the coupling term in this Hamiltonian was a phenomenological parameter, that is commonly taken to be independent of frequency [4, 5]. We derive an explicit expression for the coupling term. The form of the Hamiltonian is important to describe quantum field effects, such as non-classical output fields from a cavity or spontaneous decay of atoms in cavities.

2   Total loss rates

We consider a laser resonator of length L, that is lasing in a single transverse mode. As usual, we map the round trip of the light travelling up and down the cavity on the interval $-2L < z < 0$, with z the coordinate in the propagation direction. The gain and loss are represented by the functions $g(z)$ and $\kappa(z)$ respectively. A localized lossy element such as an aperture, positioned at z_i with effective intensity transmissivity T_i, is described by the loss function

$$\kappa(z) = -\ln(T_i)\delta(z - z_i) .$$ (4)

For an outcoupling mirror with intensity reflectivity R, a similar expression holds with T_i replaced by R. The total loss factor over a round trip can be written as the product of the loss factors of each lossy element, according to

$$T = \Pi_i T_i = \exp[-\int_{-2L}^{0} dz\kappa(z)] .$$ (5)

The periodicity of the system implies that

$$\int_{-2L}^{0} dz[g(z) - \kappa(z)] = 0,$$ (6)

which states that the total gain factor balances the total loss factor.

For a system with a total loss factor T the cold-cavity loss rate is determined by the relation

$$e^{-\Gamma_c \tau} \equiv T ,$$ (7)

with τ the round-trip time. When v_{gr} is he group velocity in the laser cavity, then its round trip time is

$$\tau = \int_{-2L}^{0} dz\frac{1}{v_{gr}(z)} .$$ (8)

Above threshold the number of photons per unit length $u(z)$ in the laser is constant in time. Then we find from the continuity equation

$$(g - \kappa)v_{gr}u - \frac{\partial}{\partial z}(v_{gr}u) = \frac{\partial}{\partial t}u = 0 \,, \tag{9}$$

where $v_{gr}(z)u(z)$ is the photon current. The first term in eq. (9) represents the rate of change of the photon number per unit length due to gain or loss, the second term gives the change due to flow. Formal integration of Eq. (9) gives for the photon current the expression

$$v_{gr}(z)u(z) = v_{gr}(-2L)u(-2L) \exp \left(\int_{-2L}^{z} dz'[g(z') - \kappa(z')] \right), \quad -2L < z < 0 \,. \tag{10}$$

The internal photon number W is found by integrating u over one round trip, which gives

$$W = \int_{-2L}^{0} dz \frac{v_{gr}(-2L)u(-2L)}{v_{gr}(z)} \exp \left(\int_{-2L}^{z} dz'[g(z') - \kappa(z')] \right). \tag{11}$$

The total photon loss rate can be found by integrating the loss of the local photon number density $\kappa(z)v_{gr}(z)u(z)$ over a round trip. This gives

$$P_{tot} = \int_{-2L}^{0} dz \kappa(z)v_{gr}(-2L)u(-2L) \exp \left(\int_{-2L}^{z} dz'[g(z') - \kappa(z')] \right). \tag{12}$$

After integration of Eq. (12) by parts, and using the periodic boundary condition $\kappa(-2L) = \kappa(0)$, this may alternatively be written as an integration of the power density gain, in the form

$$P_{tot} = \int_{-2L}^{0} dz g(z)v_{gr}(-2L)u(-2L) \exp \left(\int_{-2L}^{z} dz'[g(z') - \kappa(z')] \right). \tag{13}$$

The identity of equations (12) and (13) reflects the fact that the power gain exactly compensates the power loss.

This way we arrive at a general expression for the hot-cavity loss rate Γ_h as the ratio between Eq. (12) (or (13)) and Eq. (11). One notices that the result is by no means always identical to the expression for Γ_c, as determined by Eq. (7). Three different situations can be identified where Γ_h and Γ_c are identical. In all cases, the group velocity v_{gr} must be uniform. The first case occurs when also the gain g is uniform, as one recognizes when using eq. (13) for P_{tot}. The second case corresponds to the situation of uniform loss κ, which follows after using eq. (12). Finally, the identity of Γ_h and Γ_c also holds when in addition to v_{gr} the photon density u is uniform, which requires that the gain and the loss compensate each other locally. Then the exponential terms in eq. (10) disappears. In these three cases the loss rates are given by

$$\Gamma_h = \frac{v_{gr}}{2L} \int_{-2L}^{0} dz g(z) = \frac{v_{gr}}{2L} \int_{-2L}^{0} dz \kappa(z) = \Gamma_c \,. \tag{14}$$

We recall that a non-uniform intensity tends to give rise to a longitudinal excess noise factor, due to the combined action of gain and loss [6]. This longitudinal factor must be combined with the transverse enhancement factor [7].

3 Partial loss rates

Laser cavities can have various loss channels, both at optical elements or due to absorption in the laser medium. Typical for unstable laser cavities is that intensity is also lost by absorption at an aperture, which is equivalent to spillover at the outcoupling mirror. Accordingly, the total power loss P_{tot} can be written as the sum over the power losses P_i at each lossy element. Then the loss rate (3) can be written as the sum over partial loss rates. According to eqs. (5) and (7), the cold-cavity loss rate can also formally be expressed as a sum over lossy elements. We now consider the case that the group velocity and the gain are uniform, so that Γ_h and Γ_c are identical, and equal to $v_{gr}g$. Then we obtain the identity

$$\Gamma_h = \Gamma_c = \sum_i P_i/W = -\sum_i \frac{v_{gr}}{2L} \ln T_i \; . \tag{15}$$

This identity (15) might suggest that the separate terms in the two summations are equal term by term, so that $\Gamma_i \equiv P_i/W = -v_{gr} \ln T_i/(2L)$. However, this suggestion is wrong in general, as we illustrate by a simple example. We consider a laser cavity with length L, with one perfect mirror, and an outcoupling mirror with reflectivity R. An aperture is positioned in front of the outcoupling mirror, and the effective aperture transmissivity is T_a. This transmissivity obviously depends on the transverse mode profile incident on the aperture. The gain obeys the relation $v_{gr}g = \Gamma_c = \Gamma_h$. In order to extract the excess noise factor from measurements, we have to express the Schawlow-Townes linewidth (2) in terms of measurable quantities, as

$$\Delta\omega_{ST} = \frac{\Gamma_h \Gamma_m}{2 P_m} \; . \tag{16}$$

The mirror output P_m and the hot-cavity loss rate Γ_h can be measured directly [8]. The partial loss rate through the mirror $\Gamma_m = P_m/W$ can be calculated for this system, with the result

$$\Gamma_m = v_{gr}g \frac{(1-R)T_a}{1-RT_a} = \Gamma_h \frac{(1/R-1)\exp(-\Gamma_h\tau)}{1-\exp(-\Gamma_h\tau)} \; , \tag{17}$$

where we used that $RT_a = \exp(-\Gamma_h\tau)$. Note that all quantities appearing in the last term in (17) can be deduced from experiment. The point is now that this expression (17) can deviate appreciably from the expression for the loss rate through the mirror $-v_{gr} \ln R/(2L)$, which one would guess on the basis of the identity (15). This deviation is particularly important when the loss over the aperture is appreciable.

4 Quantum mechanical coupling Hamiltonian

We consider a similar model of cavity decay, now from a quantum mechanical point of view. Photon loss from a cavity is a prototype of quantum dissipation. The cavity extends between a perfect mirror at $z = -L$ and a non-absorptive semi-transparent mirror of amplitude

reflectivity r and transmissivity t at $z = 0$. The global mode functions of this system can be denoted as

$$F_k(z) = -\sqrt{\frac{2}{\pi}} e^{ikL} \mathcal{L}(k) \sin([z+L]k) \tag{18}$$

for $-L < z < 0$, and

$$F_k(z) = -i \frac{1}{\sqrt{2\pi}} \left(e^{-ikz} + e^{ikz}[r - te^{2ikL}\mathcal{L}(k)] \right) \tag{19}$$

for $z > 0$. The intra-cavity field strength for a global mode is

$$\mathcal{L}(k) = \sum_{l=0}^{\infty} t \left(-re^{i2kL} \right)^l . \tag{20}$$

The operators for the electric and magnetic field are given by their standard expressions

$$\hat{E}(z) = i \int_0^\infty dk \sqrt{\frac{\hbar ck}{2\epsilon_0}} \hat{a}(k) F_k(z) + H.c. \tag{21}$$

and

$$\hat{B}(z) = \int_0^\infty dk \sqrt{\frac{\hbar}{2\epsilon_0 ck}} \hat{a}(k) \frac{dF_k(z)}{dz} + H.c. \tag{22}$$

The global operators $\hat{a}(k)$ satisfy the usual commutation relations for continuous annihilation and creation operators, i.e. $[\hat{a}(k), \hat{a}(k')] = 0$ and $[\hat{a}(k), \hat{a}^\dagger(k')] = \delta(k - k')$. The field Hamiltonian is given by the standard expression

$$\hat{H} = \frac{\hbar c}{2} \int_0^\infty dk\, k \left\{ \hat{a}^\dagger(k)\hat{a}(k) + \hat{a}(k)\hat{a}^\dagger(k) \right\}. \tag{23}$$

In order to introduce field operators inside and outside the cavity, we start from the normalized mode functions corresponding to the perfect cavity. These functions are given by

$$S_n(z) = -\sqrt{\frac{2}{L}} \sin([z+L]k_n) , \tag{24}$$

where $k_n = n\pi/L$ with $n = 1, 2, \cdots$. We know from the theory of Fourier series that these modes form a complete normalized set of functions inside the cavity. However, this statement does not properly account for arbitrary boundary conditions. The field in a perfect cavity always vanishes at the boundary, which is not true in a lossy cavity. This boundary effect of the set $S_n(z)$ is expressed by the closure relation

$$\sum_{n=1}^{\infty} S_n(z)S_n^*(z') = \delta(z - z') - \delta(z + z') - \delta(z + z' + 2L) , \tag{25}$$

for $-L \leq z \leq 0$. The last two terms in (25) contribute only when both z and z' located exactly at a boundary. For arbitrary continuous functions $f(z)$, the well-known expansion

$$f(z) = \sum_{n=1}^{\infty} S_n(z) \int_{-L}^{0} dz' S_n^*(z') f(z') \tag{26}$$

is valid for z in the open interval $(-L, 0)$. However, exactly at the boundaries $z = -L$ or $z = 0$ the expansion (26) is valid only for functions $f(z)$ that vanish at the boundary. In fact, the r.h.s. of eq. (26) vanishes for $z = 0$ and for $z = -L$, regardless the value of f in those points. This failure to reproduce the electric field on the boundary with the outside is the reason why a quantum description in terms of perfect cavity modes breaks down as the cavity quality factor Q decreases.

We choose to expand the quantized electric field operator inside the cavity (i.e. for $-L \leq z < 0$) as

$$\hat{E}_{in}(z) = \sum_{n=1}^{\infty} \sqrt{\frac{\hbar c k_n}{2\epsilon_0}} \hat{\mathcal{E}}_{in,n} S_n(z) . \tag{27}$$

This operator must be identical to the expression (21) for $-L \leq z < 0$, which defines the operators $\hat{\mathcal{E}}_{in,n}$ in terms of the global field operators $\hat{a}(k)$.

Another complete normalized set is formed by

$$C_n(z) = -\sqrt{\frac{2}{L}} \cos([z + L]k_n) , \tag{28}$$

with $n = 0, 1, 2, \cdots$. These functions obey the natural boundary conditions for the magnetic field in a perfect cavity. The quantized magnetic field operator inside the cavity is now expanded as

$$\hat{B}_{in}(z) = \sum_{n=1}^{\infty} \sqrt{\frac{\hbar k_n}{2\epsilon_0 c}} \hat{\mathcal{B}}_{in,n} C_n(z), \tag{29}$$

which basically defines the operators $\hat{\mathcal{B}}_{in,n}$. Because the mode functions are real, $\hat{\mathcal{E}}_{in,n}$ and $\hat{\mathcal{B}}_{in,n}$ are Hermitian operators. We want to introduce local field operators $\hat{a}_n$, in such a way that the expansions for the electric and the magnetic field operator inside the cavity have the same form as in a perfect cavity. This is accomplished by the expressions

$$\begin{aligned} i(\hat{a}_n - \hat{a}_n^\dagger) &= \hat{\mathcal{E}}_{in,n}, \\ \hat{a}_n + \hat{a}_n^\dagger &= \hat{\mathcal{B}}_{in,n}. \end{aligned} \tag{30}$$

If we equate the expressions (27) and (29) to the global expressions (21) and (22) for $-L \leq z < 0$, we can express the local operaors $\hat{a}_n$ in terms of the global operators $\hat{a}(k)$. Explicit expressions are obtained after multiplying eqs. (21) and (22) with $S_n(z)$ and $C_n(z)$ respectively, and integrating over the cavity length. The resulting expressions are found as

$$\hat{a}_n = \int_0^{\infty} dk \left\{ \alpha_{n1}^*(k)\hat{a}(k) - \alpha_{n2}(k)\hat{a}^\dagger(k) \right\} , \tag{31}$$

where

$$\alpha_{n1}(k) = \frac{1}{\sqrt{\pi L}}\sqrt{\frac{k}{k_n}}\frac{\sin([k-k_n]L)}{k-k_n}e^{-ikL}\mathcal{L}^*(k), \tag{32}$$

$$\alpha_{n2}(k) = -\frac{1}{\sqrt{\pi L}}\sqrt{\frac{k}{k_n}}\frac{\sin([k+k_n]L)}{k+k_n}e^{-ikL}\mathcal{L}^*(k). \tag{33}$$

In a similar way, we can introduce field operators $\hat{b}(k)$ corresponding to the outside, by starting from the expressions for the electric and magnetic field in the form

$$\hat{E}_{out}(z) = \int_0^\infty dk\sqrt{\frac{\hbar ck}{2\epsilon_0}}\hat{\mathcal{E}}_{out}(k)S_k(z), \tag{34}$$

$$\hat{B}_{out}(z) = \int_0^\infty dk\sqrt{\frac{\hbar k}{2\epsilon_0 c}}\hat{\mathcal{B}}_{out}(k)C_k(z), \tag{35}$$

with the continuum of mode functions for the outside part with a perfect mirror at $z = 0$ defined by

$$\begin{aligned} S_k(z) &= -\sqrt{\tfrac{2}{\pi}}\sin(kz), \\ C_k(z) &= -\sqrt{\tfrac{2}{\pi}}\cos(kz). \end{aligned} \tag{36}$$

Then the outside field operators are defined by the expressions

$$\begin{aligned} i\left(\hat{b}(k) - \hat{b}^\dagger(k)\right) &= \hat{\mathcal{E}}_{out}(k), \\ \hat{b}(k) + \hat{b}^\dagger(k) &= \hat{\mathcal{B}}_{out}(k), \end{aligned} \tag{37}$$

which makes the external field operators identical in form as in the case of a perfect mirror. Again, we can derive expressions for the outside operators $\hat{b}(k)$ in terms of the global operators $\hat{a}(k)$. The expressions (21) and (22) obey the well-known canonical commutation relations, from which one can argue that also the inside and outside operators obey the standard commutation relations

$$\begin{aligned} [\hat{a}_n, \hat{a}_{n'}] &= 0, \\ [\hat{a}_n, \hat{a}_{n'}^\dagger] &= \delta_{nn'}, \end{aligned} \tag{38}$$

and

$$\begin{aligned} [\hat{b}(k), \hat{b}(k')] &= 0, \\ [\hat{b}(k), \hat{b}^\dagger(k')] &= \delta(k - k'). \end{aligned} \tag{39}$$

In order to derive an explicit form of the Hamiltonian in terms of the inside and outside operators $\hat{a}_n$ and $\hat{b}(k)$, we have to express the global operators $\hat{a}(k)$ in terms of these. However, the set of inside and outside operators is not complete in general, since they cannot

properly describe the field at the mirror. For most models of the mirror, the reflection r deviates from its perfect-cavity value already to first order in the transmittivity, and non-orthogonal modes (with non-vanishing field values at the mirror) are needed already in this order. Therefore, we consider a simple case where $r \approx -1$ up to first order for non-vanishing t. We take $r = -\sqrt{1 - \epsilon^2}$ and $t = i\epsilon$ for real, positive $\epsilon < 1$. In this case, the global operators can be expressed as expansion in the the inside and outside operators $\hat{a}_n$ and $\hat{b}(k)$. Substituting this expansion in Eq. (23), and retaining only first order terms in ϵ leads to the expression for the Hamiltonian

$$
\begin{aligned}
\hat{H} &= \sum_{n=1}^{\infty} \frac{\hbar c k_n}{2} \left(\hat{a}_n^\dagger \hat{a}_n + \hat{a}_n \hat{a}_n^\dagger \right) \\
&+ \int_0^\infty dk \frac{\hbar c k}{2} \left\{ \hat{b}^\dagger(k)\hat{b}(k) + \hat{b}(k)\hat{b}^\dagger(k) \right\} \\
&+ \sum_{n=1}^{\infty} \int_0^\infty dk \left\{ V_n(k)\hat{b}^\dagger(k)\hat{a}_n + V_n^*(k)\hat{a}_n^\dagger \hat{b}(k) \right\},
\end{aligned}
\tag{40}
$$

with the coupling term given by

$$
V_n(k) = -\frac{\hbar\epsilon}{2\sqrt{\pi L}} e^{-ikL} \frac{\sin([k - k_n]L)}{(k - k_n)L}.
\tag{41}
$$

The Hamiltonian (40) has the same form as the phenomenological Hamiltonian introduced by Gardiner and Collett (1985), which has also been used by Barnett and Radmore (1988). However, we have obtained an explicit expression for the coupling term V, which deviates from the common assumption of a constant strength. Moreover, we did not make the rotating-wave approximation. The counter-rotating terms, consisting of products of two creation or two annihiltaion operators, vanish exactly in first order in the transmissivity.

The Hamiltonian (40) can be used to study the decay of the cavity. One readily obtains the result

$$
\frac{d}{dt} < \hat{a}_n^\dagger \hat{a}_n > = -\Gamma < \hat{a}_n^\dagger \hat{a}_n >,
\tag{42}
$$

with $\Gamma = |\epsilon|^2/(2cL)$. However, it is more interesting to study the properties of the outside field. The explicit Hamiltonian allows us to study the quantum properties of the radiation field leaking out of a cavity containing a non-classical field initially. Moreover, the derivation indicates that for low-Q cavities, the operators for the cavity field and the outside can no longer be expected to commute. The modes needed to describe all possible fields inside, including the correct boundary conditions, must be expected to be non-orthogonal.

5   Acknowledgements

References

[1] K. Petermann. IEEE J. Quantum Electron. 15(1979) 566

[2] A.L. Schawlow and C.H. Townes. Phys. Rev. 112(1958) 1940

[3] A.E. Siegman. Phys. Rev. A 39(1989) 1253

[4] C.W. Gardiner, M.J. Collett. Phys. Rev. A 31(1985) 3761

[5] S.M. Barnett, P.M. Radmore. Opt. Commun. 68(1988) 364

[6] P. Goldberg, P.W. Milonni, B. Sundaram. Phys. Rev. A 44(1991) 1969

[7] K. Joosten, G. Nienhuis. Phys. Rev. A 58(1998) 4937

[8] Å.M. Lindberg, M.A. van Eijkelenborg, J.P. Woerdman. IEEE J. Quantum Electron. 33(1997) 1767

Author's address

Huygens Laboratorium,
Universiteit Leiden,
P. O. Box 9504, 2300 RA Leiden,
The Netherlands.

N.J. van Druten, A.M. van der Lee, M.P. van Exter and J.P. Woerdman

Excess Quantum Noise is Colored

Abstract

We demonstrate both theoretically and experimentally that excess quantum noise is colored. The experiments were performed on a a miniature He-Xe gas laser, operating at 3.5 μm, with an adjustable nonorthogonality of the polarization modes.

Spontaneous emission is a fundamental source of noise in a laser. Usually, this quantum noise amounts to a level of "one photon per mode", leading for instance to the well-known Schawlow-Townes limit to the laser linewidth. Recently, there has been much interest [1, 2] in *excess* quantum noise, which appears when the eigenmodes of the laser resonator become nonorthogonal [3, 4]; the spontaneous emission noise has an apparent strength of "K photons in the lasing mode" in this case. The enhancement factor K can become quite large, $K \approx 500$ has been demonstrated in recent experiments, and the possibility of K values larger than 10^4 has been predicted [5]. This leads naturally to the question: what are the limitations to the concept of excess quantum noise?

We have demonstrated both theoretically and experimentally one such limitation, namely that excess quantum noise is spectrally colored [6]. This is in contrast to the usual spontaneous emission noise in a laser with orthogonal eigenmodes, which is essentially white noise. The coloring can be attributed to the finite time it takes for the excess quantum noise to build up from the "one-photon per mode" level. Thus, the picture of simply having "K noise photons in the lasing mode" breaks down.

The experiments were performed by measuring the intensity noise of a miniature He-Xe gas laser, operating at 3.5 μm, with an adjustable nonorthogonality of the polarization modes [7]. The theory of the coloring of excess quantum noise applies here in its simplest form, since a two-mode description is sufficient. A typical result is shown in Fig. 1, together with the theoretical prediction. The coloring of the excess noise factor is clearly visible, and the agreement with theory is excellent. Clearly, the maximum value of K is only reached for zero frequency, and the excess noise disappears ($K = 1$) for high frequencies. The coloring bandwidth was typically a few megahertz in our experiments (1.1 MHz in Fig. 1). This corresponds to the time scale on which the polarization-modifying elements in the laser resonator convert polarization-angle fluctuations into excess intensity fluctuations.

The origin of excess quantum noise, including the coloring, can be conveniently explained using a geometrical picture, illustrated in Fig. 2. It shows two nonorthogonal eigenmodes (the
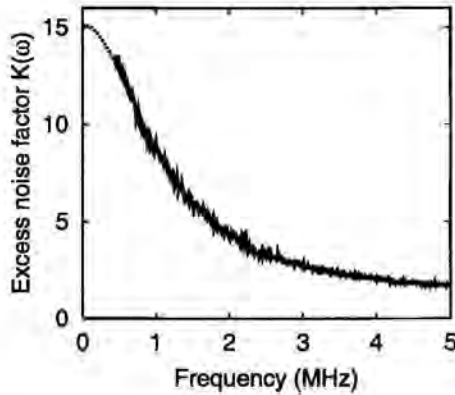
Figure 1: Demonstration of the coloring of excess quantum noise. The solid line is the experimental data, normalized intensity noise of a HeXe gas laser having nonorthogonal polarization modes. The dotted line is the theoretical prediction.

lasing mode and a nonlasing eigenmode) as vectors in the state space describing the optical field in the resonator. In the case of our experiments on nonorthogonal polarization modes, these vectors can be thought of as simply representing the direction of (linear) polarization of the light in the laser resonator. Spontaneous emission that is directly emitted into the polarization direction of the lasing mode contributes the usual "one photon per mode" to the laser noise. More interesting is what happens to spontaneous emission that is emitted in a direction orthogonal to the lasing eigenmode, as depicted in Fig. 2. This is equally likely to occur, since spontaneous emission will be isotropic in polarization direction. For orthogonal eigenmodes, these spontaneous emission events do not contribute to noise in the lasing eigenmode. In contrast, they are important for nonorthogonal eigenmodes. The time evolution of such a spontaneously emitted photon can be visualized by decomposing it into the separate components along the two eigenmodes, as indicated by the dashed lines. Each of these components will evolve according to the eigenvalue of the corresponding eigenmode. Hence the component along the nonlasing eigenmode (which has a net loss compared to the lasing mode) will rapidly decay, and only the component along the lasing eigenmode, labeled as "excess noise" will remain. Thus, spontaneous emission in a direction orthogonal to the lasing eigenmode will evolve into noise in the lasing eigenmode, with a strength corresponding to "$K - 1$ photons". The timescale for this to occur is the decay rate of the nonlasing mode, and this is what sets the timescale for the coloring.

We are currently further exploring the limitations to the concept of excess quantum noise. Our results indicate that several other mechanisms can limit the amount of excess noise observed. Examples include the anisotropy of the gain saturation and the case that the excess quantum noise becomes so strong that it can no longer be treated perturbatively. In addition, we have studied the effects of mode-nonorthogonality on other fundamental sources of laser noise, such as the Poissonian pump noise.

Excess Quantum Noise is Colored
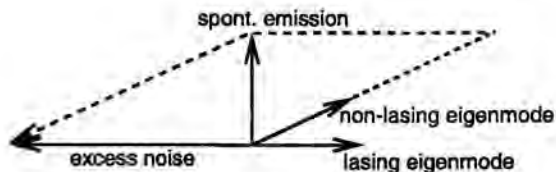
Figure 2: A geometrical representation of nonorthogonal eigenmodes, and the origin of excess quantum noise. This geometrical picture can also be used to explain the coloring of excess quantum noise.

Acknowledgements

References

[1] Y.-J. Cheng, C.G. Fanning, A.E. Siegman. Phys. Rev. Lett. 77(1996) 627–630
[2] M.A. van Eijkelenborg, Å. M. Lindberg, M.S. Thijssen, J.P. Woerdman. Phys. Rev. Lett. 77(1996) 4314–4317
[3] A.E. Siegman. Phys. Rev. A 39(1989) 1253–1263
[4] A.E. Siegman. Phys. Rev. A 39(1989) 1264–1268
[5] G.H.C. New. J. Mod. Opt. 42(1995) 799–810
[6] A.M. van der Lee, M.P. van Exter, A.L. Mieremet, N.J. van Druten, J.P. Woerdman. Phys. Rev. Lett. 81,(1998) 5121–5124
[7] A.M. van der Lee, N.J. van Druten, A.L. Mieremet, M.A. van Eijkelenborg, Å.M. Lindberg, M.P. van Exter, J.P. Woerdman. Phys. Rev. Lett. 79(1997) 4357–4360

Author's address

Huygens Laboratory,
Leiden University,
P.O Box 9504, Leiden,
The Netherlands.

C.L.A. Hooijer, K. Allaart and D. Lenstra

Probing Field Mode Densities in a Multilayer Structure with a Quantum Well

Abstract

A calculation of the spontaneous emission rate from a quantum well in a multilayer structure is presented. The dependence of the spontaneous emission rate on the parameters of the structure, (i.e. thickness of layers, position of quantum well, dielectric constants) is shown to be smooth. In common dielectric waveguide structures, the guided modes and radiation modes have comparable contributions to the spontaneous emission rate and the ratio of these contributions increases with increasing dielectric contrast.

Recently the influence of the dielectric environment on the spontaneous emission rate was studied for an atom inside a dielectric three-layer structure [1, 2]. Within a quantum-electrodynamical approach we have theoretically investigated similar effects for a quantum well embedded in a multilayer structure. Using the Heisenberg equations of motion for the charge carriers, the spontaneous emission rates may be obtained without an explicit modal decomposition of the radiation field. Considering a two-band model with an electron in the upper band (1), we find the following expression for the spontaneous emission rate in terms of the charge current densities and the electromagnetic transverse Greens function [3] as a summation over empty valence band (2) states:

$$\gamma = \frac{2}{\hbar} \sum_{\mathbf{k_2}} \mathrm{Im} \left(\int \int d^3r d^3r' \mathbf{j}_{12}(\boldsymbol{\rho}, \mathbf{k}_1, \mathbf{k}_2) \cdot \overset{\leftrightarrow}{G}{}^{\perp} (\boldsymbol{\rho}, \boldsymbol{\rho}', z_0, \omega) \cdot \mathbf{j}_{21}(\boldsymbol{\rho}', \mathbf{k}_1, \mathbf{k}_2) \right). \tag{1}$$

Using a parabolic two-band model, we found the current density matrix element [3]:

$$\mathbf{j}_{12}(\mathbf{r}, \mathbf{k}_1, \mathbf{k}_2) = \frac{i\hbar e}{mV} \mathbf{K} \exp[i(\mathbf{k}_2 - \mathbf{k}_1) \cdot \boldsymbol{\rho}]. \tag{2}$$

where $\mathbf{K} = < 1|\nabla|2 >$. The multilayer structure consists of n layers of dielectric material, each with a constant index of refraction illustrated in Fig.1. The index steps are in the z-direction, there is no variation in dielectric constant in the x- and y-direction. A quantum well is assumed to be embedded in the j-th layer with permittivity ε_j. The Greens tensor relating an observation point $\mathbf{r} = (\boldsymbol{\rho}, z)$ and a source point $\mathbf{r}_0 = (\boldsymbol{\rho}_0, z_0)$ was derived by
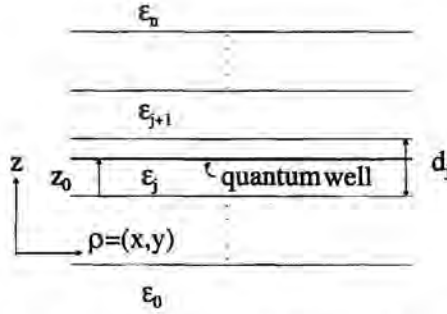
Figure 1: Multilayer structure with a quantum well embedded in one of its layers. Each layer has a constant index of refraction. The index of the quantum well, which is very thin, is set equal to ε_j of the cladding layer (with thickness d_j). The position of the quantum well is given by z_0.

Tomaš and reads for $\mathbf{r}$ and $\mathbf{r}_0$ both in the j-th layer as [4]:

$$
\begin{aligned}
\overset{\leftrightarrow(j)}{G_j}(\mathbf{r},\mathbf{r}_0,\omega) = \sum_{q=E,H} \frac{i\mu_0}{4\pi^2} \int \frac{d^2k}{2\beta_j} \zeta^q \frac{\exp(i\beta_j d_j)}{D_j^q} \Big[\varepsilon_j^{q>}(\mathbf{k},\omega;z)\varepsilon_j^{q<}(-\mathbf{k},\omega;z_0)\theta(z-z_0) \\
+\varepsilon_j^{q<}(\mathbf{k},\omega;z_0)\varepsilon_j^{q>}(-\mathbf{k},\omega;z_0)\theta(z-z_0) \Big] \exp[i\mathbf{k}\cdot(\rho-\rho_0)] e^{i\beta_j(z-z_0)} \\
0 < z, \; z_0 < d_j
\end{aligned}
\tag{3}
$$

where the index q indicates the polarization of the field, which is either E-polarization or H-polarization, $\mathbf{k} = (k_x, k_y)$ is the conserved component of the wave vector parallel to the system interfaces, $\beta_j = \sqrt{\varepsilon_j \frac{\omega^2}{c^2} - k^2}$ is the local z-component of the wave vector, $\zeta^E = -1$, $\zeta^H = 1$ and

$$
D_j^q = 1 - r_{j-}^q r_{j+}^q e^{2i\beta_j d_j}
\tag{4}
$$

with r_{j+}^q (r_{j-}^q) being the reflection coefficients of the upper (lower) interface. These coefficients obey the usual recurrence relations [4]

$$
r_{j,\pm}^q = \frac{1}{D_{j\pm1}^q} \left[\tilde{r}_{j,j\pm1}^q + r_{j\pm1,\pm}^q \exp(2i\beta_{j\pm1} d_{j\pm1}) \right]
\tag{5}
$$

with $\tilde{r}_{j,j\pm1}^q$ the reflection coefficients for a single interface $j/k(= j \pm 1)$ reduce to

$$
\tilde{r}_{jk}^H = \frac{\varepsilon_k \beta_j - \varepsilon_j \beta_k}{\varepsilon_k \beta_j + \varepsilon_j \beta_k}; \quad \tilde{r}_{jk}^E = \frac{\beta_j - \beta_k}{\beta_j + \beta_k}.
\tag{6}
$$

The vectors $\varepsilon_{qj}^<$ and $\varepsilon_{qj}^>$ describe the z-dependence of the electric field in the cavity of a $q = H$ polarized or a $q = E$ polarized plane wave of unit strength incident on the system from its upper (downward) and lower (upward) side, respectively. They are defined by

$$
\begin{aligned}
\varepsilon^<(\mathbf{k},\omega;z) &= \mathbf{e}_j^{q-}(\mathbf{k})e^{-i\beta_j z} + r_{j-}^q \mathbf{e}_j^{q+}(\mathbf{k})e^{i\beta_j(d_j-z)} \\
\varepsilon^>(\mathbf{k},\omega;z) &= \mathbf{e}_j^{q+}(\mathbf{k})e^{-i\beta_j(d_j-z)} + r_{j+}^q \mathbf{e}_j^{q-}(\mathbf{k})e^{i\beta_j z} \\
\mathbf{e}_j^{H\mp} &= \frac{c}{\sqrt{\varepsilon_j}\omega}(\pm\beta_j\hat{\mathbf{k}} + k\hat{\mathbf{z}}), \quad \mathbf{e}_j^{E\mp} = \hat{\mathbf{k}} \times \hat{\mathbf{z}}
\end{aligned}
\tag{7}
$$

where $\mathbf{e}_j^{q\mp}$ are the orthonormal polarization vectors associated with the downward and upward propagating waves in the cavity respectively; $\hat{\mathbf{k}}$ and $\hat{\mathbf{z}}$ are unit vectors.

We assume that the quantum well is just a thin sheet at the $z = z_0$ plane. The transverse Greens tensor $\overset{\leftrightarrow(j)\perp}{G_j}(\rho, \rho', z_0, \omega)$ at the z_0-plane is obtained by subtracting the longitudinal part. The result is:

$$\overset{\leftrightarrow(j)\perp}{G_j}(\rho, \rho', z_0, \omega) = \frac{i\mu_0}{4\pi^2}\sum_{q=p,s}\int \frac{d^2k}{2\beta_j}\zeta_q \frac{e^{i\beta_j d_j}}{D_{qj}}\vec{\varepsilon}_{qj}^{>}(\mathbf{k}, \omega, z_0)\vec{\varepsilon}_{qj}^{<}(-\mathbf{k}, \omega, z_0)\exp[i\mathbf{k}\cdot(\rho - \rho')] \quad (8)$$

with

$$
\begin{aligned}
\vec{\varepsilon}_j^{E>}(\mathbf{k}, \omega, z_0) &= \left(\hat{\mathbf{k}}\times\hat{\mathbf{z}}\right)(e^{-i\beta_j(d_j-z_0)} + r_{j+}^E e^{i\beta_j(d_j-z_0)}) \\
\vec{\varepsilon}_j^{E<}(\mathbf{k}, \omega, z_0) &= \left(\hat{\mathbf{k}}\times\hat{\mathbf{z}}\right)(e^{-i\beta_j z_0} + r_{j-}^E e^{i\beta_j z_0}) \\
\vec{\varepsilon}_j^{H>}(\mathbf{k}, \omega, z_0) &= \hat{\mathbf{z}}\left(e^{-i\beta_j(d_j-z_0)} + r_{j+}^H e^{i\beta_j(d_j-z_0)}\right) \\
\vec{\varepsilon}_j^{H<}(\mathbf{k}, \omega, z_0) &= \hat{\mathbf{z}}\left(e^{-i\beta_j z_0} + r_{j-}^H e^{i\beta_j z_0}\right).
\end{aligned}
\quad (9)
$$

The spontaneous emission coefficient then reduces to

$$\gamma = \gamma^E + \gamma^H, \quad (10)$$

where γ^E is associated with the E-polarized waves and γ^H is associated with the H-polarized waves and

$$
\begin{aligned}
\gamma^E &= \frac{\mu_0\hbar e^2}{4\pi m^2}\text{Re}\left(\int_0^\infty dk\frac{k}{\beta_j}\frac{K_\perp^2}{D_j^E}(1 + r_{j+}^E e^{2i\beta_j(d_j-z_0)})(1 + r_{j-}^E e^{2i\beta_j z_0})\right), \\
\gamma^H &= \frac{\mu_0\hbar e^2}{4\pi m^2}\text{Re}\left(\int_0^\infty dk\frac{k}{\beta_j}\frac{2K_z^2}{D_j^H}(1 + r_{j+}^H e^{2i\beta_j(d_j-z_0)})(1 + r_{j-}^H e^{2i\beta_j z_0})\right).
\end{aligned}
\quad (11)
$$

According to eq. (11), the spontaneous emission rate depends on the reflectivity coefficients of upper and lower layer stacks, the thickness of the j-th layer and the position of the quantum well in this layer. The E-polarized emission is only related to the current matrix element parallel to the quantum well, the H-polarized emission to that perpendicular to the quantum well.

Typical results are shown in Fig. 2. The values for the index of refraction used are taken from Saleh and Teich [5]. In Fig. 2(a) and 2(b) cusps are seen in the separate contributions of guided and radiation modes. These cusps can be attributed to the birth of new guided modes [3], causing the suddenly higher contribution from the guided modes. Just before each cusp, the precursor of the new guided mode is composed of radiation modes. That is why the contribution from the radiation modes drops in the complimentary fashion at the birth of the new guided modes, such that the total spontaneous emission rate shows no effect.

The results presented here show that changing the thickness of the cladding layer and the position of the quantum well in the cladding layer can modify the spontaneous emission
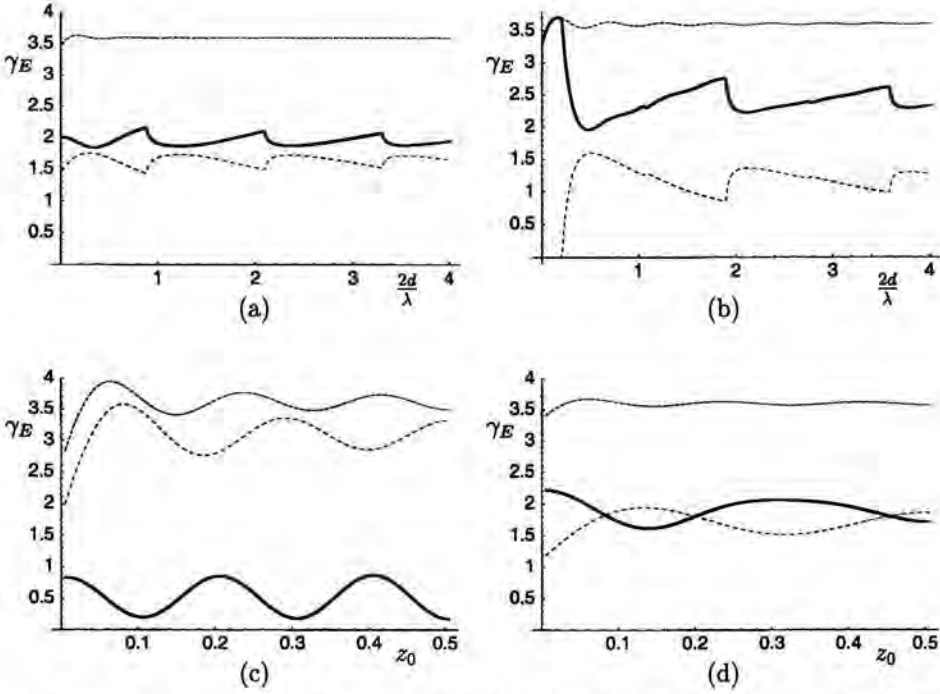
Figure 2: Spontaneous emission rate into E-polarized modes versus thickness d of the middle layer (figures (a) and (b)) and versus position z_0 of the quantum well in this layer at a fixed thickness of 0.75λ (figures (c) and (d)). The contribution of the radiation modes (solid line) and the guided modes (long-dashed line) is summed to give the total spontaneous emission rate (short-dashed line). Configuration from top to bottom layer, figure (a): five layer, AlAs, $Ga_{0.5}Al_{0.5}As$ (thickness 0.5λ), GaAs, $Ga_{0.5}Al_{0.5}As$ (thickness 0.5λ), AlAs; figure (b): three-layer, AlAs, GaAs, $Ga_{0.5}Al_{0.5}As$; figure (c): three-layer, AlO, GaAs, AlO; figure (d): three-layer, AlAs, GaAs, AlAs; refractive indices: AlAs 3.2, $Ga_{0.5}Al_{0.5}As$ 3.4, GaAs 3.6, AlO 1.76. Plots for the H-polarized modes are very similar.

rate of the quantum well significantly. This can be used to control the spontaneous emission lifetime of the quantum well. Moreover the guided modes do play an important role in the spontaneous emission rate. One can see from Fig. 2(c) and 2(d) that, as long as one stays away from the interfaces, the spontaneous emission rate is not very sensitive to the position of the quantum well.

Acknowledgements

References

[1] H.P. Urbach, G.L.J.A. Rikken. Phys. Rev. A 57(1998) 3913–3930
[2] M. Höijer, G. Björk. Optics Commun. 150(1998) 319–330
[3] C.L.A. Hooijer, G.-X. Li, K. Allaart, D. Lenstra. In *SPIE proceedings 3625*, 1999. paper 3625-71, presented at Photonics West, 23-29 Jan. '99, San Jose, California
[4] M.S. Tomaš. Phys. Rev. A 51(1995) 2545–2559
[5] B.E.A. Saleh, M.C. Teich. *Fundamentals of photonics*. Wiley, New York (1991)

Author's address

Quantum Electronics Theory Group, Division of Physics and Astronomy,
Vrije Universiteit,
De Boelelaan 1081, 1081 HV Amsterdam,
The Netherlands.

Email address: hooijer@nat.vu.nl

A. Tip

Quantization and Microscopic Background of Macroscopic Dielectrics

Abstract

A microscopic linear response expression for the electric susceptibility of a finite dielectric is presented. Its form justifies the use of the experimentally accessible macroscopic susceptibility in the quantisation of phenomenological absorptive dielectrics.

1 Background

Quantization of macroscopic dielectrics is required for a proper description of processes such as the radiative decay of atoms embedded in absorptive photonic crystals, transition and Čerenkov X-ray radiation by fast electrons moving through absorptive dielectric layers, the Casimir force between absorptive media and quantum friction. In particular the atomic decay and X-ray cases have important technological implications.

The quantization of conservative (non-absorptive) media, characterized by the real frequency-independent electric permeability $\varepsilon(\mathbf{x})$, has a long history but a corresponding approach for the absorptive case, involving a complex, frequency-dependent $\varepsilon(\mathbf{x}, \omega)$, has only become available quite recently and is at the moment still confined to the linear case. Two general approaches exist:

- The addition of a Langevin noise current [1, 2, 3, 4], describing the absorption, to the free quantized free field equations.

- The introduction of auxiliary fields in the classical absorptive case [5], restoring energy conservation and allowing a canonical formalism and its quantisation.

In these setups the only input required is $\varepsilon(\mathbf{x}, \omega)$, which can be obtained from experiment. Another line of attack starts from a microscopic quantum model for the material system [6, 7, 8] So far its scope is limited to spatially homogeneous situations and it uses a specific model for the material system. This situation leads to the following questions:

- Are the two macroscopic approaches equivalent?

- Can a microscopic justification be given that goes beyond [6, 7, 8]?

Both questions have an affirmative answer. It is easy to show that the auxiliary field model immediately leads to a Langevin current with the correct properties. In fact the converse route can be followed as well. The second problem is more intriguing. An obvious starting

point would be some linear (and higher order) response approach, involving a material system interacting with the free electromagnetic field, followed by the derivation of an effective set of equations for the electromagnetic subsystem. Its feasibility strongly depends on the actual material system. The first choice to be made is that between an infinite and finite system. In actual situations one is dealing with a finite piece of material, which is often so large that its spectrum approaches the simpler band structure of the infinite system in the crystalline case, suggesting the use of an infinite system to exploit this feature. However, there is an important drawback. In order to study the dielectric properties of the system an electric field is generated outside the material and its effect is studied with outside detectors. This gives serious problems in the infinite case. But even in the finite case a linear response expression may be meaningless (consider a single moving charge). Assuming our piece of material to be initially in a bound state (i.e., we look upon it as a large molecule) and the initial field state that of a wavepacket moving towards the material, we have a realistic situation which is amenable to a scattering theoretical description. The idea is then to derive a set of Maxwell's equations for the field subsystem. This set is not unique but will in general depend on the observed process. Elastic scattering of the field wavepacket from the material can be handled by linear response theory, the coupling constant between the subsystems being the small fine structure constant α. Non-linear processes, such as harmonic generation, require a higher order response approach.

2 The system

We consider a finite material system, made up from spinless Schrödinger particles interacting through Coulomb forces, which is coupled to the transverse quantized Maxwell field. Its Hamiltonian is

$$H \;=\; H_m + H_f + H_{int} = H_0 + H_{int} = H_m + H_f - \int d\mathbf{x} \mathbf{J}^{\perp}(\mathbf{x}) \cdot \mathbf{A}(\mathbf{x}), \qquad (1)$$

$$H_m \;=\; \sum_{j=1}^{N} \frac{\mathbf{p}_j^2}{2m_j} + \sum_{i>j=1}^{N} V_{ij}(\mathbf{x}_i - \mathbf{x}_j), \quad H_f = \sum_{\alpha} \int d\mathbf{k} k \, a^{*}(\mathbf{u}_{k\alpha}) a(\mathbf{u}_{k\alpha}), \qquad (2)$$

$$\mathbf{A}(\mathbf{x}) \;=\; \sum_{\alpha} \int d\mathbf{k} (2k)^{-1/2} \{ a^{*}(\mathbf{u}_{k\alpha}) \bar{\mathbf{u}}_{k\alpha}(\mathbf{x}) + a(\mathbf{u}_{k\alpha}) \mathbf{u}_{k\alpha}(\mathbf{x}) \} \qquad (3)$$

where H_m is the matter Hamiltonian, consisting of a kinetic energy term and a sum of Coulomb interactions, H_f the free field Hamiltonian, $\mathbf{A}(\mathbf{x})$ the vector potential and $\mathbf{J}^{\perp}(\mathbf{x})$ the transverse part of the current operator

$$\mathbf{J}(\mathbf{x}) = \sum_{j} \frac{e_j}{2m_j} \{ \mathbf{p}_j \delta(\mathbf{x} - \mathbf{x}_j) + \delta(\mathbf{x} - \mathbf{x}_j) \mathbf{p}_j \} - \sum_{j} \frac{e_j^2}{m_j} \delta(\mathbf{x} - \mathbf{x}_j) \, \mathbf{A}(\mathbf{x}_j) = \mathbf{J}_a(\mathbf{x}) + \mathbf{J}_b(\mathbf{x}).$$

$$(4)$$

Here the a^{*}'s and a's are creation and annihilation operators and the $\mathbf{u}_{k\alpha}$ are the free transverse free field modes. Initially, as $t \to -\infty$ the system approaches the freely evolving product state

$$\rho_{in} = \rho_m \otimes \rho_f. \qquad (5)$$

Here ρ_m is the density operator describing the initial matter state, which we assume to commute with H_m, $[\rho_m, H_m] = 0$, whereas ρ_f is the density operator for the initial field wavepacket. It can be constructed in such a way that it does not reach the material target untill some finite time t which we set equal to zero. This cannot strictly be true, since eigenvectors of Schrödinger operators have infinite tails. The latter decay rapidly over a distance in the order of Ångstrøms and it makes sense to set the system density operator at $t = 0$ equal to ρ_{in},

$$\rho(0) \approx \rho_{in}. \tag{6}$$

This description can be improved, using wave operators to relate the initial situation to that at $t = 0$. The time evolution of an observable in the Heisenberg picture is given by ($LX = [H, X]$)

$$X(t) = \exp[iHt]X\exp[-iHt] = \exp[Lt]X = U(t)X \tag{7}$$

and for the field operators this leads to

$$\partial_t \boldsymbol{E}(\mathbf{x}, t) = \partial_\mathbf{x} \times \boldsymbol{B}(\mathbf{x}, t) - \boldsymbol{J}^\perp(\mathbf{x}, t), \tag{8}$$
$$\partial_t \boldsymbol{B}(\mathbf{x}, t) = -\partial_\mathbf{x} \times \boldsymbol{E}(\mathbf{x}, t). \tag{9}$$

We then obtain effective equations for the field operators by taking the (partial) trace over the initial matter density operator, i.e., denoting $\langle X \rangle = \mathrm{tr}_m \rho_m X$, we have

$$\partial_t \langle \boldsymbol{E} \rangle (\mathbf{x}, t) = \partial_\mathbf{x} \times \langle \boldsymbol{B} \rangle (\mathbf{x}, t) - \langle \boldsymbol{J} \rangle^\perp(\mathbf{x}, t), \tag{10}$$
$$\partial_t \langle \boldsymbol{B} \rangle (\mathbf{x}, t) = -\partial_\mathbf{x} \times \langle \boldsymbol{E} \rangle (\mathbf{x}, t). \tag{11}$$

or

$$-\partial_t^2 \langle \boldsymbol{A} \rangle (\mathbf{x}, t) = -\partial_\mathbf{x}^2 \langle \boldsymbol{A} \rangle (\mathbf{x}, t) - \langle \boldsymbol{J} \rangle^\perp(\mathbf{x}, t). \tag{12}$$

3 Linearisation

A expression for $\boldsymbol{J}^\perp(\mathbf{x}, t)$, linear in the fields, can be obtained by making a Dyson series expansion of $U(t)$ with $L_{int} X = [H_{int}, X]$ as the perturbation and retaining the first two terms. Thus, in terms of $U_0(t)$ ($U_\gamma(t) = \exp[iL_\gamma t]$, $L_\gamma X = [H_\gamma, X]$),

$$U(t) = U_0(t) + i \int_0^t ds\, U_0(t - s) L_{int} U_0(s) + \mathcal{O}(L_{int}^2). \tag{13}$$

However, note that L_{int} contains linear and quadratic contributions in $\boldsymbol{A}$. Expanded in increasing orders in $\boldsymbol{A}$, we have

$$\boldsymbol{J}^\perp(\mathbf{x}, t) = \sum_{n=0}^\infty \boldsymbol{J}_n^\perp(\mathbf{x}, t), \tag{14}$$

where

$$\boldsymbol{J}_0^\perp(\mathbf{x},t) = U_0(t)\boldsymbol{J}_a^\perp(\mathbf{x}) = U_m(t)\boldsymbol{J}_a^\perp(\mathbf{x}), \tag{15}$$

$$\boldsymbol{J}_1^\perp(\mathbf{x},t) = U_0(t)\boldsymbol{J}_b^\perp(\mathbf{x}) - i\int_0^t ds \int d\mathbf{y} U_0(t-s)[\boldsymbol{J}_a^\perp(\mathbf{y})\cdot \boldsymbol{A}(\mathbf{y}), U_0(s)\boldsymbol{J}_a^\perp(\mathbf{x})], \tag{16}$$

etc. We now average over ρ_m, leading to $\langle \boldsymbol{J}_0^\perp(\mathbf{x},t)\rangle = \langle \boldsymbol{J}_a^\perp(\mathbf{x})\rangle$, which may or may not vanish, depending on the symmetry properties of ρ_m. Next, after some rewriting,

$$\langle \boldsymbol{J}_1^\perp(\mathbf{x},t)\rangle = \langle U_f(t)\boldsymbol{J}_b^\perp(\mathbf{x})\rangle - i\int_0^t ds \int d\mathbf{y}\langle [\boldsymbol{J}^\perp(\mathbf{y})\cdot U_f(t-s)\,\boldsymbol{A}(\mathbf{y}), U_m(s)\boldsymbol{J}_a^\perp(\mathbf{x})]\rangle, \tag{17}$$

where the second term has the structure of an autocorrelation expression. Here the right hand side features the freely evolving $U_f(u)\boldsymbol{A}(\mathbf{y})$ and our final step is to keep these first two terms in (12) in a self-consistent approximation where we replace $U_f(u)\boldsymbol{A}$ with $\langle \boldsymbol{A}\rangle(u)$, i.e. the same object as featured on the left hand side. Now it is straightforward to identify the quantity corresponding to the phenomenological electric susceptibility χ, relating the polarisation $\boldsymbol{P}$ to the electric field

$$\boldsymbol{P}(\mathbf{x},t) = \int_0^t ds \int d\mathbf{y}\chi\,(\mathbf{x},\mathbf{y},t-s)\cdot\boldsymbol{E}(\mathbf{y},s), \tag{18}$$

which in general is a second rank tensor and a kernel in coordinate space as well. This is most easily done by switching to Laplace transforms,

$$\hat{f}(z) = \int_0^\infty dt\,\exp[izt]f(t), \quad \mathrm{Im}\,z > 0, \tag{19}$$

so

$$\widehat{\boldsymbol{E}}(z) = -\boldsymbol{E}(0) - iz\,\widehat{\boldsymbol{A}}(z), \tag{20}$$

which relation can be used to express the current in terms of $\widehat{\boldsymbol{E}}(z)$. Apparently the above straightforward procedure in this general form has not been considered in the literature, although it has recently been applied to a description of collective excitations [9].

References

[1] R. Matloob, R. Loudon, S. Barnett, J. Jeffers. Phys. Rev. A 52(1995) 4823
[2] R. Matloob, R. Loudon. Phys. Rev. A 53(1996) 4567
[3] R. Matloob, R. Loudon, M. Artoni, S. Barnett, J. Jeffers. Phys. Rev. A 55(1997) 1623
[4] H.T. Dung, L. Knöll, D.-G. Welsch. Phys. Rev. A 57(1998) 3931
[5] A. Tip. Phys. Rev. A 57(1998) 4818
[6] B. Huttner, S. Barnett. Phys. Rev. A 46(1992) 4306
[7] T. Gruner, D.-G. Welsch. Phys. Rev. A 51(1995) 3246
[8] S.M. Dutra, K. Furuya. Phys. Rev. A 57(1998) 3050
[9] T. Toyoda. Physica A 253(1998) 498

Author's address

FOM-Instituut voor Atoom- en Molecuulfysica,
Kruislaan 407, 1098 SJ Amsterdam,
The Netherlands.

Email address: tip@amolf.nl.

M. Zong, M.A.F.H. van den Broek and H.J. Bakker

Spatio-Temporal Correlation of the Zero-Photon Electromagnetic Field

Abstract

We propose a new imaging technique based on parametric generation to investigate the correlation properties of the zero-photon electromagnetic field. In a first measurement this technique is used to investigate the time correlation of this field. In the near future, the technique will be used to study the spatio-temporal correlation of the zero-photon electromagnetic field.

1 Introduction

Atoms in an excited state can decay to the ground state by spontaneous emission of a photon. In spite of its name, the rate of the spontaneous emission process is not only determined by the excited atom itself but also by the properties of the zero-point (zero-photon) electromagnetic field. For instance, the rate of spontaneous emission can be modified by changing the mode density of the zero-point field at the spontaneous-emission frequency with a cavity. [1, 2, 3, 4]. Clearly, excited atoms can thus be used as a probe of the zero-point electromagnetic field. However, a major disadvantage of using an atom is that the field can only be probed at the *resonant* emission frequencies. The zero-point electromagnetic field can only be studied over a wide frequency range with a *non-resonant* process in which the properties of the light at the quantum-noise level are retained. Such a process is parametric generation.

Parametric generation is a second-order nonlinear optical proces in which the photons of an intense pump pulse are split into two photons of smaller energy (signal and idler) in a nonlinear crystal under the condition of energy conservation : $\omega_p = \omega_s + \omega_i$, with p, s and i denoting pump, signal and idler respectively [5]. This process has been widely used for the generation of intense mid-infrared pulses [6, 7, 8].

Interestingly, although parametric generation can be used to generate high-intensity pulses, the process cannot be described using a classical description of the electromagnetic fields and the nonlinear optical interaction. In such a classical description there will only be a conversion from pump light to signal and idler if either the signal or the idler is already present at the beginning of the process to stimulate the conversion. However, it is important to realize that the absence of a classical signal and idler field only implies that the *expectation value* of these fields will be zero. Due to the positive zero-point energy of every mode of the electromagnetic field, there will be a certain spread/uncertainty in the electric fields of signal and idler. This uncertainty is referred to as quantum fluctuations of the zero-point field and seeds the parametric-generation process.

In the parametric generation process, the quantum fluctuations of the zero-photon electromagnetic field are amplified and result in a (stochastic) phase modulation of the signal and idler fields. Due to the phase-sensitive nature of the parametric-generation process the phase modulations of the amplified signal and idler will be complimentary [9]. If the signal and idler fields overlap in time within their coherence time, the phase modulations cancel and the sum-frequency spectrum consists of a narrow peak (with the width of the pump-pulse spectrum) even though the individual spectra of signal and idler can be extremely broad. The occurence of a narrow peak in the sum-frequency spectrum can also be explained with a quantum-mechanical description of parametric generation. The frequencies of signal and idler photons that originate from a common pump photon will be anticorrelated since the sum of their frequencies must be equal to the pump frequency. Hence, if signal and idler are recombined without any delay between the two, there is a large chance that the photons recombine with their twin brothers leading to a narrow peak in the sum-frequency spectrum (twin-correlation peak) [10].

2 Imaging the spatio-temporal correlation of the zero-photon electromagnetic field

In previous twin-correlation experiments the signal and idler fields always originated from the same spatial region of the crystal. Hence, up to now there exists no information on the correlation of the quantum fluctuations at *different* positions. Here we present an imaging technique by which this spatio-temporal correlation of the zero-photon electromagnetic field can be investigated in detail.

A schematic picture of the experimental set-up is presented in Fig. 1. A short nonlinear crystal is used for parametric generation. In this process the crystal is illuminated with a strong pump beam (Nd:YAG) that is relatively homogeneous both longitudinally (having a pulse duration of 35 picoseconds) and transversally (having a beam diameter of ≈ 7 mm). In the illuminated volume of the crystal, the quantum fluctuations of the zero-photon field will be amplified leading to the generation of signal and idler. We intend to investigate the time correlation of two signal fields that started at different positions r_1 and r_2 in the crystal. These two positions are imaged using a microscope objective in combination with two pinholes. The distance $r_1 - r_2$ between the imaged regions of the crystal can easily be varied by changing the distance $r_a - r_b$ between the two pinholes.

The imaged signal fields are parametrically amplified in two different chains of LiNbO$_3$ crystals. These crystals allow the amplification of mid-infrared pulses tunable between 1.4 and 4.5 μm to an energy of a few hundred μJ per pulse. The parametric amplification of the signal field at r_b will lead to the generation of an idler field. This idler field is combined with the parametrically amplified signal field at r_a in a short nonlinear crystal to generate the sum frequency. In the experiment the sum-frequency spectrum is measured as a function of time delay and distance between the imaged regions of the crystal. When signal and idler have time overlap, the sum-frequency spectrum will contain a strong twin-correlation peak [10]. Mathematically, the twin-correlation peak can be described as follows. The sum-frequency
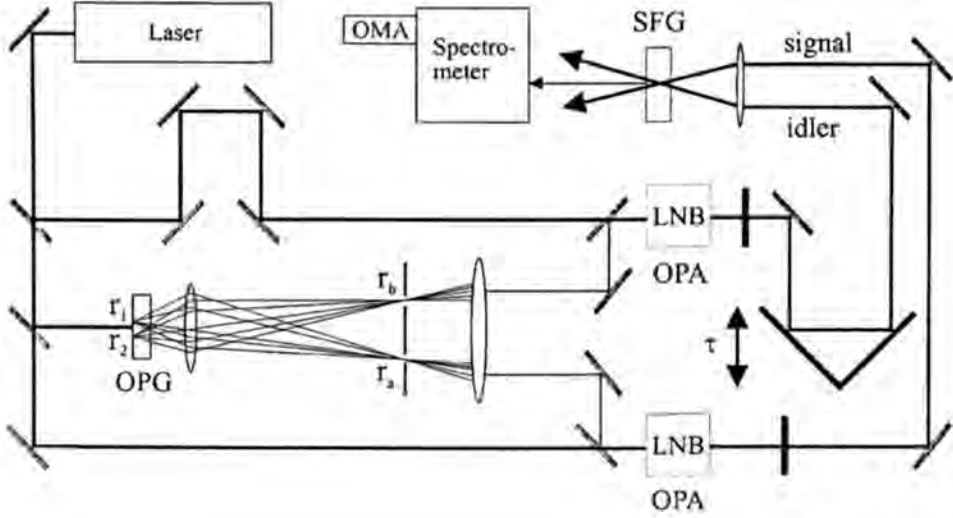
Figure 1: Schematic picture of the experimental set-up for measuring the correlation of the signal fields generated in different directions. The abbreviations have the following meaning : OPG : optical parametric generation; OPA : optical parametric amplification; LNB : LiNbO₃; SFG : sum-frequency generation; OMA : optical multichannel analyzer.

electric field $\mathcal{E}_{sf}(t)$ is given by :

$$\mathcal{E}_{sf}(t,\tau) \sim \mathcal{E}_s(r_a,t)\mathcal{E}_i(r_b,t+\tau), \tag{1}$$

with $\mathcal{E}_s(r_a,t)$ the signal field coming from position r_a and $\mathcal{E}_i(r_b,t+\tau)$ the idler field coming from position r_b with a delay τ with respect to the signal.

The sum-frequency spectrum is measured as a function of the delay τ. The power spectrum $I_{sf}(\omega)$ is given by :

$$I_{sf}(\omega) = \int dt e^{-i\omega t}\langle\mathcal{E}_{sf}(t,\tau)\mathcal{E}_{sf}^*(0,\tau)\rangle, \tag{2}$$

with $\langle\mathcal{E}_{sf}(t,\tau)\mathcal{E}_{sf}^*(0,\tau)\rangle$ the time correlation function of the sum-frequency field. Substitution of equation (1) in this correlation function and using the fact that the idler field $\mathcal{E}_i(r_b,t)$ is the complex conjugate of the signal field $\mathcal{E}_s(r_b,t)$ gives :

$$\langle\mathcal{E}_{sf}(t,\tau)\mathcal{E}_{sf}(0,\tau)\rangle \sim \langle\mathcal{E}_s(r_a,t)\mathcal{E}_s^*(r_b,t+\tau)\mathcal{E}_s^*(r_a,0)\mathcal{E}_s(r_b,\tau)\rangle \tag{3}$$

This fourth-order correlation function can be investigated as a function of τ and the positions r_a and r_b. In the twin-correlation experiments reported up to now, the idler has only been recombined with a signal coming from the same position r_a. If $r_a = r_b$, the fourth-order correlation function can be evaluated making use of the fact that the modulation of signal and idler are Gaussian processes:

$$\langle\mathcal{E}_s(r_a,t)\mathcal{E}_s^*(r_a,t+\tau)\mathcal{E}_s^*(r_a,0)\mathcal{E}_s(r_a,\tau)\rangle \sim (e^{-(4ln2)t^2/\tau_p^2}e^{-(4ln2)\tau^2/\tau_c^2} + e^{-(4ln2)\tau^2/\tau_p^2}e^{-(4ln2)t^2/\tau_c^2}), \tag{4}$$
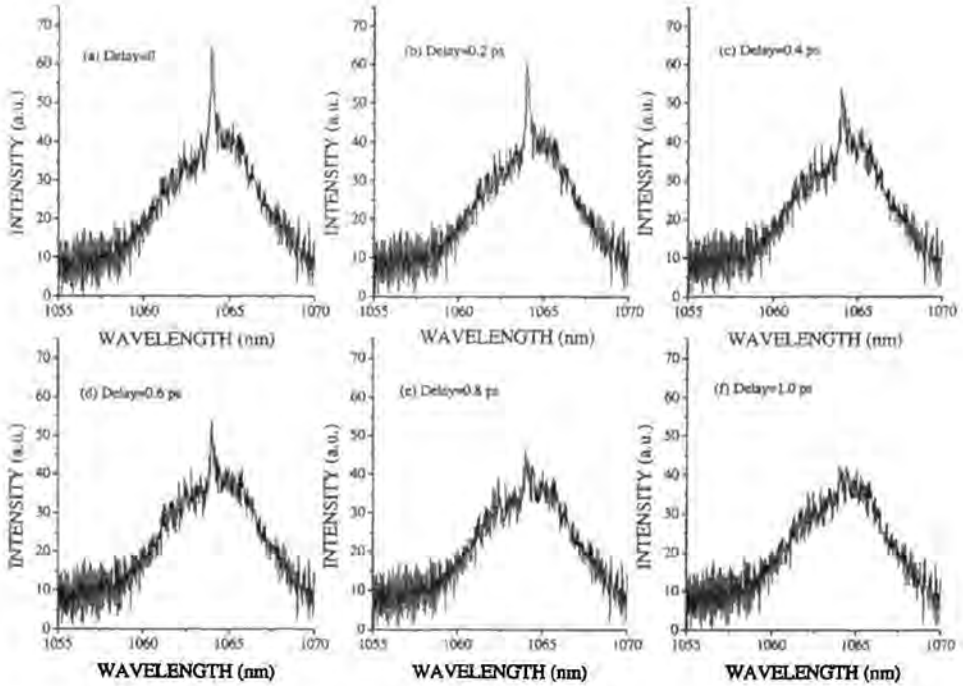
Figure 2: Sum-frequency spectra at different time delays between signal and idler. The central wavelength of signal and idler is 1.8 μm and 2.6 μm, respectively.

with τ_p the full-width-at-half-maximum (FWHM) determined by the duration of the intensity profile of the signal pulse and τ_c the correlation time of the signal field. In this equation it is assumed that the second-order correlation functions of the fields have a Gaussian dependence on the delay time τ. The value of τ_p is determined by the pulse duration of the Nd:YAG pulse used to pump the parametric-generation process and will in general be much larger than the value of the correlation time τ_c. As a result, the sum-frequency spectrum will consist of a narrow twin-correlation peak with the width of the pump-pulse spectrum (proportional to $1/\tau_p$) superposed on a broad background with a width proportional to $1/\tau_c$.

3   Results and discussion

In Fig. 2 spectra of the sum-frequency light are shown obtained at different time delays between signal and idler in case the imaged regions are the same, $r_1 = r_2$ and $r_a = r_b$. The wavelengths of signal and idler are 1.8 and 2.6 μm, respectively. The sum-frequency spectra clearly show a strong twin-correlation peak when signal and idler have time overlap. With increasing delay τ the amplitude of the twin-correlation peak decreases. From this delay dependence the correlation time constant τ_c can be determined.

In Fig. 3 the intensity of this twin-correlation peak is presented as a function of the
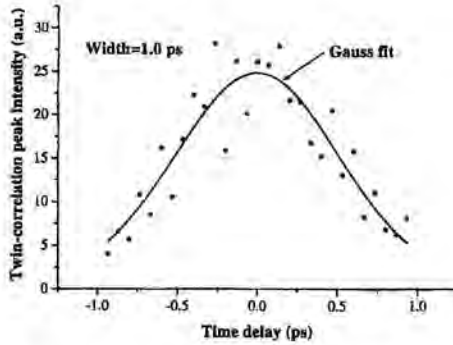
Figure 3: Intensity of the twin-correlation peak as a function of the time delay between signal and idler.

time delay between signal and idler. From a Gaussian fit to the delay dependence we find that this peak has a full-width-at-half-maximum (FWHM) of 1.0 picosecond. This correlation time is inversely proportional to the phase-matching bandwidth of the parametric generation process. The phase-matching bandwidth is determined by the wavelength of signal and idler and increases with increasing wavelength of the signal and decreasing wavelength of the idler for type I phase matching. If the wavelengths of signal and idler are the same (degeneracy), the phase-matching bandwidth reaches its maximum value. The phase-matching bandwidth also depends on the dispersion and length of the nonlinear crystal used in the parametric generation process and decreases with increasing length of the nonlinear crystal.

The experimental results shown in Figs. 2 and 3 only give information on the *time* correlation of the zero-point electromagnetic field, they do not give information on the *spatio-temporal* correlation, the length scale over which the time evolution of the field is correlated for a certain time. By measuring the amplitude of the twin-correlation peak as a function of the distance $r_1 - r_2$ the spatio-temporal correlation can be determined.

A spatio-temporal correlation of the zero-photon field can result from several effects. In the first place it can result from a structuring of the modes of the electromagnetic field. Such a mode structuring will occur in periodic or random media for which the length scale is on the order of the wavelength of light. Examples of such periodic media are Bragg reflectors and photonic crystals. A spatio-temporal correlation of the quantum fluctuations can also result from a nonlocality of the linear and nonlinear polarization in the nonlinear crystal used for parametric generation. The linear and nonlinear polarization will radiate and amplify the zero-photon signal and idler field. The non-locality of the polarization will lead to a phase relation of the fields at different points for a certain time and thus to a spatio-temporal correlation. It can be expected that the non-locality of the linear and second-order dielectric susceptibility will strongly depend on the dielectric properties of the crystal. Especially for ferroelectric crystals like $LiNbO_3$ and $LiTaO_3$ long-range interactions are important so that the quantum fluctuations will be correlated over relatively large distances.

4 Conclusions

We investigated the time correlation of the zero-photon electromagnetic field using parametric generation. In this process a signal and idler field are generated that contain the phase information of the quantum fluctuations of the zero-photon electromagnetic field. Sum-frequency generation of signal and idler gives rise to the so-called twin-correlation peak. The dependence of the intensity of this peak on the delay between signal and idler gives information on the temporal correlation of the signal and idler fields. At a signal wavelength of 1.8 μm (idler 2.6 μm) we observe a Gaussian twin-correlation peak with a FWHM of 1.0 picosecond. In the near future we will use this technique to investigate the spatio-temporal correlation of the zero-photon electromagnetic field by combining signal and idler pulses that originate from different spatial regions.

References

[1] P. Goy, J.M. Raimond, M. Gross, S. Haroche. Phys. Rev. Lett. 50(1983) 1903

[2] R.G. Hulet, E.S. Hilfer, D. Kleppner. Phys. Rev. Lett. 55(1985) 2137

[3] E. Yablonovitch, T.J. Gmitter, R. Bhat. Phys. Rev. Lett. 61(1988) 2546

[4] F. De Martini, G. Innocenti, G.R. Jacobovitz, P. Mataloni. Phys. Rev. Lett. 59(1987) 2955

[5] Y.R. Shen. *Principles of nonlinear optics.* Wiley, New York (1984)

[6] A. Laubereau, L. Greiter, W. Kaiser. Appl. Phys. Lett. 25(1974) 87

[7] A. Lohner, P. Kruck, W.W. Rühle. Appl. Phys. B 59(1994) 211

[8] G.R. Holton, R.A. Crowell, X.S. Sunney Xie. J. Opt. Soc. Am. B 12(1995) 1723

[9] R. Ghosh, L. Mandel. Phys. Rev. Lett. 59(1987) 1903

[10] I. Abram, R.K. Raj, J.L. Oudar, G. Dolique. Phys. Rev. Lett. 57(1986) 2516

Author's address

FOM Institute AMOLF,
Kruislaan 407, 1098 SJ Amsterdam,
The Netherlands.

Part III

Quantum Optics in Semiconductors

F. Jahnke, M. Kira and S.W. Koch

Quantum Theory of the Semiconductor Luminescence

Abstract

A fully quantum mechanical theory for the interaction of light and electron-hole excitations in semiconductor quantum-well systems is developed. The resulting many-body hierarchy for the correlation equations is truncated using a dynamical decoupling scheme leading to the semiconductor luminescence equations. Numerical results are presented for the photoluminescence of incoherently excited quantum wells.

1 Introduction

Recombination of electron-hole pairs and luminescence are fundamental processes in semiconductors. It is known from atomic systems that luminescence is modified when various atoms are optically coupled [1] or when atoms are positioned in a high-quality cavity [2, 3]. An analogous situation in semiconductors can be realized e.g. with an array of quantum wells (QW) [4] or for QWs in a semiconductor microcavity [5]. Like in atomic systems, strong coupling effects [5, 6] and suppressed or enhanced spontaneous emission [7, 8, 9, 10] due to the high quality optical resonances have been observed. For low excitations, the semiconductor material shows excitonic resonances below the fundamental absorption edge. In a microcavity, such a resonance is strongly coupled to the cavity mode leading to the double peaked normal-mode coupling spectrum which has been observed, e.g., in transmission and reflection [5] as well as in photoluminescence [6].

The transmission spectrum can experimentally be determined using pump-probe techniques. Such experiments can be explained in great detail [11, 12] on the basis of a classical description of the light field [13, 14]. The theory/experiment agreement might suggest that a quantum treatment of light only leads to minor corrections. However, this is usually true only as long as the classical fields exceed the vacuum fluctuations. Therefore, photoluminescence in such a correlated system is an important phenomenon which cannot be explained semiclassically.

Without external driving field the polarization and the coherent microcavity field $\langle E \rangle$ typically decays on a ps time scale after the excitation pulse. However, in many cases a substantial number of incoherent electrons and holes remain excited in the system. The system can then reach its ground state via non-radiative electron-hole recombination and through spontaneous emission leading to photoluminescence, which cannot be explained by the classical properties of the light.

The quantum mechanical analysis of the interacting photon-semiconductor system poses a considerable challenge to current theories. In the classical description of light, the major difficulties arise from the consistent inclusion of carrier-carrier Coulomb interaction effects.

In this paper, we review a general theory for the semiconductor luminescence of electron-hole pairs where many-body effects are included. Staring point is a quantum mechanical treatment of the interacting carrier-photon system in the electron-hole picture. The operator equations presented provide a general starting point for investigating quantum properties of light in semiconductor systems. The approach is not only valid for stationary emission under equilibrium conditions but also for the temporal emission dynamics under nonequilibrium conditions resulting from the interplay of incoherent and coherent fields, e.g., luminescence in the presence or after excitation by external laser fields [15, 16].

The emission properties critically depend on the excitation conditions of the system. Even though incoherent excitonic populations are not included at the present level of the theory, excitonic effects enter through the Coulomb interaction between the carriers [17]. For the description of incoherent photoluminescence, we develop the "semiconductor luminescence equations" which are based on a generalization of the Hartree-Fock decoupling scheme. In some respect, these equations are the analog to the "Maxwell-Semiconductor Bloch equations" describing the coherent excitation dynamics. In their most elementary form the semiconductor Bloch equations are based on the Hartree-Fock decoupling; the addition of many-body-correlations is subject of intense current research, see [13] and references therein. On the other hand, carrier-correlations and non-Markovian effects are already partially included in the presented semiconductor luminescence equations.

2 Equations of Motion for Photons and Carriers

For a classical field, the light-matter coupling is described by the dipole interaction Hamiltonian proportional to the scalar product of the field and the carrier polarization. When the treatment includes a quantum field, the specific form of the interaction Hamiltonian cannot be extracted trivially from the semiclassical Hamiltonian [18]. In [16], the quantized interaction Hamiltonian is derived in order to correctly include the quantum aspects of the light and the carrier systems.

In principle, we could use the vector potential operator to describe the quantum properties of light, e.g., within a Green's function method [19, 20]. However, in this paper we choose an alternative method where the quantum aspects of light are derived directly from the nonlocal boson operators $b_{\mathbf{q}}^{\dagger}$ and $b_{\mathbf{q}}$ describing the creation and anihilation of photons in the mode $\mathbf{q}$. This scheme directly leads us to a generalization of the semiclassical semiconductor Bloch equations [21] for the quantum case.

The dynamics of the photon operator $b_{\mathbf{q}}$ is obtained from the Heisenberg equation of motion $i\hbar \partial b_{\mathbf{q}}/\partial t = [b_{\mathbf{q}}, H]$ with the Hamiltonian of the interacting system [16],

$$i\hbar \frac{\partial}{\partial t} b_{q_z,\mathbf{q}_\|}^{\dagger} = -\hbar\omega_{|\mathbf{q}|}\, b_{q_z,\mathbf{q}_\|}^{\dagger} + i\mathcal{E}_{\mathbf{q}}\bar{u}_{\mathbf{q}}\hat{P}_{QW}^{\dagger}(\mathbf{q}_\|), \tag{1}$$

where $\mathcal{E}_{\mathbf{q}}$ and $\bar{u}_{\mathbf{q}}$ determine the vacuum field amplitude and mode strength at the QW, respectively. The evolution of the photon operators is coupled to the QW polarization

operator

$$\hat{P}^\dagger_{QW}(\mathbf{q}_\|) = \sum_{\mathbf{k}} \left[d^*_{cv}(\mathbf{q}_\|)v^\dagger_{\mathbf{k}+\mathbf{q}_v}c_{\mathbf{k}-\mathbf{q}_c} \right.$$
$$\left. +d_{cv}(\mathbf{q}_\|)c^\dagger_{\mathbf{k}+\mathbf{q}_c}v_{\mathbf{k}-\mathbf{q}_v} \right] \tag{2}$$

with the dipole matrix element $d_{cv}(\mathbf{q}_\|)$. In a Bloch basis for a two-band semiconductor, the interacting carrier system is described by creation ($c^\dagger_\mathbf{k}$, $v^\dagger_\mathbf{k}$) and annihilation ($c_\mathbf{k}$, $v_\mathbf{k}$) operators for conduction and valence band electrons, respectively. According to Eq. (2), optical processes can be described with the microscopic polarization operators

$$\hat{P}_\mathbf{k}(\mathbf{q}_\|) = v^\dagger_{\mathbf{k}-\mathbf{q}_v}c_{\mathbf{k}+\mathbf{q}_c}; \quad \hat{P}^\dagger_\mathbf{k}(\mathbf{q}_\|) = c^\dagger_{\mathbf{k}+\mathbf{q}_c}v_{\mathbf{k}-\mathbf{q}_v}, \tag{3}$$

where $\mathbf{q}_c + \mathbf{q}_v = \mathbf{q}_\|$. The operator $\hat{P}^\dagger_\mathbf{k}(\mathbf{q}_\|)$ simultaneously creates an electron in the conduction band and destroys an electron in the valence band, i.e., it creates an electron-hole pair. The center of mass of this electron-hole pair moves with the momentum $\hbar\mathbf{q}_\|$. In principle, the ratio of $\mathbf{q}_c$ and $\mathbf{q}_v$ can be chosen arbitrarily, here we use the center of mass coordinates

$$\mathbf{q}_c = \frac{m_e}{m_e+m_h}\mathbf{q}_\|; \quad \mathbf{q}_v = \frac{m_h}{m_e+m_h}\mathbf{q}_\|. \tag{4}$$

The Heisenberg equation of motion for $P_\mathbf{k}(\mathbf{q}_\|)$ in the fully quantized case differs from the semiclassical calculation [21] only in those terms that involve commutators with the light-matter interaction Hamiltonian. We obtain

$$i\hbar\frac{\partial}{\partial t}\hat{P}_\mathbf{k}(\mathbf{q}_\|) = \left(\epsilon^c_{\mathbf{k}+\mathbf{q}_c} - \epsilon^v_{\mathbf{k}-\mathbf{q}_v}\right)\hat{P}_\mathbf{k}(\mathbf{q}_\|)$$
$$+ d_{cv}(\mathbf{q}_\|)\left[c^\dagger_{\mathbf{k}+\mathbf{q}_c}\hat{E}(\mathbf{q}_\|)c_{\mathbf{k}+\mathbf{q}_c} - v^\dagger_{\mathbf{k}-\mathbf{q}_v}\hat{E}(\mathbf{q}_\|)v_{\mathbf{k}-\mathbf{q}_v}\right]$$
$$+ \sum_{\mathbf{q}'_\|\neq\mathbf{q}_\|}\left\{\left[\hat{P}_\mathbf{k}(\mathbf{q}_\|), \hat{P}^\dagger_{QW}(\mathbf{q}'_\|)\right]\hat{E}(\mathbf{q}'_\|)\right\}_N + \sum_{\mathbf{k}',\mathbf{k}''}V_{\mathbf{k}'-\mathbf{k}}$$
$$\times\left[v^\dagger_{\mathbf{k}-\mathbf{q}_v}\left(c^\dagger_{\mathbf{k}'+\mathbf{k}''-\mathbf{k}}c_{\mathbf{k}''} + v^\dagger_{\mathbf{k}'+\mathbf{k}''-\mathbf{k}}v_{\mathbf{k}''}\right)c_{\mathbf{k}'+\mathbf{q}_c}\right.$$
$$\left. -v^\dagger_{\mathbf{k}'-\mathbf{q}_v}\left(c^\dagger_{\mathbf{k}''}c_{\mathbf{k}'+\mathbf{k}''-\mathbf{k}} + v^\dagger_{\mathbf{k}''}v_{\mathbf{k}'+\mathbf{k}''-\mathbf{k}}\right)c_{\mathbf{k}+\mathbf{q}_c}\right] \tag{5}$$

where $\epsilon^{c(v)}_\mathbf{k}$ determines the free carrier energies,

$$\epsilon^c_{\mathbf{k}+\mathbf{q}_c} - \epsilon^v_{\mathbf{k}-\mathbf{q}_v} = E_g + \frac{\hbar^2\mathbf{k}^2}{2\mu} + \frac{\hbar^2\mathbf{q}^2_\|}{2M}, \tag{6}$$

using $M = m_e + m_h$ and $\frac{1}{\mu} = \frac{1}{m_e} + \frac{1}{m_h}$. In Eq. (5), $V_\mathbf{k}$ is the QW matrix element of the Coulomb potential, and $\{...\}_N$ denotes normal ordering. The operator for the electric field in the dipole picture [18] is given by [16]

$$\epsilon_0\hat{E}(\mathbf{q}_\|) = \hat{D}(\mathbf{q}_\|) - \frac{\tilde{g}}{n^2S}\hat{P}_{QW}(\mathbf{q}_\|), \tag{7}$$

with the mode expansion of the displacement operator,

$$\frac{1}{\epsilon_0}\hat{D}(\mathbf{q}_\parallel) = \frac{1}{\sqrt{S}}\sum_q i\mathcal{E}_\mathbf{q}\left[\bar{u}_{q_z,\mathbf{q}_\parallel}b_{q_z,\mathbf{q}_\parallel}\right.$$
$$\left.-\ \bar{u}_{q_z,-\mathbf{q}_\parallel}^* b_{q_z,-\mathbf{q}_\parallel}^\dagger\right]. \tag{8}$$

The QW confinement wavefunctions $\xi(z)$ enter via

$$\tilde{g} = \int dz\ |\xi(z)|^4. \tag{9}$$

For the carrier occupation number operators $\hat{n}_\mathbf{k}^c = c_\mathbf{k}^\dagger c_\mathbf{k}$ and $\hat{n}_\mathbf{k}^v = v_\mathbf{k}^\dagger v_\mathbf{k}$ as we obtain the equations of motion

$$i\hbar\frac{\partial}{\partial t}\hat{n}_\mathbf{k}^c = \left[\sum_{\mathbf{q}_\parallel} d_{cv}^*(\mathbf{q}_\parallel)v_{\mathbf{k}+\mathbf{q}_\parallel}^\dagger \hat{E}(\mathbf{q}_\parallel)c_\mathbf{k}\right.$$
$$-\sum_{\mathbf{k}',\mathbf{k}''}V_{\mathbf{k}'-\mathbf{k}}c_{\mathbf{k}'}^\dagger\left(c_{\mathbf{k}''}^\dagger c_{\mathbf{k}'+\mathbf{k}''-\mathbf{k}}\right.$$
$$\left.\left.+v_{\mathbf{k}''}^\dagger v_{\mathbf{k}'+\mathbf{k}''-\mathbf{k}}\right)c_\mathbf{k}\right] - \text{h.c.}, \tag{10}$$

$$i\hbar\frac{\partial}{\partial t}\bar{n}_\mathbf{k}^v = \left[-\sum_{\mathbf{q}_\parallel} d_{cv}^*(\mathbf{q}_\parallel)v_\mathbf{k}^\dagger \hat{E}(\mathbf{q}_\parallel)c_{\mathbf{k}-\mathbf{q}_\parallel}\right.$$
$$+\sum_{\mathbf{k}',\mathbf{k}''}V_{\mathbf{k}'-\mathbf{k}}v_\mathbf{k}^\dagger\left(c_{\mathbf{k}'+\mathbf{k}''-\mathbf{k}}^\dagger c_{\mathbf{k}''}\right.$$
$$\left.\left.+v_{\mathbf{k}'+\mathbf{k}''-\mathbf{k}}^\dagger v_{\mathbf{k}''}\right)v_{\mathbf{k}'}\right] - \text{h.c.} \tag{11}$$

In Eqs. (5), (10), and (11), the ordering of $\hat{E}$ and carrier operators is crucial since $\hat{E}$ contains both field and particle operators. Together with the operator equations (1), these equations serve as a general starting point for our investigations of quantum correlations.

The equations of motion for $\hat{P}_\mathbf{k}(\mathbf{q}_\parallel)$ and $\hat{n}_\mathbf{k}^{c,v}$ contain four-particle operator combinations as a consequence of the Coulomb interaction and the dipole self-energy. As usual, this leads to an infinite hierarchy of equations since expectation values consisting of n particle operators are always coupled to higher order terms having $n+2$ particle operators. In practice, this hierarchy has to be truncated using a suitable decoupling. In the semiclassical regime, the simplest decoupling scheme is the dynamic Hartree-Fock approximation,

$$\langle a_1^\dagger a_2^\dagger a_3 a_4\rangle|_{HF} = \langle a_1^\dagger a_4\rangle\langle a_2^\dagger a_3\rangle$$
$$- \langle a_1^\dagger a_3\rangle\langle a_2^\dagger a_4\rangle, \tag{12}$$

combined with the random phase approximation,

$$\langle c_\mathbf{k}^\dagger c_{\mathbf{k}'}\rangle = \delta_{\mathbf{k},\mathbf{k}'}\langle\hat{n}_\mathbf{k}^c\rangle; \qquad \langle v_\mathbf{k}^\dagger v_{\mathbf{k}'}\rangle = \delta_{\mathbf{k},\mathbf{k}'}\langle\hat{n}_\mathbf{k}^v\rangle. \tag{13}$$

This approach can be extended for the fully quantized system where it is important to retain also field-particle correlations in terms like $\langle a_1^\dagger a_2^\dagger \hat{O}_F a_3 a_4 \rangle$ with a single photon operator $\hat{O}_F$. The corresponding truncation [16, 17] permutes $\hat{O}_F$ between all possible Hartree-Fock terms of the carriers. For the incoherent excitations studied here, the intraband transitions vanish such that we find additional factorizations

$$\langle c_{\mathbf{k}}^\dagger c_{\mathbf{k}'} \hat{O}_F \rangle = \delta_{\mathbf{k},\mathbf{k}'} \langle \hat{n}_{\mathbf{k}}^c \rangle \langle \hat{O}_F \rangle;$$
$$\langle v_{\mathbf{k}}^\dagger v_{\mathbf{k}'} \hat{O}_F \rangle = \delta_{\mathbf{k},\mathbf{k}'} \langle \hat{n}_{\mathbf{k}}^v \rangle \langle \hat{O}_F \rangle. \tag{14}$$

3 Semiconductor Luminescence Equations

Quantum corrections to the semiclassical limit can be determined by studying terms like $\Delta \langle b_{\mathbf{q}}^\dagger \hat{P}_{\mathbf{k}}(\mathbf{q}_{\|}) \rangle = \langle b_{\mathbf{q}}^\dagger \hat{P}_{\mathbf{k}}(\mathbf{q}_{\|}) \rangle - \langle b_{\mathbf{q}}^\dagger \rangle \langle \hat{P}_{\mathbf{k}}(\mathbf{q}_{\|}) \rangle$ and $\Delta \langle b_{q_z,\mathbf{q}_{\|}}^\dagger b_{q'_z,\mathbf{q}_{\|}} \rangle = \langle b_{q_z,\mathbf{q}_{\|}}^\dagger b_{q'_z,\mathbf{q}_{\|}} \rangle - \langle b_{q_z,\mathbf{q}_{\|}}^\dagger \rangle \langle b_{q'_z,\mathbf{q}_{\|}} \rangle$, where the classical factorization is subtracted from the full term. The significance of such corrections increases as the coherent terms $\langle b_{q_z,\mathbf{q}_{\|}} \rangle$ and $\langle \hat{P}_{\mathbf{k}}(\mathbf{q}_{\|}) \rangle$ become smaller.

In the following, we focus on the theoretical analysis of incoherent photoluminescence where carriers are nonresonantly generated in the QW by stationary or pulsed optical excitation high above the semiconductor band-edge. Since there is no coherent field or intraband polarization generated in the vicinity of the exciton resonances we can use

$$\langle \hat{P}_{\mathbf{k}}(\mathbf{q}_{\|}, t_0 = 0) \rangle = 0, \qquad \langle b_{\mathbf{q}}(t_0 = 0) \rangle = 0. \tag{15}$$

Starting from these initial values, our equations show that for $t > t_0$

$$\langle \hat{P}_{\mathbf{k}}(\mathbf{q}_{\|}) \rangle = \langle b_{\mathbf{q}} \rangle = \langle \hat{n}_{\mathbf{k}}^{c,v} b_{\mathbf{q}} \rangle$$
$$= \langle b_{\mathbf{q}} \hat{P}_{\mathbf{k}}(\mathbf{q}_{\|}) \rangle = \langle b_{\mathbf{q}} b_{\mathbf{q}'} \rangle = 0. \tag{16}$$

Under these incoherent conditions the quantum correlations are obtained directly from the full terms, i.e. $\Delta \langle b_{\mathbf{q}}^\dagger \hat{P}_{\mathbf{k}}(\mathbf{q}_{\|}) \rangle = \langle b_{\mathbf{q}}^\dagger \hat{P}_{\mathbf{k}}(\mathbf{q}_{\|}) \rangle$ and $\Delta \langle b_{q_z,\mathbf{q}_{\|}}^\dagger b_{q'_z,\mathbf{q}_{\|}} \rangle = \langle b_{q_z,\mathbf{q}_{\|}}^\dagger b_{q'_z,\mathbf{q}_{\|}} \rangle$. Furthermore, the only non-zero quantities are $f_{\mathbf{k}}^{e,h}$, $\langle b_{\mathbf{q}}^\dagger \hat{P}_{\mathbf{k}}(\mathbf{q}_{\|}) \rangle$, and $\langle b_{q_z,\mathbf{q}_{\|}}^\dagger b_{q'_z,\mathbf{q}_{\|}} \rangle$. The equation of motion for $\langle b_{\mathbf{q}}^\dagger b_{\mathbf{q}'} \rangle$ is obtained from Eq. (1) without the need of a factorization approximation

$$i\hbar \frac{\partial}{\partial t} \langle b_{q_z,\mathbf{q}_{\|}}^\dagger b_{q'_z,\mathbf{q}_{\|}} \rangle = \hbar (\omega_{\mathbf{q}'} - \omega_{\mathbf{q}}) \langle b_{q_z,\mathbf{q}_{\|}}^\dagger b_{q'_z,\mathbf{q}_{\|}} \rangle$$
$$+ i\mathcal{E}_{\mathbf{q}} \bar{u}_{\mathbf{q}} \langle b_{\mathbf{q}'} \hat{P}_{QW}^\dagger(\mathbf{q}_{\|}) \rangle + i\mathcal{E}_{\mathbf{q}'} \bar{u}_{\mathbf{q}'}^* \langle b_{\mathbf{q}}^\dagger \hat{P}_{QW}(\mathbf{q}_{\|}) \rangle. \tag{17}$$

Thus, the photon number expectation values are coupled to field-matter correlations of the type $\langle b_{\mathbf{q}}^\dagger \hat{P}_{\mathbf{k}}(\mathbf{q}_{\|}) \rangle$. The equations of motion for $\langle b_{\mathbf{q}}^\dagger \hat{P}_{\mathbf{k}}(\mathbf{q}_{\|}) \rangle$ and $f_{\mathbf{k}}^{e,h}$ can be derived from the quantum operator equations (1) and (5)-(11) combined with the dynamic decoupling and

the initial condition (16),

$$i\hbar\frac{\partial}{\partial t}\langle b_{\mathbf{q}}^{\dagger}\hat{P}_{\mathbf{k}}(\mathbf{q}_{\|})\rangle$$
$$= [\epsilon_{\mathbf{k}+\mathbf{q}_c}^c - \epsilon_{\mathbf{k}-\mathbf{q}_v}^v - \hbar\omega_{\mathbf{q}} - \Sigma(\mathbf{k},\mathbf{q}_{\|})]\langle b_{\mathbf{q}}^{\dagger}\hat{P}_{\mathbf{k}}(\mathbf{q}_{\|})\rangle$$
$$- \left(1 - f_{\mathbf{k}+\mathbf{q}_c}^e - f_{\mathbf{k}-\mathbf{q}_v}^h\right)\Omega(\mathbf{k},\mathbf{q})$$
$$+ f_{\mathbf{k}+\mathbf{q}_c}^e f_{\mathbf{k}-\mathbf{q}_v}^h \Omega_{SE}(\mathbf{k},\mathbf{q}) \qquad (18)$$

$$\frac{\partial}{\partial t}f_{\mathbf{k}}^e = \frac{2}{\hbar}\sum_{q_z,\mathbf{q}_{\|}}\mathrm{Im}\left[-id_{cv}^{\star}(\mathbf{q}_{\|})\mathcal{E}_{\mathbf{q}}\bar{u}_{\mathbf{q}}^{\star}\langle b_{q_z,\mathbf{q}_{\|}}^{\dagger}\hat{P}_{\mathbf{k}-\mathbf{q}_c}(\mathbf{q}_{\|})\rangle\right], \qquad (19)$$

$$\frac{\partial}{\partial t}f_{\mathbf{k}}^v = \frac{2}{\hbar}\sum_{q_z,\mathbf{q}_{\|}}\mathrm{Im}\left[-id_{cv}^{\star}(\mathbf{q}_{\|})\mathcal{E}_{\mathbf{q}}\bar{u}_{\mathbf{q}}^{\star}\langle b_{q_z,\mathbf{q}_{\|}}^{\dagger}\hat{P}_{\mathbf{k}+\mathbf{q}_v}(\mathbf{q}_{\|})\rangle\right]. \qquad (20)$$

Equations (17)-(20) give a closed set of *semiconductor luminescence equations* with the energy renormalization,

$$\Sigma(\mathbf{k},\mathbf{q}_{\|}) = \sum_{\mathbf{k}'}V_{\mathbf{k}'-\mathbf{k}}\left(f_{\mathbf{k}'+\mathbf{q}_c}^e + f_{\mathbf{k}'-\mathbf{q}_v}^h\right), \qquad (21)$$

and the renormalized stimulated contribution,

$$\Omega(\mathbf{k},\mathbf{q}) = d_{cv}(\mathbf{q}_{\|})\langle b_{\mathbf{q}}^{\dagger}\hat{E}(\mathbf{q}_{\|})\rangle$$
$$+ \sum_{\mathbf{k}'}V_{\mathbf{k}'-\mathbf{k}}\langle b_{\mathbf{q}}^{\dagger}\hat{P}_{\mathbf{k}'}(\mathbf{q}_{\|})\rangle. \qquad (22)$$

In Eq. (18) the term proportional to $1 - f_{\mathbf{k}}^e - f_{\mathbf{k}}^h$ introduces either stimulated emission or absorption depending on the excitation conditions. The strength of the spontaneous emission,

$$\Omega_{SE}(\mathbf{k},\mathbf{q}) = i\mathcal{E}_{\mathbf{q}}\bar{u}_{\mathbf{q}}d_{cv}(\mathbf{q}_{\|}), \qquad (23)$$

is determined by the dipole matrix element d_{cv} and the effective mode strength at the QW position $\bar{u}_{\mathbf{q}}$.

The term $\langle b_{\mathbf{q}}^{\dagger}\hat{P}_{\mathbf{k}}(\mathbf{q}_{\|})\rangle$ gives the amplitude of a process where an electron hole pair, with center of mass momentum $\mathbf{q}_{\|}$, recombines by emitting a photon with the same in-plane momentum. As long as there are carriers excited in the QW, this correlation starts to build up even if the field-particle and field-field correlations are initially taken to be zero, because the term $f_{\mathbf{k}+\mathbf{q}_c}^e f_{\mathbf{k}-\mathbf{q}_v}^h \Omega_{SE}(\mathbf{k},\mathbf{q})$ entering Eq. (18) is nonzero. Thus, it provides a spontaneous emission source to the recombination process. According to the factor $f_{\mathbf{k}+\mathbf{q}_c}^e f_{\mathbf{k}-\mathbf{q}_v}^h$, the spontaneous recombination takes place only if an electron at $\mathbf{k}+\mathbf{q}_c$ and a hole at $\mathbf{k}-\mathbf{q}_v$ are present simultaneously. As the field correlations start to build up, the stimulated contribution $\Omega(\mathbf{k},\mathbf{q})$ can alter the photoluminescence spectrum. In other words, the observed photoluminescence is a result of the dynamic interplay of the field-field and field-particle correlations affected by the elementary processes of spontaneous emission and the stimulated contributions. These effects have been shown to explain nonlinear effects in semiconductor

microcavity systems which previously had been incorrectly attributed to "boser" transitions [22].

Under coherent excitation conditions, quantum correlations of the type $\Delta \langle b_{\mathbf{q}}^{\dagger} \hat{P}_{\mathbf{k}}(\mathbf{q}_{\parallel}) \rangle$ contain contributions form the coherent dynamics well-known from the semiconductor Bloch equations and incoherent dynamics described by the semiconductor luminescence equations. The resulting interplay of coherent and incoherent dynamics is studied in [15, 16].

4   Quantum-Well Luminescence

To illustrate the theory we study in the following examples of the semiconductor photoluminescence when the carrier occupation functions can be approximated as Fermi-Dirac distributions with equal carrier density for electrons and holes. Such an approach is reasonably well justified for situations where the intraband carrier scattering time is much faster than the carrier recombination and generation times. An experimentally relevant example is the situation where near band-gap luminescence is measured after an excitation of the system into interband-absorption region. After the excited carriers are thermalized due to carrier-carrier and carrier-phonon interaction, there exists a temporal window of several tenth of picoseconds, where the carrier distribution is practically constant, provided that the recombination is weak.

For a description of the incoherent excitation regime, we start our calculation by setting all correlations initially to zero and evolve Eqs. (17)-(20) to steady state. The simplest way to include the effects of screening and dephasing is to phenomenologically replace the bare Coulomb potential by a screened one $V_{\mathbf{k}}^{S}$. Furthermore, one has to add a term $(\Delta E_g - i\gamma)\langle b_{\mathbf{q}}^{\dagger} \hat{P}_{\mathbf{k}}(\mathbf{q}_{\parallel}) \rangle$ in Eq. (18) where γ is the dephasing rate, and $\Delta E_g = \sum_{\mathbf{k}} (V_{\mathbf{k}}^{S} - V_{\mathbf{k}})$ is the Coulomb-hole gap shift. The microscopic treatment of interaction-induced dephasing and screening is further discussed in [16].

Under steady-state conditions, the measured luminescence spectrum is determined by the photon flux in a detector, i.e., the number of photons in the detector modes per time interval. The steady-state photon flux is given by

$$I_{PL}(\mathbf{q}) \propto \frac{\partial}{\partial t} \langle d_{\mathbf{q}}^{\dagger} d_{\mathbf{q}} \rangle. \tag{24}$$

For a similar definition, see [23]. If the light field is changing rapidly, a more general detector model has to be used [24].

For a QW embedded in a spatially homogeneous background, the free-field modes are plane waves. Using standard GaAs parameters, the resulting 3D exciton binding energy is $E_B = 4.2$ meV and the Bohr radius is $a_0 = 12.5$ nm. Then, assuming an 8 nm QW width, the quantum confined exciton has its 1s-resonance 2.45 E_B below the band gap energy E_g.

Figure 1 shows the computed photoluminescence in comparison with the absorption for different temperatures. The top row of figures displays the absorption spectra for low carrier densities and the middle row presents the corresponding photoluminescence spectra. We see that absorption and luminescence are peaked at the same exciton resonance energy, showing that even though our theory does not include population of incoherent excitonic states, the spectra are still peaked at the exciton resonance. This is a consequence of the well-known
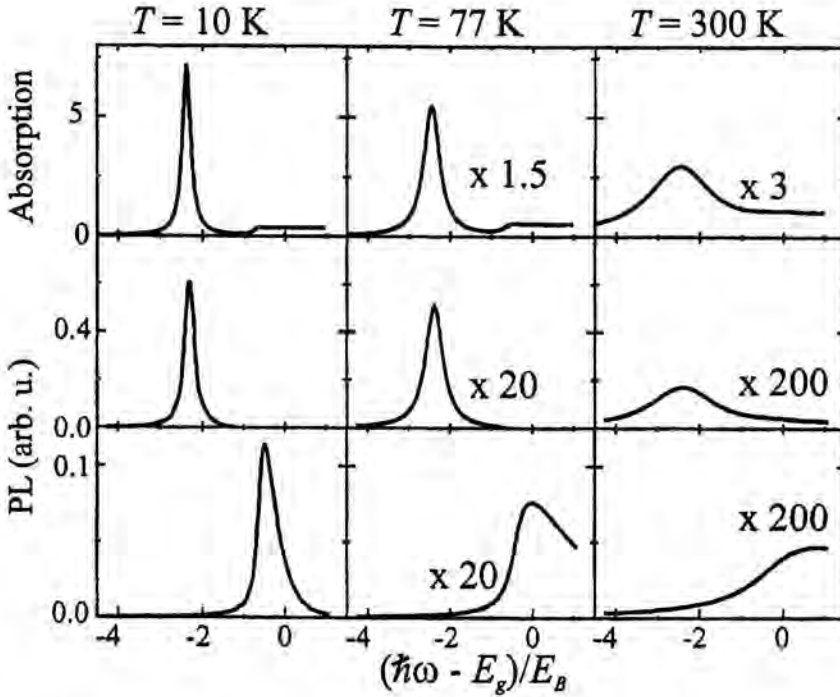
Figure 1: Quantum-well absorption and luminescence for three different carrier temperatures and carrier density 1×10^{10} cm^{-2}. The middle row shows the photoluminescence obtained from the full calculation while for the bottom row the Coulomb terms have been neglected. E_g is the unrenormalized band gap energy and E_B is the 3D exciton binding energy.

fact, that the strong interband Coulomb correlations in semiconductors lead to excitonic resonances in the interband polarization (in a semiclassical picture) and in the photon assisted polarization (in the full quantum theory). The bottom row of figures shows the artificial results obtained by shutting off the interband Coulomb term. Then the photoluminescence peak shifts to the band edge, as expected from free, i.e., non-interacting carrier theory. Further inversitgations [17] show, that for increased carrier density, where the exciton is gradually bleached and eventually gain occurs the QW luminescence stays peaked at the exciton resonance energy even when the absorption peak vanishes. For these elevated excitations, the band edge nonlinearities make the photoluminescence increasingly asymmetric.

In summary, this article presents a quantum theory of semiconductor light emission. Examples for the evaluation of this theory have been shown for the electron-hole regime, where incoherent excitonic populations can be ignored. The theory has also been evaluated in the low excitation purely excitonic regime and interesting results regarding exciton formation dynamics and related photoluminescence have been reported [25]. Work is in progress to include excitonic populations also in the electron-hole approach and to study the influence of structural sample disorder on the exciton formation and light emission dynamics.

5 Acknowledgements

References

[1] M. Gross, S. Haroche. Phys. Rep. 93(1982) 301

[2] J. J. Sanchez-Mondragon, N. B. Narozhney, J. H. Eberly. Phys. Rev. Lett. 51(1983) 550

[3] R. J. Thompson, G. Rempe, H. J. Kimble. Phys. Rev. Lett. 68(1992) 1132

[4] T. Stroucken, A. Knorr, P. Thomas, S. W. Koch. Phys. Rev. B 53(1996) 2026

[5] C. Weisbuch, M. Nishioka, A. Ishikawa, Y. Arakawa. Phys. Rev. Lett. 69(1992) 3314

[6] R. Houdré, C. Weisbuch, R. P. Stanley, U. Oesterle, P. Pellandini, M. Ilegems. Phys. Rev. Lett. 73(1994) 2043

[7] Y. Yamamoto, S. Machida, G. Björk. Phys. Rev. A 44(1991) 657

[8] D. G. Deppe, C. Lei. Appl. Phys. Lett. 60(1992) 527

[9] Y. Hanamaki, H. Kinoshita, H. Akiyama, N. Ogasawara, Y. Shiraki. Phys. Rev. B 56(1997) R4379

[10] S. Park, V. Zapasskii, D. V. Wick, T. R. Nelson, C. Ell, H. M. Gibbs, G. Khitrova, A. Schülzgen, M. Kira, F. Jahnke, S. W. Koch. Optics Express 4(1999) 512

[11] F. Jahnke, M. Kira, S. W. Koch, G. Khitrova, E. K. Lindmark, Nelson Jr., T. R., D. V. Wick, J. D. Berger, O. Lyngnes, H. M. Gibbs, K. Tai. Phys. Rev. Lett. 77(1996) 5257

[12] O. Lyngnes, J. D. Berger, J. P. Prineas, S. Park, G. Khitrova, H. M. Gibbs, F. Jahnke, M. Kira, S.W. Koch. Solid State Commun. 104(1997) 297

[13] F. Jahnke, M. Kira, S. W. Koch. Z. Physik B 104(1997) 559

[14] Y. Zhu, D. J. Gauthier, S. E. Morin, Q. Wu, H. J. Carmichael, T. W. Mossberg. Phys. Rev. Lett. 64(1990) 2499

[15] M. Kira, F. Jahnke, S. W. Koch. Phys. Rev. Lett. 82(1999) 3544

[16] M. Kira, F. Jahnke, W. Hoyer, S. W. Koch. Prog. Quant. Electron. (1999)

[17] M. Kira, F. Jahnke, S. W. Koch. Phys. Rev. Lett. 81(1998) 3263

[18] C. Cohen-Tannoudji, J. Dupont-Roc, G. Grynberg. *Photons & Atoms*. Wiley, New York, 3th edition, (1989)

[19] D. F. DuBois. In W. E. Brittin and others, editors, *Lectures in Theoretical Physics*, volume 9 C, page 469. Gordon and Breach, New York (1967).

[20] F. Jahnke, S. W. Koch. Phys. Rev. A 52(1995) 1712

[21] H. Haug, S. W. Koch. *Quantum Theory of the Optical and Electronic Properties of Semiconductors*. World Scientific Publ., Singapore, 3th edition, (1994)

[22] M. Kira, F. Jahnke, S. W. Koch, J. D. Berger, D. V. Wick, Nelson Jr., T. R., G. Khitrova, H. M. Gibbs. Phys. Rev. Lett. 79(1997) 5170

[23] M. Lindberg, S. An, S. W. Koch, M. Sargent III. Phys. Rev. A 40(1989) 4415

[24] J. H. Eberly, K. Wodkiewicz. J. Opt. Soc. Am. 67(1977) 1252

[25] A. Thränhardt, S. Kuckenburg, A. Knorr , T. Meier, S. W. Koch. submitted to Phys. Rev. B; see also S. Kuckenburg, A. Thränhardt, A. Knorr, M. Kira, F. Jahnke, S.W. Koch, phys. stat. sol. b (accepted for publication).

Author's address

F. Jahnke and S.W. Koch:
Department of Physics and Material Sciences Center,
Philipps-University,
Renthof 5, D-35032 Marburg,
Germany;

M. Kira:
Royal Institute of Technology,
Lindstedsvägen 24,
S-10044 Stockholm,
Sweden.

Y. Yamamoto

Single Photon Turnstile Device

Abstract

We demonstrate a semiconductor device that generates single photons with a well regulated time interval. We also propose a new method of generating pairs of entangled photons. The semiconductor device consists of a single quantum dot as active medium embedded in a p-i-n junction and surrounded by a microcavity. Resonant tunneling of electrons and holes into the quantum dot ground states, together with the Pauli-exclusion principle, produce regulated pairs of entangled photons at a well-defined repetition rate.

1 Introduction

Quantum interference between indistinguishable quantum particles profoundly affects their arrival time and counting statistics. Photons from a thermal source tend to arrive together (bunching) and their counting distribution is broader than the classical Poisson limit [1]. Electrons from a thermal source, on the other hand, tend to arrive separately (anti-bunching) and their counting distribution is narrower than the classical Poisson limit [2, 3, 4]. Manipulation of quantum statistical properties of photons with various non-classical sources is at the heart of quantum optics: Fermionic features such as anti-bunching, sub-Poissonian and squeezing (sub-shot noise) behaviors were demonstrated [5, 6]. A single photon turnstile device was proposed [7, 8, 9] to realize a similar effect to conductance quantization. Only one electron can occupy a single state due to Pauli exclusion principle and thus the electrical conductance for a ballistic single-mode channel is quantized to $G_Q = e^2/h$ [10]. Here we report experimental progress for generation of similar single photon flow and entangled photon-pairs with a well-regulated time interval.

2 Generation of regulated single photons

When a light emitting $p-n$ junction is driven with a high-impedance constant current source, injection of electron-hole pairs can be regulated to below the classical shot noise limit and the light with sub-shot noise intensity fluctuations can be generated [11]. This is possible because the inelastic scattering of electrons in a highly dissipative resistor can suppress the current noise due to Pauli exclusion principle [12, 13], and the Coulomb repulsive interaction between electrons in a $p-n$ junction can suppress the electron injection noise due to collective Coulomb blockade effect [14, 15, 16]. In these squeezing experiments with a macroscopic $p-n$ junction, however, only large number of photons on the order of $\sim 10^8$ can be regulated due to a small single charging energy.
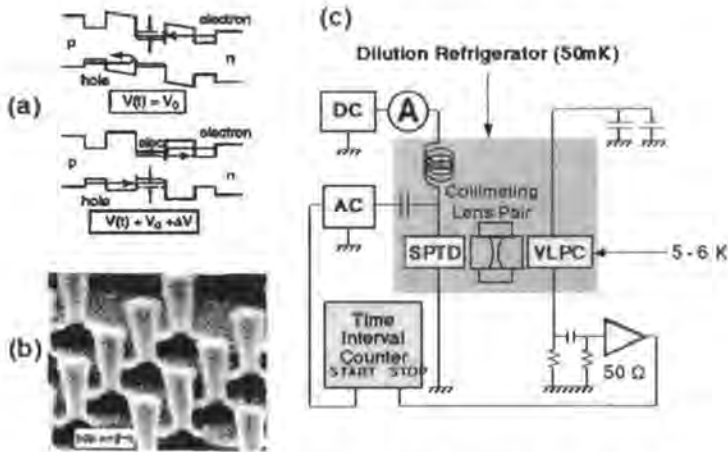
Figure 1: (a) The operational principle of a single photon turnstile device. (b) Scanning electron microscope (SEM) photograph of typical etched post structures. The diameters of the devices range between 200 - 1000 nm and the height of the posts is about 700 nm. (c) Schematic of the experimental setup.

It has been demonstrated in mesoscopic physics that an ultra-small tunnel junction regulates the electron transport one by one due to large single charging energy compared to thermal background energy [17, 18, 19]. If such single electron control technique can be extended to simultaneous control of electron and hole in a $p-n$ junction, a single photon will be regularly emitted one by one [7].

A single photon turnstile device utilizes simultaneous Coulomb blockade for electrons and holes in a mesoscopic double barrier $p-n$ junction (Fig. 1a). The structure consists of an intrinsic central quantum well (QW) in the middle of a $p-n$ junction and the $n-$type and $p-$type side QWs isolated by tunnel barriers from the central QW. The lateral size of the device is reduced to increase the single charging energy $e^2/2C_i$, where C_i ($i = n$ or p) is the capacitance between the central QW and the $i-$side QW. The m-th electron resonant tunnel condition into an electron sub-band in the central QW is satisfied at a certain bias voltage V_0. When the m-th electron tunnels, the Coulomb repulsive interaction between electrons shifts the electron sub-band energy to above the Fermi level of the $n-$side QW, so the $(m + 1)$-th electron tunneling is inhibited. In our single photon turnstile device, the number of electrons in the central quantum well is approximately $m \simeq 10$ at an operating bias condition. At this bias voltage, hole resonant tunnel condition is not satisfied (the Fermi level of the $p-$side QW is higher than the hole sub-band energy level of the central QW), so there is no hole in the central QW. Then the bias voltage is increased to $V_0 + \Delta V$ to satisfy the hole resonant tunneling condition. If a single hole tunnels into the hole sub-band of the central QW, the negative charge of the central QW is decreased by one and the subsequent hole tunneling is inhibited due to the decreased Coulomb attractive interaction between electrons and holes. By modulating the bias voltage between V_0 and $V_0 + \Delta V$ periodically, we can inject a single
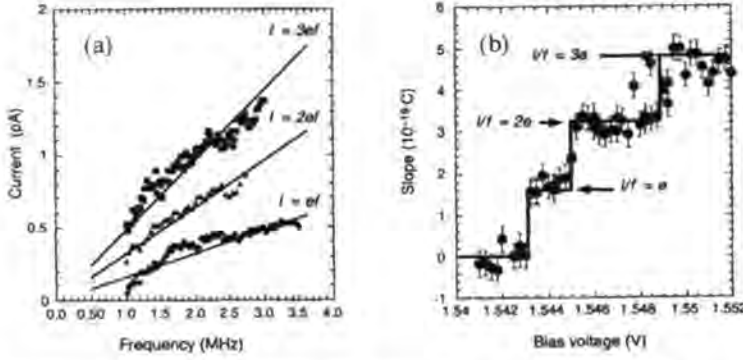
Figure 2: (a) The modulation frequency dependence of the DC current in the 600 nm turnstile device. (b) The slopes I/f in the current-frequency curve vs. DC bias voltage.

(m-th) electron and a single (first) hole into the central QW periodically. If the tunnel time and the radiative recombination time of an electron-hole pair are much shorter than the pulse duration, one and only one photon is emitted for every modulation period.

A $GaAs/AlGaAs$ three QW structure sandwiched by n-type and p-type $AlGaAs$ bulk layers was grown using a molecular beam epitaxy (MBE) technique. Post structures with diameters of $200 - 1000$ nm were made by electron-beam lithography followed by metal evaporation, lift-off, and BCl_3/Cl_2 electron cyclotron resonance (ECR) plasma etching. An SEM micrograph of typical etched posts is shown in Fig. 1b. The surface of the device was passivated with sulfur in ammonium sulfide ($(NH_4)_2S$) solution, and encapsulated by silicon nitride film. Finally, the structure was planarized with hard-baked photoresist and electrical connection was made to each one of the posts independently. The top semi-transparent metal served as the p-type contact from which an emitted photon is detected, and the n-type contact was formed in the substrate.

The device was installed in a dilution refrigerator with base temperature of ~ 50 mK, and was biased with a DC and AC voltage source (Fig. 1c). A DC current flowing through the device was measured as a function of DC bias voltage with a square wave AC modulation voltage. The emitted photon from this device was detected by a Si solid state photomultiplier (SSPM). This detector features a high quantum efficiency of $\sim 88\%$, high multiplication gain of $\sim 30,000$, fast response time of ~ 2 ns and absolutely no multiplication noise [20]. The detector was installed on the mixing chamber of the dilution refrigerator, but the temperature was held at $6.5 K$ with good thermal isolation.

We measured the DC current-voltage characteristics and observed a well-defined resonant tunneling current peak with very small background current, which indicates that a surface (leakage) current is well suppressed in spite of the very small size of the post by the above mentioned passivation process. Measurement of the photons generated from this device indicated that the internal efficiency for the electron-hole pair to emit a photon is $\geq 33\%$.

When an AC modulation voltage was applied to the device in addition to the DC bias voltage, we observed that the DC current increased linearly as a function of the modulation frequency. Figure 2a shows the measured current as a function of AC modulation frequency,

with a fixed AC amplitude of 72 mV at three different DC bias voltages for a device with a diameter of 600 nm [21]. The measured current was in close agreement with the relation $I = ef$, $I = 2ef$, and $I = 3ef$ (solid lines), when a frequency-independent background current was subtracted. This background current varies from device to device, and ranges from 0.5 pA to 6.5 pA. In Fig. 2b we evaluate the slope I/f from the current vs. frequency curves and plot it as a function of the DC bias voltage. We find that the slope increases discretely, creating plateaus at $I/f = ne$, where $e = 1.6 \times 10^{-19}C$ is the charge of an electron and $n = 1, 2$ and 3.

The locking of the current at multiples of the modulation frequency ($I = nef$) suggests that the charge transfer through the device is strongly correlated with the external modulation signal [17, 18, 19]. At the first current plateau at $I = ef$, single (m-th) electron and single (first) hole are injected into the central QW per modulation period, resulting in single photon emission. At the second current plateau at $I = 2ef$, two (m-th and ($m + 1$)-th) electrons and two (first and second) holes are injected into the central QW per modulation period, resulting in two photon emission. Similarly at the third current plateau at $I = 3ef$, three electrons and three holes are injected per modulation period, resulting in three photon emission. This multiple charge operation becomes possible because of relatively broad inhomogeneous linewidths of the n-side and p-side QWs. The experimental result was well reproduced by the Monte-Carlo numerical simulation with a finite resonance linewidth.

To observe the time correlation between the modulation input and photon emission, we measured the time delay from the rising edge of the modulation input to the photon detection event at first current plateau ($I = ef$) and second current plateau ($I = 2ef$). The probability for a single electron-hole pair injected to the central QW of the turnstile device to be detected as a photon in the detector was about 1×10^{-4} due to a poor optical coupling efficiency between the two devices in the present setup. However, the detection quantum efficiency does not affect the time correlation characteristics. The histograms of the measured time delay with 10 MHz modulation frequency is shown in Fig. 3a (for $I = ef$) and Fig. 3c (for $I = 2ef$) [21]. The photon emission probabilities have peaks near the rising edge of the modulation input. The rapid increase of the photon emission probability is associated with the hole tunneling time ($\tau_h \simeq 4$ ns), and the slow decay of the photon emission probability corresponds to the radiative recombination lifetime ($\tau_{ph} \simeq 25$ ns). Photon emission probability in Fig. 3a decays to a non-zero value during the on-pulse due to photons generated by background current. The ratio of the counts contained in the peak to those contained in the non-zero background is $\sim 3 : 1$, consistent with the ratio of the turnstile current to the background current in this device. The second and faster decay for $I = 2ef$ (Fig. 3c) stands for the decay of the hole via backward tunneling and radiative recombination. The associated lifetime for this decay is $(\tau_h^{-1} + \tau_{ph}^{-1})^{-1}$. The dashed lines show the analytical solutions using these parameters. The experimental results as well as the analytical traces are well reproduced by the Monte-Carlo numerical simulation, as shown in Fig. 3b ($I = ef$) and Fig. 3d ($I = 2ef$). The fact that the photon emission probability decreases during the on-pulse duration is a unique signature that the number of holes injected during an on-pulse is restricted to either one or two due to the Coulomb blockade effect. Figure 3e shows the experimental result on a larger area device at a higher temperature of 4 K, where Coulomb blockade effect is absent. In this case, arbitrary number of holes are allowed to tunnel into the central QW during an on-pulse, and so the resulting photon emission probability should
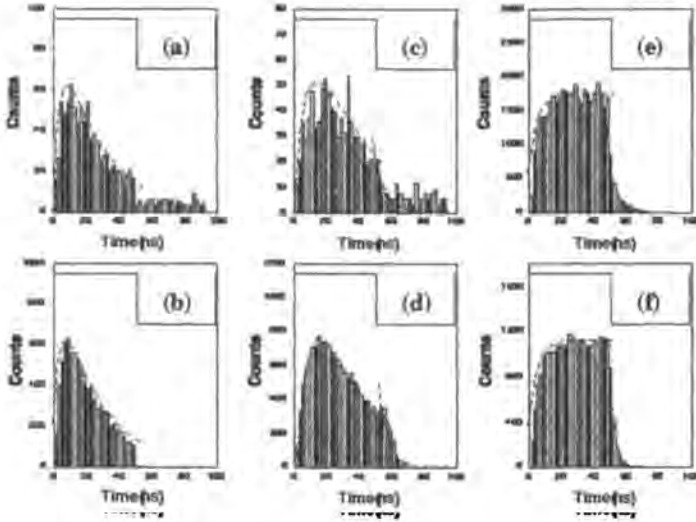
Figure 3: (a) Measured histogram of a time delay between the rising edge of the modulation input and the photon detection event at the first plateau ($I = ef$). (b) Monte-Carlo numerical simulation result for the photon emission probability vs. the time delay at the first plateau ($I = ef$). (c) Measured histogram of a time delay at the second plateau ($I = 2ef$). (d) Monte-Carlo numerical simulation result for the photon emission probability vs. the time delay at the second plateau ($I = 2ef$). (e). Measured histogram of a time delay for a larger area device (diameter of $1.4\,\mu$m) at higher temperature ($4\,$K), where Coulomb blockade effect is absent. (f) Monte-Carlo numerical simulation result for this modulated classical light emitting diode case.

increase monotonically with a time constant τ_{ph} to the steady state value. This result is well-reproduced by the simulation (Fig. 3f).

3 Regulated and entangled photons from a single quantum dot

Even stronger non-linear interactions are expected in semiconductor quantum dots (QD's). QD's are very attractive for possible applications in electro-optic devices due to their atom-like properties and the strong confinement of electrons and holes. The Coulomb blockade effect [22], the quantum confined Stark effect [23] and electromagnetically induced transparency [24] have been studied with the aim of realizing single electron transistors that operate at room temperature [25], ultra-fast electro optical modulators [26], and novel lasers [27].

A fundamental non-linear effect in a QD is the saturation of a single energy level by two electrons (or holes) of opposite spin due to the Pauli exclusion principle. In this section, we will show how this effect can be used in a realistic device to produce non-classical field states. We propose a device that produces regulated photons as well as pairs of entangled photons.

Figure 4 (a) illustrates a scheme for the device, which consists of a single InAs QD as

Figure 4: (a) Proposed device structure. (b) Energy-band diagram of the structure.

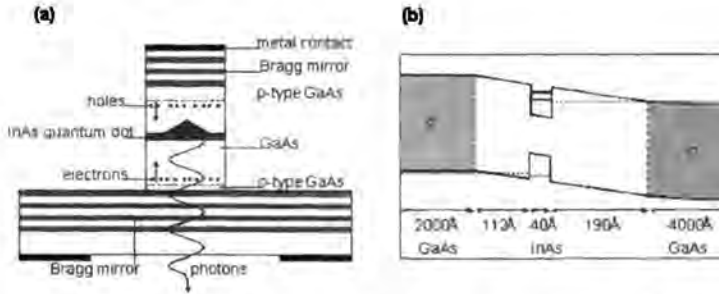the active medium embedded in a GaAs p-i-n junction. Electrical contacts are made from a top metal contact and via the n^+-doped substrate. The GaAs substrate is transparent for the ground state emission from the InAs QD's, and photons can be collected through the back side. It has been demonstrated that single QD's can be isolated from an ensemble of self-assembled QD's by etching small mesa or post structures [28], as sketched in the figure. The structure is surrounded by an optical microcavity, which modifies the spatial emission pattern and increases the spontaneous emission rate into resonant cavity modes [29]. A very large fraction β of photons is thus spontaneously emitted into a single mode of the cavity, and the outcoupling efficiency from the high refractive index material is improved as well. For the present state of the art, β values as high as 0.9 should be possible [30].

An energy-band diagram of the structure is shown in Fig. 4(b) for doping levels of 10^{18} cm^{-3} on the $n-$side and 10^{19} cm^{-3} on the $p-$side. The QD layer is separated from the $n-$ $(p-)$ side by 190 Å(112 Å) wide GaAs intrinsic layers, which act as tunnel barriers. We assumed a typical dot diameter of 20 nm and height of 4 nm. For a qualitative discussion of the device operation, the Coulomb blockade energy can be estimated in a single particle picture [31, 32] for simplicity, with strain and piezoelectric effects [33] neglected. We assumed that the one and two electron ground state energy levels are 210 meV and 190 meV below the conduction band edge of GaAs, respetively, and that the one and two hole ground state energy levels are 100 meV and 80 meV above the valence band edge of GaAs, respectively. The first excited electron (p-like) state is about 70 meV above the ground state [34, 35]. These values are consistent with experimental observations [31, 34] and calculations [36, 37]. If the junction voltage V_j is well below the built-in potential, the carrier transport takes place by resonant tunneling of electrons and holes.

Figure 5 shows the calculated resonant tunneling rates for electrons and holes *versus* the applied bias voltage. The calculation uses the WKB approximation with an effective electron and hole mass of $0.067\,m_0$ and $0.082\,m_0$, respectively, and a temperature of 4 K. The different lines correspond to the following (from left to right): Electron tunneling into the dot containing zero or one electron (solid lines) and hole tunneling into the dot containing two electrons and zero or one hole (dashed lines). Tunneling into the first excited electron state is indicated by dotted lines, where the three lines correspond to two electrons and two, one, or zero holes. The difference in the widths of electron and hole tunneling resonances is due to the asymmetric tunnel barriers and different doping levels. We chose the position of the QD

Single Photon Turnstile Device

within the GaAs-layer in order to have the first hole resonant tunneling condition fulfilled at a junction voltage above the second electron tunneling resonance. In this situation, we can switch on and off hole and electron tunneling by switching between different bias voltages.

Two-photon turnstile operation is achieved as follows: At a low bias voltage V_e (indicated in Fig. 5), two electrons can tunnel into the initially empty QD. Further electron tunneling is now completely suppressed due to the Pauli exclusion principle, since the ground state is filled and the next available electron state, the first excited state, is far off of resonance. Then, we switch up to a higher voltage V_h (indicated in Fig. 5), where two holes tunnel. Again, further hole tunneling is suppressed due to the Pauli exclusion principle since the hole ground state is filled and the first excited hole state (not shown) is off resonance. The first excited electron state shifts by typically 7 mV [34] to lower voltages when a hole tunnels. This is indicated by the three dotted lines in Fig. 5. However, even after two holes have tunneled into the QD, electron tunneling is inhibited. Once the holes have tunneled, radiative recombination annihilates two holes and produces exactly two photons. Thus, modulating the bias voltage between V_e and V_h produces a regulated stream of photons, where two photons are emitted per modulation cycle. The intensity spectrum of the light emitted from the proposed device exhibits a squeezed background at low frequencies and pronounced peaks at integer multiples of the modulation frequency. The squeezing reflects the control of the number of photons per modulation cycle and the negligible hole (electron) tunneling at low (high) bias voltage. The peaks at integer multiples of modulation frequency indicate a regulation of the photon emission events. We performed a Monte-Carlo simulation in order to check that properties hold for realistic experimental parameters.

The two photons arise from the decay of the biexcitonic ground state of the QD, where the correlated electrons and holes have opposite spins. If this anti-correlation translates into an anti-correlation in polarization of the emitted photons, it is easy to realize a single photon turnstile operation by selecting out only one photon per modulation cycle with the help of a polarizer. For quantum wells in direct-gap materials with a cubic lattice, any photons emitted are circularly polarized, because the $J_z = \pm 1/2$ electron recombines with the $J_z = \pm 3/2$ heavy hole [38]. This is illustrated in the inset in Fig. 5, where solid arrows indicate the σ^+ and σ^- ground state transitions. In the case of a QD, the strong confinement introduces level mixing and the hole ground state may have contributions from the $J_z = \pm 1/2$ hole states. Possible transitions to the $J_z = \pm 1/2$ states are indicated by dashed arrows in Fig. 5. Accordingly, when a $J_z = +1/2$ electron radiatively recombines with a hole in a QD, the emitted light is predominately σ^+-polarized, but may also have a σ^- component. Thus, the two photons that arise from the decay of the biexcitonic ground state are not necessarily perfectly anti-correlated with respect to σ^+- and σ^-- polarization. An asymmetric dot shape, strain, and piezoelectric effects [39] further reduce the anti-correlation. However, there is experimental evidence from polarized photoluminescence [40] and two photon absorption measurements [41] that the anti-correlation in σ^+- and σ^-- polarization is preserved in QD's. An exact calculation of the energy levels and oscillator strength including spin for the system discussed here would be desirable (so far optical and electronic properties of self-assembled InAs QD's have been calculated neglecting spin [39]).

We would like to point out that a previous single photon turnstile device relies on the relatively small Coulomb splitting [21] . This limits the operation of this device to very low temperatures (40 mK) in order to guarantee that thermal energy fluctuations are negligible.
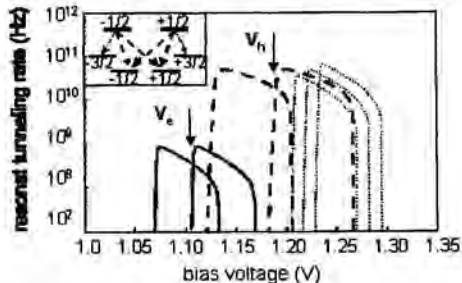
Figure 5: Calculated resonant tunneling rates at 4 K into the QD ground state for electrons (solid lines) and holes (dashed lines) *versus* the applied bias voltage. Tunneling into the first excited electron state is indicated by dotted lines. The inset illustrates optical transitions in a cubic lattice.

In the proposed device, the turnstile operation is maintained up to much higher temperatures due to the very large splitting between the electron and hole ground and excited states. Electron and hole tunneling could be controlled merely by the Pauli exclusion principle, even if the Coulomb blockade effect were absent. For the parameters we assumed here, an operation at above 20 K should be possible. At higher temperatures, the electron and hole tunneling curves are broadened, mainly due to the thermal energy distribution of the electrons and holes in the $n-$ and $p-$doped layers. The broadening leads to a significant hole (electron) tunneling rate at lower (higher) bias voltage V_e (V_h), and photon emission can no longer be controlled. With a smaller QD and a larger splitting between ground and excited states, a larger broadening could be tolerated and thus a higher temperature operation is possible. We calculated that, up to a temperature of 50 K, thermionic emission can be neglected in the proposed structure.

We now focus on a unique property of the proposed device, which is the production of pairs of entangled photons at well-defined time intervals. Starting from the biexcitonic ground state of the QD, a first electron can recombine with a hole and emit a σ^+ or a σ^- photon. Then, the second electron of opposite spin recombines with a hole, and a photon of opposite polarization is emitted. This situation is very similar to a two-photon cascade decay in an atom [42]. The two-photon state has the same form in any basis and is a maximally entangled (Bell) state: $|\psi\rangle = \frac{1}{\sqrt{2}}(|\sigma^+\rangle_1|\sigma^-\rangle_2 + |\sigma^-\rangle_1|\sigma^+\rangle_2)$. Due to additional binding energy, the biexcitonic ground state has a smaller energy than twice the excitonic ground state [41]. Therefore, the first emitted photon 1 and the second emitted photon 2 have different energies (by approximately 4 meV).

The advantage of the proposed structure compared to other sources of entangled photons, such as two-photon cascade decay in atoms or parametric down conversion in non-linear crystals, is that entangled photon pairs are provided one by one with a tunable repetition rate of up to 1 GHz by a compact semiconductor device. The source is electrically pumped and the photons are emitted in resonant modes of an optical resonator, which greatly improves, e.g., the efficiency of subsequent fiber coupling.

The inset in Fig. 6 sketches the setup of a possible experiment, where the non-local quantum correlation between photon 1 and 2 leads to a violation of Bell's inequality. The two
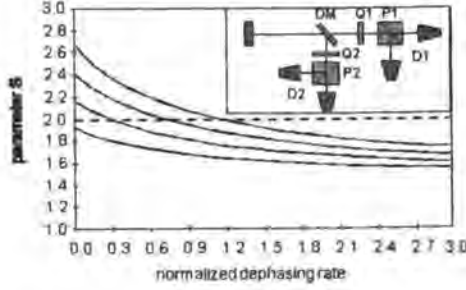
Figure 6: The inset shows the setup for a proposed experiment. The figure shows the calculated left side of Eqn.1 (parameter S) versus the dephasing rate R_d. R_d is normailzed to the radiative recombination rate R_p and $R_h = 10\,R_p$. Values above 2 (dashed line) are a violation of Bell's inequality. From top to bottom $\Delta_{corr} = 1$, 0.9, 0.8, and 0.7.

photons are separated with the help of a dichroic mirror (DM) and analyzed by a combination of quarter-wave plates (Q1, Q2), polarizing beam splitters (P1, P2) and detectors (D1, D2). Bell's inequality in the version of Ref. [43] is:

$$S = |E(\alpha, \beta) - E(\alpha', \beta)| + |E(\alpha', \beta) + E(\alpha', \beta')| \leq 2 \tag{1}$$

where

$$E(\alpha, \beta) = C_{++}(\alpha, \beta) + C_{--}(\alpha, \beta) - C_{+-}(\alpha, \beta) - C_{-+}(\alpha, \beta) \tag{2}$$

Each photon is subject to a measurement of linear polarization along an arbitrary angle α or β with two-channel polarizers whose outputs are + and -. Then, e.g., $C_{++}(\alpha, \beta)$ is the number of coincidences between the + output of the polarization measurement of photon 1 along α and + output of the polarization measurement of photon 2 along β. Maximal violation of Bell's inequality is observed for a particular set of angles of the two polarizers: $\alpha = 0$, $\alpha' = -\pi/4$, $\beta = 3\pi/4$, $\beta' = \pi/8$. For this set, quantum mechanics predicts $S = 2\sqrt{2}$, although the local hidden-variables theory is constrained by 2.

In the proposed device, several procecces may degrade the entanglement and cause an evolution of the pure state into a statistical mixture of anti-correlated photons. For example, the QD initially contains two electrons, and then the bias voltage is changed to allow hole tunneling. It is possible that a first photon is emitted right after the first hole has tunneled, before the biexcitonic ground state has formed. A second photon can be emitted after the second hole has tunneled, but the final state is then a statistical mixture. Alternatively, even if the QD is in the biexcitonic ground state, spin dephasing may occur between the photon emission events. If the dephasing rate R_d is much larger than the radiative recombination rate R_p, then the final photon state is again a statistical mixture.

In order to demonstrate that it is possible to measure a violation of Bell's inequality we performed a numerical calculation. A rate-equation model of the tunneling and radiative recombination processes in the QD, similar to that presented in Ref. [44], is used. In order to account for the above mentioned problem of imperfect correlation, we define the degree

of anti-correlation Δ_{corr} in the following way:

$$\Delta_{corr} = \frac{R_p^+}{R_p^+ + R_p^-} \qquad (3)$$

In this equation R_p^+ (R_p^-) denotes the radiative recombination rate of a $J_z = +1/2$ electron with a hole in the biexcitonic ground state of the QD through to the emission of σ^+ (σ^-) photons. In this notation, $\Delta_{corr} = 0.5$ corresponds to no anti-correlation and $\Delta_{corr} = 1$ to perfect anti-correlation.

Figure 6 shows the left side of Eqn.1 vs. the dephasing rate R_d for a hole tunneling rate of 10 times the radiative recombination rate, in agreement with the calulated hole tunneling rate of 10 Ghz and radiative recombination rate greater than 1 Ghz in the proposed device. Values above 2 (dashed line) are a violation of Bell's inequality. The different curves correspond to different values of the degreee of anti-correlatin Δ_{corr}; from top to bottom, $\Delta_{corr} = 1$, 0.9, 0.8, and 0.7. Clearly, a violation of Bell's inequality can be measured even with imperfect anti-correlation if the dephasing rate is small enough. Recent experiments in QD's indicate that the spin dephasing rate of conduction band electrons is much lower than 0.3 GHz [45], and thus much lower than the radiative recombination rate and tunneling rates.

4 Conclusion

We demonstrated a semiconductor device which acts as a turnstile for single photons and also proposed a new structure for generating pairs of entangled photons. The latter device utilizes Pauli-exclusion principle and takes advantage of the large energy separation of the QD energy levels. A higher temperature operation than with previous device structures is possible. We demonstrate that it is possible to measure a violation of Bell's inequality using the proposed device as a source of entangled photon pairs.

References

[1] R. Hanbury Brown, R. Q. Twiss. Nature 177(1956) 27–29
[2] M. Reznikov, M. Heiblum, H. Shtrikman, D. Mahalu. Phys. Rev. Lett. 75(1995) 3340–3343
[3] A. Kumar, L. Saminadayar, D. C. Glattli, Y. Jin, B. Etienne. Phys. Rev. Lett. 76(1996) 2778–2781
[4] R. C. Liu, B. Odom, Y. Yamamoto, S. Tarucha. Nature 391(1998) 263–265
[5] D.F. Walls, G.J. Milburn. *Quantum Optics.* Springer-Verlag, Berlin (1994)
[6] Y. Yamamoto, A. Imamoglu. *Mesoscopic Quantum Optics.* Wiley, New York (1999)
[7] A. Imamoğlu, Y. Yamamoto. Phys. Rev. Lett. 72(1994) 210–213
[8] A. Imamoğlu, H. Schmidt, G. Woods, M. Deutsch. Phys. Rev. Lett. 79(1997) 1467–1470
[9] Y. Yamamoto. Nature 390(1997) 17–18
[10] K. von Klitzing, G. Dorda, M. Pepper. Phys. Rev. Lett. 45(1980) 494–497
[11] Y. Yamamoto. In M. Ducloy, D. Bloch, editors, *Quantum Optics of Confined Systems.* Kluwer, Dordrecht (1996).
[12] C.W.J. Beenakker, M. Büttiker. Phys. Rev. B 46(1992) 1889–1892
[13] R.C. Liu, Y. Yamamoto. Phys. Rev. B 49(1994) 10520–10532
[14] A. Imamoğlu, Y. Yamamoto. Phys. Rev. Lett. 70(1993) 3327–3330

[15] J. Kim, H. Kan, Y. Yamamoto. Phys. Rev. B 52(1995) 2008–2012

[16] J. Kim, Y. Yamamoto. Phys. Rev. B 55(1997) 9949–9959

[17] P. Delsing, K.K. Likharev, L.S. Kuzmin, T. Claeson. Phys. Rev. Lett. 63(1989) 1861–1864

[18] L.J. Geerligs, V.F. Anderegg, P.A.M. Holweg, J.E. Mooij, H. Pothier, D. Esteve, C. Urbina, M.H. Devore. Phys. Rev. Lett. 64(1990) 2691–2694

[19] L.P. Kouwenhoven, A.T. Johnson, N.C. van der Vaart, C.J.P.M. Harmans, C.T. Foxon. Phys. Rev. Lett. 67(1991) 1626–1629

[20] J. Kim, Y. Yamamoto, H.H. Hogue. Appl. Phys. Lett. 70(1997) 2852–2854

[21] J. Kim, O. Benson, H. Kan, Y. Yamamoto. Nature 397(1999) 500

[22] For a review, see Z. Phys. B 85(1991) 317

[23] D.A.B. Miller. *Confined Electrons and Photons*. Plenum, New York (1995). p. 675

[24] H. Schmidt, K.L. Campman, A.C. Gossard, A. Imamoğlu. Appl. Phys. Lett. 70(1997) 3455

[25] D.L. Klein, R. Roth, A.K.L. Lim, A.P. Alivisatos, P.L. McEuen. Nature 389(1997) 699

[26] S.A. Empedocles, M.G. Bawendi. Science 278(1997) 2114

[27] S.E. Harris. Phys. Rev. Lett. 62(1989) 1033

[28] J.Y. Marzin, J.M. Gérard, A. Izraël, D. Barrier, G. Bastard. Phys. Rev. Lett. 73(1994) 716

[29] G. Björk, S. Machida, Y. Yamamoto, K. Igeta. Phys. Rev. A 44(1991) 669

[30] J.M. Gérard, B. Sermage, B. Legrand, E. Costard, V. Thierry-Mieg. Phys. Rev. Lett. 81(1998) 1110

[31] H. Drexler, D. Leonard, W. Hansen, J.P. Kotthaus, P.M. Petroff. Phys. Rev. Lett. 73(1994) 2252

[32] E. Dekel, D. Gershoni, E. Ehrenfreund, D. Spektor, J. M. Garcia, P.M. Petroff. Phys. Rev. Lett. 80(1998) 4991

[33] M. Grundmann, O. Stier, D. Bimberg. Phys. Rev. B 52(1995) 11969

[34] M. Fricke, A. Lorke, J.P. Kotthaus, G. Medeiros-Ribeiro, P.M.Petroff. Europhys. Lett. 36(1996) 197

[35] B.T. Miller, W. Hansen, S. Manus, R.J. Luyken, A. Lorke, J.P. Kotthaus. Phys. Rev. B 56(1997) 6764

[36] A. Wojs, P. Hawrylak. Phys. Rev. B 53(1996)

[37] F.M. Peeters, V.A. Schweigert. Phys. Rev. B 53(1996) 1468

[38] C. Weisbuch, B. Winter. *Quantum Semiconductor Structures*. Academic Press, San Diego (1991)

[39] O. Stier, M. Grundmann, D. Bimberg. Phys. Rev. B 59(1999) 5688

[40] Y. Toda, S. Shinomori, K. Suzuki, Y. Arakawa. Phys. Rev. B 58(1998) R10147

[41] K. Brunnner, G. Abstreiter, G. Böhm, G. Tränkle, G. Weiman. Phys. Rev. Lett. 73(1994) 1138

[42] A. Aspect, J. Dalibard, G. Roger. Phys. Rev. Lett. 49(1982) 1804

[43] J.F. Clauser, M.A. Horne, A. Shimony, R.A. Holt. Phys. Rev. Lett. 23(1969) 880

[44] O. Benson, Y. Yamamoto. Phys. Rev. A 59(1999) 4756

[45] J.A. Gupta, D.D. Awschalom, X. Peng, A.P. Alivisatos. Phys. Rev. B 59(1999) R10421

Author's address

Quantum Entanglement Project, ICORP, JST ,E. L. Ginzton Laboratory,
Stanford University
Stanford, CA 94305,
U.S.A;

and:
NTT Basic Research Laboratories,
Atsugi-shi,
Kanagawa 243-0198,
Japan.

W. Elsäßer

Quantum Noise Properties and Generation of Nonclassical States of Light by Vertical Cavity Surface Emitting Lasers: Theory and Experiment of Squeezing with VCSELs

Abstract

We present comprehensive investigations on the polarization resolved quantum noise behaviour of vertical cavity surface emitting lasers (VCSELs) with various cavity designs. These experiments are accompagnied by detailed studies using a semiclassical approach to calculate and model theoretically the amplitude fluctuations and correlations of a two orthogonal polarization-mode semiconductor laser as realized by a VCSEL, and, to explore theoretically the squeezing potential of VCSELs. First, we demonstrate that there exists the possibility of squeezing also in the two-mode regime besides sub-shot noise emission in the well known ideal single-mode operation regime confirming the recently published first experimental demonstration of the generation of amplitude squeezed light with VCSELs. Second, we demonstrate the successful generation of amplitude squeezed light by a lateral *and* polarization single mode VCSEL with the achievement of a maximum squeezing of 0.9dB. These experimental findings are in extremely good coincidence with the modelling results. Finally the future trends, the applications and the limitations of these non-classical states of light with respect to metrology applications are discussed.

1 Introduction

The possibility of generating non-classical states of light with sub-shot noise amplitude fluctuations (amplitude squeezing) was demonstrated a few years ago theoretically [1] and experimentally [2]. Since then numerous work with the aim of first to understand and second to improve the squeezing performances of semiconductor lasers have been performed [3, 4, 5, 6, 7]. The pursued strategies and the ingredients for the realisation of the optimum squeezing with semiconductor lasers have been low threshold current, high quantum efficiency, low internal loss, high longitudinal mode suppression, equivalent to the ideal single mode laser, and low gain non-linearity and no spatial hole burning [8, 9, 10, 11]. However, the real world of lasers showed up to be more or less far away from this ideal candidate leading to the fact that 8.3 dB of squeezing [3] still represents the record and that conveniently between 1 and 3 dB are obtained with straightforward experiments [4, 5, 6, 7]. Only quite recently, two physical further progressing approaches have been made to overcome this actual state-of-the-art. First, to understand the possible squeezing limits from the device point of view and thereby

improving it [12, 13], and second, to explore theoretically physical limitation mechanisms for the squeezing performance [14].

With the advent of a new laser structure, the VCSEL, the goal of generating sub-shot noise light seemed to be even easier accessible with their superior spectral longitudinal behavior [15, 16]. However, the trade-off with the complicated polarization modes [17] modified these first optimistic estimations. Therefore, sub-shot noise emission even with VCSELs seemed to remain a dream always ending up with the emission of light with fluctuations above the shot noise limit [18]. It was demonstrated quite recently that with a two polarization-mode VCSEL intensity squeezed light can be generated [19]. This result seems in contradiction to former theoretical work where the need for single mode behavior seems to be the first requirement [1, 9]. Consequently a better understanding of the influence of the polarization on the quantum noise of a semiconductor laser is needed [20]. The purpose of this contribution is threefold: First, we show results of comprehensive studies of the quantum noise properties of VCSELs demonstrating the relevance of the amplitude noise of both polarization modes and the importance of their respective correlations on the generation of sub-shot noise light. Then we present a theoretical description based on a new semiclassical laser noise model incorporating two polarization modes. The most important parameter determining the laser amplitude noise is the parameter M defined as the ratio between the power in the secondary mode S and the power in the primary mode P. We demonstrate that in a two-mode laser indeed two operation regimes exist in which amplitude squeezing is possible. Besides, the single mode (SM) regime, as characterized by M close to zero, the two-mode (TM) regime exists with M=1. In this case, the anticorrelation of the intensity fluctuations between the two modes leads to a strong reduction of the amplitude noise of the total emitted field enabling finally the generation of squeezed light. This ideal TM laser is very well realized by a laser with two orthogonal polarization modes as it can be the case for a VCSEL. Finally, we demonstrate the successful generation of amplitude squeezed light by a lateral *and* polarization single mode VCSEL. A maximum squeezing of 0.9dB is achieved [21]. From the experimental data we derive a direct dependence of the laser noise on the polarization mode suppression ratio, which is in excellent agreement with our theoretical predictions.

2   Experimental setup

We have investigated various types of VCSELs:

1.) Polarisation multi mode VCSELS: Etched air-post $GaAs/GaAlAs$ VCSELs, where the active zone consists of 3 quantum wells and the emission wavelength amounts to 770 nm. We have studied the noise and polarization properties of 2 different 2 ×2 arrays with 2 different diameters of the emission window of 7 and 12μm, respectively [22].

2.) Polarization single mode VCSELs: Oxide confined GaAs/AlGaAs VCSELs with 3.5 μm apertures [23]. They offer typical values of more than 3.5 mW lateral single mode emission at a center wavelength $\lambda \approx 840$ nm and threshold currents of less than 0.5 mA.

The experimental setup consists of the laser supply circuit (under quiet pumping conditions) and the detection circuit. The injection current is delivered by a dry battery with a fixed serial resistance and a subsequent passive network for current adjustment. The sum of all serial resistances, including the VCSEL's dielectric mirrors' resistances is estimated to

exceed twice the diode junction's differential resistance for any current in order to match the quiet pumping condition [1]. The multimode VCSELs have been mounted in a TO-8 can, the single mode VCSELs operate "on-wafer" at room temperature without active temperature stabilisation. For the investigations of the quantum noise behaviour we used either a balanced detection set-up [24] where the shot noise calibration has been performed using a weakly coupled LED or a direct detection set-up. For the latter one the emitted light is collected with a large-area photodiode (EG&G FFD200, bandwidth 150 MHz) which is connected via a bias-tee (PPL) and an amplifier (Miteq) to an electrical spectrum analyser (HP70000). The absence of collimating lenses in the beam reduces optical losses and prevents local saturation of the detector. The light of an incandescent lamp (white light source) is used to calibrate the standard quantum limit (SQL). A systematic comparison of different shot-noise sources, such as a white light source, an IR-filtered (Schott RG9) cold-light source and a high-power light emitting diode shows exact agreement in the noise spectra and therefore assures the correct SQL calibration. For the polarization measurements we use a Glan-Thompson polariser (extinction ratio of 10^{-5}) in a collimated beam.

3 Experimental results and discussion

3.1 Quantum noise of two-polarization mode VCSELs

We started our investigations by measuring the noise of the rather large diameter VCSELs of 7 and 12 μm under quiet pumping conditions. The results are depicted in Fig. 1, simultaneously for the noise and the ratio M = S/P of the intensities of the two polarization modes which we denote by P for the primary and S for the secondary mode, respectively. First, it is quite obvious that the noise is far above the shot noise limit.

Only for the small diameter VCSEL (7 μm; left figure) an approach of 1 dB towards the SQL at an injection current of 4 mA is visible. These results can be understood when realizing that the investigated lasers exhibit always two polarization modes as can be directly seen from the value and the dependence of M (around 0.2 to 0.7) and consequently a strong contribution of mode competition noise dominates the overall noise behaviour. However, the striking result is that there is a nearly perfect coincidence between the noise behaviour and the dependence of M as can be seen for the 12 μm VCSEL (right figure). From the results for the 7 μm VCSEL (left figure) this agreement seems not to be that perfect. However, one has to note that, besides the intensity, the correlation of the fluctuations plays an important role. This is more illustrated by Fig. 2 where the measured normalized correlations and M are simultaneously plotted as a function of the injection current. Even the surprisingly high and rapidly above threshold established value of anticorrelation of -1.0 for the 7 μm VCSEL can not completely counterbalance the fluctuations because M ist not equal to 1 in this regime. These understandings of the experimental results within the framework of the counterplay and the importance of both, intensity and correlations in the two-mode picture are nicely confirmed by the theory as illustrated in the next paragraph.
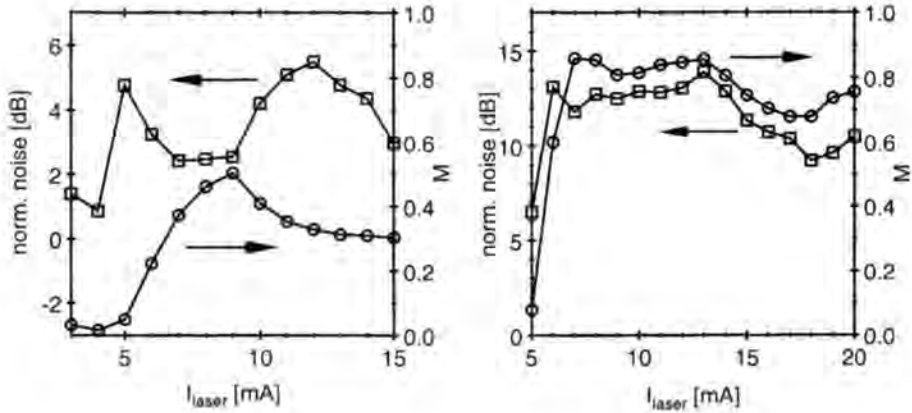
Figure 1: Intensity noise at low frequency normalized to the shot noise (left scale) and ratio M (right scale) as a function of the pumping current for the 7 μm (left figure) and the 12 μm VCSEL (right figure).

3.2 Noise theory

For the calculation we have extended our semiclassical model which is based on a Green's function method to calculate the noise performances of semiconductor lasers and especially of VCSELs. This method has proven its validity [8, 25] and has given equivalent results to those obtained by existing quantum mechanical theory [1, 11, 10]. Its first advantage is to give quasi-analytical expressions for the amplitude and phase noise even if gain suppression and spatial hole burning are considered. Therefore we have extended our one-mode-model to a two-mode-model [26] representing the two polarization modes of the VCSELs. We performed this calculation using a formalism similar to Agrawals work in the spectral domain [27]. Our model originates from a phenomenological approach, not taking into account a microscopic description [28] and no lateral effects [29, 30] are included.

In our description, the two modes P (Primary Mode) and S (Secondary Mode) are coupled to the same carrier reservoir. The following set of rate equations is obtained for the photon densities of the P and S modes and for the carrier density N inside the laser cavity :

$$\frac{dP}{dt} = v_g g_1 P - \frac{P}{\tau_{p1}} + F_P \tag{1}$$

$$\frac{dS}{dt} = v_g g_2 S - \frac{S}{\tau_{p2}} + F_S \tag{2}$$

$$\frac{dN}{dt} = \frac{I}{eV} - \frac{N}{\tau_e} - v_g (g_1 P + g_2 S) + F_N \tag{3}$$
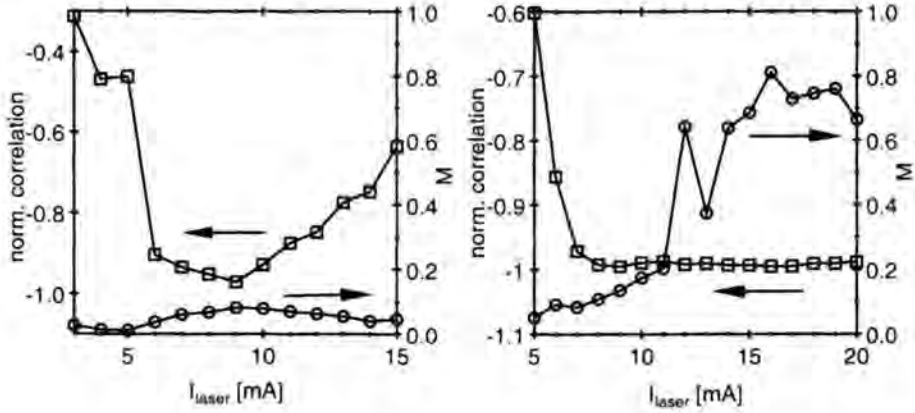
Figure 2: Normalized correlation of the fluctuations of the two polarization modes at low frequency (left scale) and ratio M (right scale) as a function of the pumping current for the 7 μm (left figure) and the 12 μm VCSEL (right figure).

where v_g is the group velocity, τ_{p1} and τ_{p2} the photon lifetime in each polarization mode, I the pumping current, τ_e the carrier lifetime and F_P, F_S and F_N the Langevin noise forces associated with the photon densities of the two polarization modes and the carriers.

The gain of each polarization mode, g_1 and g_2, is given by :

$$g_1 = g_d (N - N_0) - \beta_{11} P - \theta_{12} S \qquad (4)$$
$$g_2 = g_d (N - N_0) - \beta_{22} S - \theta_{21} P \qquad (5)$$

where g_d is the differential gain, N_0 the transparency carrier density, β_{11} and β_{22} are the gain suppression coefficients of each polarization mode and θ_{12} and θ_{21} the cross saturation coefficients, respectively. These coefficients originate from the microscopic coupling mechanisms within the semiconductor material [17, 20].

It is important for the calculation to consider the correct interference condition for the fluctuations of the amplitude of the emitted P_{ext} and S_{ext} polarization modes for reflection coefficients of the laser facets close to 1 :

$$\delta A_{Pext} = \sqrt{\frac{(1 - R)}{\tau}} \frac{\tilde{p}}{2\sqrt{P}} - \sqrt{R} f_{vac} \qquad (6)$$

$$\delta A_{Sext} = \sqrt{\frac{(1 - R)}{\tau}} \frac{\tilde{s}}{2\sqrt{S}} - \sqrt{R} f_{vac} \qquad (7)$$

where A_{Pext} and A_{Sext} are the amplitudes of the emitted P_{ext} and S_{ext} field, τ the light round-trip time in the cavity and f_{vac} the vacuum fluctuations.
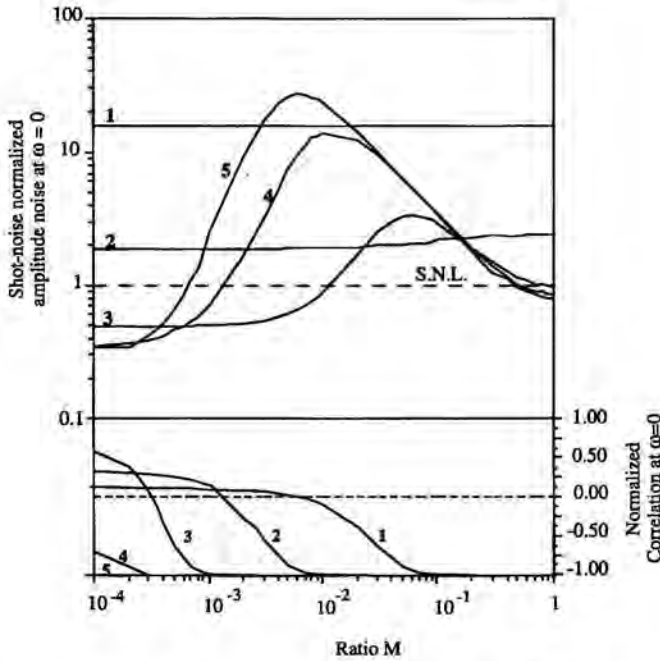
Figure 3: Amplitude noise of the total emitted field at low frequency normalized by the shot noise level (top, left scale) and normalized correlation between the amplitude fluctuation of the two polarization modes at low frequency (bottom, right scale) as a function of M for various total photon number in the cavity of $P_0 = 10^3$, 10^4, $5 \cdot 10^4$, 10^5, $5 \cdot 10^5$, and 10^6 (curves (1) to (5)).

The noise spectra for the two modes $S_P(\omega)$ and $S_S(\omega)$ and the amplitude noise of the total field $S_{S+P}(\omega)$ have been calculated as well as the normalized correlation $Cor(\omega)$

$$Cor(\omega) = \frac{S_{S+P}(\omega) - S_P(\omega) - S_S(\omega)}{2\sqrt{S_P(\omega)}\sqrt{S_S(\omega)}} \qquad (8)$$

The most important results are depicted in Fig. 3 where the amplitude noise of the total emitted field at low frequency normalized by the shot noise level (top, left scale) and the normalized correlation between the amplitude fluctuation of the two polarization modes at low frequency (bottom, right scale) are plotted as a function of the ratio M of the intensity of the two polarization modes for various total photon numbers P_0 in the cavity.

A totally different behavior of the amplitude noise is observed, depending on the photon number inside the cavity , or, equivalently on the pumping level R_p defined as $R_p = I/I_{th} - 1$ with I the current applied to the laser and I_{th} the laser threshold current. The noise is constant above the shot noise level (SNL), independent on the parameter M when the laser is very close to threshold, i.e. for $P_0 = 10^3$ or $R_p = 1.5 \cdot 10^{-2}$. This independence of the noise can be understood because the light emission under these conditions is mostly spontaneous emission which is not polarized. The situation is completely different highly above threshold
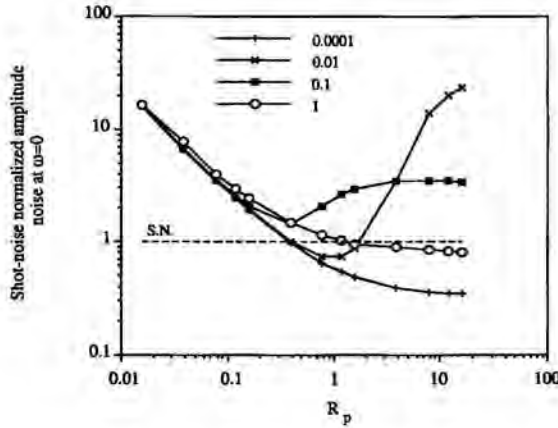
Figure 4: Amplitude noise normalized by the shot noise at low frequency (ω=0) as a function of the pump rate for various values of M.

($P_0 = 10^6$ or $R_p = 15$), where the noise is strongly dependent on M, as depicted in the upper part of Fig. 3. The most interesting result is that in fact amplitude noise squeezing is possible in two regimes, which are M close to 0 ($M < 10^{-4}$) and M close to 1, these two regimes being separated by a maximum of the noise. For intermediate values of P_0, this maximum increases and shifts towards lower M with increasing P_0.

The bottom part of Fig. 3 shows the normalized correlation between the amplitude fluctuations of the two polarization modes at low frequency as a function of the parameter M. The normalized correlation depends strongly on the photon number inside the cavity. Close to threshold, a negative correlation only occurs for M close to 1 and with decreasing M a transition to a correlation equal to 0 takes place. With increasing P_0, this transition regime shifts towards lower M, the negative correlation occurs over a wider range and the maximum correlation for M close to 0 approaches to positive values.

The same results are depicted in a different representation in Fig. 4, where the dependence of the normalized noise on the pump rate is plotted for different values of M. We find for extreme values of M, i.e. both for the single mode (M=0.0001) and the two mode laser (M=1), a continuous decrease of the noise level with increasing R_P. As already mentioned above, the achievable amount of squeezing as well as the range of M for which squeezing is possible is smaller for the two-mode than for the single mode laser, the pump rate being kept constant. For intermediate values of M, a minimum of the noise appears at $R_P \approx 0.1..1$, which depending on the exact value of M can be either above or slightly below the shot noise level, expressing once more again the delicate counterbalance between individual mode noise, correlation, and total noise. However, this noise minimum is of no practical relevance, because these intermediate values of M normally are difficult to be realized.

Therefore, two regimes exist, in which squeezing is possible. In the ideal two-mode laser it is the necessary and delicate perfect anticorrelation of the fluctuations of the two modes which leads to a noise suppression, whereas in the ideal single mode laser mode competition is excluded, by definition. The range of M for which squeezing is possible as well as the
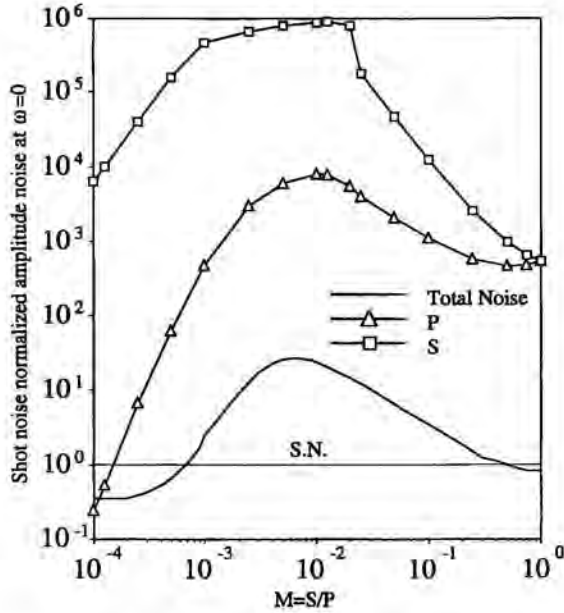
Figure 5: Shot noise normalized amplitude noise of the two polarization modes P and S and the total amplitude noise at low frequency (ω=0) as a function of M for $P_0 = 10^6$.

possible amount of squeezing is superior for the single mode laser.

The strong influence of M on the noise in each single mode is clearly illustrated in Fig. 5 where the amplitude noise at low frequency ($\omega = 0$) of the individual P and S modes as well as the total amplitude noise, all of them normalized to the shot noise, are presented as a function of M for a photon number $P_0 = 10^6$ inside the cavity corresponding to a pump rate $R_P = 15.7$. The amplitude noise of the P mode normalized to the shot noise level is always smaller than that of the S mode. The amplitude noise values for both S and P mode are strongly influenced by the ratio M. The weaker secondary S mode shows a weaker dependence on M than the stronger primary P mode, which is the only one to exhibit squeezing at all.

Finally, our model can be also applied to study the influence of gain saturation and carrier lifetime on the amplitude noise. Their influence on the noise and squeezing properties has been already demonstrated for edge emitting lasers [1, 8, 9]. We have therefore studied the influence of the efficiency of the laser determined by the losses inside the cavity lasers or equivalently the photon lifetime in the cavity on the VCSELs quantum noise including gain saturation effect via the gain suppression coefficients in order to deduce appropriate "design rules" for the most suitable VCSEL structure [31].

3.3 Squeezing of single polarization mode VCSELs

On the basis of these theoretical confirmations for the two-mode VCSEL we have now concentrated our research towards the realisation of squeezing with the ideal single polarization

Figure 6: Top: Normalized amplitude noise versus pump rate R_p at $f_1 = 44.8$ MHz (solid line), $f_2 = 62.5$ MHz (dashed line), $f_3 = 122.9$ MHz (dotted line); Bottom: PMR versus pump rate R_p.
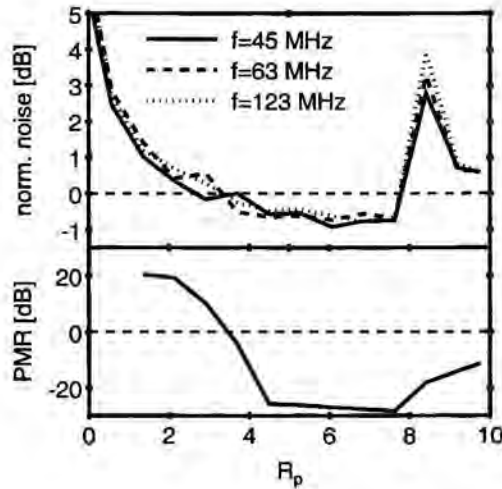
mode VCSEL. This goal has been succeeded with the superior performance VCSELs from University of Ulm.

Figure 6 shows the dependence of the normalized noise (thermal noise being substracted from all noise figures) (top) and the polarization mode suppression ratio (PMR) (bottom) on the pump rate $R_p = I/I_{th} - 1$ for various measurement frequencies. The PMR is defined as the logarithmic ratio of the powers in the two orthogonal linear polarization modes P and S, i.e. $\text{PMR} = 10 \log S/P$. The normalized noise graphs for the frequencies f=44.8 MHz, f=62.5 MHz, and f=122.9 MHz show a very similar behaviour. For low values of R_p, the noise amounts to more than 5dB above SQL. With increasing pump rate, the laser noise decreases, crosses the SQL at $R_p \approx 3.5$ and reaches a minimum of -0.9dB for f=44.8MHz at $R_p \approx 6$. At $R_p \geq 7.5$ a strong peak arises in the laser noise and for $R_p \geq 8.5$ the noise decreases again. Our experimental data show clearly the dependence of the laser noise on the PMR: Starting at $R_p = 0$, the laser noise decreases as long as the PMR decreases until both simultaneously reach their minima at R_p between 5 and 7.5. As a striking fact, the PMR changes from positive values to negative values at $R_p \approx 3.5$ as the laser emission changes from S-polarization to P-polarization. This behaviour is known as polarization switching and has already been investigated experimentally and theoretically in proton-implanted AlGaAs/GaAs multiple quantum well VCSELs [32]. Beyond this switching point, the modulus of the PMR exceeds 20dB in the range of pump levels between 4 and 8. Only in this range of high PMR squeezing is achieved. The strong peak in the laser noise at $R_p \geq 8$ coincides with an redecrease in the modulus of the PMR which is caused by the appearance of the first lateral mode, which is then the source for additional mode partition noise. The decrease of the normalized noise for $R_p > 8.5$ can be attributed to the fact that in this regime
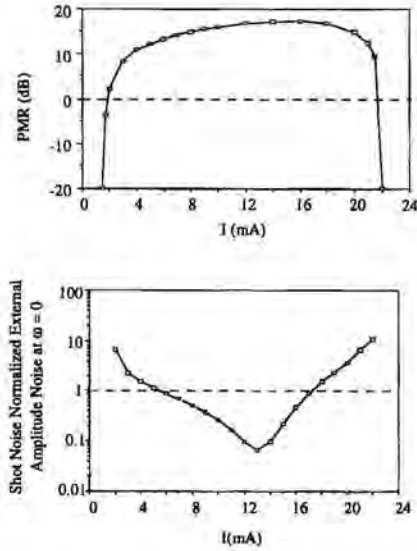
Figure 7: Calculated dependence of the PMR (top) and the shot-noise normalized amplitude noise at low frequency (bottom) on the pumping current I for a typical model VCSEL.

the normalized correlation of the emitted modes is approaching to -1 with the consequence that the noise in both modes can at least partly cancel each other, in agreement with the modelling results.

These results are in total agreement with our theoretical calculations and confirm the direct link between the ratio M and the quantum noise behaviour of a VCSEL. For a more quantitative confirmation, we have calculated the dependence of PMR and the amplitude noise on the pump rate for a typical VCSEL in order to compare these results to the experimental results from Fig. 6. The upper part of Fig. 7 presents for a 'model' VCSEL with particular but realistically chosen parameters the PMR as a function of the pumping current. A polarization flip to the orthogonal mode occurs close to threshold. Then PMR reaches its maximum close to 20 dB with a plateau before strongly decreasing high above threshold accompagnied by the occurrence of a secondary polarization flip. The lower part of Figure 7 presents for the same conditions the total amplitude noise normalised by the shot noise level at low frequency also as a function of the pumping current. The shot noise normalised amplitude noise decreases as long as PMR increases and reaches the noise minimum (with the occurrence of squeezing) where PMR exhibits a maximum plateau. Then, the noise increases with decreasing PMR. At a first sight, this increase in the laser noise may seem unexpected, because the absolute value of the PMR is in the range of 20dB for all injection currents (except for the range, where the polarization flip occurs). However, the model already included saturation effects which may even lead to a roll-over characteristics of the VCSEL, i.e. for high injection currents, the slope efficiency is already decreasing and

may even become negative. This strongly reduced efficiency then leads to the pronounced re-increase in the laser noise for $I \geq 13$ mA. The features of these calculations correspond very well to the obtained experimental results. However, a more precise comparison of experimental data with the theory still needs the exact knowledge of all laser parameters which indeed can be extracted by various experiments [33]. Therefore, our performed modelling of the VCSEL polarization and noise properties is a good tool to estimate the quantum noise and the squeezing properties even if a quite good knowledge of the VCSELs parameters is needed.

4 Summary and conclusion

In conclusion, we have presented theoretical and experimental results on the quantum noise performance and the generation of intensity squeezed light with VCSELs. Taking into account the polarization behaviour of these circular sysmmetric lasers, squeezing is possible with single polarization mode VCSELs as well as with the ideal two polarization mode VCSEL. However, the achievable amount of sub-shot noise compression is determined by the real laser's performance, even if theoretically better performances are predicted for VCSELs than for edge emitters. Therefore, the requirements for ideal VCSELs are rather severe. They have to exhibit single spatial lateral and single polarization mode behaviour, no saturation, and high efficiency, all performances which hopefully are only a question of technological maturity. Besides being very interesting candidates for basic research in quantum optics and semiconductor laser physics [28, 34] they offer also very interesting perspectives for applications in metrology and remote sensing. Very recently there have been numerous proposals and very interesting examples for the relevance of amplitude noise squeezed light for practical applications [35]. Gas sensing spectroscopy [36, 35] as well as interferometrical measurements [37] have benefitted from the reduction of laser noise below the Standard Quantum Limit [38]. These trends can be even increased incorporating squeezed light emitted by VCSELs. However, it is always desirable to increase the amount of squeezing, even if particularly designed experiments already benefit from small degrees of compression [39]. Therefore "the dream of realisation and application of ultimately squeezed VCSELs has to be continued".

5 Acknowledgements

References

[1] Y. Yamamoto, S. Machida, O. Nilsson. Phys. Rev. A 34(1986) 4025

[2] S. Machida and Y. Yamamoto, Y. Itaya. Phys. Rev. Lett. 58(1987) 1000

[3] W.H. Richardson, S. Machida, Y. Yamamoto. Phys. Rev. Lett. 66(1991) 2867

[4] F. Marin, A. Bramati, E.Giacobino, T.-C. Zhang, J. Ph. Poizat, J.F. Roch, P. Grangier. Phys. Rev. Lett. 75(1995) 4606

[5] M.J. Freeman, H. Wang, D.G. Steel, R. Craig, D.R. Scifres. Opt. Lett. 18(1993) 2141

[6] T.-C. Zhang, J.-Ph. Poizat, P. Grelu, J.-F. Roch, P. Grangier, F. Marin, A. Bramati, V. Jost, M.D. Levenson, E. Giacobino. Quantum Semiclass. Opt 7(1995) 601

[7] J. Kitching, A. Yariv, Y. Shevy. Phys. Rev. Lett. 74(1995) 3372

[8] J.-L. Vey, P. Gallion. IEEE J. Quantum Electron. 33(1997) 2097

[9] J.-L. Vey, P. Gallion. IEEE J. Quantum Electron. 33(1997) 2105

[10] B. Tromborg, H.-E. Lassen, H. Olesen. IEEE J. Quantum Electron. 30(1994) 939

[11] D.D. Marcenac, J.E Carroll. IEEE J. Quantum Electron. 30(1994) 2064

[12] S. Lahti, K. Tanaka, T. Morita, S. Inoue, H. Kan, Y.Yamamoto. IEEE J. Quantum Electron. 35(1999) 387

[13] S. Lathi, Y. Yamamoto. Phys. Rev. A 59(1999) 819

[14] F. Castelli, M Travagnin, L.Lugiat. submitted to Phys. Rev. Lett.

[15] G. Björk, Y. Yamamoto. IEEE J. Quantum Electron. 27(1991) 2386

[16] J.-L. Vey, W. Elsäßer. J. Opt. Soc. Am. B 14(1997) 1299

[17] M. San Miguel, Q. Feng, J.V. Maloney. Phys. Rev. A 52(1995) 1728

[18] E. Goobar, J.W. Scott, B. Thibeault, G. Robinson, Y. Akulova, L.A. Coldren. Appl. Phys. Lett. 67(1995) 3697

[19] D.C. Kilper, P.A. Roos, J.L. Carsten, K.L. Lear. Phys. Rev. A 55(1997) 3323

[20] G. P. Bava, L. Fratta, P. Debernardi. J. Opt. Soc. Am. B 16(1999)

[21] C.Degen, J.-L.Vey, W.Elsäßer, P.Schnitzer, K.J.Ebeling. Electron. Lett. 34(1998) 1585

[22] K.H. Gulden, M. Moser, S. Lüscher, H.P. Schweizer. Electron. Lett. 31(1995) 2176

[23] K.J. Ebeling, U. Fiedler, R. Michalzik, G. Reiner, B. Weigl. Int. J. Electron. Comm. 50(1996) 316

[24] J.-L.Vey, K. Auen, W. Elsäßer. Proceedings SPIE vol. 2994(1997) 178

[25] J.-L. Vey, Ph. Gallion. Opt. Lett. 20(1995) 2018

[26] J.-L. Vey, W. Elsäßer. Opt. Lett. 23(1998) 721

[27] G.P. Agrawal. Phys. Rev. A 37(1988) 2488

[28] S.W. Koch, F. Jahnke, W.W. Chow. Semicond. Sci. Technol. 10(1995) 739

[29] H.F. Hofmann, O. Hess. Phys. Rev. 59(1999) 2342

[30] Ch. Degen, I. Fischer, W. Elsäßer. Opt. Express 5(1999) 38

[31] J.-L. Vey, Ch. Degen, K. Auen, W. Elsäßer. Phys. Rev. A 60(1999)

[32] J. Martin-Regalado, F. Prati, M. San Miguel, N.B. Abraham. IEEE J. Quantum Electron. 33(1997) 765

[33] M.P. van Exter, M.B. Willemsen, J.P. Woerdman. Appl. Phys. Lett. 74(1999) 2274

[34] M.P. van Exter, A. Al-Remawi, J.P. Woerdman. Phys. Rev. Lett. 80(1998) 4875

[35] F. Marin, A. Bramati, V. Jost, E. Giacobino. Opt. Comm. 140(1997) 146

[36] E.S. Polzik, J. Carri, H.J. Kimble. Phys. Rev. Lett. 68(1992) 3020

[37] M.X., L.-A. Wu, H.J. Kimble. Phys. Rev. Lett. 59(1987) 278

[38] Y.-Q. Li, P. Lynam, M. Xiao, P.J. Edwards. Phys. Rev. Lett. 78(1997) 3105

[39] S. Kasapi, S. Lathi, Y. Yamamoto. Opt. Lett. 22(1997) 478

Author's address

Institute of Applied Physics,
Darmstadt University of Technology,
Schloßgartenstr.7, 64289 Darmstadt,
Germany.

G.P. Bava, F. Castelli, P. Debernardi and L. Fratta

Amplitude and Polarization Fluctuations in VCSEL's with Two Nearly Degenerate Modes

Abstract

The paper is concerned with the evaluation of the noise spectra of the Stokes parameters in VCSEL's with two nearly degenerate orthogonally polarized modes. It is found that the spectra inside the cavity are non symmetric with respect to frequency; however the asymmetry is eliminated at the output by the interference term arising from the reflected vacuum field fluctuations. A comparison between the numerical solution of the complete problem and an analytical one obtained with the adiabatic elimination of the spin population difference is also carried out.

1 Introduction

The quantum noise characteristics of VCSEL's with two nearly degenerate modes are very interesting mainly for two reasons: first of all they allow to validate the model adopted for the physical description of the device operation [1]; secondly, they allow to evaluate the macroscopic model parameters, such as dichroism and birefringence, on the basis of noise spectra measurements [2, 3]. The purpose of this paper is to present the noise spectra of the Stokes parameters, when all the noise sources of the system are correctly accounted for. To this aim, a complete quantum description of the VCSEL noise behaviour is developed with a rigorous calculation of the diffusion coefficients of the Langevin sources. In this way, an important difference between the noise spectra inside and outside the cavity is found.

2 Model inside the cavity

The model here adopted for the study of quantum noise in VCSEL's with two mode competition is described in [4] and the basic equations are:

$$
\begin{cases}
\dfrac{dA_1}{dt} = \left[i(\omega - \omega_1) + \tfrac{1}{2}(G - \gamma_{11})\right] A_1 - \tfrac{1}{2}\left(\gamma_{12} - ign\right) A_2 & +L_{A_1} \\[2mm]
\dfrac{dA_2}{dt} = \left[i(\omega - \omega_2) + \tfrac{1}{2}(G - \gamma_{22})\right] A_2 - \tfrac{1}{2}\left(\gamma_{21} + ign\right) A_1 & +L_{A_2} \\[2mm]
\dfrac{dN}{dt} = \dfrac{I}{q} - R - G_r(A_1^+ A_1 + A_2^+ A_2) - ig_r n(A_1^+ A_2 - A_2^+ A_1) & +L_N \\[2mm]
\dfrac{dn}{dt} = -\gamma_n n - g_r n(A_1^+ A_1 + A_2^+ A_2) - iG_r(A_1^+ A_2 - A_2^+ A_1) & +L_n
\end{cases}
\tag{1}
$$

where A_i are the field operators for the slowly varying amplitudes of the two modes, referred to the angular frequency ω; N and n are the number operators respectively for the total carriers and for the spin population difference in conduction band; in fact the population spin difference is accounted for only in conduction band where the spin relaxation rate is known to be lower. The birefringence Σ and dichroism δ of the system are related to the differences in the resonant frequencies ω_i and losses γ_{ii} of the modes: $\Sigma = \omega_1 - \omega_2$, $\delta = \frac{1}{2}(\gamma_{22} - \gamma_{11})$. $G = G_r + iG_i$ is the complex intensity gain and the quantity $gn = (g_r + ig_i)n$ introduces a coupling between the modes connected to the spin population difference; both these quantities depend on N. Moreover, I is the injected useful current, R is the recombination rate, which includes also the spontaneous emission, and γ_n is the n relaxation constant. Finally, the L terms are the Langevin noise sources.

In order to simplify the problem, the direct mode couplings given by γ_{ij} are neglected and the San Miguel model is recovered, in which, for a given choice of the parameters, only one of the two modes is lasing while the other is noise and the stationary value of n is zero. The linearization of system (1) around the stationary solution leads to two mutually decoupled problems: one for the fluctuations of the lasing mode, for example A_1, and total carriers (δA_1, δN), and one for the nonlasing mode and spin carrier difference (A_2, n). In the following we will focus on the latter problem. Reasonably neglecting the operator nature of A_1 above threshold ($A_1 = \sqrt{n_{ph}}$), the system for the non lasing mode A_2 (henceforth indicated as A) reads :

$$\begin{cases} \dfrac{dA}{dt} = (i\Sigma - \delta) A - \frac{1}{2}ign\sqrt{n_{ph}} \quad +L_A \\[2mm] \dfrac{dn}{dt} = -\Gamma n - iG_r\sqrt{n_{ph}}(A - A^+) +L_n \end{cases} \tag{2}$$

where we set $\Gamma = \gamma_n + g_r n_{ph}$. The diffusion coefficients of the Langevin noise terms have been rigorously computed in [4] starting from microscopic quantum equations for the fields, the carriers and the material polarization (the last quantity has already been adiabatically eliminated in system (1)) and the non-zero diffusion coefficients then are:

$$\begin{aligned} 2D_{A^+A} &= \gamma_{22}n_{th} + S \\ 2D_{AA^+} &= \gamma_{22}(1 + n_{th}) + S - G_r \\ 2D_{nA} &= 2D_{A^+n}^* = i\sqrt{n_{ph}}S \\ 2D_{An} &= 2D_{nA^+}^* = i\sqrt{n_{ph}}(S - G_r) \\ 2D_{nn} &= R + (2S - G_r)n_{ph} + 2\gamma_n N_0 \end{aligned} \tag{3}$$

where N_0 is the threshold carrier number, n_{th} is the number of thermal photons, practically negligible at optical frequencies, and S is the spontaneous emission in the lasing mode.

To compare our model with previous ones [2, 3] one must relate the field operator A to the operators of the Stokes parameters P_2 and P_3 naturally defined by:

$$\begin{aligned} P_2 &= -(A + A^+)/\sqrt{n_{ph}} \\ P_3 &= i(A - A^+)/\sqrt{n_{ph}} \end{aligned} \tag{4}$$

The dynamical system in this way obtained is the same as the classical ones derived in [2, 3]. However, it must be observed that if the change of variables from the field to the

Stokes operators is carried out before linearization, the quantum description leads to some additional terms, as shown in [5], which sligtly modify the stationary solution of the system. Since these terms are inversely proportional to n_{ph} and they do not influence the noise sources, here they will be neglected. The diffusion coefficients in the new variables are related to those defined in (3) through relations (4) and are:

$$
\begin{aligned}
2D_{P_2P_2} &= 2D_{P_3P_3} = (2S + 2\delta)/n_{ph} \\
2D_{P_2P_3} &= 2D_{P_3P_2}^* = i2\delta/n_{ph} \\
2D_{P_2n} &= 2D_{nP_2}^* = i\gamma_{11} \\
2D_{P_3n} &= 2D_{nP_3} = \gamma_{11} - 2S
\end{aligned}
\tag{5}
$$

where we exploited the threshold condition $G_r = \gamma_{11}$. These diffusion coefficients differ from those adopted in the previous models for the presence of the dichroism in $2D_{P_iP_i}$ and for the non-zero value of all the cross-correlations, in particular $2D_{P_iP_j}$.

An analytical solution of system (2) can be easily obtained in the frequency domain after adiabatic elimination of n. By introducing the analytical solution in the Fourier transform of (4) an explicit expression for the noise spectra of the Stokes parameters inside the cavity is found. For instance for P_3 one obtains:

$$
\langle P_3(\Omega)P_3^+(\Omega)\rangle = \left[\Sigma^2 2D'_{P_2P_2} + |i\Omega + \delta|^2 2D'_{P_3P_3} + \Sigma\left[(-i\Omega + \delta)2D'_{P_2P_3} + (i\Omega + \delta)2D'_{P_3P_2}\right]\right]|Det(\Omega)|^{-2}
\tag{6}
$$

where the system determinant is: $Det(\Omega) = n_{ph}G_r\Gamma^{-1}(g_i\Sigma - g_r\delta) - (\Sigma^2 + \delta^2) + \Omega^2 - i\Omega(2\delta + n_{ph}g_rG_r\Gamma^{-1})$ and the primed diffusion coefficients include the noise of n:

$$
\begin{aligned}
2D'_{P_2P_2} &= 2D_{P_2P_2} + g_i^2\Gamma^{-2}2D_{nn} \\
2D'_{P_3P_3} &= 2D_{P_3P_3} + (2D_{P_3n} + 2D_{nP_3})g_r\Gamma^{-1} + g_r^2\Gamma^{-2}2D_{nn} \\
2D'_{P_2P_3} &= 2D'^*_{P_3P_2} = 2D_{P_2P_3} + \Gamma^{-1}(g_r2D_{P_2n} - g_i2D_{nP_3}) - g_ig_r\Gamma^{-2}2D_{nn}
\end{aligned}
\tag{7}
$$

It turns out that the noise spectra inside the cavity are not symmetric with respect to the frequency as a consequence of the cross diffusion coefficients which are complex conjugate; the asymmetric term is:

$$
-2\Sigma\Omega\mathcal{I}m(2D'_{P_3P_2})|Det(\Omega)|^{-2} = \frac{2\Sigma\Omega}{n_{ph}|Det(\Omega)|^2}\left(\frac{n_{ph}g_rG_r}{\Gamma} + 2\delta\right)
\tag{8}
$$

However, the asymmetry of the internal spectra is not a problem since these cannot be measured; moreover, this result can find a theoretical foundation in [6].

3   Output noise spectra

In order to evaluate the output field A_o ($A_o^+A_o$ is the output photon flux) the reflected vacuum field fluctuations must be accounted for:

$$
A_o = \sqrt{\gamma_o}A - f_e
$$
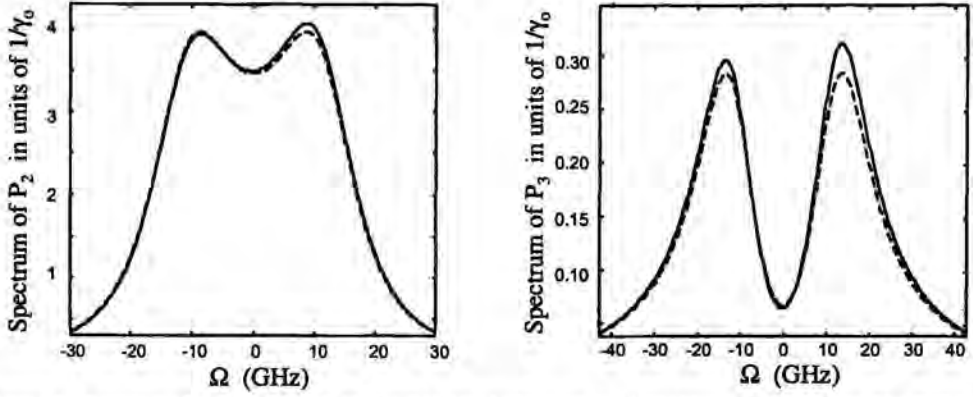
Figure 1: Spectra of P_2 (left) and P_3 (right) inside the cavity (continous line) and of the radiated field (dashed line); $\Sigma = 0.44$ GHz, $\delta = 0.007 \text{ns}^{-1}$, $\Gamma = 100 \text{ns}^{-1}$ and $P = 10$.

where γ_o is the output mirror loss for the mode under analysis and f_e is the operator which describes the incident vacuum field fluctuations; obviously the effect of f_e has already been included in L_A and therefore, in the evaluation of the output noise spectra, the interference term must be correctly considered. The presence of the interference term is in fact crucial to recover the symmetry of the output spectrum. For example, with reference to the spectrum of P_3, the interference term is:

$$-\sqrt{\gamma_o}\left(< P_3 F_{P_3}^+ > + < F_{P_3} P_3^+ >\right) \tag{9}$$

where $F_{P_3} = i(f_e - f_e^+)/\sqrt{n_{ph}}$. An explicit expression of (9) can be obtained with the same approximations as expression (6). If this is done, an asymmetric contribution with respect to Ω is deduced which exactly cancels the asymmetry (8) of the internal spectrum multiplied by γ_o, that is, transported outside the cavity.

4   Numerical examples

The general behaviour of the results for the spectra outside the cavity is very similar to that already reported [2, 3]. The following examples have been computed with refrence to the structure already adopted in [4] to which we refer for the values of the parameters. The pump parameter P is defined as $(I/I_{th} - 1)$.

In Fig. 1 an example of the spectra of P_3 and P_2 inside the cavity (continous line) and outside (dashed line) is shown, computed by numerically solving the system (2). The asymmetry of the internal spectrum can be clearly seen and is particulary significant for P_3. In Fig. 2 a comparison between the results obtained from the numerical solution of (2) and the analytical approach with adiabatic elimination of n is carried out for two values of Γ. As expected, when Γ is not large enough the adiabatic elimination is not correct and a non negligible difference is observed. In Fig. 3 , for two values of the pumping, the spectrum of P_3 obtained from the numerical solution of system (2) is compared with that computed
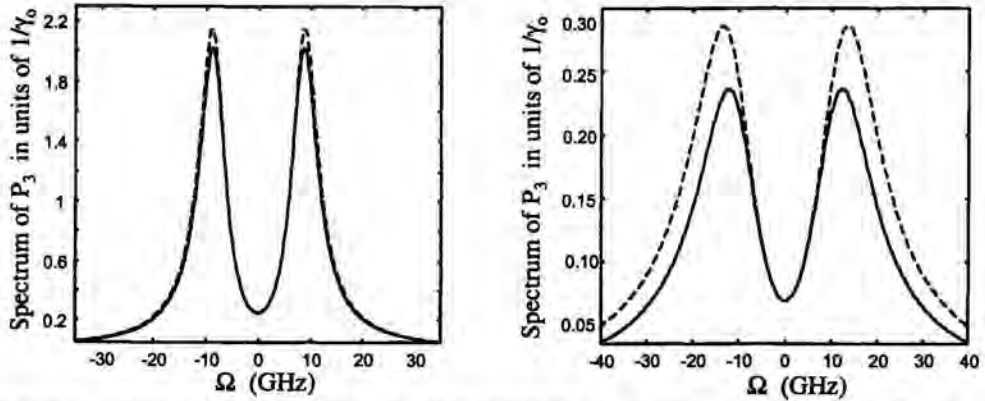
Figure 2: Spectra of P_3 outside the cavity with (continuous line) and without (dashed line) adiabatic elimination of n for $\Gamma = 300\text{ns}^{-1}$ (left) $\Gamma = 100\text{ns}^{-1}$ (right); $\Sigma = 0.44$ GHz, $\delta = 0.007\text{ns}^{-1}$ and $P = 10$.
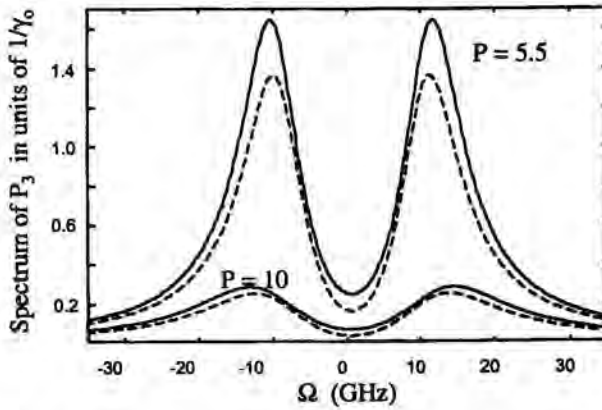
Figure 3: Spectra of P_3 outside the cavity for $\Sigma = 0.44$ GHz, $\delta = 0.007\text{ns}^{-1}$ and $\Gamma = 100\text{ns}^{-1}$. Solid lines, complete model; dashed lines, adiabatic elimination of n and cross diffusion coefficients neglected.

with adiabatic elimination of n and by neglecting the cross diffusion coefficients. This last approximation is the one adopted in [3]. The differences are more evident for higher values of pumping and a slight shift of the peaks is observed.

5   Acknowledgements

References

[1] M. San Miguel, Q. Feng, J.V. Moloney. Phys. Rev. A 52(1995) 1728–1739

[2] H.F. Hofmann. Quantum Semiclass. Opt. 10(1998) 87–96

[3] M.P. van Exter, M.B. Willemsen, J.P. Woerdman. Phys. Rev. A 58(1998) 4191–4205

[4] G.P. Bava, L. Fratta, P. Debernardi. J. Opt. Soc. Am. B 16(1999) 2147–2157

[5] W. Chow, S.W. Koch, M. Sargent III. *Semiconductor Laser Physics*. Springer-Verlag, Berlin (1994)

[6] D. Walls, G.J.Milburn. *Quantum Optics*. Springer Verlag (1995)

Author's address

G. P. Bava, P. Debernardi and L. Fratta:
Dip. di Elettronica and Cespa-CNR,
Politecnico di Torino,
Corso Duca degli Abruzzi 24, 10129, Torino,
Italy;

Tel.: +39-011-5644165,
Email: Pierluigi@polito.it.

F. Castelli:
Dip. di Fisica,
Università di Milano,
Via Celoria 16, 20100, Milano,
Italy.

M.P. van Exter, M.B. Willemsen and J.P. Woerdman

Polarization Modal Noise in Vertical-Cavity Semiconductor Lasers

Abstract

We have studied the polarization fluctuations and polarization modal noise in semiconductor VCSELs. The measurements include (polarization-resolved) optical spectra, intensity noise, correlated fluctuations in two polarization modes, and stochastic switching between these modes. Good agreement is found with a relatively simple model.

1 Introduction

The optical polarization of light emitted by Vertical Cavity Surface Emitting Lasers (VCSELs) is less stable and shows more dynamics than that of most other lasers. This has two reasons: (i) the high degree of rotational symmetry (round for proton-implanted VCSELs, square for some oxidized VCSELs) makes the two in-plane polarization directions nominally equivalent, and (ii) their small size makes quantum noise, due to spontaneous emission, relatively important. One striking consequence of this limited polarization stability is that many VCSELs switch their dominant polarization at a certain laser current. Furthermore, even at currents where only one polarization mode dominates the laser polarization is not stable, as the intensity in the other (much weaker) polarization mode fluctuates wildly. We have studied these polarization fluctuations with several experimental techniques and compared the results with a simple model.

Our model is valid for VCSELs that operate in the fundamental transverse mode, so that the (slowly-varying component of the) emitted optical field can be specified in terms of four variables: the optical phase φ_l, the intensity $I = |\mathbf{E}|^2$, and two Poincaré angles ϕ and χ that characterize the optical polarization, where ϕ $(0 \leq \phi \leq \pi)$ is the direction of the polarization ellipse and χ $(-\pi/4 \leq \chi \leq \pi/4)$ is the ellipticity angle. For practical VCSELs the output polarization is approximately linear, in a direction that we define to be the x-axis, so that:

$$\mathbf{E} \approx [\mathbf{e}_x - (\phi + i\chi)\mathbf{e}_y]\sqrt{I}e^{-i\varphi_l}. \tag{1}$$

We study the polarization dynamics in VCSELs via the natural fluctuations in the polarization angles ϕ and χ. The polarization dynamics is thus separated into a *(stochastic) diffusion*, due to noise, and a *(deterministic) flow*, due to possible polarization preferences. For VCSELs that operate not too close to the lasing threshold, the intensity I is relatively stable, and the polarization and intensity dynamics are almost decoupled.
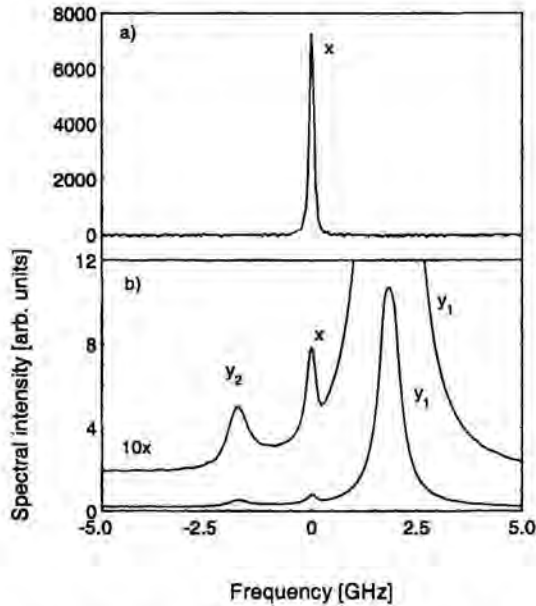
Figure 1: Optical spectra taken at: (a) the dominant x polarization, (b) close to the y polarization, showing the "nonlasing" peak y_1 and a weak polarization-type of four-wave-mixing peak y_2

2 Optical and intensity noise spectra

One way to study the polarization dynamics is via the polarization-resolved optical spectrum. The upper part of Fig. 1 shows the optical spectrum at the dominant (x) polarization, the lower part shows the spectrum in the almost orthogonal polarization (in the same units), with as little as 5×10^{-4} of the dominant polarization mixed in on purpose. The y-polarized light, which depends on the complex variable $\phi + i\chi$, is concentrated in a spectral line (y_1) that is shifted and broadened with respect to the x-polarized line and that can be associated with the "non-lasing" polarization mode. The shift or frequency difference between the two lines (≈ 1.8 GHz in Fig. 1) is associated with birefringence. The broadening (≈ 0.2 GHz in Fig. 1) is associated with a polarization-dependent gain difference of dichroism. Both comprise a linear and nonlinear part. The weak spectral line y_2 in Fig. 1 results from a polarization-type of four-wave-mixing. It can be used to quantify the mild preference for VCSELs to emit linearly polarized light, which results from (relatively fast) internal spin dynamics [1].

Another way to study the polarization dynamics is via the polarization-resolved intensity noise, as demonstrated in Fig. 2. The two curves denoted as ϕ and χ show the intensity noise spectrum as measured behind a polarizer oriented at 45° with respect to the x-axis, either without or with an additional $\lambda/4$-plate. These polarization projections mix x and y-polarized light and allows one to separately detect the dynamics of the polarization angles ϕ and χ. The ϕ and χ spectra peak around the birefringent frequency and have a width that is equal to the dichroism. The curves denote as x and y show the intensity noise after

Polarization Modal Noise in Vertical-Cavity Semiconductor Lasers
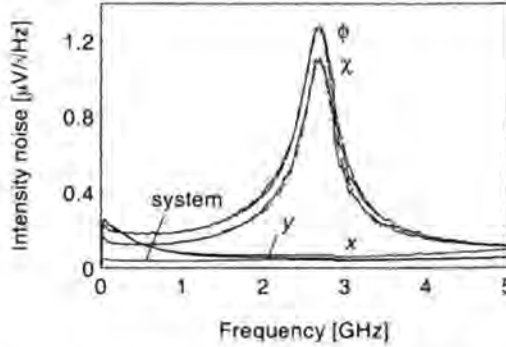
Figure 2: Intensity noise spectra, as measured behind a polarizer (i) at 45° with respect to the laser polarization (curves ϕ and χ (with additional $\lambda/4$-plate)), and (ii) aligned with the x or y-axes as defined by the dominant laser polarization.

projection on either one of the polarization modes. These noise spectra are almost identical, are strongly peaked around zero frequency, and have a width that is equal to the dichroism. The total intensity noise, as measured without any polarization projection, is generally small and peaks at the (relatively large) relaxation oscillation frequency. A tail of this peak is visible in the high-frequency intensity noise of the lasing mode (curve x).

3 Polarization modal noise

The noise spectra shown in Fig. 1 and 2 are a-typical in the sense that they belong to a VCSEL with relatively small birefringence. For the more common VCSELs, with a birefringence in the range of 10-20 GHz, the polarization evolution is fast enough to average out the nonlinear anisotropy, i.e., the intrinsic preference of VCSEL to emit linearly polarized. As a result, the four-wave mixing peak in Fig. 1 becomes too weak to observe (its magnitude scales with the inverse square of the birefringence), and the ϕ and χ spectra shown in Fig. 2 become essentially identical. This allows one to separate the polarization dynamics into a fast oscillation between ϕ and χ, and a much slower (and more interesting) evolution of the mode fraction $Y = I_y/I$, where I_y and I are the power in the nonlasing mode and the total power, respectively. For small mode fractions, Y exhibits "thermal-like" fluctuations [2] with an average amplitude

$$\langle Y \rangle = \langle \frac{I_y}{I} \rangle = \langle \phi^2 + \chi^2 \rangle = \frac{D}{\gamma}. \tag{2}$$

Typical values are $D = 10$ μs^{-1} for the diffusion rate, and $\gamma = 1$ ns^{-1} for the dichroism, making the average mode fraction $\langle Y \rangle$ about 1%.

The birefringence and dichroism change with current. In many VCSELs an increase in current leads to a reduction in dichroism, to an increase in polarization fluctuations, and finally to a switch of the dominant polarization. Polarization switches that occur at large currents often show hysteresis, whereas switches at lower current are of a stochastic nature
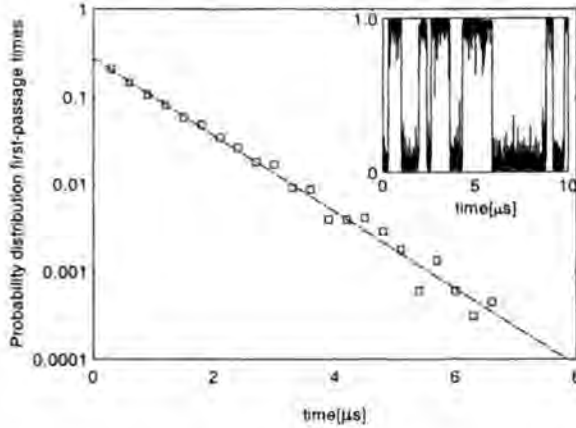
Figure 3: Distribution of average dwell times in one polarization mode for a VCSEL that spontaneously switches polarization.

(see inset of Fig. 3 for time trace of projected intensity). The random nature of this process is evident from the exponential probability distribution of the average dwell times in one of the two states, as shown in the body of Fig. 3. For this case (current 6.4 mA, corresponding to $\mu = 1.3$ time above threshold) the average dwell time was 1.0 μs [3].

Figure 4 shows how the average dwell-time for polarization switches changes by more than 7 orders of magnitude as a function of switch current, where the switching point was adjusted by modification of the VCSEL with an intense heating laser positioned $\pm$ 40 μm away from the device. The solid line is calculated on the basis of a simple Kramer's hopping model, with no adjustable parameters; the key parameters in this model, being the noise strength and the shape of the double well potential well, could be determined from independent measurements that gave the related diffusion rate D and dichroism γ, respectively.

4   Correlated modal fluctuations

Finally we again consider the polarization flucutions of a VCSEL outside the (relatively narrow) regime of polarization switches and wonder to what extent the intensity fluctuations in the x and y polarized mode are correlated, as quantified by the (real-valued) frequency-dependent correlation function

$$C_{xy}(\omega) \equiv \frac{Re\left(\langle \tilde{I}_x(\omega)\tilde{I}_y^{\,*}(\omega)\rangle\right)}{\langle|\tilde{I}_x(\omega)|^2\rangle^{1/2}\,\langle|\tilde{I}_y(\omega)|^2\rangle^{1/2}}$$

Figure 5 shows how the low-frequency component of C_{xy} changes with current, for a VCSEL that switches polarization around 8-8.5 mA [4]. The intensity fluctuations in the two polarization modes show a strong anti-correlation, with the deviation from prefect anticorrelation ($C_{xy} = -1$) being proportional to the ratio of the low-frequency noise in the total intensity I and the mode fraction Y. Close to the switching point, where the dichroism is
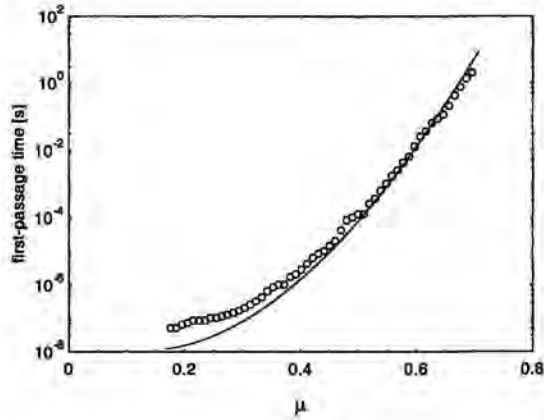
Figure 4: Average dwell time in each of the two polarization states as a function of the normalized pumping parameter $\mu = I/I_{th} - 1$. The dots are experimental data (obtained for a single VCSEL) and the curve is a theoretical fit.
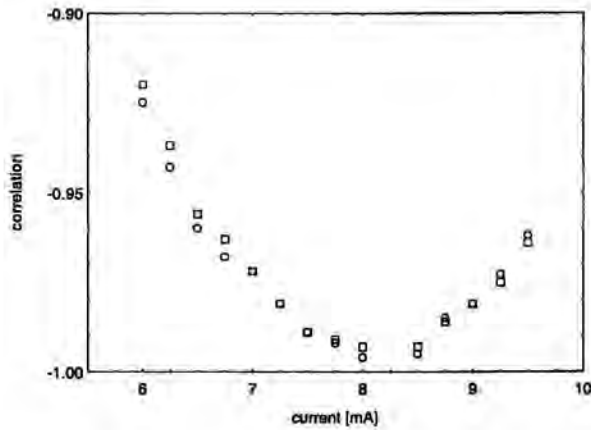
Figure 5: Low-frequency correlation C_{xy} as a function of current. Around a current of 8-8.5 mA, where the dominant laser polarization switches, the dichroism is smallest, the polarization fluctuations are strongest, and the correlation between the modal intensity fluctuations is largest.

small and the polarization fluctuations are large (large Y), the anti-correlation is strongest. The measurements presented in Fig. 5 support the earlier statement that the dynamics of the polarization mode fraction Y and the total intensity I are almost decoupled, as the squares and circles result from data analysis with and without the assumption of decoupling, respectively. A more quantitative discussion of this statement has allowed us to estimate the (limited) deteriorating effect of polarization mode partition noise on the possibility to obtain intensity squeezing.

References

[1] M. SanMiguel, Q. Feng, J.V. Moloney. Phys. Rev. A 52(1995) 1728

[2] M.P. van Exter, M.B. Willemsen, J.P. Woerdman. Appl. Phys. Lett. 74(1999) 2274

[3] M.B. Willemsen, M.U.F. Khalid, M.P. Van Exter, J.P. Woerdman. Phys. Rev. Lett. 82(1999) 4815

[4] M.B. Willemsen, M.P. Van Exter, J.P. Woerdman. to be published in Phys. Rev. A (1999)

[5] M.P. van Exter, M.B. Willemsen, J.P. Woerdman. Phys. Rev. A 58(1998)

Author's address

Huygens Laboratory,
Leiden University,
P.O Box 9504, Leiden,
The Netherlands.

O. Hess

Quantum Optical Images in the Spatial Coherence Characteristics of Mesoscopic Semiconductor Lasers

1 Quantum optical images

While spatially inhomogeneous stimulated coherent emission may very successfully be described within a semiclassical framework, by its very nature, the corresponding processes leading to spontaneous emission are a signature of the nonclassical, quantum properties of the light-matter interaction in semiconductor structures. It is this nonclassical property of radiation which has recently received large interest. Particularly since the pioneering investigations of L. Lugiato *et al.* in systems of optical parametric oscillators (OPO), *quantum optical images* have revealed the nonclassical correlations between entangled photons created by down-conversion in the OPO [1]. Recently, it has been predicted that it should be possible in the OPO to generate pairs of optical images that are quantum entangled to each other[2]. While the OPO system allows a simplified level of description, the photonics of small semiconductor structures are considerably more complex. Most importantly, the light-matter interactions are strongly determined by the presence and the particular properties of the charge carrier system forming the microscopic (interband-) dipoles – the source of the radiation. Very uniquely, the dipole system thus carries both, the nonclassical properties of the carriers and the optical field [3].

In this contribution we will use a recently developed general theoretical model taking into account the spatiotemporal coherence of spontaneous emission. This is done on the basis of Quantum Maxwell-Bloch Equations [4] (QMBE) which describe the spatiotemporal dynamics of both, stimulated amplification and (amplified) spontaneous emission on equal footing in terms of expectation values of field-field correlations, dipole-field correlations, carrier densities, fields and dipoles. In particular, the quantum dynamics of the interaction between the light field and the carrier system is formulated in terms of Wigner distributions for the carriers and of spatially continuous amplitudes for the light field.

2 Spatial coherence characteristics of mesoscopic photonic semiconductor devices

2.1 *Spontaneous emission in photonic semiconductor devices*

In an optical semiconductor device, spontaneously emitted light may have significant influence on the spatiotemporal dynamics of the (coherent) light field. It is, in particular, a whole class of modern ultra bright resonant-cavity light emitting semiconductor diodes (RC-LED) which transform electric current with extreme efficiency (internal quantum efficiencies ap-

proaching 100%) into spontaneously emitted light. The spatial coherence of spontaneous emission and amplified spontaneous emission is equally most important in semiconductor lasers close to threshold, ultra low threshold semiconductor lasers [5] or spatially distributed or coupled semiconductor lasers systems like arrays of vertical-cavity surface-emitting lasers [6] (VCSEL) or multi-stripe and broad area semiconductor lasers. There, the spontaneous emission factor is modified by the amplification and absorption of spontaneous emission into the non-lasing modes and amplified spontaneous emission may be responsible for multi mode laser operation and for finite spatial coherence [6].

2.2 Optical quantum images in the far-field of a RC-LED

Resonant cavity LEDs (RC-LED) are a particularly important example of a mesoscopic photonic semiconductor device in which spontaneous emission is the source of radiation. There the spatial coherence of amplified spontaneous emission defines an angular distribution of the emitted light in the far field. From the Quantum Maxwell-Bloch equations an analytic expression for this distribution may be derived [4] which contains both gain/absorption due to stimulated emission and spontaneous emission:

$$I_f(\Theta, \Theta) = W k_0 \frac{\arctan\left(\frac{\Omega_f - \omega(\Theta)}{\Gamma + \kappa}\right) + \arctan\left(\frac{\omega(\Theta)}{\Gamma + \kappa}\right)}{\pi(R + \frac{1}{2}) - 2\arctan\left(\frac{\Omega_f - \omega(\Theta)}{\Gamma + \kappa}\right) - \arctan\left(\frac{\omega(\Theta)}{\Gamma + \kappa}\right)},$$

$$\text{with} \qquad R = \frac{2\hbar\kappa}{g_0^2 \nu_0 \sigma} \frac{m_{eff}^e + m_{eff}^h}{m_{eff}^e m_{eff}^h} \quad \text{and} \quad \omega(\Theta) = \frac{\omega_0 \Theta^2}{2\epsilon_r}.$$

The parameter R represents the ratio between the cavity loss rate κ and the maximum amplification rate of the gain medium. g_0 is the normalized dipole matrix element, $m_{eff}^{e,h}$ the effective masses of electrons and holes, and Γ and Ω_f are the dephasing rate and Fermi frequency, respectively.

The classical laser threshold is defined by the carrier density for which the denominator of $I_f(\Theta, \Theta)$ is zero for a single specific frequency $\omega(\Theta)$. Consequently, the carrier density at which this occurs is pinned. Figure 1 shows the far field intensity distribution for different carrier densities below this pinning density.

In Fig. 1 (a), intensity distribution is for carrier densities much lower than the pinning density largely due to amplified spontaneous emission. The intensity maximum is clearly centered around $\Theta = 0$. Figure 1(b) shows the intensity distribution for carrier densities halfway towards threshold. Already, the intensity maxima move to angles of $\pm 15°$, corresponding to the frequency at which the gain spectrum has its maximum. In the case of Fig. 1(c), the threshold region is very close to the pinning density. The peaks in the far field pattern narrow as the laser intensity is increased.

3 Conclusions

Traces of *Quantum Optical Patterns* have been observed in spatially extended photonic semiconductor devices. An analytic expression derived from the Quantum Maxwell Bloch Equations shows images in the far-field which are a result of the spatial coherence of spontaneous
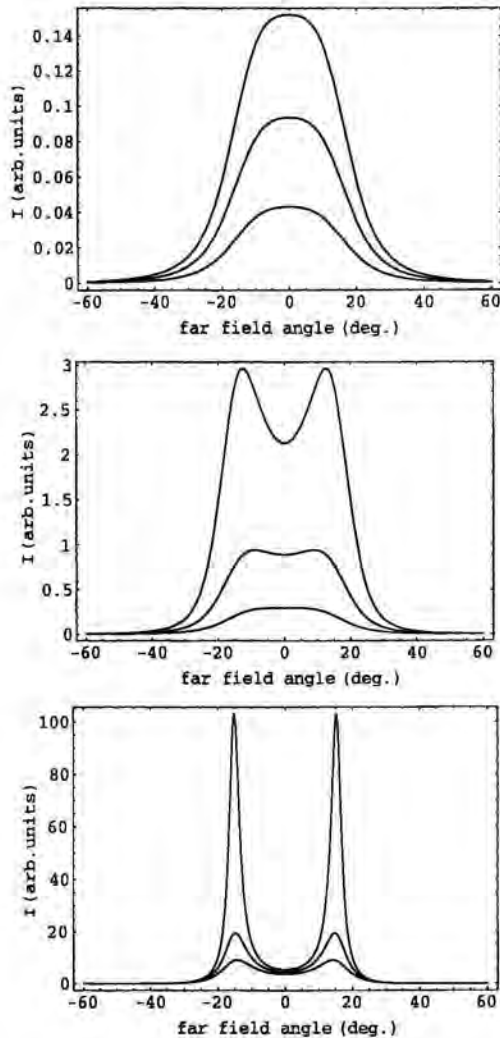
Figure 1: Fingerprints of the spatial coherence characteristics of quantum fluctuations in the formation of *Quantum Optical Image*: The cuts in the circularly symmetric far field intensity distribution of a broad-area RC-LED structure show the increased degree of spatial coherence with increasing carrier density.

and stimulated emission in a broad-area resonant-cavity light emitting diode (RC-LED). In the RC-LED the source of radiation is almost exclusively spontaneously emitted light and the far-field structures vanish if quantum-optical correlations are disregarded. Consequently, the far field pattern may indeed be regarded as a fingerprint of the quantum-optical spatial coherence – similar as the linewidth of the laser spectrum is a measure of temporal coherence.

References

[1] L.A. Lugiato, M. Brambilla, A. Gatti. In B. Bederson, H. Walter, editors, *Advances in Atomic, Molecular and Optical Physics*, volume 40. Academic Press, Boston (1998).

[2] L.A. Lugiato, M. Brambilla, A. Gatti, M.I. Kolobov. Phys. Rev. Lett. 83(1999) 1763–1766

[3] M. Kira, F. Jahnke, S. W. Koch. Phys. Rev. Lett. 82(1999) 3544–3547

[4] H.F. Hofmann, O. Hess. Phys. Rev. A 59(1999) 2342–2358

[5] Y. Yamamoto, R.E. Slusher. Physics Today (1993) 66–73

[6] H.F. Hofmann, O. Hess. Opt. Lett. 23(1998) 391–393

Author's address

Theoretical Quantum Electronics, Institute of Technical Physics,
DLR,
Pfaffenwaldring 38-40, D–70569 Stuttgart,
Germany.

Email address: Ortwin.Hess@dlr.de

C.L.A. Hooijer, K. Allaart, D. Lenstra and G.X. Li

Radiative Coherence Effects in Microstructures

Abstract

We consider a possible role of radiative coherence effects in light emission of semiconductor devices, in analogy to well known phenomena (non-exponential decay, dark line) in the decay of V-type atoms.

In the spectrum of atoms with two close-lying excited states, called V-type atoms, peculiar features may be observed when their separation in energy is comparable to the natural line width of these levels. The spectrum is then not just a superposition of two Lorentzians. The indirect coupling between the excited states via the radiative coupling to the ground state gives rise to interference between the two optical transitions. This results in a combined lineshape with zero intensity where the interference is completely destructive (dark line), while for a slightly different energy the interference becomes constructive, resulting in a strong peak of which the decay width may be smaller than that of the decay of each individual level (subnatural linewidth). Moreover the decay of the levels is no longer exponential. These phenomena were discussed at some length in [1]. When the energy separation between the excited levels is much larger than the natural linewidth, one may still generate similar phenomena by the application of a microwave field that couples the levels [2, 3].

The essential mechanism that gives rise to the aforementioned phenomena is interference due to the mutual coupling of the levels via the *optical* field. We investigate whether this coupling via the optical field could also play a role in light emitting devices, e.g. semiconductors. As a theoretical framework we distinguish between the passive dielectric structure of the device, represented by a real dielectric constant due to bound charges, and the active charge carriers which couple to the optical field by the interaction Hamiltonian

$$H_{int} = \int d^3r \, \hat{\mathbf{j}} \cdot \hat{\mathbf{A}}_{opt} \tag{1}$$

This interaction gives rise to coupled equations for the optical field and the free charge carriers. The field may be expresed as

$$\hat{\mathbf{A}}_{opt}(\mathbf{r}, t) = \hat{\mathbf{A}}_{free}(\mathbf{r}, t) + \sum_{n' \neq n, k'k_{act.reg.}} \int d^3r' \, \overset{\leftrightarrow}{G}(\mathbf{r}, \mathbf{r}', \omega_{n'n}) \cdot \mathbf{j}_{nn'}^T(\mathbf{r}', \mathbf{k}, \mathbf{k}') \hat{c}_{n\mathbf{k}}^\dagger(t) \hat{c}_{n'\mathbf{k}'}(t), \tag{2}$$

where $\overset{\leftrightarrow}{G}$ is the classical Greens tensor of the Helmholtz equation for the field of the (passive) dielectric structure and the transverse current density operator of the active charge carriers

is expressed in a basis with band index n and wave vector $\mathbf{k}$. The polarization operator of the free charge carriers obeys the Heisenberg equations of motion

$$
\begin{aligned}
i\hbar\frac{d}{dt}(\hat{c}_\gamma^\dagger(t)\hat{c}_{\gamma'}(t)) &= -\left[\sum_\alpha \int_{el.ext} d^3r \left\{ \hat{c}_\gamma^\dagger \hat{c}_\alpha \hat{\mathbf{A}}(\mathbf{r},t)\cdot\mathbf{j}_{\gamma'\alpha}(\mathbf{r}) - \hat{c}_\alpha^\dagger\hat{c}_{\gamma'}\hat{\mathbf{A}}(\mathbf{r},t)\cdot\mathbf{j}_{\alpha\gamma}(\mathbf{r}) \right\} \right] \\
&\quad + (E_{\gamma'}-E_\gamma)\hat{c}_\gamma^\dagger(t)\hat{c}_{\gamma'}(t) \\
&\quad + \left[\hat{c}_\gamma^\dagger(t)\hat{c}_{\gamma'}(t), \frac{1}{4}\sum_{\beta\beta'\delta\delta'}' V^{Coul}_{\beta\beta'\delta\delta'}\hat{c}_\beta^\dagger(t)\hat{c}_{\beta'}^\dagger(t)\hat{c}_{\delta'}(t)\hat{c}_\delta(t) \right]
\end{aligned}
\tag{3}
$$

in which the band energies E_γ are the mean-field energies of the Bloch states and the prime on the summation sign in the last term indicates that Coulomb terms already included in these energies should be omitted. For the moment we shall focus on the optical coupling terms in the first line of this equation and ignore the Coulomb terms. Limiting ourselves further to the study of possible non-exponential decay in spontaneous emission, we may apply normal ordering of the operators, thereby avoiding $\hat{\mathbf{A}}_{free}(\mathbf{r},t)$ [4, 5], and obtain in rotating wave approximation

$$
\begin{aligned}
\frac{d}{dt}<\hat{c}_{1\mathbf{k}}^\dagger\hat{c}_{1\mathbf{k}}(t)> &= (E_{\gamma'}-E_\gamma)\hat{c}_\gamma^\dagger(t)\hat{c}_{\gamma'}(t) \\
&\quad -\frac{2}{\hbar}\sum_{\mathbf{k}',\mathbf{k}_1,\mathbf{k}_2} \mathrm{Im}\,\{I(1,\mathbf{k},2,\mathbf{k}',2,\mathbf{k}_2,1,\mathbf{k}_1) \\
&\quad \times <\hat{c}_{1\mathbf{k}}^\dagger\hat{c}_{1\mathbf{k}_1}(t)(\delta_{\mathbf{k}',\mathbf{k}_2} - \hat{c}_{2\mathbf{k}_2}^\dagger\hat{c}_{2\mathbf{k}'}(t))>\},
\end{aligned}
\tag{4}
$$

in which the integrals

$$
I(n,\mathbf{k},m,\mathbf{k}',p,\mathbf{k}_p,q,\mathbf{k}_q) \equiv \int\int_{act.reg.} d^3r\,d^3r'\,\mathbf{j}_{nm}^T(\mathbf{r},\mathbf{k},\mathbf{k}')\cdot \overset{\leftrightarrow}{G}(\mathbf{r},\mathbf{r}',\omega_{qp})\cdot\mathbf{j}_{pq}^T(\mathbf{r}',\mathbf{k}_p,\mathbf{k}_q)
\tag{5}
$$

embody the properties of the light emitting device in two respects. The electronic properties are represented in the current densities (and the band energies) of the free charge carriers, which are usually confined to only a tiny active region in the device. Therefore these integrals extend over this small region only. The optical properties that are reflected in the Greens tensor, on the other hand, are barely influenced by the small active region and rather dominated by the dielectric constant(s) of the cladding material and the structure of the device as a whole. So these two aspects present two distinct mechanisms by which the properties of the emitted light may be manipulated.

To obtain a first impression of the possible relevance of the induced two-body interaction, contained in (4), we studied the occurrence of non-exponential decay within a simple two-band model with a conduction band 1 and a valence band 2 and one reciprocal lattice vector $\mathbf{K}$:

$$
\varphi_{1\mathbf{k}}(\mathbf{r}) = \sqrt{\frac{2}{V}}e^{i\mathbf{k}\cdot\mathbf{r}}\sin(\mathbf{K}\cdot\mathbf{r})
\tag{6}
$$

$$
\varphi_{2\mathbf{k}'}(\mathbf{r}) = \sqrt{\frac{2}{V}}e^{i\mathbf{k}'\cdot\mathbf{r}}\cos(\mathbf{K}\cdot\mathbf{r}).
\tag{7}
$$

With the Greens function for bulk material

$$G(\mathbf{r}, \mathbf{r}', \omega_{12}) = \frac{\mu_0 e^{i\omega_{12} \frac{|\mathbf{r}'-\mathbf{r}|}{v}}}{4\pi |\mathbf{r}' - \mathbf{r}|} \tag{8}$$

the interaction integrals may the be calculated analytically:

$$I(1, \mathbf{k}, 2, \mathbf{k}', 2, \mathbf{k}_p, 1, \mathbf{k}_q) = \delta(\mathbf{k}_q + \mathbf{k}' - \mathbf{k}_p - \mathbf{k}) \tag{9}$$

$$\times \frac{\mu_0 e^2 \hbar}{2\pi m^2} \frac{1}{V} \left(K^2 - \frac{((\mathbf{k}' - \mathbf{k}) \cdot \mathbf{K})^2}{|\mathbf{k}' - \mathbf{k}|^2} \right) \frac{2\pi}{|\mathbf{k}' - \mathbf{k}|} \left(\frac{1}{\frac{\omega_{12}}{v} - |\mathbf{k}' - \mathbf{k}| + i0} - \frac{1}{|\mathbf{k}' - \mathbf{k}| + \frac{\omega_{12}}{v} + i0} \right).$$

From this exercise one learns that in general these induced interaction matrix elements are much smaller than those of the static Coulomb potential:

$$\frac{|I|}{|V^{Coul}|} \approx \left(\frac{\hbar K}{mc} \right)^2 \frac{(\mathbf{k}' - \mathbf{k})^2}{(\mathbf{k}' - \mathbf{k})^2 - \omega^2} \approx 10^{-5} \frac{(\mathbf{k}' - \mathbf{k})^2}{(\mathbf{k}' - \mathbf{k})^2 - \omega^2} \tag{10}$$

and therefore may be neglected in the calculation of electronic properties such as band structure.

As a further exercise within this schematic model we adopt a separable (quasiparticle) approximation for the density matrix elements in the conduction band: $\rho_{1k,1k'}(t) = A_k^*(t) A_{k'}(t)$ and a factorization of the two-body densities:

$$< \hat{c}_{1k}^\dagger(t) \hat{c}_{1k'}(t) \hat{c}_{2k''}^\dagger(t) \hat{c}_{2k'''}(t) > = < \hat{c}_{1k}^\dagger(t) \hat{c}_{1k'} > < \hat{c}_{2k''}^\dagger(t) \hat{c}_{2k'''}(t) > .$$

Then an effective Schrödinger equation for the amplitudes $A_k(t)$ is obtained:

$$i\hbar \frac{d}{dt} A_k(t) = E_k A_k(t) + \sum_{k'} h_{k,k'} A_{k'}(t) \tag{11}$$

with effective potential matrix elements

$$h_{kk'} = \delta_{kk'} (\Delta_k - i\hbar \gamma_k) \tag{12}$$

$$+ \frac{e^2}{4\pi\epsilon_0} \left(\frac{\hbar K}{mc} \right)^2 \frac{1}{V} \sum_{\mathbf{q}} \left(1 - (\hat{q} \cdot \hat{K})^2 \right) \left(\frac{1}{q + \frac{\omega}{v} + i0} + \frac{1}{q - \frac{\omega}{v} - i0} \right) < \hat{c}_{2,k'+q}^\dagger \hat{c}_{2,k+q} > .$$

Neglecting the real parts (Lamb shifts), a maximal coherent effect (superradiance) is found if a constant mixing matrix element between all k-states is assumed: $h_{kk'} = -i\hbar\gamma$. Then, for the case of a quantum wire, the spontaneous emission rate of the superradiant solution appears to be roughly proportional to the square of the length L of the wire. This would imply an increase of the decay rate by several orders of magnitude as compare to that for a pure k-state. Solutions orthogonal to the superradiant one, on the other hand, then become very long living, reminiscent of a dark line in the spectrum of a V-type atom. Both the very fast and slow component are visible in the decay of the occupation probability for a state with an electron in the lowest, $\mathbf{k} = 0$, state of the conduction band, as shown in the figures. It should be noted, however, that in this very crude model the coherence effects are strongly exaggerated by the assumed form of the effective coupling between the k-states. The long-living component is expected to be washed away in practice by the much faster relaxation phenomena. So it remains to be investigated to what extent any of these features may survive for more realistic model assumptions.
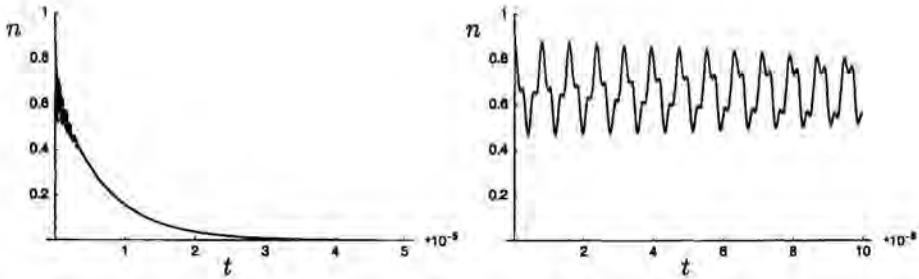
Figure 1: Decay of the amplitude n of the $k = 0$ state of the conduction band in a quantum wire, for the highly schematic model discussed in the text. Radiative coherence gives rise to a rapidly decaying component (life time inversely proportional to the length of the wire) as well as components on a intermediate time scale and, due to omission of relaxation, a long-living component reminiscent of the "dark line" in the decay of V-type atoms.

Acknowledgments

References

[1] S-Y Zhu, R.C.F. Chan, C.P. Lee. Phys. Rev. A 52(1995) 710
[2] P. Zhou, S. Swain. Phys. Rev. A 56(1997) 3011
[3] G-x Li, K. Allaart, C.L.A. Hooijer, D. Lenstra. to be published
[4] J.R. Ackerhalt, J.H. Eberly. Phys. Rev. lett. 30(1973) 456
[5] H.J. Kimble, L. Mandel. Phys. Rev. A 13(1976) 2123

Author's address

C.L.A. Hooijer, K. Allaart and D. Lenstra:
Quantum Electronics Theory Group, Division of Physics and Astronomy,
Vrije Universiteit,
De Boelelaan 1081, 1081 HV Amsterdam,
The Netherlands;

G.-x. Li:
Dep. of Physics,
Huazhong Normal University,
Wuhan,
China.

Email address: allaart@nat.vu.nl.

C.M.J. Wijers and P.L. de Boeij

Role of Wave Functions in Electromagnetism: RAS from GaAs (110)

Abstract

We have calculated the reflectance anisotropy for the GaAs (110) surface using the discrete cellular method. This method extends the range of application of standard discrete dipole calculations by incorporating nonlocal polarizabilitites. The method adds a second quantum mechanical channel of nonlocality, which turns out to be necessary and yields very good agreement between theory and experiment.

1 Introduction

Photons, electrons and nuclei are the fundamental (quasi)-particles making up the world around us. Maxwell and Schrödinger equations govern their behaviour. To be of any use photons need to interact with matter and that interaction is taken into account classically through the macroscopic Maxwell equations and some kind of dielectric function. It is an intriguing question whether the electrons, which are the most prominent actor in the interaction, have a more exciting role than the linear homogeneneous, isotropic one they are forced to play in the classical treatment. Such behaviour seems to be confirmed by the success of the simple macroscopic theory in the classical optical regime.

The reason of that success is cancellation. The simplest possible microscopic model for the dielectric function is Clausius-Mossotti (CM). This model represents a homogeneous continuum by an infinite simple cubic lattice of (independent) discrete dipoles. In this model all short range dipole-dipole interactions cancel on symmetry grounds. So the electromagnetic interaction, apart from some far field Lorentz contribution, has become mute as a source of more interesting behaviour

The electromagnetic *short range* interaction can manifest itself only if CM-like conditions are absent, like in non-cubic materials. The spatial dispersion phenomena found experimentally in cubic materials [1] also violate CM. At surfaces deviation from CM should be found in general, since symmetry gets broken there for geometry reasons. Especially there the short range electromagnetic interaction becomes manifest and can be tested directly. This makes these phenomena so exciting from the more fundamental point of view.

The difficult rigorous treatment of a semi-infinite lattice of dipoles is made tractable by the double cell method [2, 3]. This method improves previous approaches by Ewald and Litzman [4, 5] by taking into account time dependency, retardation effects and existance of the surface. Currently the discrete and continuum treatment of optics have been compared [6, 7], elucidating the nature of boundary conditions. Despite the improved mathematical

treatment, the *local* discrete dipole model has not been particularly successful in the description and interpretation of surface optical experiments [8], apart from trivial physical systems (solid noble gases, alkali-halogenides).

In these systems the assumption of *independently* polarizable entities, commonly made in dipole models, holds sufficiently well. We state that the failure of dipole models for other systems is due to a poor handling of short-range interactions, especially the fact that those short range interactions can be influenced directly by the wavefunction and require as a result explicit use of *nonlocal* polarizabilities.

The study of anisotropic surface optical properties (RAS (Reflectance Anisotropy Spectroscopy), differences in perpendicular reflectance from surfaces of cubic materials for different polarization) offers a unique opportunity to test this hypothesis. Mochán and Barrera [9] were already able to apply the *local* discrete dipole model successfully to the anisotropic reflectance of the Ge (110) surface, but at the expense of assigning two atoms to one dipole. To make the preferred assignment of one atom to one dipole work is only possible by invoking *nonlocal* polarisabilities, as we will show in this paper by focussing primarily on the correct prediction of (measured) intensities. We present the prescription how to calculate these non-local polarisabilities from first principles. We investigated the reflectance anisotropy of the GaAs (110) surface because of its rich spectroscopic structure.

2 Theory

In classical electrodynamics the induced charge and current density are the source terms. The continuity equation allows both to be derived from a single polarization density $\mathbf{P}(\mathbf{r}, t)$ without loss of generality. It can be obtained within first order linear-response theory from

$$\mathbf{P}(\mathbf{r}, \omega) = \int d\mathbf{r}'\, \chi(\mathbf{r}, \mathbf{r}', \omega) \cdot \mathbf{E}(\mathbf{r}', \omega). \tag{1}$$

Here $\mathbf{E}(\mathbf{r}, \omega)$ is the self-consistent perturbing electric field and $\chi(\mathbf{r}, \mathbf{r}', \omega)$ the nonlocal susceptibility. This kernel can be obtained within the scissors-operator approximation to the quasi-particle response theory [10, 11, 12] from LDA-type density-functional calculations. We define the susceptibility $\chi(\mathbf{r}, \mathbf{r}', \omega)$ according to

$$\chi(\mathbf{r}, \mathbf{r}', \omega) = \frac{2e^2}{\omega^2 V_{BZ}^2} \sum_{if} \frac{\mathbf{j}_{if}(\mathbf{r})\mathbf{j}_{fi}(\mathbf{r}')}{\epsilon_f - \epsilon_i - \hbar\omega^+}$$

$$\mathbf{j}_{if}(\mathbf{r}) = -\frac{i}{2}(\psi_i^*(\mathbf{r})\nabla\psi_f(\mathbf{r}) - \psi_f(\mathbf{r})\nabla\psi_i^*(\mathbf{r})) \tag{2}$$

where we corrected properly for the $\omega = 0$ singularity. We assumed adiabatic onset of the perturbation, and retained the conductivity sumrule. This induced polarization acts as source of electromagnetic radiation and contributes to the perturbing electric field,

$$\mathbf{E}(\mathbf{r}, \omega) = \mathbf{E}^{ext}(\mathbf{r}, \omega) + \int d\mathbf{r}'\, f(\mathbf{r} - \mathbf{r}', \omega) \cdot \mathbf{P}(\mathbf{r}', \omega),$$

$$f_{\mu\nu}(\mathbf{r}, \omega) = \left[k^2 \delta_{\mu\nu} + \nabla_\mu \nabla_\nu\right] \frac{\exp(ikr)}{4\pi\epsilon_0 r}, \tag{3}$$

where the transfer kernel $f(\mathbf{r}, \omega)$ describes the retarded electromagnetic interactions ($\mu, \nu = x, y, z$) and $k = \omega/c$ and $r = |\mathbf{r}|$. Direct solution of the microscopic continuum equations is not tractable for surfaces. Discretisation, however, provides an appropriate way to reduce the effort. For the treatment of optical reflection, we model the microscopic polarization as a semi-infinite lattice of point-like dipoles. Each dipole represents the polarization in a particular cell V_i belonging to atom i. It is located at the atomic nucleus $\mathbf{r}_i$ with dipole strength $\mathbf{p}_i(\omega) = \int_{V_i} d\mathbf{r}\, \mathbf{P}(\mathbf{r}, \omega)$. Assuming a uniform field $\mathbf{E}_i(\omega)$ within each cell V_i, the set of equations (1,3) becomes,

$$
\begin{aligned}
\mathbf{p}_i(\omega) &= \sum_j \alpha_{ij}(\omega) \cdot \left[\mathbf{E}_j^{ext}(\omega) + \sum_k f_{jk}(\omega) \cdot \mathbf{p}_k(\omega) \right]. \\
\alpha_{ij}(\omega) &= \int_{V_i} d\mathbf{r} \int_{V_j} d\mathbf{r}'\, \chi(\mathbf{r}, \mathbf{r}', \omega)
\end{aligned}
\tag{4}
$$

where the traditional *local* polarizabilities correspond to the case $i = j$ only. With the new *nonlocal* polarizabilities ($i \neq j$), the perturbating field (the quantity between square brackets in eq. (4)), will not only polarize cell i, but also its neighbouring cells. It is the wavefunction itself which has to be set responsible for this quantum mechanical type of nonlocality and results from the requirement that *the wavefunction needs to be continuous and differentiable across the cell boundary*. This quantum induction vanishes if the wavefunction becomes negligible at the cell boundary, as is the case e.g. for alkali-halogenides and solid noble gas systems. This explains in a very transparent way the success of local dipole calculations in such systems and its failure in case of covalent systems and metals.

The transfer tensors can be derived accordingly from eq. (3),

$$
f_{ij}(\omega) = \begin{cases} f(\mathbf{r}_i, \mathbf{r}_j, \omega) & \text{for } i \neq j \\[2mm] \dfrac{V}{|V_i|}\alpha^{-1}(\omega) - \dfrac{1}{3\epsilon_0|V_i|}\left(\dfrac{\epsilon_r(\omega) + 2}{\epsilon_r(\omega) - 1} \right) - \dfrac{ik^3}{6\pi\epsilon_0} & \text{for } i = j. \end{cases}
\tag{5}
$$

For $\mathbf{r}_i = \mathbf{r}_j$ the point-dipole interaction becomes singular and we have to take the finite extent of the cells into account. We make use of the Lorentz field for a uniformly polarised medium with the same polarization density. This field is modified by the first two terms in the expression for f_{ii}, accounting for the deviation from the homogeneous system. The third term in the f_{ii} tensors accounts for the radiation losses and is called the Lorentz' damping term. Further $V = \sum_i V_i$ is the volume of the primitive cell, $\epsilon_r(\omega)$ is the experimentally observed relative dielectric function, and the mean polarizability $\alpha(\omega)$ of the primitive cell is obtained from $\alpha(\omega) = \sum_{i \in V, j} \alpha_{ij}(\omega)$

The technical advantage of using this discretization scheme is that we can use the double cell method [2, 3], which obtains the response of a semi-infinite crystalline system of interacting dipoles to a given incident field, $\mathbf{E}_i^{ext}(\omega) = \mathbf{E}_0 \exp(i\mathbf{k} \cdot \mathbf{r}_i)$. The essence of the method is a decomposition of the system into a semi-infinite stack of dipole layers, each obeying parallel translational symmetry. To describe the response of the ith layer, it suffices to consider a single characteristic dipole $\mathbf{p}_i$. For the first N_S layers of the surface the interaction between these characteristic dipoles is taken into account explicitly. All further layers can be treated by making use of just a few normal modes, because of bulklike symmetry. Normal modes

have been introduced by Litzman and Dub [4, 5], starting from the regular arrangement of bulk sites as $\mathbf{r}_{wW} = \mathbf{r}_w^B + W\mathbf{s}_3$, where $\mathbf{s}_3$ is a lattice vector controlling the stack sequence and $\mathbf{r}_w^B$ locates a dipole within the bulk unit cell. The normal mode expansion is postulated as:

$$\mathbf{p}_{wW} = \sum_{m=1}^{M} \nu_m \mathbf{u}_{mw} e^{iW\mathbf{k}_m \mathbf{s}_3} \tag{6}$$

As for the local case the normal mode propagation vector given by $\mathbf{k}_m = \mathbf{k}_{\parallel} + q_m \mathbf{n}$ with $\mathbf{n}$ the inward surface normal, and normal mode polarization vector $\mathbf{u}_{mv}$ follow from the condition that

$$\| \mathbf{1} - \alpha_0^{-1} \mathsf{A}(\mathbf{k}_m) \mathsf{F}(\mathbf{k}_m) \| \, |\mathbf{u}| = |\mathbf{0}| \tag{7}$$

This is the (square) bulk secular matrix. F is the matrix of phase corrected sums of transfer tensors and $\mathsf{A}(\mathbf{k}_m)$ is a matrix, having sums of nonlocal polarizabilities (4) as its matrix elements. Both matrices are not square, different from the local case. Since these sums also contain $\mathbf{k}_m$ dependent phase factors, the matrix $\mathsf{A}(\mathbf{k}_m)$ is an explicit function of $\mathbf{k}_m$, again different from the local case. Once the normal mode parameters are known, the free variables of the system, the normal mode strenght ν_m and the dipole strength's $\mathbf{p}_i$ for the surface layer follow from the double cell interaction matrix,

$$\left\| \begin{array}{cc} \mathcal{M}_{SS} & \mathcal{M}_{SB} \\ \mathcal{M}_{BS} & \mathcal{M}_{BB} \end{array} \right\| \left\| \begin{array}{c} \mathbf{p}_i \\ \nu_m \end{array} \right\| = \left| \begin{array}{c} \mathsf{A}(\mathbf{k}) \mathbf{E}_{Ext,i} \\ \mathbf{t}_n^T \mathbf{E}_{Ext}^B \end{array} \right| \tag{8}$$

The components of this matrix are either the same as for the local case (BS and BB part) or constructed in a manner closely resembling the construction of (7). The S-part of the inhomogeneous vector now contains however an additional polarizability matrix $\mathsf{A}(\mathbf{k})$, due to a rearrangement of components, necessary because of nonlocality [2, 3]. Once the microscopic sources ν_m and $\mathbf{p}_i$ are found, the remote fields and connected observables, such as reflection coefficients, can be found in exactly the same way as for the local case.

3 Results

The GaAs bulk and surface polarizabilities have been obtained from the single particle energies and wavefunctions using accurate periodic DFT-LDA calculations [13, 14]. In the bulk calculation we used a lattice constant $a = 5.613$Å. The surface was modelled using a slab having 4 Ga and 4 As-layers, with the 1 As and 2 Ga-layers on top at surface reconstructed positions [15]. This slab has been made bulk terminated at the bottom by adding 2 H-layers and 2 Ga and 2 As-layers of frozen ion type to model the bulk Madelung potential. We used the scissors operator to fix the bulk(-like) band-gap to 1.52 eV. The cut-off range for the nonlocal polarizability was set to 7.93Å, resulting in eight shells of neighbouring atoms. The self correction given in (5) deviates only slightly from the Lorentz field contribution, indicating that the bulk dielecric function is reproduced accurately. Due to the limited slab thickness, we used bulk values for $\alpha_{ij}(\omega)$ throughout the system except for i, j both top-layer atoms.
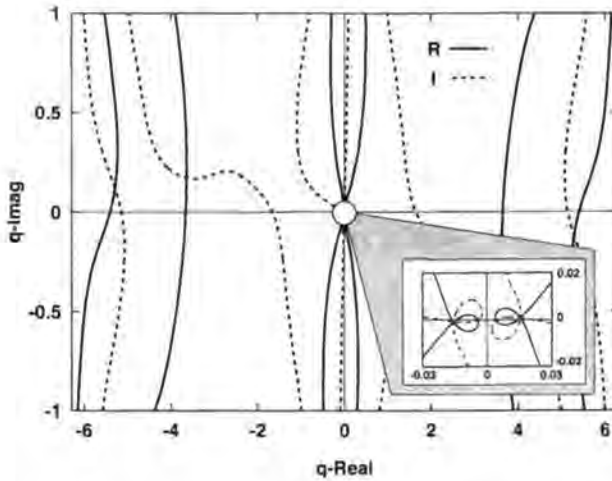
Figure 1: Zero-contours of real and imaginary part of the secular determinant at $\hbar\omega = 2.0eV$.

The first step in the dipole calculation is to obtain the normal modes. Fig. (1) shows the roots q_m of the secular determinant (7), at the intersections of the zero-contours of its real and imaginary parts. The figure has inversion symmetry and is periodic along the real axis, with period $2\pi/s_3 \cdot \mathbf{n}$. The search can be restricted along the imaginary axis to some suitably chosen cutoff value for the damping. Very close to the origin (see inset) 4 solutions are found almost coinciding with the Fresnel values in addition to the two poles at $\pm k_z$. But there are also 4 other solutions for which damping is too small to be ignored. Since for surface calculations only modes with positive imaginary part are physically acceptable, we included 4 normal modes in the calculation.

We have examined in some detail the behaviour of the extra (non-Fresnel) normal modes. For very low frequencies the extra normal modes are exactly at the boundary of the Brillouin zone, but have enough damping to be ignored. Starting from 1.1 eV two definitely different extra normal modes move from the zone boundary towards the imaginary axis. They start as being perfectly transparent, one being purely transverse ($\mathbf{u} \cdot \mathbf{k}_m = 0$), the other having also a strong longitudinal component ($\mathbf{u} \cdot \mathbf{k}_m \neq 0$). So this mode has to affect also the bulk behaviour. All modes start to show a nonzero imaginary component starting from the bandgap at 1.5 eV. The extra modes preserve their transverse/longitudinal character, but they continue to move towards the imaginary axis, meanwhile getting more and more absorbing. Their influence can be discarded above 2.6 eV.

The extra normal modes are indispensible for the optical properties, both of surface and bulk. Good surface optical results require close to perfect matching of dipole strength's between surface and normal mode region. For $\hbar\omega = 1.9eV$ we show in fig. (2) the individual dipole strength's for polarization parallel to the $(1\bar{1}0)$ direction. The dipole strength varies clearly from a Ga to an As site, a variation controlled already by the Fresnel-type of normal mode. But there is also a weak modulation in dipole strength of both the Ga and As sites. This modulation extends further than the depth of the surface layer (indicated by the arrow),
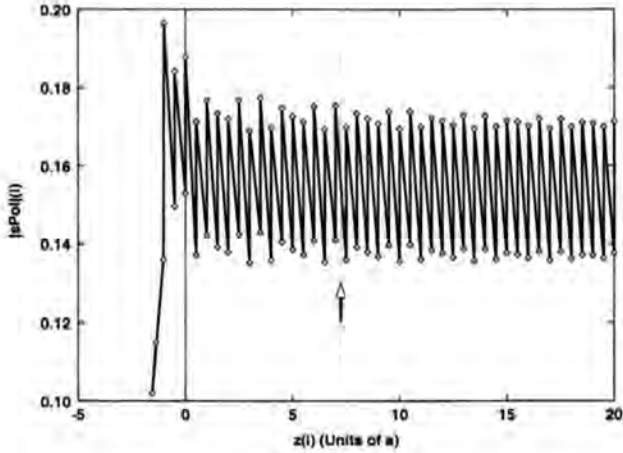
Figure 2: *Modulus* $|\mathbf{p}_i|$ *for* $\phi = 0°$ *at* $\hbar\omega = 1.9\,eV$.

	Expt	LDA	f_{LDA}	GW	f_{GW}	DsC	f_{DsC}
P_1 (max)	0.00142	——	——	0.0019	1.34	0.00100	0.70
S (max)	0.00522	0.0045	0.86	0.0044	0.84	0.00525	1.01
P_2 (max)	0.00656	0.0103	1.57	0.0141	2.15	0.00561	0.86
E_0' (max)	0.00569	0.0117	2.05	0.0144	2.53	0.00502	0.88
E_1 (min)	0.00131	-0.004	-3.05	-0.0022	-1.68	0.00314	2.40
E_2' (min)	0.00067	0.0013	1.94	0.0044	6.57	0.00269	4.01

Table 1: Anisotropic reflectances $\Delta R/R$. LDA- and GW-type results from [16], DsC-type present results. Experimental data from [17]. f-factor = Theory/Experiment

into the bulk normal mode region, but almost vanishes at the right of the figure. This is the influence of the extra normal modes. Artificial removal of these modes stronlgy affects the anisotropic reflectance.

Reflectance anisotropy spectra have been measured recently very accurately by Esser et al. [17]. We have calculated the theoretical reflectance anisotropy for GaAs (110), using the previously outlined discrete cellular (DsC) method and used the convention

$$\Delta R/R = (\Delta R/R)_{[1\bar{1}0]} - (\Delta R/R)_{[001]}. \tag{9}$$

Results of experiment and calculation are shown in table 1, comparing our results and the ones obtained by Pulci et al. [16]. We have used a background subtraction (bulk terminated GaAs) to account for the calibration of the experimental setup. The selected peak heights and minima have been labelled as in [16], but two prominent maxima have been labelled by us (P_1 at 1.7 eV and P_2 at 3.4 eV). The intensities of the three main maxima (S, P_2 and E_0') are much better replicated by the DsC method, than by the continuum method used

in [16]. Also the negative value for the minimum at E_1 is positive in the DsC approach in agreement with experiment. The other features are too weak to be conclusive. Although the DsC calculations use a conventional energy shift of 0.40 eV for the *bulk*, the comparison with experiment suggests an additional shift of -0.3 eV for the *surface*. This means that the surface contribution is almost LDA-like. Pulci et al. found an additional surface shift of +0.3 eV. We emphasize that our results are ab-initio, except for the scissors energy shift and the self term f_{ii} in (5), which have been tuned using bulk optical data.

The calculated DsC spectra have the right sign and magnitude and reproduce remarkably well the spectral structure. In that aspect DsC-type of calculations are superior to LDA/GW schemes of calculation. It is our conclusion that the good agreement of the present calculations with experiment is sufficiently demonstrated. As such the main statement of this paper, that inclusion of (real space) local field effects in surface optics requires explicit inclusion of nonlocality in the polarizabilities. This conclusion should hold in general for the optics of inhomogeneous systems.

References

[1] J. Pastrnak, K. Vedam. Phys. Rev. B 3(1971) 2567
[2] C.M.J. Wijers, G.P.M. Poppe. Phys. Rev. B 46(1992) 7605
[3] G.P.M. Poppe, C.M.J. Wijers, A. van Silfhout. Phys. Rev. B 44(1991) 7917
[4] O. Litzman, P. Rósza. Surf. Sci. 66(1977) 542
[5] P.P. Ewald. On the foundations of crystal optics Air Force Cambridge Research Laboratories publication AFCRL-70-0580 (1970)
[6] H. Fearn, D.F.V. James, P.W. Milonni. Am. J. Phys. 64(1996) 986
[7] T.D. Visser, P.S. Carney, E. Wolf. Physics Letters A 249(1998) 243
[8] C.M.J. Wijers, R. Del Sole, F. Manghi. Phys. Rev. B 44(1991)
[9] W.L. Mochán, R.G. Barrera. Phys. Rev. Lett. 55(1985) 1192
[10] Z.H. Levine and D.C. Allen. Phys. Rev. B 44(1991) 12781
[11] Z.H. Levine and D.C. Allen. Phys. Rev. B 48(1993) 14768(E)
[12] Z.H. Levine. Phys. Rev. B 49(1994) 4532
[13] G. te Velde, E.J. Baerends. Phys. Rev. B 44(1991) 7888
[14] G. te Velde, E.J. Baerends. J. Comp. Phys. 99(1992) 84
[15] C. Eckl, J. Fritsch, P. Pavone, U. Schröder. Surface Science 394(1997) 47
[16] O. Pulci, G. Onida, R. Del Sole, L. Reining. Phys. Rev. Lett. 81(1998) 5374
[17] N. Esser, R. Hunger, J. Rumberg, W. Richter, R. Delsole, A.I. Shkrebtii. Surf. Sci. 309(1994) 1045

Author's address

C.M.J. Wijers:
Faculty of Applied Science,
Twente University,
P.O. Box 217, 7500 AE Enschede,
The Netherlands;

P.L. de Boeij:
Departement of Chemical Physics,
University of Groningen,
Nijenborgh 4, 9747 AG Groningen,
The Netherlands.

Part IV

Cavity QED

H. Mack, S. Meneghini, and W.P. Schleich

Atom Optics and the Discreteness of Photons

Abstract

The deflection of atoms in a quantized light field brings out the granular structure of the photon field.

1 The Marriage of Atom Optics and Cavity QED

In the year 1933 P.L. Kapitza and P.A.M. Dirac calculated the deflection of an electron from a standing light wave [1]. They found a cross section too small to be measured experimentally in the near future:

> "We see, therefore, that the experiment could scarcely be made with ordinary continuous sources of light, and it seems to us that the only possibility would be to produce the illumination by using an intense spark discharge instead of a mercury arc."

Indeed, only recently experiments with ultra short pulses from high power lasers have provided the first indirect evidence of this phenomenon [2].

The reason for the smallness of this effect lies in the absence of the internal structure of the electron and, in particular, in the absence of a resonant enhancement. In contrast, atoms have internal structures and we can have a resonance between the frequencies of an atomic transition and of the light field. (See, for example, [3, 4]). This has led to the pioneering experiments by Moskowitz *et al.* [5] observing the deflection of atoms due to a laser field. Here, the center of mass motion of the atom is treated quantum mechanically and the atom displays wave features. This has suggested the name *atom optics* for this field. In the meantime interferometers, mirrors and cavities for atoms have been realized experimentally. (For a review we refer to [6, 7, 8, 9, 10]. This field has blossomed over the last years and many interesting branches of atom optics have developed. Space does not allow us to elaborate more on the physics of Bose-Einstein condensates or atom optics as a testing ground of quantum chaos [11] nor can we but mention atom optics as a tool for nanotechnology [12].

Another exciting field of quantum optics is the area of cavity QED. The development of high-Q cavities for microwave fields in combination with Rydberg atoms has lead to unique light sources such as the micromaser. Moreover, the use of gyroscope mirrors has resulted in high-Q cavities in the optical regime.

It is therefore an interesting enterprise to combine both fields and consider atom optics in quantized light fields [13, 14]. In particular, we can consider the deflection of atoms from

a quantized light field [15, 16]. This phenomenon allows us to measure the photon statistics and the discreteness of the electromagnetic field [17, 18, 19, 20].

A hundred years ago M. Planck proposed the quantization of the energy of a material harmonic oscillator in order to derive the correct black body radiation law [21]. In the context of the micromaser Rempe *et al.* [22] showed by measuring quantum revivals [23] that the maser field consists of discrete photons. Recently, Brune *et al.* [24] has used the time evolution of an atom in a high-Q cavity to prove the discreteness of the photon field. Moreover, Varcoe *et al.* [25] have realized for the first time in a controlled way Planck oscillators, that is electromagnetic fields of one or two photons. Despite this impressive progress, it is still interesting to see the granular structure of photons in a direct way. The deflection of atoms is such a method.

In this context it is interesting to note that the Paris group has made a similar suggestion using the whispering gallery mode of a microcavity [26]. However, no experiment has been made so far. In contrast, K.A.H. van Leeuwen reports in these proceedings the first experiments on the way towards the deflection of atoms from a quantum field (see also [27]).

Our paper is organized as follows. We first briefly summarize our model. We then derive the generalized Rabi equations for the probability amplitudes describing the state vector of the total system consisting of the center of mass motion, internal states of the atom and the states of the electromagnetic field. We reduce the problem to a one-dimensional scattering problem and solve the resulting equations in the Raman-Nath approximation. This allows us to obtain analytical expressions for the momentum distribution of the scattered atoms.

We consider various scattering situations: In the joint measurement scheme we make use of the entanglement between the center of mass motion and the cavity field. Here, we only retain those atoms that have not changed the phase of the field. This allows us a perfect read out of the photon statistics of the cavity field without extracting the field. (For a deflection experiment, making use of the entanglement between the center of mass motion and internal states see [28].

In the averaged momentum distribution we ignore the information contained in the field since we do not measure the field. Therefore the momentum distribution does not contain the full information about the initial photon statistics of the field. However, there are still some imprints of the field statistics left. In both cases we consider the so-called Kapitza-Dirac regime in which the initial wave packet is broad compared to the period of the standing wave.

The other extreme is the so-called Stern-Gerlach regime. Here the width of the wave packet is small compared to the period of the grating provided by the light field. The name originates from the analogy to the deflection of atoms in an inhomogeneous magnetic field [29].

In order to focus on the main ideas we do not present detailed derivations but still give enough steps to follow the calculations. For more information we refer to the literature.

2 Formulation of the Problem

Throughout this article we consider the scattering situation shown in Fig. 1. An atomic wave of a two-level atom with dipole moment $\wp$ propagates through a resonator and interacts res-

standing light field
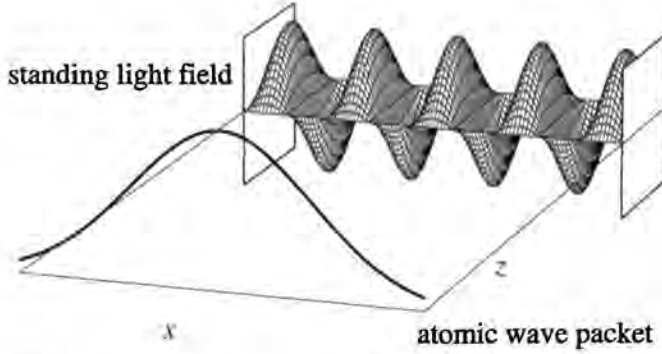
x

z

atomic wave packet

Figure 1: An atomic wave propagates through a cavity and interacts resonantly with a single mode of the standing light field. Here we consider the case where the atomic wave packet covers many wavelengths of the light field. The atomic wave packet is a plane wave in z-direction. Therefore we only show a cut through the probability distribution for one value of z.

onantly with a single mode of the radiation field. In the interaction picture the Hamiltonian for this process takes the form

$$\hat{H} = \frac{\hat{\mathbf{p}}^2}{2M} + \wp \cdot \mathbf{u}(\hat{\mathbf{p}}) \, \mathcal{E}_0 \left(\hat{\sigma} \mathbf{a}^\dagger + \hat{\sigma}^\dagger \mathbf{a} \right). \tag{1}$$

Here $\hat{\mathbf{p}}^2/(2M)$ describes the kinetic energy of the center of mass motion, $\mathbf{u}(\hat{\mathbf{p}})$ and $\mathcal{E}_0$ are the mode function at the position $\mathbf{r}$ of the atom and the vacuum electric field of this mode, respectively.

Since we are now treating the center of mass motion quantum mechanically the position $\mathbf{r}$ and the momentum $\mathbf{p}$ are conjugate operators and obey the commutation relation

$$[r_l, p_m] = i\hbar \delta_{lm}.$$

Moreover, $\mathbf{a}$ and $\mathbf{a}^\dagger$ denote the annihilation and creation operators of the field and the Pauli spin matrices $\hat{\sigma}$ and $\hat{\sigma}^\dagger$ destroy and create an atom in the excited state.

The dynamics of the state vector

$$|\Phi(t)\rangle = \sum_{m=0}^{\infty} \int d^3r' \left[\Phi_{a,m-1}(\mathbf{r}',t)|a, m-1\rangle + \Phi_{b,m}(\mathbf{r}',t)|b,m\rangle \right] |\mathbf{r}'\rangle, \tag{2}$$

describing the combined system of center of mass motion, internal states of the atom and the states of the electromagnetic field follows from the Schrödinger equation

$$i\hbar \frac{\partial |\Phi\rangle}{\partial t} = \hat{H} |\Phi\rangle. \tag{3}$$

Here $\Phi_{a,m-1}(\mathbf{r},t)$ or $\Phi_{b,m}(\mathbf{r},t)$ denote the probability amplitudes to find the atom at time t and position $\mathbf{r}$ and in the internal state $|a\rangle$ with $m-1$ photons in the field or in the internal state $|b\rangle$ with m photons in the field, respectively.

When we substitute this ansatz into the Schrödinger equation (3) we find with the Hamiltonian (1) the generalized Rabi equations

$$i\hbar \frac{\partial \Phi_{a,n-1}(\mathbf{r},t)}{\partial t} = \frac{\hat{\mathbf{p}}^2}{2M} \Phi_{a,n-1}(\mathbf{r},t) + \wp \cdot \mathbf{u}(\mathbf{r}) \, \mathcal{E}_0 \sqrt{n} \, \Phi_{b,n}(\mathbf{r},t) \tag{4}$$

and

$$i\hbar \frac{\partial \Phi_{b,n}(\mathbf{r},t)}{\partial t} = \frac{\hat{\mathbf{p}}^2}{2M} \Phi_{b,n}(\mathbf{r},t) + \wp \cdot \mathbf{u}(\mathbf{r}) \, \mathcal{E}_0 \sqrt{n} \, \Phi_{a,n-1}(\mathbf{r},t). \tag{5}$$

We can decouple these two equations by introducing the linear combinations

$$\Phi_n^{(\pm)} \equiv \Phi_{b,n} \pm \Phi_{a,n-1}. \tag{6}$$

In this case the generalized Rabi equations read

$$i\hbar \frac{\partial \Phi_n^{(\pm)}(\mathbf{r},t)}{\partial t} = \left[\frac{\hat{\mathbf{p}}^2}{2M} + U_n^{(\pm)}(\mathbf{r}) \right] \Phi_n^{(\pm)}(\mathbf{r},t) \tag{7}$$

where we have introduced the potentials

$$U_n^{(\pm)}(\mathbf{r}) \equiv \pm \wp \cdot \mathbf{u}(\mathbf{r}) \, \mathcal{E}_0 \sqrt{n}. \tag{8}$$

Hence the probability amplitudes $\Phi_n^{(\pm)}$ satisfy a Schrödinger equation corresponding to a particle of mass M moving in a potential $U_n^{(\pm)}$. This potential is formed by the scalar product of the dipole moment $\wp$ and the mode function $\mathbf{u}(\mathbf{r})$. Moreover, it scales with the vacuum electric field strength $\mathcal{E}_0$ and the square root of the photon number. Since the nodes of the potential are independent of the photon number and the amplitude of the modulation in space is proportional to $\sqrt{n}$, the potentials $U_n^{(\pm)}$ get steeper as n increases. The potential $U_n^{(-)}$ is just the negative of $U_n^{(+)}$.

The initial condition for $|\Phi\rangle$ at time $t = 0$, that is, before the interaction, is a direct product

$$|\Phi(t=0)\rangle = |b\rangle \otimes \sum_{n=0}^{\infty} \psi_n |n\rangle \otimes \int d^3 r' \, \mathcal{F}(\mathbf{r}') |\mathbf{r}'\rangle$$

of the atomic state which we take to be the ground state, the field state in a superposition of photon number states with probability amplitudes ψ_n and the initial distribution $\mathcal{F}$ of the atom in space.

When we compare this initial condition with the ansatz Eq. (2) we find

$$\Phi_n^{(\pm)}(\mathbf{r},0) = \mathcal{F}(\mathbf{r}) \, \psi_n. \tag{9}$$

Hence the dynamics of the state vector $|\Phi\rangle$ of the combined system follows from the dynamics of the wave functions $\Phi_n^{(\pm)}$ moving in the potentials $U_n^{(\pm)}$ subject to the initial condition Eq. (9). Note that since in general the potential is three-dimensional and can be rather complicated it is a non-trivial task to solve the Schrödinger equation (7) for $\Phi_n^{(\pm)}$.

3 Reduction to One-Dimensional Scattering

We now consider a situation in which the atomic beam propagates initially orthogonal to the wave vector of the field in the cavity. In the remainder of this article we call this the x-direction, or the transverse direction. The motion along the z-axis, that is the longitudinal motion, we treat classically since we assume that the initial kinetic energy $Mv_z^2/2$ in z-direction is much larger than the change of the longitudinal momentum due to the interaction with the light field.

In this case the equations reduce to a one-dimensional Schrödinger equation of the form

$$i\hbar \frac{\partial \Psi_n^{(\pm)}(x,t)}{\partial t} = \left[\frac{\hat{p}_x^2}{2M} \pm \wp \mathcal{E}_0 \sqrt{n} \, \sin(\pi v_z t/L_z) \sin(kx) \right] \Psi_n^{(\pm)}(x,t). \tag{10}$$

Here we have also assumed for the sake of simplicity the specific mode function

$$\mathbf{u}(\mathbf{r}) = \mathbf{e}_y \sin(kx) \sin(\pi z/L_z)$$

of a box-shaped resonator of length L_z in the z-direction. Moreover, k denotes the wave number along the x-axis and $\wp \equiv \boldsymbol{\wp} \cdot \mathbf{e}_y$.

We have therefore reduced the three-dimensional scattering problem to the problem of solving a one-dimensional time dependent Schrödinger equation. We emphasize, however, that even this problem is non-trivial, since due to the motion of the atom through the resonator—the interaction switches on and switches off via the mode function $\sin(\pi v_z t/L_z)$— the potential is explicitly time dependent. Moreover, the potential in x-direction is periodic and can allow for rather complicated solutions.

4 State Vector in Raman-Nath Approximation

In the present discussion we confine ourselves to an approximate but analytical analysis of Eq. (10). For this purpose we recall that the atomic beam enters the resonator orthogonal to the wave vector of the electromagnetic field. Therefore its classical kinetic energy along the standing wave initially vanishes. Consequently the kinetic energy gained by the atom is due to the interaction with the light field. When the displacement caused by the electromagnetic field is smaller than its wavelength we can neglect the transverse kinetic energy term.

In this Raman-Nath approximation we can solve the Schrödinger equation (10) in an exact way and find

$$\begin{aligned} |\Psi(t)\rangle &= \sum_{n=0}^{\infty} \psi_n \int dx' \, f(x') \left\{ \cos[\kappa\sqrt{n} \, \sin(kx)]|b,n\rangle \right. \\ &\quad \left. -i \sin[\kappa\sqrt{n} \, \sin(kx)]|a,n-1\rangle \right\} |x'\rangle. \end{aligned} \tag{11}$$

Here we have introduced the dimensionless interaction parameter

$$\kappa \equiv \frac{2}{\pi} \frac{\wp \mathcal{E}_0}{\hbar} \tau.$$

We note that the position dependent interaction of the atom with the quantized light field has created a strong entanglement between the transverse motion, the field and the energy levels of the atom.

In order to discuss the momentum transfer from the electromagnetic field to the atom we express the state vector

$$|\Psi(t)\rangle = \sum_{n=0}^{\infty} \psi_n \int dp' \left[c_n(p')|b,n\rangle - i s_n(p')|a,n-1\rangle \right] |p'\rangle \tag{12}$$

in the momentum representation where

$$c_n(p) \equiv \frac{1}{\sqrt{2\pi\hbar}} \int dx\, f(x) \cos\left[\kappa \sqrt{n} \sin(kx) \right] e^{-ipx/\hbar} \tag{13}$$

and

$$s_n(p) \equiv \frac{1}{\sqrt{2\pi\hbar}} \int dx\, f(x) \sin\left[\kappa \sqrt{n} \sin(kx) \right] e^{-ipx/\hbar}. \tag{14}$$

The state vector of the combined system allows us to answer questions concerning the momentum distribution of the scattered atoms, especially when we consider joint measurements between the transverse motion and the quantum field in the cavity.

5 Deflection of Atoms

In the present section we consider the deflection of the atom in the Raman-Nath approximation. In this regime the field does not displace the atom significantly but still changes the momentum.

One of the initial conditions in the scattering process is the transverse position amplitude $f(x)$ of the atoms. According to Eqs. (13) and (14) the probability amplitudes c_n and s_n for finding the momentum p are Fourier transforms of the product of the initial position amplitude $f(x)$ and trigonometric functions of the mode function $\sin(kx)$ of the electromagnetic field. We can therefore distinguish two characteristic cases for these Fourier integrals: *(i)* In the Kapitza-Dirac regime the initial position distribution $|f(x)|^2$ of the atoms is broad compared to the period of the standing wave, or *(ii)* in the Stern-Gerlach regime the distribution is narrow.

Throughout the paper we focus on the Kapitza-Dirac regime. However, we emphasize that the case of the Kapitza-Dirac scattering with a mask reduces in the limit of a single slit to the Stern-Gerlach regime.

5.1 Measurement Schemes

The three degrees of freedom of this quantum system, the center of mass motion, the field and the internal degrees of freedom are entangled. We can therefore make joint measurements of these variables. In principle we can use all three of them. However, in the present discussion we confine ourselves to the motion and the field only.

Joint Measurements

In this situation the atom traverses the cavity prepared in a given field state $|\psi_{\text{field}}\rangle$, interacts with it and as a consequence gets deflected. After the atom has left the cavity we observe the field and measure the momentum. We reprepare the complete atom-field system and repeat the experiment.

Quantum mechanics predicts the conditional probability distribution

$$W(p, |\tilde{\psi}_{\text{field}}\rangle) \equiv \frac{1}{W(|\tilde{\psi}_{\text{field}}\rangle)} \sum_{j=a,b} \left| \langle j | \langle p | \langle \tilde{\psi}_{\text{field}} | \Psi \rangle \right|^2$$

to find the momentum p given that the field is in the reference state

$$|\tilde{\psi}_{\text{field}}\rangle \equiv \sum_{n=0}^{\infty} \tilde{\psi}_n |n\rangle \tag{15}$$

and the probability that the vector $|\Psi\rangle$ contains this reference state reads

$$W(|\tilde{\psi}_{\text{field}}\rangle) \equiv \frac{1}{N} = \int_{\infty}^{\infty} p \sum_{j=a,b} \left| \langle j | \langle p | \langle \tilde{\psi}_{\text{field}} | \Psi \rangle \right|^2 .$$

Since we do not make a measurement of the internal states $|j\rangle = |a\rangle \text{or} |b\rangle$ we take the trace over them.

When we substitute the photon number representation Eq. (15) of the reference state into the above expression for W we find

$$W(p, |\tilde{\psi}_{\text{field}}\rangle) = N \sum_{j=a,b} \left| \sum_{n=0}^{\infty} \tilde{\psi}_n^* \langle j | \langle p | \langle n | \Psi \rangle \right|^2 , \tag{16}$$

and consequently the probability distribution originates from the coherent sum, that is the interference of many probability amplitudes.

We now make use of the explicit expression Eq. (12) for the state vector $|\Psi\rangle$ and the probability distribution reads

$$W(p, |\tilde{\psi}_{\text{field}}\rangle) = N \left\{ \left| \sum_{n=0}^{\infty} \tilde{\psi}_n^* \psi_n c_n(p) \right|^2 + \left| \sum_{n=0}^{\infty} \tilde{\psi}_n^* \psi_n s_n(p) \right|^2 \right\} . \tag{17}$$

Indeed, the two internal levels contribute in an incoherent way. In contrast, the field states represented by the probability amplitudes $\tilde{\psi}_n^*$ and ψ_n enter in a coherent way.

Averaged Measurements

We now consider a completely different experiment. The atom traverses the cavity and we only measure the momentum of the atom. We therefore ignore the change of the field due to

the atom. In this case we have to take the trace over the cavity state. When we use photon number states to perform this trace, the resulting probability reads

$$W(p) = \sum_{j=a,b} \sum_{n=0}^{\infty} |\langle j|\langle p|\langle n|\Psi\rangle|^2 .$$

In contrast to Eq. (16) here we first square and then take the sum. The resulting probability distribution therefore originates from an incoherent sum, that is a sum of probabilities.

When we substitute the explicit representation Eq. (12) of the state vector into the above expression for the averaged momentum distribution we arrive at

$$W(p) = \sum_{n=0}^{\infty} |\psi_n|^2 \left[|c_n(p)|^2 + |s_n(p)|^2 \right] . \tag{18}$$

Indeed, here we only sum probabilities.

5.2 Kapitza-Dirac Regime

We now consider the case where the initial atomic position distribution of width L reaches over N periods λ of the standing wave. For the sake of simplicity we assume it to be constant.

Momentum Quantization

In this case we can evaluate the amplitudes c_n and s_n explicitly and find

$$c_n(p) = \frac{1}{\sqrt{\hbar k}} \delta_N^{(1/2)} \left[\frac{p}{\hbar k} \right] \frac{1}{2} \left[1 + (-1)^{p/(\hbar k)} \right] J_{p/(\hbar k)}(\kappa\sqrt{n}) \tag{19}$$

and analogously

$$s_n(p) = \frac{1}{\sqrt{\hbar k}} \delta_N^{(1/2)} \left[\frac{p}{\hbar k} \right] \frac{1}{2i} \left[1 - (-1)^{p/(\hbar k)} \right] J_{p/(\hbar k)}(\kappa\sqrt{n}). \tag{20}$$

We notice that the function

$$\delta_N^{(1/2)}(\xi) \equiv \frac{1}{\sqrt{N}} \sum_{\nu=0}^{N-1} \exp(-2\pi i \xi \nu)$$

is periodic and has maxima at integer values of ξ. Indeed, at these positions the phase factors are integer multiples of 2π and each term in the sum is unity giving the value $\sqrt{N}$ for the function $\delta_N^{(1/2)}$. Hence, as $N \to \infty$ the maxima of $\delta_N^{(1/2)}$ approach infinity. For non integer values ξ the individual terms cancel each other.

This behavior suggests that $\delta_N^{(1/2)}$ acts as a comb of δ-functions at integer values of ξ. However, we can show that only the square of $\delta_N^{(1/2)}$ displays this behavior. Since we are interested in momentum distributions and hence probabilities the function $\delta_N^{(1/2)}$ only appears as a square. The argument of $\delta_N^{(1/2)}$ is $p/(\hbar k)$. Consequently the momentum of the atom can take on only multiple integers of the momentum $\hbar k$.

We therefore find a quantization of the atomic momentum in multiples of the photon momentum. However, the association with the momentum of the light field is slightly misleading. This quantization does not arise from the quantization of the radiation field. It rather emerges from the periodicity of the potential, namely the mode function of the electromagnetic field.

Moreover, we recognize from Eqs. (19) and (20) that the probability amplitude $c_n(p)$ is only nonzero for even integer multiples of $\hbar k$. In contrast, $s_n(p)$ only takes on nonzero values for odd integer multiples of $\hbar k$. We recall that $c_n(p)$ and $s_n(p)$ are associated with the atom leaving the cavity in the ground or excited state, respectively when it has entered the cavity in the ground state. Therefore, in order to leave it in the ground state it has to undergo an even number of Rabi cycles and thus exchanges an even number of photon momenta. Likewise, an atom leaving in the excited state needs an odd number of momenta exchange in order to make the transition from its initial ground state. This is just another manifestation of the entanglement of the field variables with the momentum of the atom.

Momentum Distribution

We are now in a position to derive explicit expressions for the momentum distributions discussed in the preceding section. We start our analysis with the averaged momentum distribution, Eq. (18).

We can combine the contributions from the atoms leaving the cavity in the ground state or in the excited state coresponding to the probabilities $|c_n(p)|^2$ and $|s_n(p)|^2$ when we note that due to the special form Eqs. (19) and (20) of c_n and s_n the first sum only contains the even multiples of $\hbar k$ whereas the second contribution only contains the odd multiples. However, in both cases the probability is given by the square of the Bessel function. Hence, we arrive at

$$W(p) = \sum_{\wp=-\infty}^{\infty} \delta(p - \wp \hbar k) W_\wp \tag{21}$$

where we have introduced the dimensionless and discrete momentum distribution

$$W_\wp\left[|\psi_{\text{field}}\rangle\right] \equiv \sum_{n=0}^{\infty} W_n\left[|\psi_{\text{field}}\rangle\right] J_\wp^2(\kappa\sqrt{n}). \tag{22}$$

We note that this averaged momentum distribution $W_\wp$ involves only the photon statistics $W_n \equiv |\psi_n|^2$ of the cavity field. In particular, it does not bring in the probability amplitudes ψ_n. In Figs. 2, 3 and 4 we depict the averaged momentum distributions for a number state $|n\rangle$, a coherent state $|\alpha\rangle$ and a highly squeezed state $|\psi_{sq}\rangle$ in the cavity. All three momentum distributions are different. For the number state we find oscillations and a dominant maximum at $\wp = \kappa\sqrt{n}$. The oscillations are very reminiscent of the Franck-Condon oscillations in molecules. Indeed, we can show, that both oscillations have a common origin: Interference in phase space. For the coherent and the squeezed state the oscillations for small momenta have been averaged out but the dominant maximum at $p = \kappa\sqrt{\bar{n}}$ remains. Moreover, for the case of the squeezed state we note, that the oscillatory photon statistics manifests itself in the decay of the right side of the maximum.
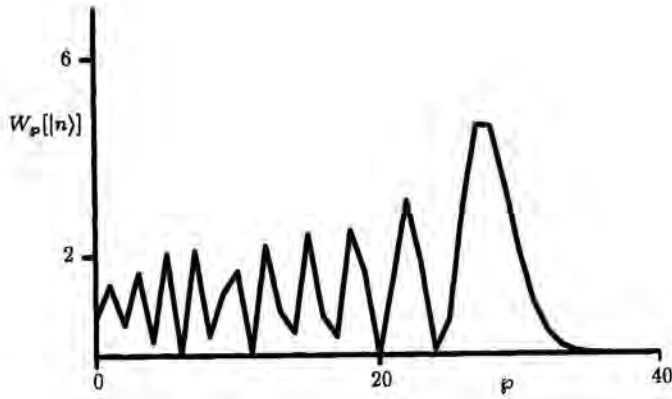
Figure 2: Momentum distribution of atoms scattered off a single mode of a cavity field in a number state $n = \bar{n} = 9$ photons for an interaction parameter $\kappa = 10$. The distribution shows a dominant peak at $\wp = \kappa\sqrt{\bar{n}} = 30$ and a strong decay for momenta larger than this critical value. For $\wp$ smaller than $\kappa\sqrt{\bar{n}}$ the distribution is oscillatory. These oscillations result from quantum interference of translational motion. The envelope follows the classical cross section.

Joint Measurements

We now turn to the case of a joint measurement between the momentum of the atom and the field. When we substitute the explicit expressions Eqs. (19) and (20) for s_n and c_n into the expression for the joint momentum distribution Eq. (17) we arrive at

$$W\left[p, |\bar{\psi}_{\text{field}}\rangle\right] = \sum_{\wp=-\infty}^{\infty} \delta(p - \wp\hbar k) W_{\wp}(|\bar{\psi}_{\text{field}}\rangle, |\psi_{\text{field}}\rangle) \tag{23}$$

where we have introduced the dimensionless and discrete momentum distribution

$$W_{\wp}\left[|\bar{\psi}_{\text{field}}\rangle, |\psi_{\text{field}}\rangle\right] \equiv \frac{1}{W(|\bar{\psi}_{\text{field}}\rangle)} \left| \sum_{n=0}^{\infty} \bar{\psi}_n^* \psi_n J_{\wp}(\kappa\sqrt{n}) \right|^2 \tag{24}$$

and

$$W(|\bar{\psi}_{\text{field}}\rangle) = \sum_{\wp=-\infty}^{\infty} \left| \sum_{n=0}^{\infty} \bar{\psi}_n^* \psi_n J_{\wp}(\kappa\sqrt{n}) \right|^2$$

denotes the probability to find the reference field state $|\bar{\psi}_{\text{field}}\rangle$ after the interaction.

Nowhere clearer than in the comparison between the averaged and the joint momentum distributions $W_{\wp}[|\psi_{\text{field}}\rangle]$ and $W_{\wp}\left[|\bar{\psi}_{\text{field}}\rangle, |\psi_{\text{field}}\rangle\right]$ do we recognize the power of entanglement: In the averaged distribution we sum the squares of Bessel functions. In the joint distribution we first sum the Bessel functions and then square the result. Since the Bessel functions oscillate between positive and negative values cancellations can occur in the summation over Bessel functions. No such cancellation arises in the averaged distribution.

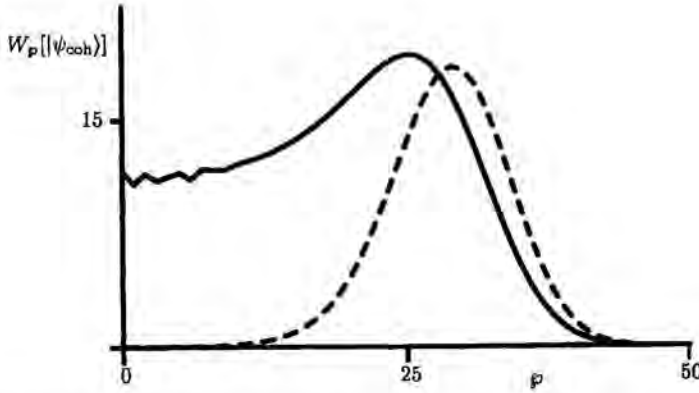Atom Optics and the Discreteness of Photons

Figure 3: Influence of the photon distribution of a coherent state of average number of photons $\bar{n} = 9$ on the momentum distribution. The Poissonian photon distribution (dashed curve) creates a smooth momentum distribution. The maximum of W_n governs the maximum of W_p. The right edge of W_n controls the right edge of W_p.

Bessel functions enjoy a dominant maximum when the index is equal to the argument. When we assume that the product $\tilde{\psi}_n^* \psi_n$ is slowly varying on the scale of the oscillations in the Bessel function the main contribution to the sum arises for $\wp = \kappa \sqrt{n}$, that is $n = (\wp/\kappa)^2$. This yields the approximate expression

$$W_\wp \left[|\tilde{\psi}_{\text{field}}\rangle, |\psi_{\text{field}}\rangle \right] \cong \mathcal{N} W_{n=(\wp/\kappa)^2}$$

where $\mathcal{N}$ denotes a normalization constant.

This expression clearly shows that in this case the joint momentum distribution follows precisely the photon statistics of the field state in the cavity. This is very different from the case of the averaged momentum distribution where we have to average the photon statistics with respect to the square of the Bessel function.

We illustrate this for the example of a highly squeezed state as the initial state in the cavity and a phase state

$$|\tilde{\psi}_{\text{field}}\rangle \equiv |\varphi = 0\rangle \equiv \frac{1}{\sqrt{2\pi}} \sum_{n=0}^{\infty} |n\rangle$$

as a reference state. We note, that this reference state satisfies the requirement that the product $\tilde{\psi}_n^* w_n$ is slowly varying since $\tilde{\psi}_n^* = const$. Indeed, we find that the momentum distribution follows precisely the oscillatory photon statistics.

In this context it is interesting to understand why there is such a close connection between the momentum and photon distributions. We note, that this is not true if the reference state is a single photon number state or, likewise, if the initial field state is a photon number state. In both cases the summation over the photon number states reduces to a single term and the cancellation due to the oscillatory behavior of the Bessel function does not occur. We
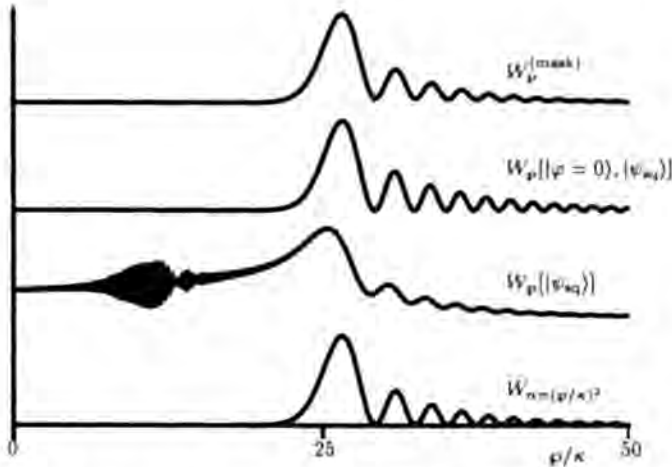
Figure 4: The photon statistics of a squeezed, displaced state of squeezing parameter $s = 50$ and displacement parameter $\alpha = 10$ (lower curve) and its read out via the momentum distribution of deflected atoms. The curve $W_p([|\varphi = 0\rangle, |\psi_{sq}\rangle])$ corresponds to a joint measurement of the atomic momentum and the field phase whereas the distribution $W_p[|\psi_{sq}\rangle]$ ignores the field phase. The top curve $W_p^{(mask)}$ gives the momentum distribution of atoms filtered by a mask of slit width $d = \lambda/10$ placed at the nodes of the standing wave. The joint measurement strategy gives an adequate readout while ignoring the field phase results in a less effective readout as well as in additional rapid oscillations. We note that there is a modulation on the left side of the first maximum of $W_p[|\varphi = 0\rangle, |\psi_{sq}\rangle]$ and the period of the oscillations is slightly different from W_n. Here we have chosen $\kappa = 110$.

obviously need an initial and a reference field state that have broad photon distributions. In the case of the squeezed state and the phase state this condition is satisfied.

There is a simple explanation for this phenomenon of exact read out of photon statistics from momentum statistics. Since we are performing joint measurements, we are selecting from our ensemble very specific atoms. The squeezed state we have choosen has a phase distribution that is centered around the origin. Likewise, the phase state corresponds to the phase $\varphi = 0$. Hence, the joint measurement selects atoms that have not changed the phase of the field. These are the atoms that have traversed the cavity at the nodes where the electric field vanishes. However, at the nodes the gradient of the field is nonzero. Consequently the atoms obtain a momentum. The steepness of the gradient depends on the photon number and therefore the momentum transfer depends on the photon number. Since photon numbers are discrete the momentum transfer is discrete. Moreover, the probability for a given deflection angle is determined by the probability to find the corresponding electric field gradient, that is to find the corresponding photon number. Hence, there is a one-to-one correspondence between the momentum distribution and the photon number distribution.

Atom Optics and the Discreteness of Photons

5.3 Kapitza-Dirac Scattering with a Mask

In the preceding section we have found that a joint measurement selecting only those atoms that pass the resonator at the nodes provides a perfect readout of the photon statistics. This suggests to replace the joint measurement strategy by a simple mask with narrow slits around the nodes of the field. These slits are then separated by half of the period λ of the standing wave and have to be narrower than $\lambda/2$. In the optical regime it is impossible to obtain such mechanical slits. However, it is possible to obtain such a grating by using an extra light field and absorption.

We therefore assume a DeBroglie wave

$$f(x) = \frac{1}{\sqrt{N}} \sum_{\nu=0}^{N-1} g(x - \nu\lambda/2), \tag{25}$$

that is a coherent superposition of N Gaussian wave packets $g(x)$ located at the nodes of the field and with a width $d \ll \lambda/2$. The case of a single narrow wave packet corresponds to the Stern-Gerlach regime.

We substitute this form $f(x)$ of the DeBroglie wave into the definition Eqs. (13) and (14) of $c_n(p)$ and $s_n(p)$ and perform the integration. Here we make use of the fact that the slits are much narrower than the period, that is $dk = 2\pi d/\lambda \ll 1$. This allows us to linearize the sine function and we can immediately perform the remaining Gauss integrals. We arrive at

$$c_n(p) = \delta_N^{(1/2)} \left[\frac{p}{2\hbar k} \right] \frac{1}{2} \left[\widetilde{g}(p - \kappa\sqrt{n}\hbar k) + \widetilde{g}(p + \kappa\sqrt{n}\hbar k) \right]$$

where $\widetilde{g}(p)$ is a Gaussian in momentum space of width $\Delta p \equiv \hbar/d$.

We first note that the period $\lambda/2$ of the grating instead of λ as in the first example has produced a discreteness of the scattered momenta of integer multiples of $2\hbar k$ rather than $\hbar k$. Moreover, we note that the initial momentum distribution $\widetilde{g}$ gets displaced to momenta $\pm\kappa\sqrt{n}\hbar k$. Hence, every number state in the cavity gives rise to a momentum transfer by $\pm\kappa\sqrt{n}\hbar k$. When the width Δp of the initial momentum distribution is smaller than the separation

$$\delta p \equiv \kappa(\sqrt{n+1} - \sqrt{n})\hbar k \cong \frac{\kappa}{2\sqrt{n}}\hbar k$$

of neighboring momentum peaks caused by neighboring number states the discreteness of the number states manifests itself in discrete peaks in the momentum distribution of the deflected atoms.

Similarly we find the probability amplitude

$$s_n(p) = \delta_N^{(1/2)} \left[\frac{p}{2\hbar k} - \frac{1}{2} \right] \frac{1}{2i} \left[\widetilde{g}(p - \kappa\sqrt{n}\hbar k) - \widetilde{g}(p + \kappa\sqrt{n}\hbar k) \right].$$

We note that the antisymmetry of the sine function together with the period $\lambda/2$ has created odd integer multiples of $\hbar k$.

When we substitute these expressions for c_n and s_n into the formula Eq. (18) for the averaged momentum distribution we arrive at

$$W(p) = \sum_{\wp=-\infty}^{\infty} \delta(p - \wp\hbar k) W_\wp^{(\text{mask})}$$

where

$$W_{\wp}^{(\text{mask})} \left[|\psi_{\text{field}}\rangle \right] \equiv \sum_{n=0}^{\infty} W_n \left[|\psi_{\text{field}}\rangle \right] \frac{1}{2} \left[W(\wp - \kappa\sqrt{n}) + W(\wp + \kappa\sqrt{n}) \right].$$

Here $W(p) \equiv |\widetilde{g}(p)|^2$ is the initial momentum distribution.

According to this result the momentum is again quantized in units of $\hbar k$. This is a manifestation of the coherence of the initial atomic distribution Eq. (25) over many periods of the standing wave. Moreover, the distribution consists of symmetrically located copies of the initial momentum distribution $W(p)$. They are located at $\wp = \pm\sqrt{n}\kappa$. The envelope of these peaks is the photon statistics W_n of the cavity field.

6   Acknowledgement

References

[1] P.L. Kapitza, P.A.M. Dirac. Proc. Camb. Philos. Soc. 29(1933) 297–300
[2] P.H. Bucksbaum, D.W. Schumacher, M. Bashkansky. Phys. Rev. Lett. 61(1988) 1182–1185
[3] A.F. Bernhardt, B.W. Shore. Phys. Rev. A 23(1981) 1290–1301
[4] R.J. Cook, A.F. Bernhardt. Phys. Rev. A 18(1987) 2533–2537
[5] P.E. Moskowitz, P.L. Gould, S.R. Atlas, D.E. Pritchard. Phys. Rev. Lett. 51(1983) 370–373
[6] C.S. Adams, M Sigel, J. Mlynek. Phys. Rep. 240(1994) 143–210
[7] E. Arimondo, H.-A. Bachor. J. Quant. Semicl. Opt. 8(1996) 495
[8] P.R. Berman. In *Advances in Atomic, Molecular, and Optical Physics*. Academic Press, Boston (1996).
[9] A.P Kazantsev, G.I. Surdutovich, V.P. Yakovlev. In *Mechanical Action of Light on Atoms*. World Scientific, Singapore (1990).
[10] J. Mlynek, V. Balykin, P. Meystre. Appl. Phys. B 54(1992)
[11] M.G. Raizen. In B. Bederson, H. Walther, editors, *Advances in Atomic, Molecular and Optical Physics*, volume 41, pages 43–81. Academic Press, Boston (1998).
[12] Meneghini *et al.* to be published (2000)
[13] A.M. Herkommer, W.P. Schleich. Comments At. Mol. Phys. 33(1997) 145–157
[14] M. Freyberger, A.M. Herkommer, D.S. Krähmer, E. Mayr, W.P. Schleich. In B. Bederson, H. Walther, editors, *Advances in Atomic and Molecular Physics*, volume 41, pages 143–180. Academic Press, Boston (1999).
[15] P. Meystre, E. Schumacher, S. Stenholm. Opt. Commun. 73(1989) 443–447
[16] P. Meystre, E. Schumacher, E.M. Wright. Ann. Physik (Leipzig) 48(1991) 141–148
[17] V.M. Akulin, Fam Le Kien, W.P. Schleich. Phys. Rev. A 44(1991) R1462–R1465
[18] A. Herkommer, V.M. Akulin, W.P. Schleich. Phys. Rev. Lett. 69(1992) 3298–3301
[19] I.Sh. Averbukh, V.M. Akulin, W.P. Schleich. Phys. Rev. Lett. 72(1994) 437–441

[20] E. Mayr, D. Krähmer, A.M. Herkommer, V.M. Akulin, W.P. Schleich, I.Sh. Averbukh. Acta Phys. Pol. A 86(1994) 81–95

[21] M. Planck. In *Vorlesungen über die Theorie der Wärmestrahlung.* J.A. Barth, Leipzig (1906).

[22] G. Rempe, H. Walther, N. Klein. Phys. Rev. Lett. 58(1987) 353–356

[23] J.H. Eberly, N.B. Narozhny, J.J. Sanchez-Mondragon. Phys. Rev. Lett. 44(1980) 1323–1326

[24] M. Brune, F. Schmidt-Kaler, A. Maali, J. Dreyer, E. Hagley, J.M. Raimond, S. Haroche. Phys. Rev. Lett. 76(1996) 1800–1803

[25] B.T.H. Varcoe, S. Brattke, M. Weidinger, H. Walther. Nature 403(2000) 743–746

[26] F. Treussart, J. Hare, L. Collot, V. Lefèvre, D.S. Weiss, V. Sandoghdar, J.M. Raimond, S. Haroche. Opt. Lett. 19(1994) 1651–1653

[27] R.M.S. Knops, A.E.A. Koolen, H.C.W. Beijerinck, K.A.H. van Leeuwen. Laser Phys. 9(1999) 286–292

[28] S. Kunze, K. Dieckmann, G. Rempe. Phys. Rev. Lett. 78(1997) 2038–2041

[29] W. Gerlach, O. Stern. Z. Physik 9(1922) 349–352

Author's address

Abteilung für Quantenphysik,
Universität Ulm,
89069 Ulm,
Germany

J.M. Raimond

Atoms and Cavities:
Fundamental Quantum Mechanics Studies

Abstract

Circular Rydberg atoms in a superconducting cavity make it possible to realize a situation very close to the ideal one of a two–level atom interacting with a single field mode. The coherent coupling of the atom with the mode overwhelms couplings to the environment causing dissipation, an exceptional situation in optics. This prototype system can be used to test our understanding of intimate features of the quantum world, such as entanglement and non-locality.

1 Introduction

Quantum optics techniques make it now possible to work on isolated quantum systems and to realize some of the gedankenexperiments used by the founders of quantum mechanics to assess their interpretation of the formalism. The most intimate features of the quantum world, such as entanglement and non–locality are directly accessible. Besides their fundamental interest, these situations could be used to implement new types of quantum information processing functions [1]. Quantum non–locality is at the heart of the quantum cryptography techniques [2, 3], allowing to share secure information. More complex information processing systems, involving entangled states of many qubits (two-level systems used as information carriers) have also been proposed [4].

Rydberg atom–microwave cavity–QED experiments [5] realize an ideal situation where two–level atoms are coupled, one after the other, with a single field mode containing a few photons in a well–defined quantum state. This textbook situation makes it possible to demonstrate fundamental light–matter interaction effects and to perform various tests of quantum theory. The quantum Rabi nutation [6], resulting from the resonant coupling of the atom with the cavity mode, produces or processes entangled atoms–cavity states. A complete control of the transformations applied to a string of atoms crossing successively the cavity allows us to engineer complex entangled states and to perform elementary quantum information processing operations.

We recall briefly the main components of the experimental set–up. We describe then the quantum Rabi nutation and recent experiments on entangled states: generation of an EPR pair of atoms [7], quantum non demolition detection of a single photon [8], preliminary evidences of three–atoms entangled states.
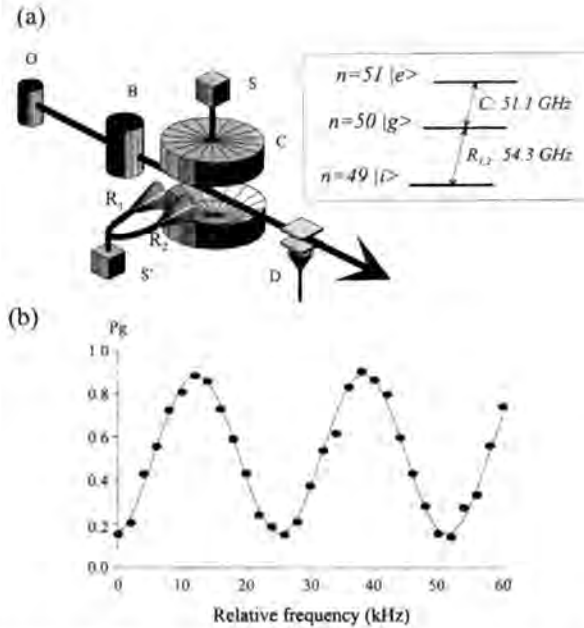
Figure 1: (a) Scheme of the Rydberg atom–cavity experiment. Relevant energy levels in the insert. (b) Typical Ramsey fringes signal on the $g \to i$ transition.

2   The cavity–QED set–up

The general scheme of our experiments [6, 7, 8, 9, 10] is depicted in Fig. 1(a). Rubidium atoms effusing from oven O are promoted to circular Rydberg states in region B [11]. These states, with a high principal quantum number n and maximum orbital and magnetic quantum numbers, combine a great lifetime (30 ms for $n = 50$) and an extremely strong coupling to the millimeter-wave radiation, with an efficient state-selective detection by field ionization. The atoms are velocity–selected by laser optical pumping and prepared at a given time. Their position is known at any time within ± 1 mm. This precise control of the timing is essential to apply selective transformations to successive atoms crossing the apparatus. In order to operate with single atoms, we prepare much less than one (0.2) atom on the average in each sample. When one atom is detected, the probability of an unwanted two–atoms event is low enough.

The atoms interact with the superconducting cavity C, made of two niobium mirrors in a Fabry Perot configuration. It is close to resonance with the transition between circular states $n = 51$ (e in the following) and $n = 50$ (g) at 51.1 GHz. The gaussian mode has a $w = 6$ mm waist. The cavity damping time (single photon lifetime) reaches values up to 1 ms. This is much longer than the typical atom–cavity interaction time, about 20 μs.

A small electric field is applied across the mirrors to stabilize the anisotropic circular states orbit. The same field can be used to Stark–shift the atomic line in and out of resonance, enabling us to control precisely the effective atom–cavity interaction time. The atoms are

finally detected in the state–selective field–ionization detector D (efficiency about 40%).

Before they interact with the cavity mode, the atoms can be prepared in a state superposition by a classical microwave pulse R_1, resonant either on the $e \to g$ transition or on the transition from g to i (circular state $n = 49$) at 54.3 GHz. The three relevant energy levels e, g and i are shown in the inset of Fig. 1(a). After C and before D, the atomic superposition may be probed by another pulse R_2 driven by the same source S' as R_1. These two interactions with S' realize a Ramsey interferometer [12]. An atom prepared in g and detected in i, for instance, may undergo the transition either in R_1 or in R_2. Two indistinguishable quantum paths lead to the same final quantum state and thus interfere. When scanning the frequency ν of S', the probability of detecting the atom in g or i oscillates. Typical experimental "Ramsey fringes" are represented in figure 1(b). They provide a very sensitive probe of the atom–cavity interaction, as well as a convenient handle to tailor atom–cavity entangled states.

The whole set–up is cooled to 0.6 or 1.3 K by a Helium cryostat. Residual thermal fields or photons left by a previous experimental sequence can be removed by a "photon erasing" procedure [8]. A few samples with 3 to 9 atoms in level g are sent through C before the experimental sequence. They efficiently absorb any residual field in C. The complete experiment (timing, velocity selection, Ramsey pulses timing and frequencies, detection) are under full computer control.

3   Quantum Rabi nutation

The basic tool for entanglement processing is the quantum Rabi nutation [6] of a single atom in an empty cavity. This oscillation between the coupled levels $|e, 0\rangle$ and $|g, 1\rangle$ (atom in e in an empty cavity or atom in g with one photon) is an oscillatory spontaneous emission process, typical of the strong coupling regime of cavity–QED. In order to observe it, we send atoms prepared in e and detect their final state after they have crossed C. The Ramsey zones are not active in this case. We repeat the experiment many times, for various atom–cavity interaction times t, and reconstruct the probability $P_e(t)$ to detect the atom in e downstream. Figure 2 shows the vacuum Rabi oscillation signal obtained when C is initially empty. The Rabi frequency $\Omega/2\pi$ is 47 kHz, which corresponds to a period of about 20 μs, shorter than the cavity and atomic damping times. The damping of the observed oscillations is due to various perturbations (inhomogeneous electric and magnetic fields in C, variation of the Rabi coupling across the transverse profile of the atomic beam, effect of residual thermal fields...). The arrows in the figure indicate three important interaction times, corresponding to $\pi/2$, π and 2π Rabi pulses.

If the $\Omega t = \pi/2$ condition is satisfied, the atom–cavity system ideally ends up in the maximally entangled state:

$$|\Psi_{\pi/2}\rangle = (1/\sqrt{2})(|e, 0\rangle + |g, 1\rangle) \tag{1}$$

where the first and the second symbol in each ket represent the atom state and the photon number, respectively. For $\Omega t = \pi$ the system, initially in state $|e, 0\rangle$, ends up in $|g, 1\rangle$: the atom and the field exchange with unit probability their excitation. We have used this process
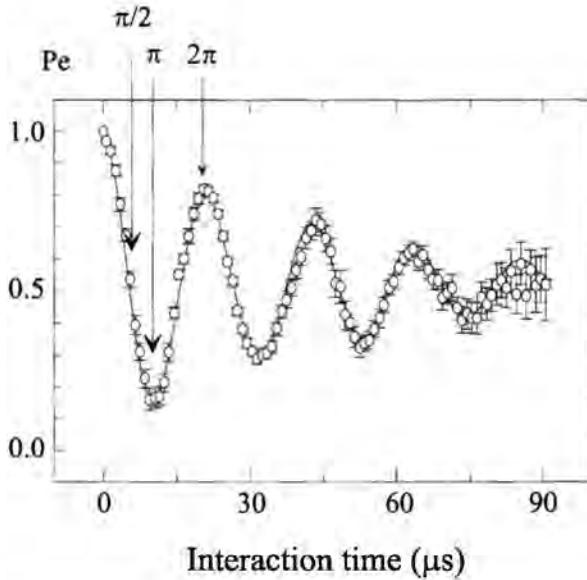
Figure 2: Quantum Rabi oscillation on the $e \to g$ transition.

to generate a single photon Fock state in the cavity and to demonstrate the operation of a quantum memory [10].

When $\Omega t = 2\pi$, the atom undergoes a full Rabi cycle of absorption and emission and the field comes back in the initial state. Such complete Rabi cycles play an essential role in the physics of micromaser trapping states [13]. Let us focus here on a subtle effect of this 2π pulse: after its completion, the atom–cavity quantum state has undergone a π–phase shift, $|e, 0\rangle \xrightarrow{2\pi} -|e, 0\rangle$. In the same way, if the atom–cavity system starts in state $|g, 1\rangle$, it becomes $-|g, 1\rangle$ after a 2π Rabi pulse. Note that $|g, 0\rangle$ is not affected by the coupling: this phase shift, analogous to the sign change of the wave function of a spin $1/2$ undergoing a 2π rotation [14, 15], is conditioned to the presence of one photon in the cavity. It has been used to perform the non–destructive detection of a single photon.

The $\pi/2$, π and 2π Rabi pulses are the basic bricks used in the following experiments to build complex entangled states.

4   Generation of an EPR pair of atoms

The basic entanglement processing features of the quantum Rabi nutation can be used to prepare an entangled pair of atoms [7] of the EPR type [16]. The first atom undergoes in the cavity a $\pi/2$ Rabi pulse, preparing the atom–cavity entangled state described by Eq. (1). Since the cavity field cannot be detected, this entanglement cannot be directly revealed. We thus "copy" the state of the cavity onto a second atom. This atom, prepared in g, undergoes a π Rabi pulse in the field of one photon. It absorbs with unit probability the photon left by

Atoms and Cavities: Fundamental Quantum Mechanics Studies

the first atom. The atoms are then in the entangled state $(1/\sqrt{2})(|e_1, g_2\rangle - |g_1, e_2\rangle)$, equivalent to a singlet state for the two fictitious spins 1/2 associated with the atomic transitions. The cavity ends up empty, playing the role of a catalyst for the entanglement of the two atoms.

An essential feature of the singlet state is that the projections of the two spins along an arbitrary axis are always anti–correlated. This basis–independent correlation, which cannot be explained in classical terms, is at the heart of the EPR paradox. We have first tested the energy correlation (equivalent to a detection of the spin along the z axis). We have also studied the correlations along an arbitrary axis in the xOy plane. Measurements along this axis are performed with a $\pi/2$ pulse R_2, resonant on the $e \rightarrow g$ transition, equivalent to a spin rotation, followed by an energy measurement. The detection of the first atom creates, through the quantum correlations at a distance (1.5 cm), an e/g coherence in the second atom. This coherence is analyzed later by another R_2 pulse. We thus obtain Ramsey fringes, where the two pulses are applied to different atoms, after their common interaction with the cavity mode. The coherence is transferred between the atoms via the non–local quantum correlations.

Analyzing the imperfections of the set–up, we determined that an EPR pair is prepared in about 65% of the two–atoms experimental sequences. Some improvements would be required to increase this figure of merit to the point where tests of Bell's inequalities would become possible. Note that, at variance with most previous experiments, we prepare a pair of entangled matter particles instead of a pair of photons. Moreover, this preparation is completely deterministic, since all the weights and phases of the final state are under control.

5 Measuring a single photon without destroying it

The conditional π phase shift undergone by level g in the field of one photon during a 2π Rabi pulse can be used to detect the presence of this single photon without absorbing it [8]. Such an absorption–free detection amounts to a Quantum Non Demolition measurement [17] of the field intensity, restricted to the subspace spanned by the zero and one photon states (single photon QND or SP–QND). Many optical intensity Quantum Non Demolition measurements have been realized [18]. They rely on the coupling between two light beams (a "signal" and a "meter") in a non-linear crystal. Based on non-linear effects, they operate only on beams with macroscopic photon fluxes. The huge coupling of Rydberg atoms with the field makes it possible to detect in a QND way a single photon.

We record Ramsey fringes on the $g \rightarrow i$ transition, while the cavity, on resonance with the $e \rightarrow g$ transition, contains 0 or 1 photon. The atom, initially in level g, has a velocity of 503 m/s, corresponding to the 2π Rabi pulse condition. If there is 1 photon in C, we expect the probability amplitude associated with the atom entering C in level g to be π–phase shifted with respect to the zero photon case, resulting in a Ramsey fringes inversion: the fringe maxima at zero photon become minima for one photon in C. For such ν values, the state of the outgoing atom is directly correlated to the presence of the photon.

In order to observe this effect, we first send a "source" atom across C to generate a single photon. It undergoes a $\pi/2$ pulse in C (R_1 and R_2 are off). The reduction of the effective atom–field interaction time needed to fulfill the $\pi/2$ pulse condition is obtained by using the Stark tuning method described above (all atoms have the same 503 m/s velocity). The
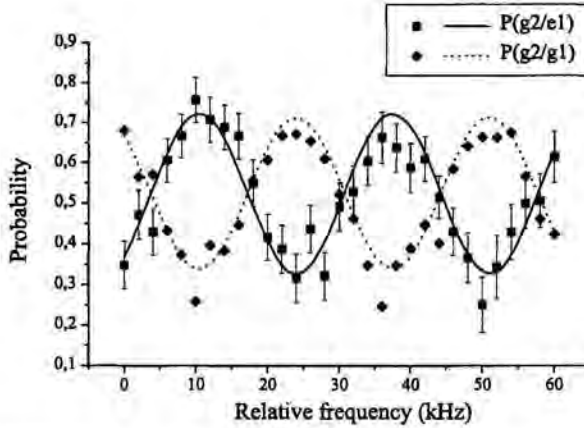
Figure 3: Ramsey fringes on the $g \to i$ transition conditioned on the source atom state. Setting the interferometer frequency at a fringe extremum provides a SP–QND measurement.

source atom + field system ends up in the state described by Eq. (1). Detecting the source atom in e (g) thus projects the field to the 0 (1) photon state. We then send the "meter" atom across the interferometer. Here, the Ramsey fields are switched on and the $\Omega t = 2\pi$ condition is restored. We repeat the sequence many times and register, as a function of ν, the correlations between the outcomes of the source and the meter detection signals. Figure 3 shows the conditional probabilities $P(g_2/e_1)$ (squares) and $P(g_2/g_1)$ (diamonds) for finding the meter in g, provided the source has been found in e and g respectively. Ideally, $P(g_2/e_1)$ and $P(g_2/g_1)$ are equal to the conditional probabilities $P(g/0)$ and $P(g/1)$ for finding the meter in g if there is 0 or 1 photon in C.

We clearly observe two sets of fringes with opposite phases. The signal contrast is reduced below 100% by known imperfections of our apparatus (limited contrast of the Ramsey and Rabi pulses, residual thermal fields...). The lines in Fig. 3 are results of numerical simulations taking these imperfections into account. By setting the interferometer to a fringe extremum, we have a maximum correlation between the atom output (g or i) and the photon number (0 or 1).

An additional experiment showed that the photon is not destroyed during this measurement process. We have measured again the field after this first "QND" measurement. We have observed that the probability for finding a photon in C in the second measurement is considerably increased when the meter atom has already determined that C contains one photon (ideally, this probability should be one, as required by the projection postulate). The fact that the measurement by the meter atom leaves a photon with a great probability in C after detecting it is a clear indication of the non–destructive nature of the meter–field interaction.

This resonant method does not apply to larger fields since the Rabi angle becomes $\Omega t \sqrt{N} = 2\pi \sqrt{N}$ for N photons, which makes it impossible to suppress photon absorption for arbitrary photon numbers. It is therefore non–destructive only in the subspace spanned by the zero and one photon states. We proposed, however, an unrestricted QND scheme which

consists in slightly detuning the cavity frequency and the $|e\rangle \to |g\rangle$ transition (atom–cavity detuning δ) [19]. Photon absorption can be thereby almost completely suppressed. In that case, the AC–Stark effect results in a phase shift of the atomic coherence equal to $\Omega^2 t N / 4\delta$ (n being the photon number) that could again be measured by Ramsey interferometry. We plan to demonstrate this method in the future.

6 A conditional phase gate with a photon and an atom

The photon and the atom in these experiments can be viewed as quantum bits (qubits) which carry binary information and which interact in the cavity following conditional dynamics. Applying this terminology, the resonant 2π Rabi pulse is a quantum phase gate (QPG) [20, 21], which transforms the four combined photon–atom states according to the simple rule: $|0, i\rangle \to |0, i\rangle$, $|0, g\rangle \to |0, g\rangle$, $|1, i\rangle \to |1, i\rangle$, $|1, g\rangle \to e^{i\phi}|1, g\rangle$, with $\phi = \pi$. This gate, combined with unitary rotations acting on each qubit, can produce any unitary two–qubit operation. For example, with the Ramsey interferometer, we perform $\pi/2$ rotations on the atomic qubit before and after the QPG. The resulting SP–QND measurement obeys to the conditional dynamics of a controlled–not (C–NOT) gate [22]. Such gates have already been demonstrated on other simple systems [23, 24].

The phase ϕ of the cavity–QED QPG is equal to π when the cavity mode and the $e \to g$ atomic transition are exactly resonant. However, we can adjust ϕ to any value by tuning the difference δ between the cavity and the $e \to g$ transition frequencies, while leaving the atom–cavity interaction time set to the value corresponding to a 2π Rabi pulse at resonance. If the atom is initially in g with 1 photon in C, numerical simulations show that the tip of the Bloch vector representing the $|1, g\rangle$, $|e, 0\rangle$ system evolves on an almost closed trajectory on the Bloch sphere and ends up in the initial state, after having undergone a phase shift which varies between 0 and 2π when δ is swept across 0. The theoretical residual absorption rate is below 3% for all detuning values. At resonance, photon absorption is forbidden by the 2π pulse condition or by energy conservation far from resonance. Finally, for intermediate δ values, the slow variation of the atom–field coupling during cavity mode crossing plays an important role to keep the absorption rate low. Note that this theoretical absorption could be avoided by slightly adjusting the atomic velocity for each δ value.

To demonstrate the phase–tuning of the QPG, we have measured, for various detunings δ, the relative phase–shift between levels i and g when C contains 0 or 1 photon prepared by a first source atom. The phase difference between the same conditional fringes as in Fig. 3 when the source atom is in e (0 photon) or in g (1 photon) directly yields ϕ. Figure 4 shows the measured phase shift as a function of δ (experimental points), along with the corresponding theoretical curve. The agreement between experiment and theory is very good. The measured residual absorption rate, of the order of 20%, is well understood when taking into account the presence of a residual thermal field in C.

The QPG is symmetrical. The photon in state 1 can be viewed either as the control qubit which produces a phase shift of the atom in state g or, conversely, the atom in g is the control qubit which dephases the 1 photon state. The QPG properties are verified by comparing the atom or field qubit state phases to each other after the gate operation. The Ramsey interferometer, which mixes g and i, provides a way to compare the phases of the atomic
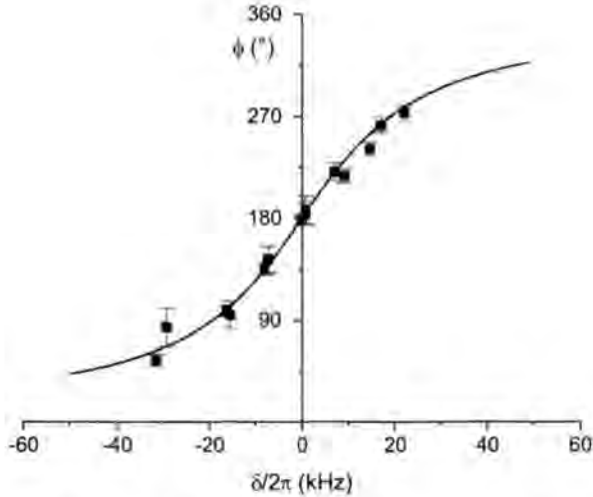
Figure 4: Conditional phase–shift of the QPG as a function of the atom–cavity detuning

levels. In order to make a field phase measurement, we prepare and probe in the cavity a superposition of 0 and 1 photon states. Such states, of the form $C_0|0\rangle + C_1|1\rangle$, are, to a very good approximation, produced by injecting, with the source S, a very small coherent field in C, with an average photon number much smaller than 1. After the gate operation, a "homodyning" field is injected in C and the resulting field is absorbed with a probe atom. This phase measurement shows that our QPG gate operates in a symmetrical and coherent way, creating and preserving qubit entanglement throughout the two–qubit evolution. We note that a QPG based on somewhat different principles has already been demonstrated in an optical cavity–QED experiment [21]. The present QPG has a wider ϕ–tuning range and exhibits directly qubit entanglement.

7   Three atoms entanglement

We have combined our SP-QND scheme with the preparation of an EPR pair of atoms to produce an entangled state of three atoms [25, 26]. A first atom enters the empty cavity in state e and undergoes a $\pi/2$ Rabi rotation, preparing the entangled atom-cavity state of Eq. (1). A second atom then performs a SP-QND detection of the field left in C. Being coherent, this process entangles the second atom and the cavity. We thus get an entangled state of the form $(|e_1, i_2, 0\rangle + |g_1, g_2, 1\rangle)/\sqrt{2}$, assuming that the SP-QND is set so that i corresponds to zero photon and g to one. Finally, a third atom, prepared in g, undergoes a π Rabi pulse in one photon. Its state copies the state of C as well its entanglement with the other two atoms. The cavity ends up empty, and the three atoms are in the state $(|e_1, i_2, g_3\rangle - |g_1, g_2, e_3\rangle)/\sqrt{2}$. This is a triplet of entangled systems of the Greenberger Horne and Zeilinger type. Such triplets could be used to get a vivid demonstration of the non–local properties of quantum mechanics. At least in principle, a single measurement could vindicate
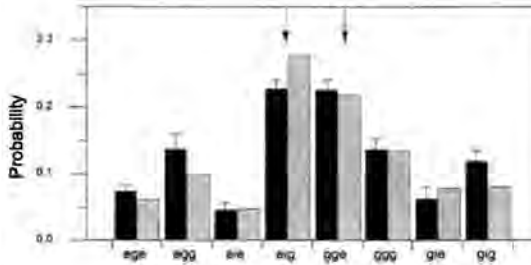
Figure 5: Histograms displaying energy correlations of the three detected atoms; in black: experiment, in grey: numerical simulation

quantum mechanics against the "local" hidden variables theories [25].

As for the EPR pair, we have checked the produced state by two kinds of experiments. We have first checked that the energy states of the three atoms are correlated in the predicted way. Figure 5 presents (dark bars) the probabilities of detection of the eight possible energy configurations. The two expected ones $(e, i, g$ and $g, g, e)$ clearly dominate the other channels filled by spurious effects. The gray bars present a simulation of the experiment taking into account the known experimental imperfections. The analysis of the results show that we prepare the required state in about 50% of the cases. We have also checked the correlations of "transverse" atomic observables, using the Ramsey pulse R_2 to analyze the fictitious spins $1/2$ along a direction in the xOy plane.

8 Conclusion

The Rydberg atom–cavity experiment is now a mature system to test fundamental quantum behaviors. The quantum Rabi nutation [6] provides us with tools to generate complex entangled states of a string of atoms. The methods described above to generate triplets of entangled atoms could in principle be generalized to larger number of atoms. The non-resonant, dispersive, atom–cavity interaction provides other tools. It can be used first to perform an unrestricted QND measurement of the cavity field intensity [19] applicable to arbitrary photon numbers. In the same conditions, it leads to a direct measurement of the cavity field Wigner function at any point in the phase space [27]. More importantly, it allows the quantum control of the phase of a mesoscopic coherent field stored in the cavity. It is possible to generate, through this interaction, quantum mesoscopic superposition states, reminiscent of the famous Schrödinger cat, and to study the dynamics of their decoherence due to cavity damping [9]. We are planning experiments with two microwave cavities, aiming at the preparation of non–local mesoscopic quantum states [28]. Studies of the decoherence of such complex mesoscopic entangled states could lead to a better understanding of the subtle quantum/classical boundary.

References

[1] D.P. DiVicenzo. Science 270(1995) 255
[2] A. Ekert. Phys. Rev. Lett. 67(1991) 661
[3] C.H. Bennett. Phys. Rev. Lett. 68(1992) 3121
[4] A. Ekert, R. Josza. Rev. Mod. Phys. 68(1997) 3733
[5] S. Haroche, J.M. Raimond. In P. Berman, editors, *Cavity Quantum electrodynamics*, page 123. Academic Press, (1994).
[6] M. Brune, F. Schmidt-Kaler, A. Maali, J. Dreyer, E. Hagley, J.M. Raimond, S. Haroche. Phys. Rev. Lett. 76(1996) 1800
[7] E.Hagley, X. Matre, G. Nogues, C. Wunderlich, M. Brune, J.M. Raimond, S. Haroche. Phys. Rev. Lett. 79(1997) 1
[8] G. Nogues, A. Rauschenbeutel, S. Osnaghi, M. Brune, J.M. Raimond, S. Haroche. Nature 400(1999) 239
[9] M. Brune, E. Hagley, J. Dreyer, X. Matre, A. Maali, C. Wunderlich, J.M. Raimond, S. Haroche. Phys. Rev. Lett. 77(1996) 4887
[10] X. Maître, E. Hagley, G. Nogues, C. Wunderlich, P. Goy, M. Brune, J.M. Raimond, S. Haroche. Phys. Rev. Lett. 79(1997) 769
[11] P. Nussenzveig, F. Bernardot, M. Brune, J. Hare, J.M. Raimond, S. Haroche, W. Gawlik. Phys. Rev. A 48(1993) 3991
[12] N.F. Ramsey. *Molecular beams.* Oxford Univ. Press, N.Y. (1985)
[13] M. Weidinger, B.T.H. Varcoe, R. Heerlein, H. Walther. Phys. Rev. Lett. 82(1999) 3795
[14] H. Rauch *et al.* Phys. Lett. A 54(1975) 425
[15] S.A. Werner *et al.* Phys. Rev. Lett. 35(1975) 1053
[16] A. Einstein, B. Podolski, N. Rosen. Phys. Rev. 47(1935) 777
[17] V.B. Braginsky, F.Y. Khalili. *Quantum measurement.* Cambridge Univ. Press. (1992)
[18] P. Grangier, J.A. Levenson, J.P. Poizat. Nature 396(1998) 537
[19] M. Brune, S. Haroche, V. Lefevre, J.M. Raimond, N. Zagury. Phys. Rev. Lett. 65(1990) 976
[20] S. Lloyd. Phys. Rev. Lett. 75(1995) 346
[21] Q.A. Turchette, C.J. Hood, W. Lange, H. Mabuchi, H.J. Kimble. Phys. Rev. Lett. 75(1995) 4710
[22] A. Barenco, D. Deutsch, A. Ekert, R. Jozsa. Phys. Rev. Lett. 74(1995) 4083
[23] C. Monroe, D.M. Meekhof, B.E. King, W.M. Itano, D.J. Wineland. Phys. Rev. Lett. 75(1995) 4714
[24] N.A. Gershenfeld, I.L. Chuang. Science 275(1997) 350
[25] D.M. Greenberger, M.A. Horne, A. Shimony, A. Zeitlinger. Am. J. Phys. 58(1990) 1131
[26] S. Haroche. Ann. N.Y. Acad. Sci. 755(1995) 73
[27] L.G. Lutterbach, L. Davidovich. Phys. Rev. Lett. 78(1997) 2547
[28] L. Davidovich, A. Maali, M. Brune, J.M. Raimond, S. Haroche. Phys. Rev. Lett. 71(1993) 2360

Author's address

Labatoire Kastler Brossel,
ENS,
24, rue Lhomond, 75231 Paris Cedex 05,
France.

K.A.H. van Leeuwen, A.E.A. Koolen, M.J. de Koning, H.C.W. Beijerinck and W.P. Schleich

Quantum Optics with Metastable Helium Atoms

Abstract

We have constructed a setup which produces a highly collimated, monochromatic (single axial velocity) and intense beam of metastable helium atoms. This beam can, for many purposes, be considered as a plane, monochromatic atomic wave. It is the highest resolution atomic beam diffraction setup presently available and will be used for a variety of experiments in the field of quantum optics and cavity QED, as well as for atom optics and atom interferometry experiments. One of these experiments is the direct demonstration of the quantization of the electromagnetic field in a high-finesse optical cavity. Another experiment entails the construction of a true single-atom laser. The setup has been tested by studying Bragg scattering of the atoms by a (classical) standing light wave. This has resulted in an adjustable coherent atomic beamsplitter which leads to true macroscopic ($> 10 \, \text{mm}$) separation between the split halves of the atomic wavepackets on the detector.

1 Single-atom cavity QED

In single-atom cavity quantum-electrodynamics (SC-QED) the interaction of a single atom with the quantized radiation field in a cavity is studied. Conceptually, this constitutes perhaps the simplest system in the field of quantum optics. This simplicity is also the strength of this research field. It allows comparisons between theory and experiments to be made on a very basic level. Often, these experiments are of the kind which have formerly only been considered as "thought experiments". They allow us to illustrate and check assumptions on fundamental subjects such as quantum measurement and entanglement. Thus, it is not surprising that SC-QED has often stimulated discussions on the interpretation of quantum mechanics. However, SC-QED has also been the primary instigator of the recent upsurge in interest in the field of quantum computing. Thus, this very fundamental field in physics may have a large impact on applications - albeit in the long term.

Even in this simple system, a variety of subjects can be studied. The atom can be used simply as a probe for the electromagnetic field in the cavity, studying field properties such as photon number statistics [1]. To use the atom as a probe, either the internal electronic state or the external motional state of the atom may be used.

By preparing the atom in an excited state before it interacts with the cavity, it can also be used as the *source* of the field in the cavity. This is exploited in single-atom laser [2, 3] and −maser [4, 5, 6] experiments.

In experiments on, e.g., optical bistability of a cavity the atom is used as a field *modifier*.

In these experiments, the transmission of light through the cavity is studied. The fact that the resonant frequency of the cavity is changed by the presence of atoms in the cavity leads to the bistability [7].

Finally, the delicate entanglement between the quantized field state and the state of the atom can be explored in experiments in the field of "quantum information" [8, 9, 10, 11].

2   Experimental approaches

Connected to the variety of subjects to be studied, also a variety of experimental approaches is used. In "traditional" cavity QED experiments, atoms in a thermal atomic beam interact with the cavity field. Thus, the atoms are relatively fast ($500 - 2000\,\mathrm{m/s}$) and the interaction time of each individual atom with the field correspondingly short. In one approach, microwave cavities are used [4, 5, 6, 12, 13]. Superconducting microwave cavities can have a very high quality factor, leading to photon storage times much longer than the interaction time. This is very important for quantum information type experiments, where the information is not supposed to "leak out" during the experiment. Other advantages are that the spontaneous decay of the atomic Rydberg states used to interact with the microwaves can be neglected, and that the interaction strength is very large. Therefore, the strong coupling limit is easily achieved and a simple Jaynes-Cummings model can be used. A disadvantage of the microwave regime is that individual microwave photons cannot be detected. Also, the effect of the field on the motion of the atom cannot be studied due to the small recoil momentum of the microwave photons. Thus, the only source of atomic information which can be used is the electronic state.

With optical cavities, these two disadvantages do not exist. Both the deflection of the atoms by the cavity field and the light transmitted through or emitted by the cavity can be detected [2, 3, 7]. Unfortunately, the strong coupling limit is much more difficult to achieve and the maximum quality factor (or finesse in optical terminology) of optical cavities is limited to $\approx 10^6$. Consequently, the photon storage time of the cavity is generally on the order of the interaction time or shorter.

A new category of cavity QED experiments uses slow atoms, increasing the interaction time. Atoms can be launched or dropped from a magneto-optic trap [14, 15] or can even be trapped *inside* the cavity [16] to obtain essentially infinite interaction times. Future possibilities include using the beam from an atom laser or trapping a Bose-Einstein condensate inside a cavity, thus making the transition from single-atom cavity QED to coherent multi-atom cavity QED.

3   Time scale ordering

The choice for using fast or slow atoms depends on the requirements imposed by the specific subject to be studied. These requirements can generally be expressed in terms of four different rates (or time scales) characterizing the experiment:

- g Vacuum Rabi frequency

- Γ_{cavity} Cavity decay rate

- Γ_{atom} Spontaneous emission rate

- $\Gamma_{transit}$ Inverse of interaction time

All cavity QED experiments should ideally be performed in the strong-coupling limit, defined by $g \gg \Gamma_{atom}, \Gamma_{cavity}$. However, the place which $\Gamma_{transit}$ should have in the time scale ordering (and hence the choice for slow or fast atoms) depends on what is studied. For slow or trapped atoms, $\Gamma_{transit} \ll \Gamma_{atom}, \Gamma_{cavity}$. The decay of the upper electronic state and the decay of the field in the cavity during the measurement time cannot be neglected. Experiments with slow atoms are ideal to study the stationary state of the atom-light system in the cavity (e.g., in cavity transmission and for single-atom lasers).

For "fast" atoms and high-finesse cavities, the interaction time can be shorter than the photon storage time: $\Gamma_{transit} > \Gamma_{cavity}$. A steady state is not reached during the measurement. This allows experiments which take a "snapshot" of the field properties, such as photon number statistics analyzed via atomic diffraction measurements [1, 17, 18].

4   Eindhoven setup

In the framework of a research project on single-atom cavity QED and atom optics, we have constructed a setup optimized for experiments which use the diffraction of an atomic beam as the main source of information. The original motivation is a planned experiment on photon number measurement [18], which is still a primary experimental goal. This experiment also dictated the use of an atomic beam instead of trapped atoms. However, the setup is designed to function as an atomic beam facility for a variety of experiments, including research on single atom lasers and atomic interferometry.

In order to effectively use atomic diffraction as a source of information for cavity QED experiments, the choice for an optical cavity and for light atoms is natural, as the recoil velocity associated with the emission or absorption of a single photon should be large. We have chosen metastable helium atoms and a cavity resonant with the $2^3S_1 \rightarrow 2^3P_2$ optical two-level transition of helium, with a wavelength of 1083 nm. The recoil velocity is then 0.092 m/s.

The practical demands, which the setup has to satisfy, pose many difficulties to the design:
- The analysis of the diffraction of atoms by light fields requires the ability to detect changes in transverse momentum of the atom with a resolution smaller than the recoil momentum $\hbar k$ associated with the absorption or emission of a single photon with wavenumber k. In our case, this corresponds to a required resolution in transverse velocity of the atoms $\Delta v_T < 0.092$ m/s. For the photon number measurement scheme described in Ref. [18], Δv_T has to be an order of magnitude smaller. The initial spread in transverse velocity of the atoms in the beam has to be correspondingly small.
- To translate the deflection angle of an atom, as determined from the position at which the atom impacts on the detector, to a transverse velocity change, the axial velocity of the atom has to be known. This can be achieved by time-of-flight velocity measurements, or by producing a "monochromatic" (single axial velocity) atomic beam by an axial laser cooling technique such as "Zeeman slowing", which highly compresses the axial velocity distribution.
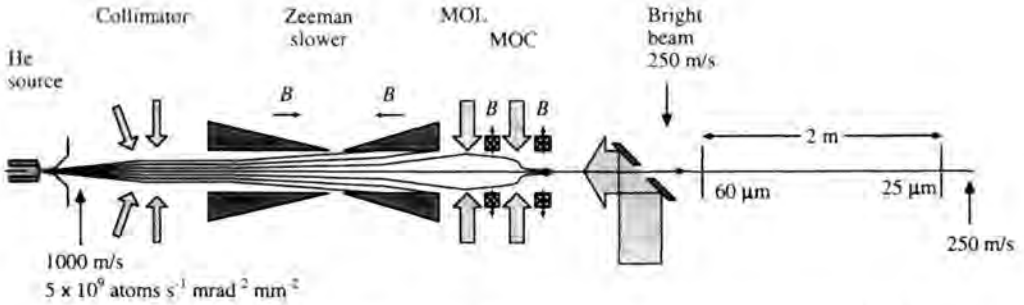
Figure 1: Overview of the helium beam line. The total length of the setup is 9.5 m.

• For a thermal helium beam (with an axial velocity $v_{ax} \approx 2000\,\text{m/s}$), the initial beam has to be collimated to an angular spread smaller than $5\,\mu$rad in order to achieve $\Delta v_T \leq 1\,\text{cm/s}$. The spatial detector resolution has to satisfy $\Delta x \leq 5\,\mu$m at a distance of 1 m from the interaction region. These are rather extreme demands. Slowing the atoms to a lower axial velocity increases the allowed angular spread and detector resolution proportionally. At an axial velocity of $250\,\text{m/s}$, the required angular spread of $40\,\mu$rad can be achieved by $50\,\mu$m apertures in the beam separated by $1.25\,\text{m}$, with a matching $50\,\mu$m detector resolution. Slowing may also be required in order to increase the interaction time of the atoms with the light field. Preferably, the axial velocity should be adjustable over a wide range in order to provide control over the interaction time.

• Perhaps trivial to state, but very difficult to realize in practice, is the demand that the collimated, single-axial-velocity atomic beam has sufficient flux to ensure a usable count rate in the experiments.

• For experiments with high-finesse optical cavities, maintaining a clean, hydrocarbon-free UHV environment is essential. At the present state-of-the-art, cavities with a finesse $\mathcal{F} \approx 10^6$ are used. These are constructed with mirrors that have a reflectivity around 0.999995. Any contamination by oil from, e.g., diffusion pumps or roughing pumps will quickly reduce the reflectivity and thus decrease the finesse.

• High-finesse cavities are also extremely sensitive to vibrations. In order to keep the cavity resonant with laser light used to excite a cavity mode, the distance d between the mirrors has to be stable to $\lambda/\mathcal{F}$. For the example above, this results in a required stability $\Delta d \leq 10^{-12}\,\text{m}$. Therefore care should be taken to avoid any source of vibration in the atomic beam setup that can excite cavity vibrations.

5   Implementation

The demands discussed above can be satisfied by making extensive use of laser cooling techniques to manipulate the atomic beam. A schematic view of the setup is shown in Fig. 1. Metastable 2^3S_1 helium atoms are produced in a liquid-nitrogen cooled discharge supersonic expansion source. A Zeeman-tuned laser decelerator is used to reduce the axial velocity of the atoms to a single, adjustable value from 50 to $500\,\text{m/s}$. At $250\,\text{m/s}$, the root-mean-square (rms) spread in axial velocity is $1.4\,\%$. The final collimation is achieved
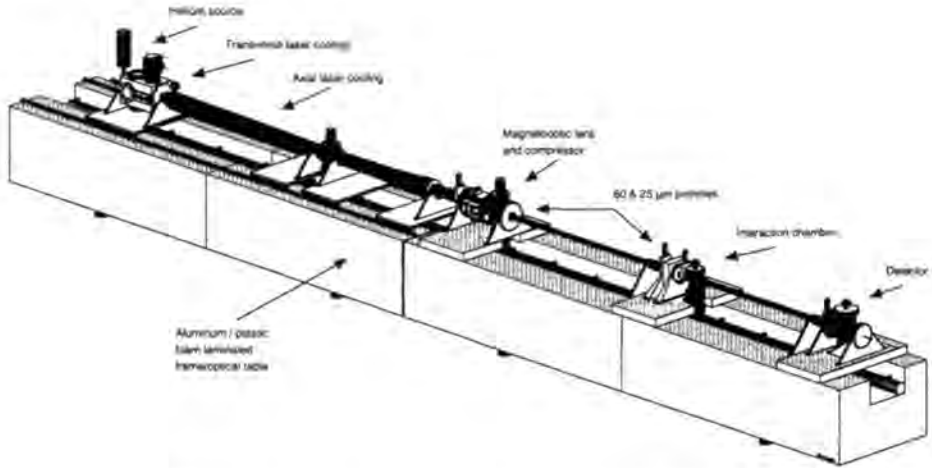
Figure 2: Artist's impression of the experimental setup.

by inserting apertures in the compressed beam. Using a 60 μm square aperture and a 25 μm diameter round aperture separated by 2 m, the geometric rms transverse velocity spread at $v_{ax} = 250$ m/s is 2.5 mm/s. The measured transverse velocity spread is 10 mm/s. We assume that the increase with respect to the geometric value is caused by Stern-Gerlach broadening in a small but strongly inhomogeneous magnetic field in the second aperture.

If we would use only source, Zeeman slower, and apertures to produce the beam, numerical simulations show that the resulting atom flux in the collimated beam is below 10^{-3} s^{-1}. Obviously this is unacceptable. In order to increase the flux, we apply various laser cooling techniques.

First, we add a two-dimensional laser cooling section directly behind the discharge source. In this section we try to capture as many atoms as possible in a parallel beam. Then, the atoms pass the Zeeman slower. Here the axial velocity is decreased, which, together with the diffusion in the transverse velocity direction, causes an increase of the beam divergence. Next, the atoms pass two stages which compress the beam to a diameter of 0.25 mm. The first stage, a magneto-optic lens (MOL), focuses the beam; the second stage, a magneto-optic compressor (MOC), is positioned near the focus of the MOL and takes care of the final beam compression. The collimated beam intensity is now increased to 250 s^{-1}.

For all laser cooling stages we use the $2^3S_1 \rightarrow 2^3P_2$ optical two-level transition of helium, with a transition wavelength of 1083 nm. The light is provided by DBR diode lasers.

We have tried to eliminate as many sources of vibrations as possible. Turbomolecular vacuum pumps with magnetic bearings, which produce roughly a factor of 10 less vibration than turbopumps with conventional bearings, are used exclusively in the setup. Other vibrations can arise from the atomic beam source and the water cooling of the Zeeman magnets. Therefore, we split the vacuum setup in two mechanically isolated parts mounted on separate frames, only connected by bellows. An artist's impression of the experimental setup is shown in Fig. 2. On the first frame we find the source, the Zeeman slower magnets and the

off-resonant
standing light wave

25 μm
aperture

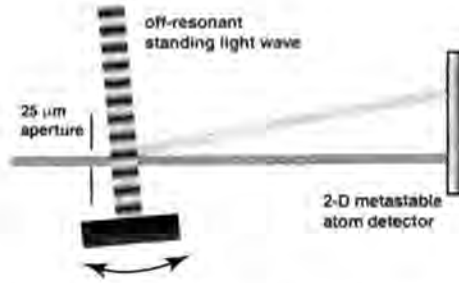2-D metastable
atom detector

Figure 3: Schematic view of the Bragg scattering setup (not to scale).

magneto-optic lens. On the second frame the magneto-optic compressor, the Doppler cooler, the interaction chamber and the detector are situated. The critical parts of the setup are thus isolated from possible vibration sources on the first frame. The second frame rests on airmounts for isolation of floor vibrations.

The frames proper consist of PVC-foam and aluminum sandwich constructions, combining low weight and high rigidity with good vibration damping. The aluminum top plates of the frames serve double duty as optical table tops.

Contamination of the vacuum by hydrocarbons could deposit on the mirror surfaces and quickly decrease the finesse of the cavity. The use of turbomolecular pumps with magnetic bearings, backed by a "dry" scroll pump, allows us to construct a completely oil-free vacuum system. The design of the setup is described in more detail in Ref. [19].

6   Coherent atomic beam splitting by Bragg scattering

In order to test the setup, we have studied Bragg scattering of the atoms in the collimated atomic beam by a "classical" standing light wave, strongly detuned with respect to the atomic resonance. The standing light wave is tilted slightly with respect to a direction transverse to the atomic beam, introducing a small angle between the wavefront planes of the light wave and the propagation direction of the atoms. The interaction length is 2 mm. Two meter downstream of the interaction region, a position-sensitive metastable atom detector allows us to register the deflection of each individual atom by the interaction with the light wave. The setup is shown schematically in Fig. 3. The periodicity of the scattering medium imposes the usual grating diffraction condition, which can be expressed for atoms as $\Delta p_t = 2n\hbar k$, with Δp_t the change in transverse momentum, n the scattering order and $\hbar k$ the single-photon recoil momentum. As in Bragg scattering of X-rays by a crystal, the finite length of the scattering medium superimposes on this the condition of either unmodified transmission or specular reflection from the scattering planes $p_t^{final} = \pm p_t^{initial}$.

In general, *individual atoms* are partially transmitted and partially reflected. Thus, a Bragg scattering region forms a *coherent* atomic beam splitter, with applications in atomic interferometry [20]. Furthermore, the splitting ratio can be adjusted from 0 to 1 simply by changing the intensity of the standing light wave.

Bragg scattering of atoms has been extensively studied [21, 22, 23, 24, 25, 26]. The

oscillatory behavior of the splitting ratio as a function of either the intensity of the standing wave or the interaction time was studied for first and second order Bragg scattering by the group of Rempe [23, 24, 26]. Up to 6th order Bragg scattering has been observed for sodium atoms in condensates [25] and for neon atoms [22] in thermal beams. However, due to the spread in axial velocity of the atoms in the beam, the diffraction orders are beginning to overlap in diffraction *angle* and thus in position on the detector.

7 Bragg scattering results

By changing the angle between the light field and the atomic beam, we have studied Bragg scattering up to 8th order. This sets a new record for Bragg diffraction of atomic beams. As Bragg scattering of order n can be considered as a $2n$−photon Raman transition, the required light intensity increases strongly with n. The available laser power (2.5 mW for the diffracting laser beam) thus forms the limiting factor for the order which can be reached.

Figure 4 shows detector images for each diffraction order studied. Up to 5th order, the laser intensity was optimized for maximum reflection: for the higher orders, optimization was for equal reflection and transmission. The detuning of the laser light from the atomic resonance was around 200 MHz. At this detuning, spontaneous emission in the interaction region cannot be completely neglected. At the maximum laser power, 30% of the atoms undergo spontaneous emission. As the spontaneously emitting atoms obtain a momentum recoil in a random direction, they do not appear in the bright spots in Fig. 4. From the detector image, we can therefore effectively discriminate between atoms which have and which have not spontaneously emitted a photon.

The rms width of the peaks in Fig. 4 corresponds to $0.15\,\hbar k$ in transverse momentum. Figure 5 shows a one-dimensional cross-section through the 5th order data. In this figure not only the transmitted and reflected peaks are visible, but also the intermediate orders can be observed. This is caused by imperfections in the wavefronts of the standing light wave. All diffraction orders are clearly separated with no trace of overlap.

For 5th order scattering we have studied the oscillatory behavior of the splitting ratio as a function of light intensity (the *Pendellösung*-effect) in detail. The results demonstrate the expected highly nonlinear behavior of the oscillation, which is a consequence of the 10-photon transition involved. The results will be published in extenso elsewhere.

8 Planned QED experiments

8.1 Quantum (non)demolition photon number measurements

The first cavity QED experiment to be performed with the beam setup is the quantum (non)demolition photon number measurement scheme discussed in Ref. [18]. The basic setup is schematically shown in Fig. 6. The high-finesse cavity ($\mathcal{F} = 650000$, distance between the mirrors $d = 0.93\,\text{mm}$) is tuned on resonance with the atomic transition. The atoms are diffracted by the quantized light field in the cavity. As the interaction region is now very short, we are now in the "thin grating" limit, with no Bragg condition imposed on the diffraction.
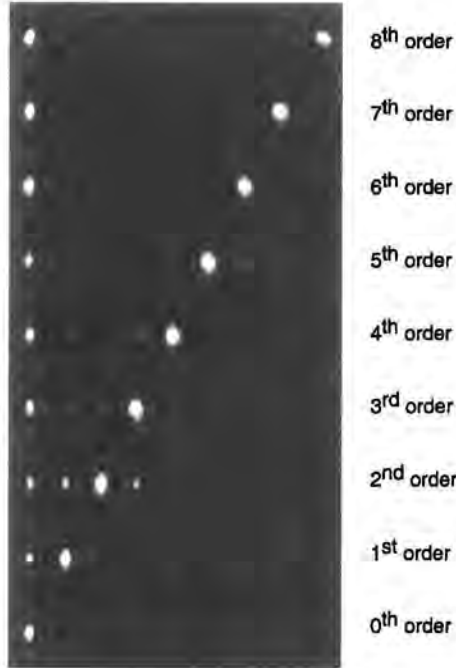
Figure 4: Detector images for 0th up to 8th order Bragg scattering.

The experimental parameters can be chosen such, that the atoms are preferentially scattered at an angle corresponding to a momentum change of of $\pm 2n\hbar k$, with n proportional to the electric field amplitude of the cavity mode. With the 0.93 mm cavity, one photon in the cavity leads to $n = 2$, i.e., scattering at an angle of $\pm 4\hbar k$. The quantization of the field in the cavity thus will be directly apparent in the absence of scattering at $\pm 2\hbar k$.

With resonant light in the cavity spontaneous emission cannot be eliminated, i.e., the interaction Hamiltonian describes a quantum demolition photon number measurement [17]. However, the ability to discriminate spontaneously emitting atoms from coherently scattered atoms allows us to select quantum nondemolition measurements from the data.

In terms of the relevant timescales for cavity QED experiments discussed previously, the ordering for the planned experiment can be expressed (with the decay rate of the upper atomic level normalized to 1):

$$g = 3.6 > \Gamma_{atom} = 1 > \Gamma_{transit} = 0.25 > \Gamma_{cavity} = 0.15.$$

8.2 Inversionless one-atom laser

Another experiment to which the setup will be applied is the study of one-atom lasers. These consist of a single atom acting as a gain medium in a small, very high-Q cavity. They provide a wonderful testing ground for cavity QED and the quantum theory of measurement. We
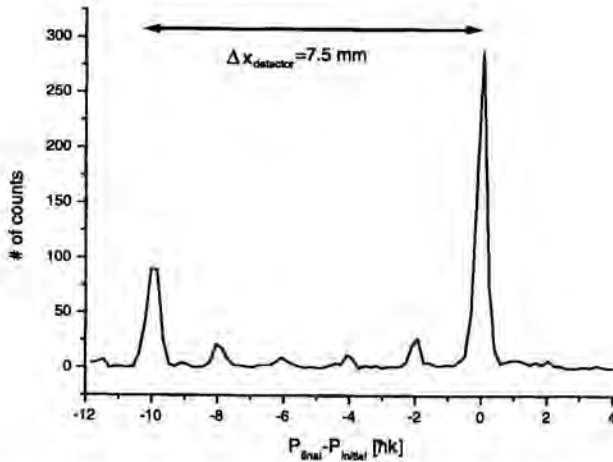
Figure 5: One-dimensional cross-section through the detector images for 5th order Bragg scattering.

Figure 6: Schematic view of the photon number measurement experiment.

propose a novel type of one-atom laser, in which a single atom in the laser cavity is continuously excited with a second (classical) light field perpendicular to the cavity mode. This two-level laser operates truly without population inversion. The gain mechanism is based on the fundamental asymmetry between absorption and stimulated emission in a quantized light field at low photon numbers. Because there is not only just one atom present in the cavity at any time, but also because the laser action is obtained with a single atom contributing to each laser pulse, the system can be described as the first *true one-atom, inversionless laser*.

The basics of the setup are shown in Fig. 7. The atoms are continuously excited on an effective two-level transition by a laser beam perpendicular to both the cavity mode and the atomic beam axis. Avalanche photodiode detectors are used to detect the output beams of the single-atom laser. In a two-level system, population inversion *cannot* be obtained with continuous pumping. However, calculations still show laser operation with several photons in the cavity on average! The origin of this 'lasing-without-inversion' effect is the fundamental asymmetry between absorption and stimulated emission in a quantum light field at low photon numbers. While the interaction matrix element for absorption scales with $\sqrt{n}$, with
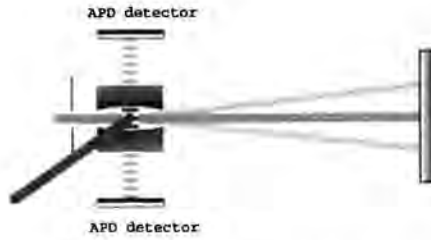
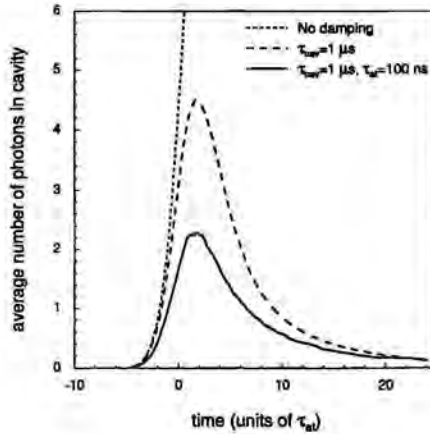Figure 7: Schematic view of the one-atom laser experiment.

Figure 8: Calculated average number of photons in the cavity for a one-atom laser with continuous coherent excitation, with the cavity initially in the vacuum state. Axial velocity 100 m/s. The center of the cavity mode is passed at $t = 0$. Dotted lines include no damping, dashed lines include only cavity damping and full lines include cavity damping and atomic decay. Time is given in units of the upper level decay time $\tau_{at} = \Gamma^{-1}$.

n the photon number, for emission it scales with $\sqrt{n+1}$. In a simple rate equation picture, where transition probabilities scale with the square of the matrix elements, this means that for zero population inversion there is a constant net "upward" transition rate for increasing the photon number equal to $g^2/2$, with g the vacuum Rabi frequency of the cavity mode.

Fig. 8 illustrates this effect. One atom traverses the cavity mode field at an axial velocity of 100 m/s, with the pump field always turned on. The atom is initially in the lower (mes-tastable) level, the cavity in the vacuum mode. The dotted line is the result of a calculation without any damping: no spontaneous emission, no cavity decay. The expectation value of the number of photons in the cavity quickly rises out of range. The dashed line incorporates cavity damping, i.e., the finite finesse of the cavity. The calculation assumes a realistic finesse of 10^6. The photon number now reaches a maximum value around 4.5. The full line includes the effects of spontaneous decay of the upper atomic level as well as of cavity damping. The maximum is reduced to 2.3, still well above 1. This demonstrates that laser action can indeed

be obtained under realistic experimental conditions.

9 Conclusions

The time (5 years), effort and money invested in the construction and testing of the setup was considerable. As a reward, we have now the highest resolution atomic beam diffraction setup available. The collimated and slowed beam which is produced can, for most purposes, be considered as a plane, monochromatic atomic wave. The two planned experiments discussed in the preceding text are just examples of a large variety of experiments in cavity QED and atom interferometry which are made possible by our setup. We have already demonstrated a large-angle coherent atomic beamsplitter, based on Bragg scattering. The separation between the two halves of the split atomic wavepacket is, at 8th order scattering, 10 mm on the detector. Using three Bragg scattering regions as beamsplitter, mirror and recombiner, this technique will allow us to construct the first Mach-Zehnder type atom interferometers with true macroscopic separation between the interfering paths. By inserting a high-finesse optical cavity in either on or both of the arms of the interferometer, atom interferometry and cavity QED can be combined. This opens up a whole new range of possible experiments. As an example, the interaction of the atom with the quantized field can be studied even when both momentum and energy of the atom are unmodified.

References

[1] M.J. Holland, D.F. Walls, P. Zoller. Phys. Rev. Lett. 67(1991) 1716

[2] K. An, J.J. Childs, R.R. Dasari, M.S. Feld. Phys. Rev. Lett. 73(1994) 3375

[3] K. An, M.S. Feld. Phys. Rev. A 52(1995) 1691

[4] D. Meschede, H. Walther, G. Müller. Phys. Rev. Lett. 54(1985) 551

[5] M. Brune, J.M. Raimond, P. Goy, L. Davidovich, S. Haroche. Phys. Rev. Lett. 59(1987) 1899

[6] G. Raithel, C. Wagner, H. Walther, L.M. Narducci, M.O. Scully. In P.R. Berman, editors, *Advances in Atomic, Molecular and Optical Physics, supplement 2: Cavity Quantum Electrodynamics*, page 57. Academic Press, San Diego (1994).

[7] G. Rempe, R.J. Thompson, R.J. Brecha, W.D. Lee, H.J. Kimble. Phys. Rev. Lett. 67(1991) 1727

[8] L. Davidovich, N. Zagury, M. Brune, J.M. Raimond, S. Haroche. Phys. Rev. A 50(1994) R895

[9] P. Domokos, J. M. Raimond, M. Brune, S. Haroche. Phys. Rev. A 52(1995) 3554

[10] X. Maître, E. Hagley, G. Nogues, C. Wunderlich, P. Goy, M. Brune, J.M. Raimond, S. Haroche. Phys. Rev. Lett. 79(1997) 769

[11] A. Rauschenbeutel, G. Nogues, S. Osnaghi, P. Bertet, M. Brune, J.M. Raimond, S. Haroche. Phys. Rev. Lett. 83(1999) 5166

[12] M. Brune, F. Schmidt-Kaler, A. Maali, J. Dreyer, E. Hagley, J.M. Raimond, S. Haroche. Phys. Rev. Lett. 76(1996) 1800

[13] M. Brune, E. Hagley, J. Dreyer, X. Maître, A. Maali, C. Wunderlich, J.M. Raimond, S. Haroche. Phys. Rev. Lett. 77(1996) 4887

[14] C.J. Hood, M.S. Chapman, T.W. Lynn, H.J. Kimble. Phys. Rev. Lett. 80(1998) 4157

[15] P. Münstermann, T. Fischer, P. Maunz, P.W.H. Pinkse, G. Rempe. Phys. Rev. Lett. 823791

[16] J. Ye, D.W. Vernooy, H.J. Kimble. Phys. Rev. Lett. 83(1999) 4987

[17] A.A. Herkommer, V.M. Akulin, W.P. Schleich. Phys. Rev. Lett. 69(1992) 3298

[18] D.S. Krämer, A.M. Herkommer, E. Mayr, V.M. Akulin, I.Sh. Averbukh, T. van Leeuwen, V.P. Yakovlev, W. Schleich. In D.F. Walls, J.D. Harvey, editors, *Quantum Optics VI*. Springer, Berlin (1994).

[19] R.M.S. Knops, A.E.A. Koolen, H.C.W. Beijerinck, K.A.H. van Leeuwen. Laser Physics 9(1999) 286

[20] D.M. Giltner, R.W. McGowan, S.A. Lee. Phys. Rev. Lett. 75(1995) 2638

[21] P.J. Martin, B.G. Oldaker, A.H. Miklich, D.E. Pritchard. Phys. Rev. Lett. 60(1988) 515

[22] D.M. Giltner, R.W. McGowan, S.A. Lee. Phys. Rev. A 52(1995) 3966

[23] S. Kunze, S. Dürr, G. Rempe. Europhys. Lett. 34(1996) 343

[24] S. Dürr, S. Kunze, G. Rempe. Quantum Semiclass. Opt. 8(1996) 531

[25] M. Kozuma, L. Deng, E.W. Hagley, J. Wen, R. Lutwak, K. Helmerson, S.L. Rolston, W.D. Phillips. Phys. Rev. Lett. 82(1999) 871

[26] S. Dürr, G. Rempe. Phys. Rev. A 59(1999) 1495

Author's address

K.A.H. van Leeuwen, A.E.A. Koolen, M.J. de Koning and H.C.W. Beijerinck:
Department of Physics,
Eindhoven University of Technology,
P.O. Box 513, 5600 MB Eindhoven,
The Netherlands;

Email address: K.A.H.v.Leeuwen@tue.nl

W.P. Schleich:
Abteilung für Quantenphysik,
Universität Ulm,
D-89069 Ulm,
Germany.

G. Harel and I. Abram

Spontaneous Emission in a Cavity:
Quantum and Classical Radiation-Reaction Viewpoint

Abstract

We derive the spontaneous emission rate of a two-level atom coupled to the vacuum of a cavity electromagnetic field using the quantum mechanical radiation-reaction formalism, and relate it to the classical expression for the emission rate of an oscillating dipole in the cavity.

1 Introduction

The recent search for ways to control the spontaneous emission in condensed-matter systems has produced a large number of relatively complex constructs, such as semiconductor microcavities with distributed Bragg reflectors and 2- or 3-dimensional photonic bandgap structures, inside which the spontaneous emission of a light-emitting center is expected to be modified [1, 2, 3, 4, 5, 6, 7, 8, 9, 10]. Quantum mechanical calculations of this modification have relied initially on a normal mode analysis of the structure and considered the coupling of the point emitter with the field of each mode. This approach has an important conceptual advantage in that it deals with the eigenstates (modes) of the field in the structure and thus conforms to the traditional quantum mechanical viewpoint for spontaneous emission: the vacuum fluctuations in each mode initiate an emission into the mode. However, it is beset by the mathematical difficulties associated with the complete modal analysis of the complicated geometries of the suggested constructs.

An alternative approach for carrying out quantum mechanical calculations on spontaneous emission is provided by the *radiation-reaction* viewpoint [11, 12, 13], which is applicable whenever the detection of the emission process is described in terms of normally ordered operators [11, 12, 13]. Since most optical experiments on spontaneous emission involve photon detection techniques which are represented by normally ordered operators, the radiation-reaction viewpoint may be considered as the natural way to describe such experiments. In this viewpoint, where the emitting dipole is driven by its own electric field (rather than by the vacuum fluctuations), which interferes with its emission. The main advantage of this viewpoint is that it concentrates on the electric field generated by the dipole at only one point, the dipole position, and thus does not require complete *modal* analysis of the surrounding microstructure. In describing the field at the site of the dipole, the contributions of the different structural elements of the microstructure (such as the reflections of the cavity mirrors) can often be treated separately by use of standard procedures, such as the method of images or finite-element numerical analysis.

In parallel to the quantum mechanical calculations, a classical approach to the modifica-

tion of spontaneous emission by the cavity boundary conditions has been developed, based on the standard classical antenna theory [14], where the modification is obtained through the direct calculation of the reflected field at the site of the dipole, or by use of the dyadic Green function technique, and the results are subsequently given the correct quantum mechanical form by the *ad hoc* introduction of appropriate constants. Although this approach is widely used in practical calculations of the spontaneous emission modification, the approximations associated with it and its domain of validity are not clear.

In this paper we derive the expression for the quantum-mechanical emission rate of a point dipole inside a cavity through the radiation-reaction point of view, and relate it to the corresponding expression that is obtained in the classical approach, thus validating the classical approach and tracing out its approximations and limitations.

2 Quantum mechanical radiation-reaction viewpoint

2.1 Effective hamiltonian

As our model we consider a two-level atom interacting with the electromagnetic field of a cavity. To derive the Hamiltonian of this system we start with the minimal-coupling Hamiltonian of a bound spinless electron coupled to the cavity field, in Gaussian units [11, 12, 15]:

$$ H = \frac{1}{2m}\left(\mathbf{p}_e - \frac{q}{c}\mathbf{A}(\mathbf{r}_e)\right)^2 + q\Phi_n(\mathbf{r}_e) + \frac{1}{8\pi}\int_V \left(\mathbf{E}_\perp^2(\mathbf{r}) + \mathbf{B}^2(\mathbf{r})\right) d\mathbf{r}. \tag{1} $$

Here $\mathbf{r}_e$ and $\mathbf{p}_e$ are the electron coordinate and canonically conjugate momentum, with commutation relations $[r_{ei}, p_{ej}] = i\hbar\delta_{ij}, q$ is the electron charge, $\Phi_n(\mathbf{r})$ is the electric potential of the nuclear charge, and $\mathbf{A}(\mathbf{r})$ is the vector potential of the field, taken in the Coulomb gauge ($\nabla \cdot \mathbf{A} = 0$). The integration $d\mathbf{r}$ extends over the volume V of the cavity, with the transverse electric field defined as $\mathbf{E}_\perp(\mathbf{r}) = -4\pi c\,\mathbf{\Pi}(\mathbf{r})$ and the magnetic field as $\mathbf{B}(\mathbf{r}) = \nabla \times \mathbf{A}(\mathbf{r})$. The field $\mathbf{\Pi}(\mathbf{r})$ is the momentum canonically conjugated to the vector potential $\mathbf{A}(\mathbf{r})$, obeying the commutation relations $[A_i(\mathbf{r}), \Pi_j(\mathbf{r}')] = i\hbar\delta_{ij}^\perp(\mathbf{r}, \mathbf{r}')$, with $\delta_{ij}^\perp(\mathbf{r}, \mathbf{r}')$ the *cavity* transverse delta function [16].

We remark that the total electric field is given by $\mathbf{E}(\mathbf{r}) = \mathbf{E}_\perp(\mathbf{r}) + \mathbf{E}_\parallel(\mathbf{r})$, where $\mathbf{E}_\parallel(\mathbf{r})$ is the longitudinal electric field which depends, in the Coulomb gauge, only on the instantaneous Coulomb potential $\Phi(\mathbf{r})$ of the atomic charges and the charges induced on the cavity mirrors, $\mathbf{E}_\parallel(\mathbf{r}) = -\nabla\Phi(\mathbf{r})$. The longitudinal electric field is thus a purely atomic operator. Its exact contribution to the atom-field Hamiltonian, namely $\frac{1}{8\pi}\int_V \mathbf{E}_\parallel^2(\mathbf{r}) d\mathbf{r}$, is adequately approximated by the term $q\Phi_n(\mathbf{r}_e)$ in Eq. (1), provided that the atom remains at a macroscopic distance from the mirrors, as we will be assuming here [15].

To describe the transverse field degrees of freedom we expand the vector potential and its canonical momentum in a set of cavity mode functions $\mathbf{f}_\lambda(\mathbf{r})$,

$$ \mathbf{A}(\mathbf{r}) = \sum_\lambda \left[\frac{2\pi\hbar c^2}{\omega_\lambda}\right]^{1/2} \left(a_\lambda \mathbf{f}_\lambda(\mathbf{r}) + a_\lambda^\dagger \mathbf{f}_\lambda^*(\mathbf{r})\right) \tag{2} $$

$$ \mathbf{\Pi}(\mathbf{r}) = -i\sum_\lambda \left[\frac{\hbar\omega_\lambda}{8\pi c^2}\right]^{1/2} \left(a_\lambda \mathbf{f}_\lambda(\mathbf{r}) - a_\lambda^\dagger \mathbf{f}_\lambda^*(\mathbf{r})\right), \tag{3} $$

with mode frequencies ω_λ and annihilation and creation operators a_λ and $a_\lambda^\dagger$ obeying the commutation relations $[a_\lambda, a_{\lambda'}] = 0$ and $[a_\lambda, a_{\lambda'}^\dagger] = \delta_{\lambda\lambda'}$. The mode functions form a complete set of solutions to the Helmholtz equation

$$\nabla \times \nabla \times \mathbf{f}_\lambda(\mathbf{r}) - \frac{\omega_\lambda^2}{c^2} \mathbf{f}_\lambda(\mathbf{r}) = 0 \tag{4}$$

obeying the transversality (Coulomb gauge) condition $\nabla \cdot \mathbf{f}_\lambda(\mathbf{r}) = 0$ and the boundary conditions of the cavity [6, 15]. They are taken to be orthonormal, $\int_V \mathbf{f}_\lambda(\mathbf{r}) \cdot \mathbf{f}_{\lambda'}^*(\mathbf{r})\, d\mathbf{r} = \delta_{\lambda\lambda'}$, and their completeness relation reads

$$\sum_\lambda f_{\lambda i}(\mathbf{r}) f_{\lambda j}^*(\mathbf{r}') = \delta_{ij}^\perp(\mathbf{r}, \mathbf{r}'). \tag{5}$$

For example, for free space with periodic boundary conditions in a cubical box of volume V the modes are $\mathbf{f}_\lambda(\mathbf{r}) = \left[\frac{1}{V}\right]^{1/2} \boldsymbol{\epsilon}_\lambda e^{i\mathbf{k}_\lambda \cdot \mathbf{r}}$, with wave vector $\mathbf{k}_\lambda$ and polarization vector $\boldsymbol{\epsilon}_\lambda$ orthogonal to it (two mutually orthogonal polarizations for each wave vector). Now we can express the magnetic and transverse-electric fields in terms of the field modes,

$$\mathbf{B}(\mathbf{r}) = \sum_\lambda \left[\frac{2\pi\hbar c^2}{\omega_\lambda}\right]^{1/2} \nabla \times \left(a_\lambda \mathbf{f}_\lambda(\mathbf{r}) + a_\lambda^\dagger \mathbf{f}_\lambda^*(\mathbf{r})\right) \tag{6}$$

$$\mathbf{E}_\perp(\mathbf{r}) = i \sum_\lambda [2\pi\hbar\omega_\lambda]^{1/2} \left(a_\lambda \mathbf{f}_\lambda(\mathbf{r}) - a_\lambda^\dagger \mathbf{f}_\lambda^*(\mathbf{r})\right), \tag{7}$$

and we can write the field Hamiltonian in the simple form $H_F = \frac{1}{8\pi} \int_V (\mathbf{E}_\perp^2(\mathbf{r}) + \mathbf{B}^2(\mathbf{r}))\, d\mathbf{r} = \sum_\lambda \hbar\omega_\lambda(a_\lambda^\dagger a_\lambda + \frac{1}{2})$.

For the atomic degrees of freedom we adopt a two-level approximate description, where instead of the complete atomic Hamiltonian $H_A = \frac{1}{2m}\mathbf{p}_e^2 + q\Phi(\mathbf{r}_e)$ we take its restriction to two levels $H_A^{\text{eff}} = \frac{1}{2}\hbar\Omega(|e\rangle\langle e| - |g\rangle\langle g|) = \frac{1}{2}\hbar\Omega\sigma_3$, with $|e\rangle$ and $|g\rangle$ the upper and lower atomic levels, assumed to have definite parity, and Ω the atomic transition frequency. Here and in what follows we employ the operators $\sigma_- \equiv |g\rangle\langle e| = \sigma_+^\dagger$, $\sigma_3 \equiv |e\rangle\langle e| - |g\rangle\langle g|$, $\mathbf{1} \equiv |e\rangle\langle e| + |g\rangle\langle g|$ as a complete set of operators for the two-level atomic Hilbert space.

Finally, to obtain a practical interaction Hamiltonian, we first neglect the relativistic term $(q^2/2mc^2)\,\mathbf{A}^2$ in Eq. (1) and introduce the dipole approximation, evaluating the vector potential at the position of the nucleus, which we take to be the origin [17]. This leaves us with $H_1 = -\frac{q}{mc}\mathbf{p}_e \cdot \mathbf{A}(0) = -\frac{1}{i\hbar c}[q\mathbf{r}_e, H_A] \cdot \mathbf{A}(0)$ as the interaction term. We then restrict H_1 to the two atomic levels $|e\rangle$ and $|g\rangle$, assuming for simplicity that they correspond to a $\Delta m = 0$ transition and that their phases are chosen such that the dipole moment matrix element $\mu \equiv \mu\hat{\mu} \equiv \langle e|q\mathbf{r}_e|g\rangle$ is real. The resulting effective interaction Hamiltonian is $\frac{\Omega}{c}i(\sigma_- - \sigma_+)\mu \cdot \mathbf{A}(0)$.

Thus we obtain an effective Hamiltonian for the atom-field system, composed of free and interaction parts,

$$H^{\text{eff}} = H_0^{\text{eff}} + H_1^{\text{eff}} = \frac{1}{2}\hbar\Omega\sigma_3 + \sum_\lambda \hbar\omega_\lambda(a_\lambda^\dagger a_\lambda + \frac{1}{2}) + i(\sigma_- - \sigma_+)\sum_\lambda \hbar C_\lambda a_\lambda + \hbar C_\lambda^* a_\lambda^\dagger, \tag{8}$$

written here in terms of the interaction frequencies $C_\lambda \equiv \Omega \left[\frac{2\pi}{\hbar\omega_\lambda}\right]^{1/2} \mu \cdot \mathbf{f}_\lambda(0)$.

2.2 Dynamics

We now proceed to determine the dynamics of our system, using the Heisenberg picture. The atomic and field operators obey the *equal-time* commutation relations $[\sigma_+(t), \sigma_-(t)] = \sigma_3(t)$, $[\sigma_3(t), \sigma_\pm(t)] = \pm 2\sigma_\pm(t)$, $[a_\lambda(t), a_{\lambda'}(t)] = 0$, $[a_\lambda(t), a_{\lambda'}^\dagger(t)] = \delta_{\lambda\lambda'}$, $[a_\lambda(t), \sigma_3(t)] = [a_\lambda(t), \sigma_\pm(t)] = 0$, which result in the following Heisenberg equations:

$$\dot{\sigma}_-(t) = \frac{1}{i\hbar}[\sigma_-(t), H^{\mathrm{eff}}] = -i\Omega\sigma_-(t) + \sigma_3(t)\sum_\lambda C_\lambda a_\lambda(t) + C_\lambda^* a_\lambda^\dagger(t) \tag{9}$$

$$\dot{\sigma}_3(t) = \frac{1}{i\hbar}[\sigma_3(t), H^{\mathrm{eff}}] = -2[\sigma_-(t) + \sigma_+(t)]\sum_\lambda C_\lambda a_\lambda(t) + C_\lambda^* a_\lambda^\dagger(t) \tag{10}$$

$$\dot{a}_\lambda(t) = \frac{1}{i\hbar}[a_\lambda(t), H^{\mathrm{eff}}] = -i\omega_\lambda a_\lambda(t) + C_\lambda^*[\sigma_-(t) - \sigma_+(t)]. \tag{11}$$

Assuming that the atom-field interaction is weak relative to the action of the free Hamiltonian H_0^{eff}, namely $\max_\lambda |C_\lambda| \ll \Omega$ and $|C_\lambda| \ll \omega_\lambda$, we can account for the free dynamics by defining new variables, $\tilde{\sigma}_\pm(t) \equiv \sigma_\pm(t)e^{\mp i\Omega t}$ and $\tilde{a}_\lambda(t) \equiv a_\lambda(t)e^{i\omega_\lambda t}$, whose evolution is expected to be slow on the time scale of Ω and ω_λ [11, 12, 13]. In terms of these variables the Heisenberg equations (9-11) read

$$\dot{\tilde{\sigma}}_-(t) = \sigma_3(t)\sum_\lambda \left(C_\lambda \tilde{a}_\lambda(t)e^{-i\omega_\lambda t} + C_\lambda^* \tilde{a}_\lambda^\dagger(t)e^{i\omega_\lambda t}\right)e^{i\Omega t} \tag{12}$$

$$\dot{\tilde{\sigma}}_3(t) = -2\left(\tilde{\sigma}_-(t)e^{-i\Omega t} + \tilde{\sigma}_+(t)e^{i\Omega t}\right)\sum_\lambda \left(C_\lambda \tilde{a}_\lambda(t)e^{-i\omega_\lambda t} + C_\lambda^* \tilde{a}_\lambda^\dagger(t)e^{i\omega_\lambda t}\right) \tag{13}$$

$$\dot{\tilde{a}}_\lambda(t) = C_\lambda^*\left(\tilde{\sigma}_-(t)e^{-i\Omega t} - \tilde{\sigma}_+(t)e^{i\Omega t}\right)e^{i\omega_\lambda t}. \tag{14}$$

We now integrate Eq. (14) with the Markovian (adiabatic) approximation of taking the slowly varying $\tilde{\sigma}_\pm(t)$ outside the integral [11, 12, 17]:

$$\tilde{a}_\lambda(t) \simeq \tilde{a}_\lambda(0) + C_\lambda^*\left(\tilde{\sigma}_-(t)\int_0^t e^{i(\omega_\lambda - \Omega)t'}dt' - \tilde{\sigma}_+(t)\int_0^t e^{i(\omega_\lambda + \Omega)t'}dt'\right). \tag{15}$$

The resulting expression for the field $\tilde{a}_\lambda(t)$ is composed of a free part, $\tilde{a}_\lambda(0)$, and a source part that depends on the dipole moment (through C_λ^*) and the atomic variables $\tilde{\sigma}_\pm(t)$. This source part is the quantum analog of the field induced by the classical current source representing the dipole oscillations [11, 12]. On substituting $\tilde{a}_\lambda(t)$ into the equivalent *normally-ordered* form of (12), $\dot{\tilde{\sigma}}_-(t) = \sum_\lambda [C_\lambda e^{i(\Omega-\omega_\lambda)t}\sigma_3(t)\tilde{a}_\lambda(t) + C_\lambda^* e^{i(\Omega+\omega_\lambda)t}\tilde{a}_\lambda^\dagger(t)\sigma_3(t)]$, and making use of the identities $\sigma_3(t)\tilde{\sigma}_\pm(t) = -\tilde{\sigma}_\pm(t)\sigma_3(t) = \pm\tilde{\sigma}_\pm(t)$, the result we find is

$$\dot{\tilde{\sigma}}_-(t) = \sum_\lambda [C_\lambda e^{i(\Omega-\omega_\lambda)t}\sigma_3(t)\tilde{a}_\lambda(0) + C_\lambda^* e^{i(\Omega+\omega_\lambda)t}\tilde{a}_\lambda^\dagger(0)\sigma_3(t)$$

$$- |C_\lambda|^2 \int_0^t (e^{i(\Omega-\omega_\lambda)(t-t')} + e^{i(\Omega+\omega_\lambda)(t-t')})dt'\,\tilde{\sigma}_-(t)$$

$$- |C_\lambda|^2 \int_0^t (e^{-i(\Omega-\omega_\lambda)(t-t')} + e^{-i(\Omega+\omega_\lambda)(t-t')})dt'e^{i2\Omega t}\,\tilde{\sigma}_+(t)]. \tag{16}$$

We now restrict our attention to the case where the field is initially in the vacuum state while the atom is in an arbitrary state: $|\psi(0)\rangle = |0\rangle(\alpha|e\rangle + \beta|g\rangle)$. On taking *vacuum expectation values* in Eq. (16), which we denote by $\langle \cdot \rangle \equiv \langle\psi(0)| \cdot |\psi(0)\rangle$, the contribution of the free field is eliminated via the identity $\bar{a}_\lambda(0)|0\rangle = 0$, and we obtain

$$\langle\dot{\bar{\sigma}}_-(t)\rangle = -\sum_\lambda |C_\lambda|^2 \int_0^t (e^{i(\Omega-\omega_\lambda)(t-t')} + e^{i(\Omega+\omega_\lambda)(t-t')})dt' \langle\bar{\sigma}_-(t)\rangle, \qquad (17)$$

where we have neglected the small contribution of the antiresonant term involving $e^{i2\Omega t}$. This equation presents the reaction of the atomic radiation back on the atomic dynamics.

To see the long-term behavior of Eq. (17), after many optical periods, we approximate the integrals on its right-hand side using Heitler's ζ function, $\zeta(\omega) \equiv -i \lim_{t\to\infty} \int_0^t e^{i\omega\tau} d\tau = \mathrm{P}\frac{1}{\omega} - i\pi\delta(\omega)$ (P denoting principal value), which gives the simple rate equation

$$\langle\dot{\bar{\sigma}}_-(t)\rangle = -i\sum_\lambda |C_\lambda|^2[\zeta(\Omega-\omega_\lambda) + \zeta(\Omega+\omega_\lambda)]\langle\bar{\sigma}_-(t)\rangle \equiv (i\Delta - \Gamma/2)\langle\bar{\sigma}_-(t)\rangle, \quad (18)$$

with real frequency shift ($\Omega \to \Omega - \Delta$) and positive decay rate:

$$\Delta = -\sum_\lambda |C_\lambda|^2 \mathrm{P}\left(\frac{1}{\Omega-\omega_\lambda} + \frac{1}{\Omega+\omega_\lambda}\right) \qquad \Gamma = 2\pi\sum_\lambda |C_\lambda|^2[\delta(\Omega-\omega_\lambda) + \delta(\Omega+\omega_\lambda)]. \quad (19)$$

Following a similar derivation, we can obtain from Eq. (13) an expression for the vacuum expectation value of the rate of change of the excited-state population: $\frac{d}{dt}\langle\bar{\sigma}_+(t)\bar{\sigma}_-(t)\rangle = -\Gamma\langle\bar{\sigma}_+(t)\bar{\sigma}_-(t)\rangle$. This allows us to identify Γ as the spontaneous emission rate of the atomic excitation.

2.3 Emission in free space

Let us check the above results in the well known case of a dipole radiating in free space. Taking the free-space mode functions with $V \to \infty$, we may approximate the summation over modes in Eqs. (19), which has the form $\sum_\lambda |C_\lambda|^2 F(\omega_\lambda)$, by integration over frequencies, $\sum_\lambda |C_\lambda|^2 F(\omega_\lambda) \simeq \int_0^\infty \rho(\omega)F(\omega)d\omega$, with the smooth weight function $\rho(\omega) = \frac{2\mu^2\Omega^2}{3\pi\hbar c^3}\omega$. Indeed, we find the expected frequency shift (Lamb shift, logarithmically divergent as it should be in a non relativistic calculation [11, 18]) and spontaneous emission rate (Einstein A coefficient),

$$\Delta = \frac{2\mu^2\Omega^2}{3\pi\hbar c^3}\mathrm{P}\int_0^\infty \left(\frac{\omega}{\omega-\Omega} - \frac{\omega}{\omega+\Omega}\right)d\omega \qquad \Gamma = \Gamma_0 \equiv \frac{4\mu^2\Omega^3}{3\hbar c^3}. \quad (20)$$

3 Classical Radiation-Reaction Viewpoint

3.1 Classical Green Function

We now turn to relate the quantum spontaneous emission rate to the expression that is obtained by classical considerations. To begin, let us write the factor $i\Delta - \Gamma/2$ of Eq. (18)

in a more explicit form, using the identity $\zeta(\omega) = -i \lim_{\epsilon \to 0+} \int_0^\infty e^{i(\omega+i\epsilon)\tau} d\tau = \lim_{\epsilon \to 0+} \frac{1}{\omega+i\epsilon}$.
Denoting $\zeta(\omega) = \frac{1}{\omega+i0^+}$ for short, we have

$$i\Delta - \Gamma/2 = i\frac{4\pi\mu^2\Omega^2}{\hbar} \sum_\lambda \frac{\Omega}{\omega_\lambda} \frac{\tilde{\mu} \cdot \mathbf{f}_\lambda(\mathbf{0})\mathbf{f}_\lambda^*(\mathbf{0}) \cdot \tilde{\mu}}{\omega_\lambda^2 - (\Omega + i0^+)^2} \simeq i\frac{4\pi\mu^2\Omega^2}{\hbar} \sum_\lambda \frac{\tilde{\mu} \cdot \mathbf{f}_\lambda(\mathbf{0})\mathbf{f}_\lambda^*(\mathbf{0}) \cdot \tilde{\mu}}{\omega_\lambda^2 - (\Omega + i0^+)^2} \quad (21)$$

We have approximated $\Omega/\omega_\lambda \simeq 1$, which is justifiable since only frequencies ω_λ nearly resonant with Ω are significant. This allows for interpretation in terms of the classical Green function, as we now show.

The dyadic Green function for the classical electric field in the space enclosed by the cavity, assuming harmonic variation in time with the frequency Ω, is defined as the solution of the equation

$$\nabla \times \nabla \times \overleftrightarrow{G}_\Omega(\mathbf{r}|\mathbf{r}') - \frac{\Omega^2}{c^2} \overleftrightarrow{G}_\Omega(\mathbf{r}|\mathbf{r}') = \overleftrightarrow{\delta}^\perp(\mathbf{r},\mathbf{r}') \quad (22)$$

obeying the boundary conditions of the cavity, where $\overleftrightarrow{\delta}^\perp(\mathbf{r},\mathbf{r}') = \sum_{i,j=1}^3 \hat{e}_i \hat{e}_j \delta_{ij}^\perp(\mathbf{r},\mathbf{r}')$ is the transverse-delta-function dyadic with $\hat{e}_i$ the coordinate unit vectors [7]. Now the Green function can be expressed in terms of the mode functions as

$$\overleftrightarrow{G}_\Omega(\mathbf{r}|\mathbf{r}') = c^2 \sum_\lambda \frac{\mathbf{f}_\lambda(\mathbf{r})\mathbf{f}_\lambda^*(\mathbf{r}')}{\omega_\lambda^2 - (\Omega + i0^+)^2} \quad (23)$$

(see Appendix A), and therefore we can combine Eqs. (21) and (23) and write

$$i\Delta - \Gamma/2 = i\frac{4\pi\mu^2\Omega^2}{\hbar c^2} \tilde{\mu} \cdot \overleftrightarrow{G}_\Omega(\mathbf{0}|\mathbf{0}) \cdot \tilde{\mu}. \quad (24)$$

Noting that the Green function $\overleftrightarrow{G}_\Omega(\mathbf{r}|\mathbf{r}')$ is essentially the transverse electric field produced at $\mathbf{r}$ by a point source at $\mathbf{r}'$, we see that the quantum frequency shift and decay rate of the atomic radiation are proportional to the radiated electric field at the site of the atom. In other words, they result from *radiation reaction*.

3.2 Classical Radiation Reaction

Now the classical derivation of the *modified* spontaneous emission rate of a point dipole inside a microcavity is based on the equation of motion of an oscillating dipole, $\boldsymbol{\mu}(t) = \tilde{\mu}\mu(t)$, consisting of a harmonically bound electron that radiates in the presence of the reflecting boundaries of the cavity. This equation reads

$$\ddot{\mu}(t) + \gamma_0\dot{\mu}(t) + \Omega^2\mu(t) = \frac{q^2}{m}\tilde{\mu} \cdot \mathbf{E}^R(t), \quad (25)$$

where Ω is the undamped oscillation frequency, γ_0 is the damping constant in the absence of mirrors, q and m are the electron charge and mass respectively, and $\mathbf{E}^R(t)$ is the electric field that is reflected by the mirrors back to the site of the emitting dipole [14, 17]. To

solve Eq. (25) we assume that the reflected field depends linearly on the instantaneous dipole magnitude, and take these two variables to be of the form $\mu(t) = \mu_0 e^{-ist}$ and $\mathbf{E}^R(t) = \mathbf{E}_0^R e^{-ist}$, where μ_0 is the dipole amplitude, assumed real, and $\mathbf{E}_0^R$ is the complex amplitude of the reflected electric field. The complex frequency $s \equiv \omega - i\gamma/2$ thus determined is

$$ s \;\simeq\; \pm\Omega\left(1 - \frac{q^2}{2\mu_0 m\Omega^2}\mathrm{Re}(\hat{\mu}\cdot\mathbf{E}_0^R) - \frac{\gamma_0^2}{8\Omega^2}\right) - i\frac{\gamma_0}{2}\left(1 \pm \frac{q^2}{\mu_0 m\Omega\gamma_0}\mathrm{Im}(\hat{\mu}\cdot\mathbf{E}_0^R)\right), \quad (26) $$

assuming $\Omega^2 \gg |q^2\hat{\mu}\cdot\mathbf{E}_0^R/(\mu_0 m)|, \gamma_0^2$, and we take the root for which $s \simeq \Omega$ as the physical solution.

Introducing the classical free-space radiative decay rate of the harmonically bound electron [17], $\gamma_0 = \frac{2q^2\Omega^2}{3mc^3}$, we can write the decay rate in the presence of the cavity mirrors as

$$ \gamma = \gamma_0\left(1 + \frac{3c^3}{2\mu_0\Omega^3}\mathrm{Im}(\hat{\mu}\cdot\mathbf{E}_0^R)\right), \quad (27) $$

which shows that the decay rate is modified by a quantity proportional to a quadrature of the reflected electric field, evaluated at the site of the emitting dipole. Thus, within this approach, the calculation of the decay-rate modification is reduced to the evaluation of the electric field at a single given point, a task which does not require the modal analysis of the cavity, but rather can be carried out through the direct-space methods that constitute the traditional arsenal of antenna theory.

At this point we assume that the same proportionality that is found in Eq. (27) between the modification to the decay rate and the reflected field at the site of the dipole, $\mathbf{E}_0^R$, holds true also in the quantum regime, even though the field is calculated classically, and moreover, that it extends to give the total (modified) decay rate as a function of the total transverse field at the dipole position, $\mathbf{E}_\perp(0)$. We replace the free-space decay constant γ_0 by the quantum mechanical free-space spontaneous emission rate, Γ_0 of Eq. (20), and take the amplitude of the dipole oscillations to be equal to the quantum dipole moment transition matrix element, $\mu_0 = \mu$. This gives a markedly simple expression for the decay rate:

$$ \gamma = \Gamma_0 \frac{3c^3}{2\mu\Omega^3}\,\mathrm{Im}\left(\hat{\mu}\cdot\mathbf{E}_\perp(0)\right) = \frac{2\mu}{\hbar}\,\mathrm{Im}\left(\hat{\mu}\cdot\mathbf{E}_\perp(0)\right). \quad (28) $$

We now show that this decay rate is equal to the quantum decay rate obtained above. Indeed, the transverse field is determined by the Coulomb-gauge vector potential $\mathbf{A}(\mathbf{r})e^{-ist}$, to zeroth order in $\gamma/\Omega \ll 1$, as

$$ \mathbf{E}_\perp(\mathbf{r}) = \mathbf{E}(\mathbf{r}) + \nabla\Phi(\mathbf{r}) = \frac{is}{c}\mathbf{A}(\mathbf{r}) \simeq \frac{i\Omega}{c}\mathbf{A}(\mathbf{r}). \quad (29) $$

Moreover, using the classical Green function to relate the vector potential to the current density contributed by the atomic dipole, $\mathbf{J}(\mathbf{r}) = -is\hat{\mu}\mu\delta(\mathbf{r}) \simeq -i\Omega\hat{\mu}\mu\delta(\mathbf{r})$, we have

$$ \mathbf{A}(\mathbf{r}) \;=\; \int_V \overset{\leftrightarrow}{G}_{\mathrm{n}}(\mathbf{r}\,|\,\mathbf{r}')\left[\frac{4\pi}{c}\mathbf{J}(\mathbf{r}') + \frac{i\Omega}{c}\nabla\Phi(\mathbf{r}')\right]dr' = -\frac{4\pi i\Omega\mu}{c}\overset{\leftrightarrow}{G}_{\mathrm{n}}(\mathbf{r}\,|\,0)\cdot\hat{\mu} \quad (30) $$

(see Appendix B). This allows us to write the transverse field as a function of the dipole amplitude and the cavity geometry (Green function), $\mathbf{E}_\perp(\mathbf{0}) = \frac{4\pi\Omega^2\mu}{c^2} \overset{\leftrightarrow}{G}_\Omega(\mathbf{0}|\mathbf{0}) \cdot \hat{\mu}$, and we see that the resulting expression for the decay rate,

$$\gamma = \frac{8\pi\mu^2\Omega^2}{\hbar c^2} \operatorname{Im}\left(\hat{\mu} \cdot \overset{\leftrightarrow}{G}_\Omega(\mathbf{0}|\mathbf{0}) \cdot \hat{\mu}\right), \tag{31}$$

is exactly the same as the expression for the quantum decay rate Γ given in Eq. (24).

4 Conclusion

We have seen that the classical radiation-reaction approach to the modification of spontaneous emission rate by cavity boundaries leads to the same result that is obtained by a systematic quantum mechanical calculation through the radiation-reaction viewpoint. In both cases the transverse field plays a central role in determining the decay rate. The significance and domain of validity of the classical result can be inferred from the quantum derivation, namely, it is the decay rate of the atomic excitation vacuum-expectation-value, describing the long-term behavior after many optical periods, which is obtained from a nonrelativistic calculation ignoring spin effects, with the following assumptions and approximations: (i) two-level approximation for the atomic dynamics; (ii) atom located at macroscopic distance from cavity boundaries; (iii) weak, Markovian atom-field coupling; (iv) dipole approximation; and (v) rotating-wave approximation.

5 Acknowledgements

Appendix A

We need to show that the dyadic function $\overset{\leftrightarrow}{G}_\Omega(\mathbf{r}|\mathbf{r}') = c^2 \sum_\lambda \frac{\mathbf{f}_\lambda(\mathbf{r})\mathbf{f}_\lambda^*(\mathbf{r}')}{\omega_\lambda^2 - (\Omega + i0^+)^2}$ is a solution of Eq. (22) obeying the boundary conditions of the cavity. Indeed, $\overset{\leftrightarrow}{G}_\Omega(\mathbf{r}|\mathbf{r}')$ satisfies the boundary conditions as a function of $\mathbf{r}$, being a linear superposition of the mode functions $\mathbf{f}_\lambda(\mathbf{r})$ which have this property by definition. Moreover, in view of Eqs. (4) and (5) we have as required

$$\begin{aligned}
\nabla \times \nabla \times \overset{\leftrightarrow}{G}_\Omega(\mathbf{r}|\mathbf{r}') - \frac{\Omega^2}{c^2} \overset{\leftrightarrow}{G}_\Omega(\mathbf{r}|\mathbf{r}') &= \sum_\lambda \frac{(\omega_\lambda^2 - \Omega^2)\mathbf{f}_\lambda(\mathbf{r})\mathbf{f}_\lambda^*(\mathbf{r}')}{\omega_\lambda^2 - (\Omega + i0^+)^2} \\
&= \sum_\lambda \mathbf{f}_\lambda(\mathbf{r})\mathbf{f}_\lambda^*(\mathbf{r}') = \overset{\leftrightarrow\perp}{\delta}(\mathbf{r}, \mathbf{r}').
\end{aligned} \tag{32}$$

We note that the definition of $\overset{\leftrightarrow}{G}_\Omega(\mathbf{r}|\mathbf{r}')$ with the term $i0^+$ fixes its poles at the lower half complex plane, $\Omega = \pm\omega_\lambda - i0^+$, and therefore ensures that its inverse Fourier transform is

the *causal* Green function:

$$\overset{\leftrightarrow}{G}(\mathbf{r},t|\mathbf{r}',t') \equiv \frac{1}{2\pi}\int_{-\infty}^{\infty} d\Omega\, e^{-i\Omega(t-t')}\overset{\leftrightarrow}{G}_\Omega(\mathbf{r}\,|\mathbf{r}') \tag{33}$$

$$= \begin{cases} 0 & t \leq t' \\ c^2 \sum_\lambda \mathbf{f}_\lambda(\mathbf{r})\mathbf{f}_\lambda^*(\mathbf{r}')\frac{\sin[\omega_\lambda(t-t')]}{\omega_\lambda} & t \geq t' \end{cases}$$

$$\left[\nabla \times \nabla \times +\frac{1}{c^2}\frac{\partial^2}{\partial t^2}\right]\overset{\leftrightarrow}{G}(\mathbf{r},t|\mathbf{r}',t') = \overset{\leftrightarrow}{\delta}^\perp(\mathbf{r},\mathbf{r}')\delta(t-t'). \tag{34}$$

Appendix B

The vector potential is related to the current density and the scalar potential, assuming harmonic time variation $e^{-i\Omega t}$, through the Maxwell equation

$$\left[\nabla \times \nabla \times +\frac{1}{c^2}\frac{\partial^2}{\partial t^2}\right]\mathbf{A}(\mathbf{r},t) = \frac{4\pi}{c}\mathbf{J}(\mathbf{r},t) - \frac{1}{c}\frac{\partial}{\partial t}\nabla\Phi(\mathbf{r},t), \tag{35}$$

or, assuming harmonic time variation $e^{-i\Omega t}$, through $\left[\nabla \times \nabla \times -\frac{\Omega^2}{c^2}\right]\mathbf{A}(\mathbf{r}) = \frac{4\pi}{c}\mathbf{J}(\mathbf{r}) + \frac{i\Omega}{c}\nabla\Phi(\mathbf{r})$. With our choice of the Coulomb gauge, the vector potential $\mathbf{A}(\mathbf{r})$ and, consequently, both sides of this equation are transverse. Therefore, we can solve this equation in the space of transverse functions obeying the cavity boundary conditions, using the Green function: $\mathbf{A}(\mathbf{r}) = \int_V \overset{\leftrightarrow}{G}_\Omega(\mathbf{r}\,|\mathbf{r}')\left[\frac{4\pi}{c}\mathbf{J}(\mathbf{r}') + \frac{i\Omega}{c}\nabla\Phi(\mathbf{r}')\right]d\mathbf{r}'$. Now the term $\frac{i\Omega}{c}\nabla\Phi(\mathbf{r}')$ is longitudinal and hence does not contribute to the integration, since it is multiplied by $\overset{\leftrightarrow}{G}_\Omega(\mathbf{r}\,|\mathbf{r}')$ which is transverse in $\mathbf{r}'$. The result for the dipole current density $\mathbf{J}(\mathbf{r}) = -i\Omega\hat{\mu}\mu\delta(\mathbf{r})$ is therefore $\mathbf{A}(\mathbf{r}) = -\frac{4\pi i\Omega\mu}{c}\overset{\leftrightarrow}{G}_\Omega(\mathbf{r}\,|0)\cdot\hat{\mu}$.

References

[1] J.P. Wittke. RCA Rev. 36(1975) 655
[2] J.M. Wylie, J.E. Sipe. Phys. Rev. A 30(1984) 1185
[3] E. Yablonovitch. Phys. Rev. Lett. 58(1987) 2059
[4] D.G. Deppe, J.C. Campbell, R. Kuchibhotla, T.J. Rogers, B.G. Streetman. Electronics Letters 26(1990) 1665
[5] D.G. Deppe, C. Lei. J. Appl. Phys. 70(1991) 3443
[6] R.J. Glauber, M. Lewenstein. Phys. Rev. A 43(1991) 467
[7] J.P. Dowling, C.M. Bowden. Phys. Rev. A 46(1992) 612
[8] M.S. Tomaš. Phys. Rev. A 51(1995) 2545
[9] I. Abram, J.L. Oudar. Phys. Rev. A 51(1995) 4116
[10] I. Abram, G. Bourdon. Phys. Rev. A 54(1996) 3476
[11] J.R. Ackerhalt, P.L. Knight, J.H. Eberly. Phys. Rev. Lett. 30(1973) 456
[12] P.W. Milonni, W.A. Smith. Phys. Rev. A 11(1975) 814
[13] H.J. Kimble, L. Mandel. Phys. Rev. A 13(1976) 2123

[14] R.R. Chance, A. Prock, R. Silbey. Adv. in Chem. Phys. 37(1978) 1

[15] S. Haroche. In J. Dalibard, J.-M. Raimond, J. Zinn-Justin, editors, *Fundamental systems in quantum optics*, 1990 Les Houches Lectures Session LIII, Amsterdam (1992)

[16] The cavity transverse delta function $\delta_{ij}^{\perp}(\mathbf{r}, \mathbf{r}')$ is the projection on the space of transverse functions obeying the cavity boundary conditions (see Refs. [6, 7]). In the free space limit $V \to \infty$ with periodic boundary conditions it is the distribution $\delta_{ij}^{\perp}(\mathbf{r}, \mathbf{r}') = (2\pi)^{-3} \int d\mathbf{k}\, e^{i\mathbf{k}\cdot(\mathbf{r}-\mathbf{r}')}(\delta_{ij} - k_i k_j/k^2)$

[17] L. Allen, J.H. Eberly. *Optical resonance and two-level atoms.* Wiley, New York (1975)

[18] H.A. Bethe. Phys. Rev. 72(1947) 339

Author's address

G. Harel:
Department of Physics and Astronomy,
Vrije Universiteit, De Boelelaan 1081, 1081 HV Amsterdam,
The Netherlands;

I. Abram:
France Telecom/CNET,
Laboratoire CDP,
196 Avenue Henri Ravera, 92225 Bagneux Cedex,
France.

M. Hentschel and J.U. Nöckel

The Sequential-Reflection Model in Deformed Dielectric Cavities

Abstract

The stationary states of a microlaser are related to the decaying quasibound states of the corresponding passive cavity. These are interpreted classically as originating from sequential escape attempts of an ensemble of rays obeying a curvature-corrected Fresnel formula. Polarization-dependent predictions of this model, and its limitations for stable orbits in partially chaotic systems are discussed.

As a mechanism for achieving mode confinement, waveguiding by total internal reflection is ubiquitous in optics. However, in dielectric microresonators where three-dimensionally confined mode volumes are desired, there is always leakage because the ray picture, in which Fresnel's formulas describe the outcoupling, acquires corrections. Leaky modes corresponding to classically confined rays can be found, e.g., in optical fibers as "spiral" modes [1], or in laterally structured cylindrical VCSELs [2] as well as in microdisk lasers [3]. The classically forbidden loss in such modes is analogous to tunneling through an effective potential barrier [4].

The highest Q is achieved for modes which semiclassically correspond to rays almost at grazing incidence. Resonators with a circular cross section are a particularly simple realization of this requirement, because they exhibit *whispering-gallery* (WG) modes characterized by high intensity in an annular region near the surface. However, even Lord Rayleigh who first described the acoustic analog that gave the phenomenon its name, concluded [5] that it requires only an everywhere positive curvature, not necessarily rotational symmetry. A rigorous proof of this is difficult because in the short-wavelength limit, this "clinging" of waves to the walls has to carry over to the ray picture, in which a generic oval cavity exhibits a transition to chaos [6, 7]. Notwithstanding, this problem is fundamental to microresonator design [8], because the availability of high-Q modes is the foremost selection criterium in an otherwise unbounded space of potential resonator shapes [9]. Chaos can in fact make WG modes more useful, and moreover create other types of modes with desirable properties, such as the bowtie pattern whose confocal geometry points the way toward the strong-coupling regime in combination with focused emission [10, 11].

The robustness of whispering-gallery type intensity patterns in the modes of convex resonators extends even to nonlinear media [12]. However, in that case the distinction to the widely studied phenomenon of vortex formation [13] becomes washed out: a WG mode is

also a vortex with a phase singularity at points of vanishing intensity; for a circular resonator where the field is proportional to a Bessel function $J_m(kr) \approx r^m$ near the center $r = 0$, the vorticity is simply the angular momentum quantum number m. Therefore, since our aim is to address the fundamental aspect of the shape dependence of high-Q modes in microresonators, we focus here on linear media where amplification is taken into account by a negative imaginary part of the refractive index $\bar{n}$.

The model considered here can be derived from a homogenous cylinder by deforming its cross section and considering only propagation transverse to its axis. In this case, TE and TM polarization are decoupled and one has to consider only a scalar wave equation

$$\nabla^2 \psi + \bar{n}^2 k^2 \, \psi = 0, \tag{1}$$

assuming a steady state time dependence so that k is real. Here, $\bar{n} \equiv n - i \, n'$ inside the resonator and $\bar{n} = 1$ outside, giving rise to an exterior and interior field, ψ_{ext} and ψ_{int}, both of which are connected by the proper matching conditions at the dielectric interface, depending on polarization. For TM modes, ψ denotes the electric field, which is parallel to the cylinder axis. In this case one finds that ψ and its normal derivative are continuous at the interface, in analogy to quantum mechanics.

The system is open because it radiates energy into the environment via its modal losses. This openness increases as $n \to 1$, and the closed-resonator limit is approached for $n \to \infty$. This can be understood from Fresnel's formulas which imply total internal reflection for all angles of incidence χ satisfying $\sin\chi > 1/n \equiv \sin\chi_c$ (χ_c is the *critical angle*). Equation (1) can be recast as

$$\nabla^2 \psi + n^2 \bar{k}^2 \, \psi = 0, \tag{2}$$

where n is the real part of $\bar{n}$ as defined above, and $\bar{k} \equiv k - i \, k \, n'/n$ is a complex wavenumber inside the cavity but reduces to $\bar{k} = k$ outside. If instead of this we also had $\bar{k} = k - i \, k \, n'/n$ outside, the solutions of Eq. (2) would be the *quasibound states* of the passive resonator, as they arise when one assumes a decaying time dependence $\propto \exp[-ick\,t - \gamma\,t]$, where $\gamma = ck \, n'/n$.

For a quasibound (or metastable) state, the field at distances larger than $\approx c/(2\gamma)$ from the cavity grows epxonentially due to retardation, but within this physical range ψ_{ext} vanishes as $\gamma \to 0$, so that one can write $\psi_{\text{ext}}(\mathbf{r}) \approx \gamma\zeta(\mathbf{r})$. If one expands the dependence of ψ_{int} and ζ on γ in a Taylor series, then to linear order the γ-dependence of ζ, but not that of ψ_{int}, can be dropped in the full solution. Therefore, the stationary state of the active medium and the metastable decaying state are identical to first order in γ within an area of order γ^{-2}.

This approximate equivalence establishes a connection to the study of S-matrix poles from which quasibound states arise, see [14], and to dissipation in quantum mechanics [15, 16]. The recent resurgence of interest in these problems is motivated to a significant extent by our lack of understanding of the quantum-to-classical transition, in particular in the presence of classical chaos. Precisely this constellation is also present in Eq. (2) when one considers its short-wavelength limit for the generic case of a deformed cavity.

In the context of laser resonators, there are three main differences to previous work on open systems in the context of quantum chaos, see also [17, 18]: firstly, we are interested

The Sequential-Reflection Model in Deformed Dielectric Cavities

in the properties of *individual* states of an open system, as opposed to a statistical ensemble. Secondly, an important quantity that can be studied for such individual states is their *emission directionality*, which in other open systems of chemical or nuclear physics is averaged out. Finally, the classical limits of quantum mechanics with smooth potentials and optics with discontinuous refractive indices are qualitatively different [19]: the first yields deterministic Hamiltonian mechanics; the second leads to the probabilistic Fresnel formulas which moreover depend on polarization.

In principle, Eq. (2) can be solved numerically to find the discrete complex $\bar{k}$ and the corresponding modes. One approach is based on the Rayleigh hypothesis [20, 21] which in our implementation for quasibound states [7] assumes that the fields can be expanded in cylinder functions as

$$a\psi_{\text{int}}(r, \phi) = \sum_m A_m J_m(kr) e^{im\phi}, \tag{3}$$

$$\psi_{\text{ext}}(r, \phi) = \sum_m B_m H_m^{(1)}(kr) e^{im\phi}.$$

a where a polar coordinate system with suitably chosen origin is used. These expansions always work inside some circle of convergence for ψ_{int} and outside some other circle for ψ_{ext}, and for a large range of resonator shapes both convergence domains contain the dielectric interface where the matching conditions are imposed to obtain equations for the unknown coefficients A_m and B_m.

Computational cost can be high here, especially at short wavelengths, and hence a semiclassical approximation can lead to simplifications while preserving physical insight. The ray picture is a cornerstone of classical optics, but its value in the study of open resonators only unfolds when the ray dynamics is studied in *phase space* [22, 7, 23, 24], because Fresnel's formulas determine escape probabilities according to the angle of incidence χ, not the position of impact. One can make use of the physical information contained in this picture in two ways: Either one starts from Eq. (2) and takes a short-wavelength limit [25]; or alternatively, one starts from the classical dynamics and makes *classical* approximations that allow one to impose simple quantization conditions and thus make the connection to the resonator modes [8]. The question whether these different routes meet "in the middle" is not straightforward because the problem of semiclassical quantization in a generic deformed resonator is not completely solved as yet, owing to the coexistence of both regular and chaotic motion in their classical phase space.

Among the advantages of the ray-based approach [8] are its flexibility and computational ease. However, in order for the prescription outlined in Ref. [8] to correctly describe the limiting case of a circular cylinder, one must include the tunneling which in the circle is the only loss mechanism. This can be done in the ray picture with a curvature- and wavelength dependent "rounding" of Fresnel's formulas which the simulation uses at each reflection along a ray path. The idea used in [8] was to interpret the resonance widths of a cirular cylinder in terms of a "sequential-tunneling" ansatz: if the intensity of a quasibound state decays as $\exp[-2\gamma t]$, this can be interpreted in the ray picture as the result of ν sequential escape attempts with reflection probability p_0, where ν is the number of reflections the ray undergoes during the time t. In a circle of radius R, a trajectory characterized by the angle of incidence

χ has $\nu = ct/(nL)$ reflections during t (c/n is the speed of light in the passive medium and $L = 2R \cos \chi$ is the geometric path length between reflections). Therefore, one expects a decay law $\propto p_0^\nu = \exp[ct \ln p_0/(nL)]$. Comparison with the wave result yields

$$p_0 = \exp(-2\,nL\gamma/c) \tag{4}$$

An analytic approximation for γ in the circle with TM polarization has been derived in [26],

$$\gamma \approx -\frac{c}{2nR} \ln \left[\frac{n-1}{n+1} \right] \times \tag{5}$$
$$\frac{J_m(kR)Y_{m-1}(kR) - J_{m-1}(kR)Y_m(kR)}{J_m^2(kR) + Y_m^2(kR)}.$$

Using the semiclassical expression

$$m = nkR \sin \chi \tag{6}$$

for the angular momentum [7], one then obtains the reflecticity in terms of purely classical variables, $p_0(kR, \sin \chi)$. It reduces to Fresnel's formula in the limit of large radius of curvature R, and by construction reproduces the width of a mode in the circle if applied locally at each reflection in in our classical ray model. The latter does not hold uniformly for a similar correction derived in [27].

One drastic consequence of the different classical limits for smooth and discontinuous potentials is that in the latter, all resonances of the passive dielectric are narrower than a certain *maximum width* if we choose the polarization in which ψ is continuosly differentiable as in quantum mechanics. But in quantum mechanics (or for smooth index profiles) one generally finds resonances of arbitrarily large width at increasing k. The classical argument for this statement will be given further below.

From the classical limit, it follows that there exists an *upper bound* on resonance widths for dielectric cavities with stepped index profiles and "quantum-mechanical" continuity conditions on ψ, because the reflectivity p_0, (for polarization perpendicular to the plane of incidence), is bounded away from zero. This minimum $p_{0,min}$ will limit the width of resonances in a cavity of characteristic size l to $\gamma_{max} = -c \ln p_{0,min}/(2nl)$. Smooth index profiles can also appear discontinuous on the scale of the wavelength but are eventually resolved as $k \to \infty$, allowing arbitrarily small reflectivities at perpendicular incidence.

However, extending these arguments to *TE polarization* where the electric field is in the plane of incidence, we furthermore conclude that a similar upper bound on the widths does *not exist* even for sharp interfaces. The reason is that Fresnel's formula yields zero reflectivity at the *Brewster angle* χ_B at $\sin \chi_B = (1 + n^2)^{-1}$. The normal derivative of ψ (which now represents the magnetic field) exhibits a jump proportional to n^2 at the dielectric interface – reminding us that this is a situation unique to optics. These general considerations have important implications for microresonator design especially at the large n typical for semicondutors, because in that case $\sin \chi_B \to 1/n$, i.e., the "hole" in the reflectivity for TE polarization approaches χ_c for total internal reflection from below. Taking tunneling due to finite curvature into account as in Eq. (4), the rounded Fresnel formula then exhibits reduced
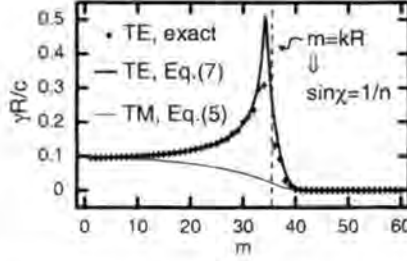
Figure 1: Exact resonance widths of a circle (radius R, refractive index $n = 3.29$) at $35 < kR < 35.5$ versus angular momentum m. Dashed line indicates χ_c in Fresnel's law, using Eq. (6). Also shown are the TM widths. The Brewster angle is at $m \approx 34$ and causes a peak in the TE widths.

reflectivity even for incidence somewhat above χ_c. One can approximately obtain the TE widths of the circle from $\gamma = -c\,\mathrm{Im}[\sigma]/(nR)$,

$$\sigma \approx \arctan\left[\left(n\frac{H_{m-1}^{(1)}(kR)}{H_m^{(1)}(kR)} - \frac{m}{kR}\left(n - 1/n\right)\right)^{-1}\right] \tag{7}$$

This is illustrated in Fig. 1, where refractive index and kR are chosen close to those of Ref. [10]. The reason is that the *quantum-cascade* material used there emits preferentially TM polarization, whereas the pioneering MQW microdisk lasers with sub-micron thickness permit guiding in the vertical direction only for TE modes [cf. McCall [3]; there, TE/TM must be interchanged to get from the slab-waveguide to our cylinder convention]. It is thus important to ascertain whether the identical oval lateral design of the quantum-cascade lasers in Ref. [10] would also permit a microdisk laser to operate in TE polarization.

The lasing mode in Fig. 3D of [10] was identified as a bowtie-shaped pattern corresponding to a periodic ray path with angle of incidence given by $\sin \chi \approx 1/n$, i.e., directly at the critical angle. That this mode provides high Q can be seen by comparing to γ in Fig. 1: assuming that the width γ_B of a bowtie mode results from the sequential application of p_0 as determined for the circle, the argument leading to Eq. (4) implies that $\gamma_B \approx \gamma L/l$ where $L/l \approx 1.13$ is the ratio of the classical path lengths between reflections in the WG orbit and bowtie, respectively. One sees that the TM line intersects the critical angle (corresponding to $m = kR$) at a much smaller width than the TE curve, and this Q-spoiling due to Brewster transmission is borne out by the actual TE resonances as well. This leads to the prediction that conventional microdisk lasers with a shape designed to yield a bowtie pattern just at χ_c as in Fig. 3D of [10] will *not lase*.

These ray arguments are known to yield large deviations from the true resonance widths when the modes under consideration are quantized on stable phase-space domains in a partially chaotic system, cf. Ref. [8] where this was attributed to chaos-assisted tunneling. The latter yields enhanced outcoupling and hence the true widths are *underestimated* by the sequential ray picture. Therefore, the above Q-spoiling for TE modes is not counteracted by a correction of this nature. The prediction of an upper bound for TM widths is also not affected by chaos-assisted tunneling because it cannot be faster than the fasted classical pro-
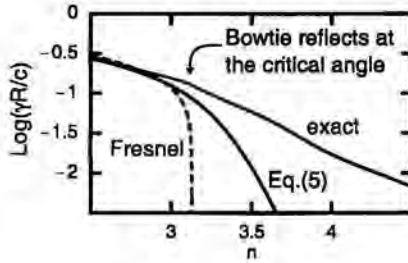
Figure 2: Width of a TM bowtie mode vs. refractive index, from numerical and ray calculations.

cess, which in turn is limited by p_0 at $\sin \chi = 0$. Beyond this, however, quantitative widths for stable-orbit modes in mixed phase spaces are not provided by the ray model.

The disagreement is illustrated in Fig. 2 for a bowtie mode similar to the ones studied in [25], as a function of n, but at a deformation of $\epsilon = 0.16$ [defined as in [10]] and $nkR \approx 119.8$. Since nk is the wavenumber inside the resonator, it should remain approximately independent of n as long the outcouplig can be taken into account in the form of a boundary phase shift intermediate between Dirichlet and Neumann. Indeed, for the state shown in Fig. 2, the change in nkR in the plotted range of n is only ≈ 0.2. The length scale R here is the radius of curvature at the points of reflection. At small n where χ_c is larger than the angle of incidence of the bowtie, escape is classically allowed in Fresnel's formula and hence curvature corrections are unimportant. At $n > 3$, the tunneling correction in Eq. (5) does improve on the classical Fresnel prediction ($\gamma = 0$) but clearly still underestimates the true width. As tunneling in general is definable only with respect to a classical expectation, we could again label the discrepancy as chaos-assisted tunneling. However, a semiclassical theory starting from Eq. (2) which reproduces the exact behavior in Fig. 2 very well [25] can shed more light on the physics of the phenomenon.

References

[1] A.W. Poon, R.K. Chang, J.A. Lock. Opt. Lett. 23(1998) 1105
[2] J.C. Ahn, K.S. Kwak, B.H. Park, H.Y. Kang, J.Y. Kim, O'Dae Kwon. Phys. Rev. Lett. 82(1999) 536
[3] S.L. McCall, A.F. Levi, R.E. Slusher, S.J. Pearton, R.A. Logan. Appl. Phys. Lett. 60(1992) 289
[4] B.R. Johnson. J. Opt. Soc. Am. 10(1993) 343
[5] J.W. Strutt, Baron Rayleigh. *The Theory of Sound*, volume II. Dover, New York (1945)
[6] V.F. Lazutkin. *KAM Theory and Semiclassical Approximations to Eigenfunctions*. Springer, New York (1993)
[7] J.U. Nöckel, A.D. Stone. In R.K. Chang, A.J. Campillo, editors, *Optical Processes in Microcavities*. World Scientific, Singapore (1996).
[8] J.U. Nöckel, A.D. Stone. Nature 385(1997) 45
[9] G. Angelow, F. Laeri, T. Tschudi. Opt. Lett. 211324
[10] C. Gmachl, F. Capasso, E.E. Narimanov, J.U. Nockel, A.D. Stone, J. Faist, D.L. Sivco, A.Y. Cho. Science 280(1998) 1556

[11] S.E. Morin, C.C. Yu, T.W. Mossberg. Phys. Rev. Lett. 73(1994) 1489

[12] T. Harayama, P. Davis, K.S. Ikeda. Phys. Rev. Lett. 82(1999) 3803

[13] C.O. Weiss, M. Vaupel, K. Staliunas, G. Slekys, V.B. Taranenko. Appl. Phys. B 68(1999) 151

[14] M. Patra, H. Schomerus, C.W.J. Beenakker. cond-mat/9905019 (1999)

[15] I. Prigogine. Phys. Rep. 219(1992) 93

[16] D. Braun, P.L. Braun and F. Haake. Physica D 131(1999) 265

[17] G.Casati, G. Maspero, D.L. Shepelyanski. Phys. Rev. E 56(1997) R6233

[18] G.Casati, G. Maspero, D.L. Shepelyanski. Physica D 131(1999) 311

[19] A. Kohler, R. Blümel. Ann. Phys. 267(1998) 249

[20] P.M. van den Berg, J.T. Fokkema. IEEE Trans. Anten. Propag. AP-27(1979) 577

[21] J.P. Barton. Appl. Opt. 36(1997) 1312

[22] J.U. Nöckel, A.D. Stone, R.K. Chang. Optics Letters 19(1994) 1693

[23] J.U. Nöckel, A.D. Stone, G. Chen, H. Grossman, R.K. Chang. Opt. Lett. 21(1996) 1609

[24] A. Mekis, J.U. Nöckel, G. Chen, A.D. Stone, R.K. Chang. Phys. Rev. Lett. 75(1995) 2682

[25] E.E. Narimanov, G. Hackenbroich, P. Jaquod, A. Douglas Stone. cond-mat/9907109 (1999)

[26] J.U. Nöckel. Dissertation, Yale University (1997)

[27] A.W. Snyder, J.D. Love. IEEE Trans. MTT-23(1975) 134

Author's address

Max-Planck-Institut für Physik komplexer Systeme,
Nöthnitzer Str. 38, 01187 Dresden,
Germany.